Hot gas and galaxies in large-scale structures: a case study of two clusters and a supercluster

by

Juhi Tiwari

A thesis submitted for the partial fulfillment of

the degree of Doctor of Philosophy

to

Department of Physical Sciences
Indian Institute of Science Education and Research Mohali
Knowledge City, Sector 81, SAS Nagar, Manauli PO, Mohali 140306, Punjab, India.

August, 2022

Declaration

The work presented in this thesis has been carried out by me under the guidance of Prof. Kulinder Pal Singh, Prof. Jasjeet Singh Bagla, and Dr. Smriti Mahajan at the *Indian Institute of Science Education and Research Mohali*, India. This work has not been submitted in part or in full for a degree, a diploma, or a fellowship to any other university or institute. Whenever contributions of others are involved, every effort is made to indicate this clearly, with due acknowledgement of collaborative research and discussions. This thesis is a bonafide record of original work done by me and all sources listed within have been detailed in the bibliography.

[Signature]
Juhi Tiwari

In my capacity as supervisor/co-supervisor of the candidate's thesis, I certify that the above statements are true to the best of my knowledge.

[Signature]	**[Signature]**	**[Signature]**
J. S. Bagla	K. P. Singh	S. Mahajan
Supervisor	Co-supervisor	Co-supervisor

To my parents,
the astronomical community,
and everyone who has been part of my bittersweet research journey...

Acknowledgements

My sincere gratitude to my primary advisor Prof. Kulinder Pal Singh (*sobriquet 'KP from TIFR'*). Thank you, Sir, for your guidance, and all that extra push and constructive feedback over these years. If it were not for you (I am glad that you joined IISER-M after TIFR), I'd probably be working in a different scientific field altogether. My special and sincere thanks to Prof. J. S. Bagla for all the kind advice he has offered me during my Ph.D. Thanks a lot, Sir, for your support, friendly suggestions, and especially for the timely submission of my annual review documents during the pandemic period. I must also thank my co-supervisor Dr. Smriti Mahajan, and my doctoral monitoring committee members Dr. H. K. Jassal and Dr. Kinjalk Lochan, for their useful inputs and encouragement. I thank the *Chandra* and *XMM-Newton* helpdesks for their assistance with the X-ray data analysis. I am grateful to Keith Arnaud (UMD, NASA GSFC) for helping me to gain a better understanding of the working and implementation of XSPEC models and Eric Greisen (NRAO) for his assistance with radio data reduction.

It is true that if you are a hostel resident while pursuing a Ph.D., the same set of people become your friends/family/colleagues. I have met some wonderful people over the past five-plus years. I thank my friends, Love, Dipayan, and Harkirat, for keeping me sane during my Ph.D. years. Thanks Love (that's his name) for giving IISER-M a feel-at-home feeling; Dipayan for the french press coffee, handling my sometimes meaningless conversations, and for all the proofreading and multiple Mathematica runs; Harkirat for all the fun and making all our parties livelier. Thanks Swati for the delicious, homely food. I have had some of the best times of my life here with you guys. I also thank my friends Anweshika, Patra, and Jasleen for their help and support during my Ph.D. years. Two very helpful people who deserve a special mention are Avinash and Manvendra, whom I thank for their help with various things, academic and non-academic. I carried out a major part of my Ph.D. work at home during the pandemic period. A special thanks to my officemates, Arpith and Vishal, and again, Manvendra and Love, for making my remote access sessions possible.

Last but foremost, I cannot forget to thank my parents and Rahul for their continuous and unparalleled love, support, and hope throughout these years. Thank you for being my constant pillars of strength and for always believing in me.

Abstract

Matter in the Universe is arranged in a network consisting of dense and long filaments ($\gtrsim$ 10 Mpc[1]) of gas, galaxies, and invisible dark matter. These filaments are interspersed with gigantic cosmic voids (diameter d $\sim$10–100 Mpc) and host massive galaxy clusters (d $\sim$1–10 Mpc) at their intersection sites. This large-scale network of structure is popularly known as the 'cosmic web'. The location of a galaxy within the cosmic web strongly influences its properties. For example, galaxies situated in higher density regions tend to be redder, have lower star formation rates, and lower neutral Hydrogen gas content, indicating that some physical mechanisms triggered in relatively high-density environments are responsible for transforming galaxy properties. Clusters of galaxies, the densest parts of the cosmic web, are home to hundreds to thousands of galaxies immersed in vast amounts of multi-million-degree hot ionized gas, dubbed the 'intracluster medium' (ICM). They are important sites to study the complex effects of environment on galaxies. These enormous objects grow by accreting matter from the surrounding cosmic web. The study of mergers in galaxy clusters is thus crucial to our understanding of how these large-scale objects form and evolve. In this thesis, we present the first detailed studies of the thermodynamic properties of the hot X-ray emitting gas in two nearby galaxy clusters – Abell 2151 and Abell 1569. We investigate the presence of substructure, merging activity, and cool cores, in these two systems. The study of Abell 1569 focuses on examining the interaction between the central radio galaxies and the surrounding intracluster gas. Both Abell 2151 and Abell 1569 show significant substructure. We confirm the bimodal X-ray structure of the central subcluster of Abell 2151 (A2151C). The two gas clumps in A2151C have notably different gas properties, confirming they are distinct galaxy groups. The brighter of the two groups exhibits the morphology of a relaxed system and hosts a cool core. The fainter group appears to be in the process of formation. In the northern subcluster of Abell 1569 (A1569N), we detect a pair of cavities carved out due to the displacement of the intracluster gas by the radio lobes of the central galaxy 1233+169. There is also some indication of cavity-induced heating of the ICM in A1569N. The southern subcluster of Abell 1569 (A1569S) shows strong evidence of merging activity which explains the bending of the tails of the central radio galaxy 1233+168. A separate study using optical data to explore the statistical trends in the luminosity-weighted age and stellar metallicity (Z) of galaxies in the Coma supercluster as a function of their stellar mass and large-scale environment, viz. clusters/groups, filaments, and voids, also constitutes a part of this thesis. Galaxies residing in clusters are older and more metal-rich than their counterparts in filaments and voids. Further, we observe an anti-correlation between age and Z of galaxies in the Coma supercluster. A key finding of this study is that Z is 0.02–0.03 dex lower for galaxies at the spine of the filament relative to their counterparts $\gtrsim$ 1 Mpc away from it, suggesting that large-scale cosmic filaments play a significant role in the evolution of galaxies.

[1] 1 parsec (pc) $= 3.086 \times 10^{16}$m

List of Publications

- *The complex intracluster medium of Abell 1569 and its interaction with central radio galaxies* by **Juhi Tiwari** & Kulinder Pal Singh, *Monthly Notices of the Royal Astronomical Society*, 509, 3321 (2022)
- *The Hercules cluster in X-rays with XMM-Newton and Chandra* by **Juhi Tiwari** & Kulinder Pal Singh, *Monthly Notices of the Royal Astronomical Society*, 500, 5524 (2021)
- *Age and metallicity of galaxies in different environments of the Coma supercluster* by **Juhi Tiwari**, Smriti Mahajan & Kulinder Pal Singh, *New Astronomy*, 81:101417 (2020)
- *Observations of AR Sco with Chandra and AstroSat soft X-ray telescope*[2] by K. P. Singh, V. Girish, **J. Tiwari**, P. E. Barrett, D. A. H Buckley, S. B. Potter, E. Schlegel, V. Rana, & G. Stewart, *Journal of Astrophysics and Astronomy*, 42:83 (2021)

[2]This publication does not form part of this thesis.

Contents

List of Tables

List of Figures

Chapter 1

Introduction

Matter in the Universe is arranged in a wispy network consisting of dense and long filaments ($\gtrsim$ 10 Mpc) of gas, galaxies, and invisible dark matter, which are interspersed with gigantic cosmic voids (diameter $d \sim 10-100$ Mpc), and host massive galaxy clusters ($d \sim 1-10$ Mpc) at their intersection sites. This large-scale network of structure is popularly known as the 'cosmic web', and is recognized in both observations and simulations, as can be seen in Figure 1.1. The components of the cosmic web differ in their properties and in turn have different effects on the properties of their constituent galaxies. While clusters of galaxies, found in the densest hubs of the cosmic web, are the best-studied large-scale structures to date, it is only in the recent years that the study of cosmic filaments and voids has picked up pace.

1.1 Clusters of galaxies

Clusters of galaxies are the largest gravitationally bound concentrations of matter in the Universe. They contain hundreds to thousands of galaxies, vast amounts of multi-million-degree hot ionized gas that shines brightly in X-rays, and enormous reservoirs ($\sim 80-90\%$ of the total cluster mass) of unseen dark matter (Babyk et al., 2012). Clusters have typical diameters of $\sim$several Mpc and total masses of $\sim 10^{14} - 10^{15}\ M_{\odot}$ (Sarazin, 1988; McNamara & Nulsen, 2007; Kravtsov & Borgani, 2012). The large sizes of galaxy clusters make them unique astrophysical laboratories in which a wide range of processes, e.g., the powerful interaction of supermassive black holes with the surrounding intracluster medium, the complex effects of the cluster environment on galaxies, as well as non-thermal phenomenon associated with magnetic fields and cosmic rays can be studied. Since galaxy clusters originate from collapsed overdensities in the early Universe and witness its history, they make powerful probes to test different cosmological models and constrain cosmological parameters (Allen et al., 2011). A composite

image showing different components of a galaxy cluster is shown in Figure 1.2.

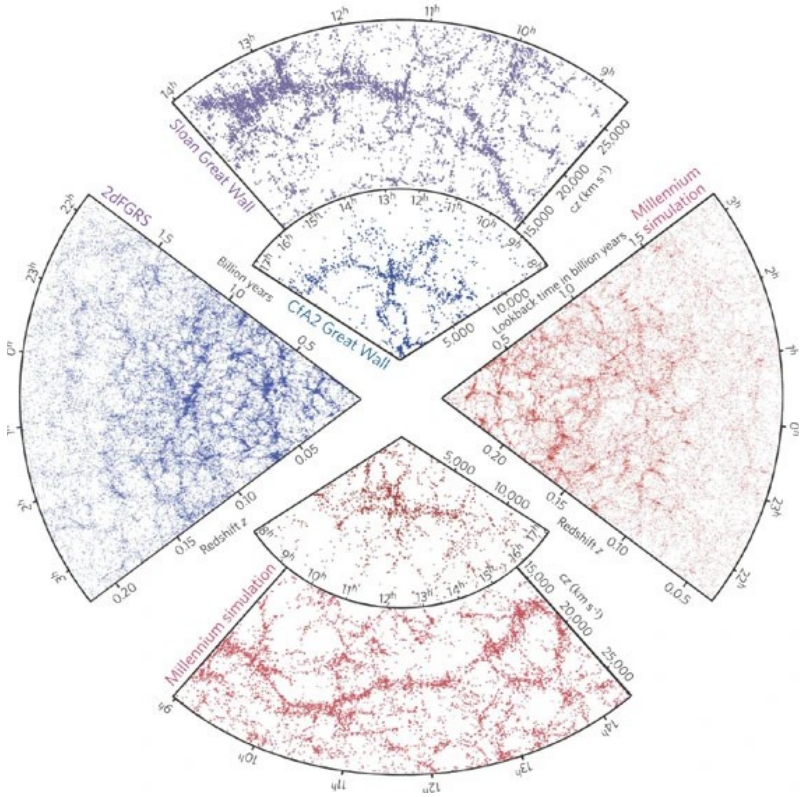

Figure 1.1: The large-scale web-like distribution of galaxies as seen in observations (*blue* and *purple*) and cosmological simulations (*red*). The sections on the *top* show the *CfA2 Great Wall* and the *Sloan Great Wall*. The slice on the *left* shows the large-scale distribution of galaxies in the southern sky from the *Two-degree-Field Galaxy Redshift Survey*. The slices on the *bottom* and *right* show simulated galaxy distributions matching the geometries of the sky surveys shown on the *top* and *left*, respectively. Image from Springel et al. (2006).

1.1.1 A bit of history...

The tendency of galaxies to group together in the sky was first noticed in the eighteenth century, a time when galaxies were thought of as giant clouds of gas and dust (nebulae) within the Milky Way (MW). In the early 1900s, Edwin Hubble discovered that these nebulae were real galaxies like the MW located at large distances from us (Hubble, 1925, 1926). Subsequently, it was established that the prominent concentrations of nebulae in the sky were truly enormous clusters of galaxies. The presence of dark matter in clusters was first proposed by Zwicky

(1937) when the virial mass of the Coma cluster of nebulae, as it was then called, estimated from the measured galaxy velocity dispersion was found to exceed the combined mass of all the visible galaxies by a factor of a few tens.

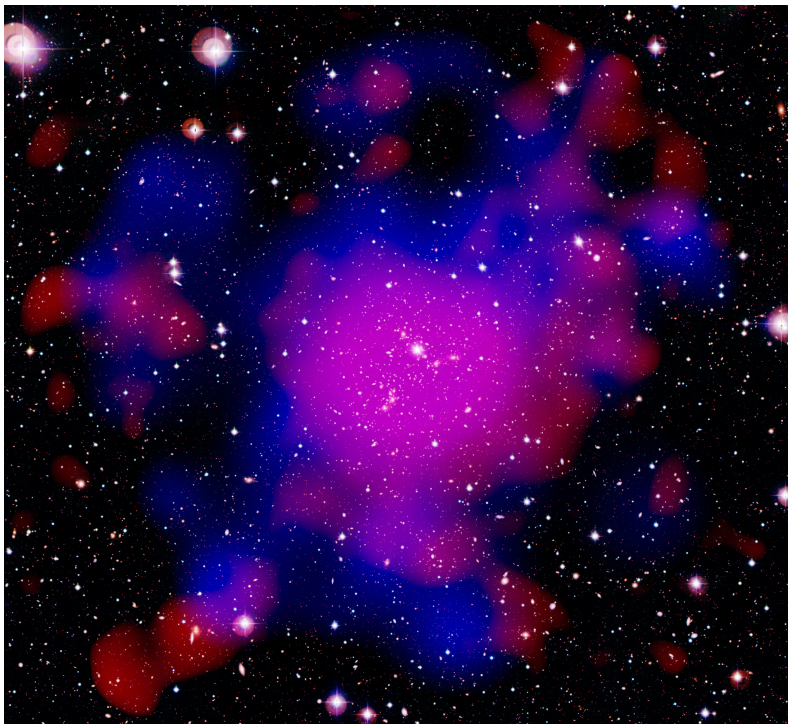

Figure 1.2: Composite image of galaxy cluster Abell 2744, also known as the Pandora's cluster, showing galaxies in *white*, hot X-ray emitting gas in *pink*, and dark matter distribution in *blue* color. The image measures about half a degree across and also shows foreground stars belonging to the Milky Way. Image retrieved from the European Space Agency (ESA) image archive. Credits: ESA/XMM-Newton: (X-rays); European Southern Observatory/Wide Field Imager (ESO/WFI): optical; NASA/ESA & Canada France Hawaii Telescope (CFHT): dark matter.

Using optical data, a number of catalogues of clusters of galaxies in the northern and southern skies, were compiled in the 1900s (Abell, 1958; Zwicky et al., 1961, 1963, 1965, 1966; Klemola, 1969; Snow, 1970; Rose, 1976; Shectman, 1985). Of these, the most extensive catalogues of rich clusters of galaxies in the northern sky were those of Abell (1958) who identified 2712 galaxy clusters north of declination -27° using data from the *Palomar Observatory Sky Survey-I* (*POSS-I*), and Zwicky and collaborators (Zwicky et al., 1961, 1963, 1965, 1966) who identified 9134 galaxy clusters north of declination -3°, also using *POSS-I* data. An all-sky catalogue of 4073 galaxy clusters, supplementing the original Abell catalogue with southern data (declination $< -27^{\circ}$), collected by the *United Kingdom Schmidt Telescope* (*UKST*), was

later given by Abell et al. (1989).

X-ray emission from extragalactic objects was first discovered in the 1960s (Byram et al., 1969). Diffuse X-ray emission from galaxy clusters was established as a distinct class by the first all sky X-ray survey carried out by the *Uhuru* satellite (Giacconi et al., 1972; Forman et al., 1978). The early *Uhuru* observations confirmed that galaxy clusters were indeed bright and extended extragalactic X-ray sources with luminosities $\sim 10^{43-45}$ erg s^{-1}. These early observations of galaxy clusters, having rather poor spectral resolution, proposed two competing models for the origin of the X-radiation – a power-law model resulting from the inverse Compton scattering of the cosmic microwave background photons by the relativistic electrons present in clusters or a thermal bremsstrahlung model resulting from electron-ion collisions in the hot intracluster gas (Sarazin, 1988). Subsequent observations with the *Eighth Orbiting Solar Observatory* (*OSO-8*), the *Ariel V Observatory*, and the *High Energy Astrophysical Observatory-1* (*HEAO-1*) in the 1970s discovered the $6-7$ keV iron line feature in the X-ray spectra of several galaxy clusters (Mitchell et al., 1976; Serlemitsos et al., 1977), and suggested that the spectra were better fit by the thermal bremsstrahlung model than the non-thermal power-law model (Mushotzky et al., 1978; Mitchell et al., 1979). It was, thus, concluded that the space permeating the constituent galaxies of clusters is filled with extremely hot ($\sim 10^7 - 10^8$ K), low particle number density ($10^{-5} - 10^{-1}$ cm^{-3}), highly ionized X-ray emitting gas, popularly known as the 'intracluster medium' (ICM). The launch of the *Einstein Observatory* (*HEAO-2*) in 1978 made it possible to image galaxy clusters and propose their classification based on their X-ray morphology (Forman & Jones, 1982). It also detected spectral lines from highly ionized elements, e.g. Mg XII[1], Mg XI, S XXVI, SXV, Si XIV, Si XIII, and Fe XVII to Fe XXIV, in the spectra of several clusters (Mushotzky et al., 1981; Nulsen et al., 1982; Rothenflug et al., 1984), indicating that at least part of the intracluster gas was contributed by stars and galaxies (Sarazin, 1988). X-ray observations of galaxy clusters with the *European Space Agency's X-ray Observatory* (*EXOSAT*) in the 1980s, and the *Roentgen Satellite* (*ROSAT*), the *Advanced Satellite for Cosmology and Astrophysics* (*ASCA*), and the *BeppoSAX* in the 1990s allowed for studying the temperature distribution of the intracluster gas, and determining the gas mass and dynamical mass of galaxy clusters (Edge & Stewart, 1991; Fabian, 1994; Böhringer, 1999; Lima Neto et al., 2003).

[1]The Roman numerals following the element symbol (Mg XII here) are a spectroscopic notation describing an emission line or a spectrum of lines resulting from electronic transitions within a Mg^{+11} ion (having a positive charge of one unit less than the Roman numeral). Likewise for other ions.

1.1.2 X-ray spectroscopy of galaxy clusters

X-ray spectroscopy of the ICM is an extremely important tool to obtain an insight into the properties and astrophysics of galaxy clusters. The intracluster gas has a very low particle number density, owing to which the observed cluster spectrum provides an account of the entire ICM, unlike the case of stellar spectrum that gives information on merely the surface of a star. This low density of the ICM is what makes the X-ray spectra of galaxy clusters straightforward to interpret, thus, enabling their simple modelling without going into complex radiative transfer calculations (Böhringer & Werner, 2010).

Contribution to radiation from hot and tenuous astrophysical plasma comes from three fundamental emission processes involving electronic transitions (Böhringer & Werner, 2010). These are:

i) *free-free* or *bremsstrahlung* radiation resulting from the deflection/collision of an electron passing in close vicinity of an ion.
ii) *free-bound* or *radiative recombination* which occurs when an electron collides and recombines with an ion, thus, emitting a photon.
iii) *bound-bound* or *deexcitation* radiation generated when an electron moves from a higher to a lower energy level in an ion.

The first two processes give rise to continuum radiation and the third generates line radiation. An exception in the *bound-bound* case is the *two-photon* process which gives rise to continuum radiation and is important for Hydrogen-like and Helium-like ions. In this process, downward electron transitions forbidden by quantum-mechanical selection rules take place by the simultaneous emission of two photons. For example, an excited electron in the 2s shell is forbidden to transit to the 1s level by emission of a single photon. The decay from the 2s orbit to the 1s orbit is, however, possible by the emission of two photons. Since a combination of two photon energies can equal the energy difference between the two transition levels involved, the *two-photon* process generates a continuum.

Figure 1.3 shows the contributions of different continuum processes in plasmas of different temperatures. The continuum contribution from *free-free* radiation grows compared to other processes as the plasma temperature increases.

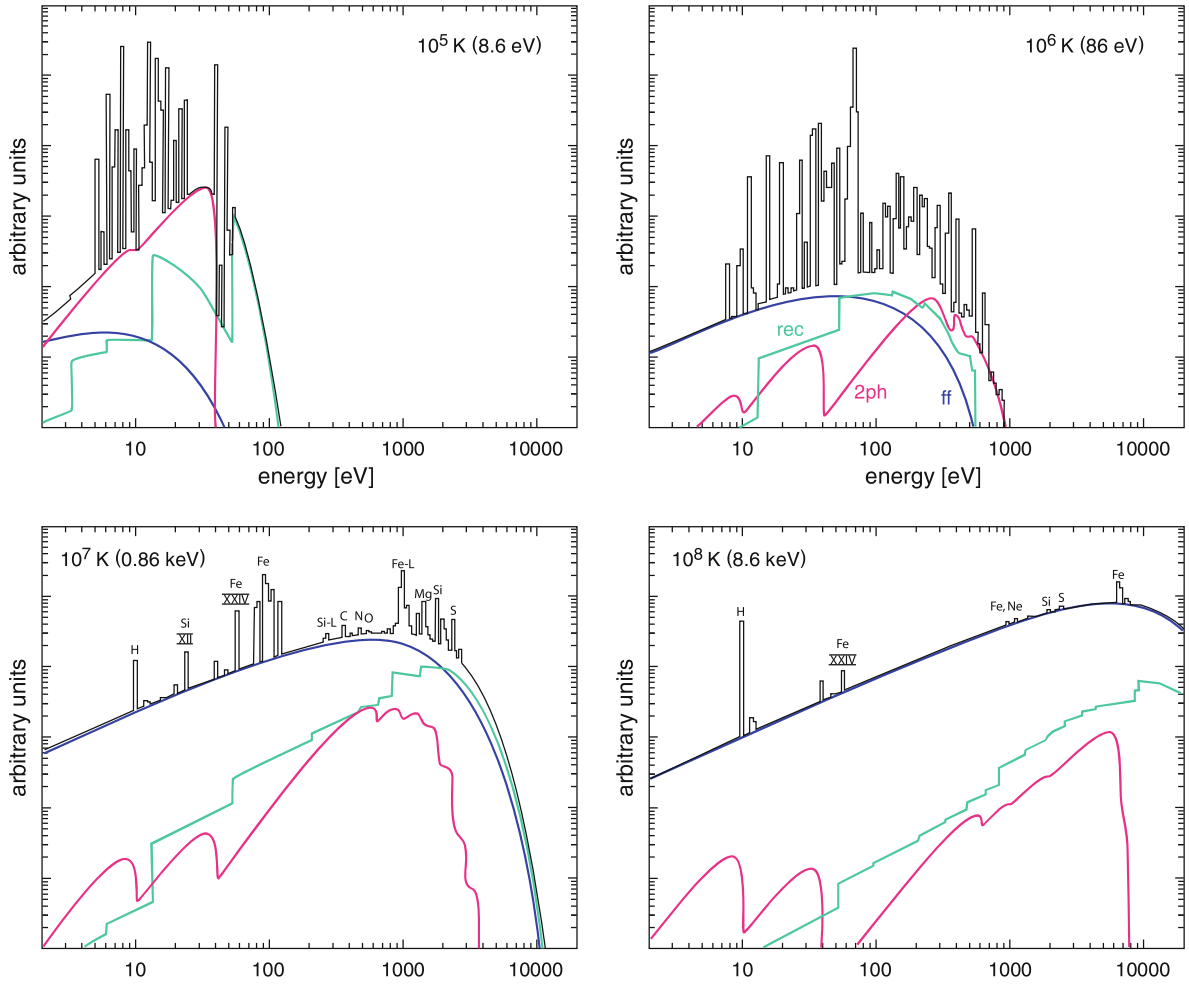

Figure 1.3: X-ray spectra at different plasma temperatures from Böhringer & Werner (2010). The continuum contributions from *bremsstrahlung* (*blue curve*), *radiative recombination* (*green curve*), and *two-photon* (*red curve*) processes are shown. *Thermal bremsstrahlung* is the dominant radiation process at high temperatures relevant for galaxy clusters. The *bottom left panel* shows that at lower cluster temperatures (kT $<$ 2–3 keV), line emission is also a major contributor to the total X-ray emission.

Thermal bremsstrahlung continuum emission: As can be seen in Figure 1.3 (*bottom panels*), *thermal bremsstrahlung* is the dominant continuum radiation process at the highest plasma temperatures ($\gtrsim 3\times10^7$ K) relevant for galaxy clusters (Sarazin, 1988). The volume emissivity (power emitted per unit volume per unit frequency from the plasma) for *free-free* radiation is given by:

$$\epsilon_\nu^{ff} = \frac{1}{(4\pi\epsilon_0)^3}\frac{32e^6}{3c^3}\left(\frac{2}{3}\frac{\pi^3}{km_e^3}\right)^{1/2} n_e \frac{exp(-h\nu/kT)}{T^{1/2}}\sum_i g_{ff}(\nu,T,Z_i)n_i Z_i^2 \qquad (1.1)$$

where, e and m_e are the charge and mass of an electron, respectively, n_e and n_i are the number densities of electrons and individual ions in the plasma, Z_i is the effective charge of the ion, and g_{ff} is the gaunt factor, a slowly varying function of frequency ν and gas temperature T, calculated from the exact quantum mechanical treatment of the electron-ion collisions (Sarazin, 1988; Bradt, 2008; Böhringer & Werner, 2010). The other symbols have the standard meaning; k is the Boltzmann's constant, c is the speed of light, and ϵ_0 is the permittivity of free space. The shape of the continuum spectrum, thus, provides information on the plasma temperature.

Line emission: At plasma temperatures $\lesssim 3 \times 10^7$ K, X-radiation is mainly in the form of spectral lines (Sarazin, 1988). Line emission may result from dielectronic recombination, inner shell collisional ionization, or by the collisional excitation of electrons. In dielectronic recombination, a free electron recombines and is bound to the ion. This recombination does not result in emission of a photon as is the case in radiative recombination. Instead, another electron in the ion is excited to a higher energy level creating an unstable doubly-excited ion. The excited electron then decays by a radiative transition creating a singly-excited state which further decays by another radiative transition, resulting in more than one line photons. In inner shell collisional ionization, an electron from an inner shell or K-shell of the ion is removed by interaction with a free electron, making the ion unstable. The ion either regains its stability by emitting a photon when an electron from an outer shell makes a radiative transition to occupy the inner-shell vacancy, or by autoionisation through the Auger process. In the latter, the energy released in the transition of the electron from the outer shell to the inner shell vacancy is not emitted as a photon, but is transferred to another electron in one of the outer shells resulting in its escape from the ion. Although dielectronic recombination and inner shell collisional ionization play a role, the main process responsible for producing X-ray line emission is collisional excitation of electrons followed by radiative cascades. The emissivity due to a collisionally excited line is given by:

$$\int \epsilon_\nu^{line} d\nu = n(X^i) n_e \frac{h^3 \nu \Omega(T) B}{4\omega_{gs}(X^i)} \left[\frac{2}{\pi^3 m_e^3 kT}\right]^{1/2} exp(-\Delta E/kT) \tag{1.2}$$

Here, $n(X^i)$ is the number density of ion X in state i, $h\nu$ is the energy of the transition, ΔE is the excitation energy of the excited level above the ground state, B is the branching ratio of the line, $\omega_{gs}(X^i)$ is the statistical weight of the ground state level of ion X^i, and Ω is the collision strength, a slowly varying function of temperature (Osterbrock, 1974).

The most popular and strongest line feature observed in the spectra of most galaxy clusters is a complex of He-like Fe XXV lines near 6.7 keV, collectively referred to as the Fe-K or 6.7 keV complex, due to the low resolution of X-ray spectra. This feature has often been used to determine the redshift of clusters (Sarazin, 1988). Features observed at high energy also include the Ly-α Fe XXVI line at $\sim$6.9 keV, and the Kα Ni XXVII and Kβ Fe XXV lines blended into a single feature at $\sim$7.8 keV. Other lower energy lines from lighter elements include OVII and OVIII ($\sim$0.55–0.8 keV), Mg XI and Mg XII ($\sim$1.35 keV and $\sim$1.47 keV, respectively), Si XIII and Si XIV ($\sim$1.86 keV and $\sim$2.01 keV, respectively), S XV and S XVI ($\sim$2.4 keV and $\sim$2.6 keV, respectively), among others. The Fe-L complex, a blend of L-lines – Fe XVII to Fe XXIV ($\sim$0.7–1.4 keV), is also commonly observed in the X-ray spectra of galaxy clusters. It also includes the Ne IX and Ne X lines around 0.9 keV and 1.02 keV, respectively. Some of these line features are shown in Figure 1.4.

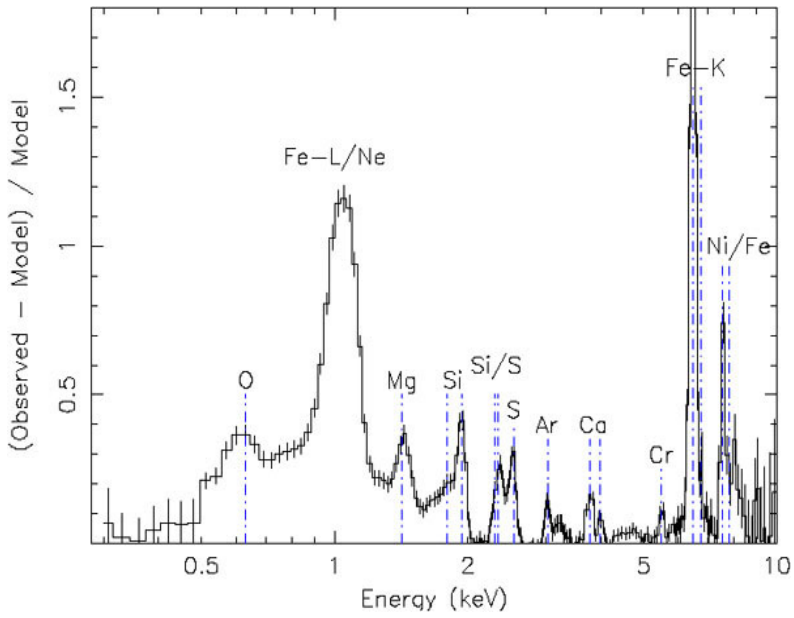

Figure 1.4: Metal lines in the X-ray spectrum of galaxy cluster 2A 0335+096, as observed with the European Photon Imaging Camera onboard the *XMM-Newton* observatory. Image retrieved from Böhringer & Werner (2010).

Modelling of the X-ray spectra of galaxy clusters provides a plethora of useful information. Temperature and density of different parts of the intracluster gas can be obtained directly from the spectral modelling. The temperature distribution of the ICM can be used to obtain cluster mass and serves as a powerful diagnostic of cluster mergers. By means of X-ray spectroscopy, cooling cores in the centres of a large number of galaxy clusters have been identified (Singh

et al., 1986, 1988; Fabian, 1994). These are interesting sites to investigate the interplay between gas cooling and energy feedback from the central galactic nucleus. Entropy structure derived from gas temperature and density is a principal indicator of non-gravitational processes important in cluster formation. Modelling of the X-ray spectral lines allows one to understand the chemical composition of the intracluster gas. Measurements of elemental abundances in the ICM provide a record of the contribution of different supernovae to the nucleosynthesis of heavy elements. Some of the aspects mentioned here are discussed in the following subsections.

1.1.3 Cool cores in galaxy clusters

An interesting aspect of many galaxy clusters is the existence of a cool core (CC). Early X-ray observations of galaxy clusters with the *Einstein Observatory* and the *EXOSAT* revealed that the surface brightness distribution of the intracluster gas in the central regions of these clusters is sharply peaked (Stewart et al., 1984; Singh et al., 1988; Edge & Stewart, 1991). This also implies that the gas is very dense ($n_e > 10^{-2}$ cm^{-3}; the term *very* here is specifically in the context of the ICM) in the cores of these clusters (Peterson & Fabian, 2006) since emissivity $\epsilon \propto n_e^2$, with thermal bremsstrahlung being the principal process of emission. The high central gas density causes a rather fast loss of energy by radiation leading to a decrease in the temperature of the cluster core relative to that in the surrounding regions. The radiative cooling time in the central regions of CC clusters is shorter than the Hubble time (Fabian, 1994). There is ample X-ray observational evidence regarding the presence of CC clusters (Peres et al., 1998; Chen et al., 2007; Hudson et al., 2010). A representative image of a CC cluster is shown in Figure 1.5.

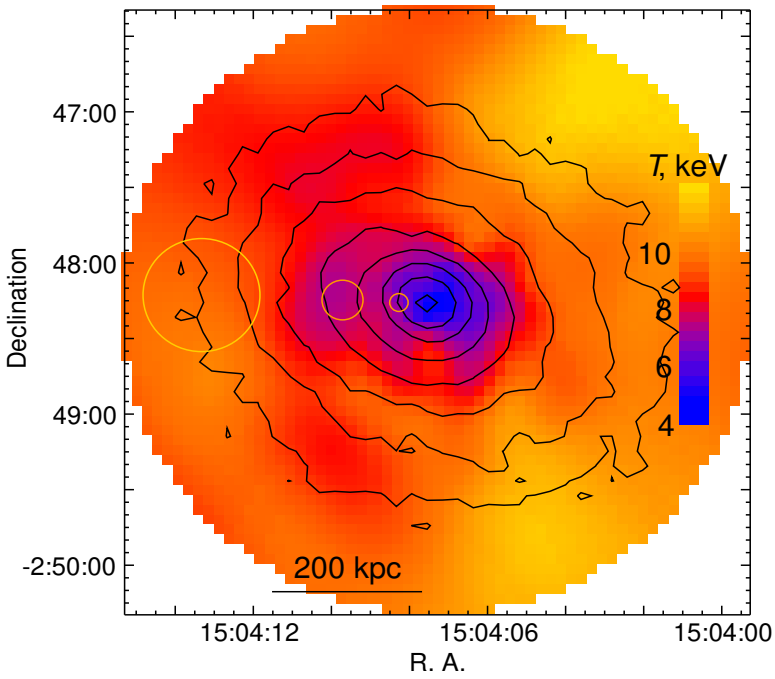

Figure 1.5: *Chandra* temperature map of the bright cool-core cluster RXCJ 1504.1-0248 ($z = 0.215$) from Giacintucci et al. (2011). The overlaid *black* contours are from the 0.8–4 keV *Chandra* X-ray image and are spaced by a factor of 2 in surface brightness. The radii of the three circles illustrate the variable smoothing width (Gaussian σ) used for the temperature map. The rms temperature uncertainties at their positions (from small to large radius) are 0.3 keV, 0.5 keV, and 0.9 keV, respectively. The cluster has a cooling radius of $\sim$140 kpc, in which the temperature drops to below 5 keV.

Observations of cool cores in galaxy clusters led to the development of the 'cooling flow' model. In this model, the cooling of the ICM in the cluster centre reduces the gas temperature, and the central gas density must rise in order to support the weight of the overlying gas. The process is essentially pressure-driven and causes the gas from the outer regions of the ICM to flow into the cluster interiors (Fabian, 1994). However, in almost all cool-core galaxy clusters observed to date, gas temperature in the central region does not drop below one-third of the mean cluster temperature. This lower limiting temperature (T_{low}) of the cooling core is still significantly above the 'drop out' temperature at which the gas would cease to emit considerable X-ray radiation (Böhringer et al., 2002). High resolution spectra of the cool cores of a number of galaxy clusters obtained with the *XMM-Newton* satellite have confirmed the lack of central cool gas having temperature less than T_{low} (Tamura et al., 2001; Peterson et al., 2001). These spectra show a complete absence or lack of emission from the Fe L charge states (Fe XXIV through Fe XVII; sensitive to gas temperatures between 0.4 and 4 keV) (Peterson et al., 2003), thus, raising questions on the standard 'cooling flow' model and ruling out the concept of complete cooling flows in galaxy clusters (Peterson & Fabian, 2006). Heating mechanisms, such as heating by the energy output of the central active galactic nucleus (AGN), or by heat

conduction from the hotter gas outside the cool core, have been proposed to explain the absence of cooler X-ray emitting gas (kT $<$ 1 keV) in the cores of clusters.

Several studies have aimed at differentiating between CC and non-CC clusters by analysing large samples of galaxy clusters observed with high resolution X-ray telescopes and via simulations. CC clusters have been defined in multiple ways: based on a central temperature drop (e.g. $\frac{T_{mean(0.1-0.2r_{500})}}{T_{core(0-0.1r_{500})}} > 1$ at greater than 3σ significance has been used by Sanderson et al., 2006), a short central cooling time (e.g. a central cooling time $t_{cool} < 2$ Gyr is used as the definition of strong cooling by Bauer et al., 2005), or a significant classical mass deposition rate (e.g. Chen et al., 2007, used $\dot{M}/M_{500} > 10^{-13}$ yr^{-1} as the definition of strong CC clusters). An elaborate study by Hudson et al. (2010), aiming to unambiguously differentiate between CC and non-CC clusters by applying various CC diagnostics, finds that t_{cool} is the best parameter to identify CC clusters (the authors identify $t_{cool} < 1.0\ h_{71}^{-1/2}$ Gyr for strong CC, $1.0\ h_{71}^{-1/2} < t_{cool} < 7.7\ h_{71}^{-1/2}$ Gyr for weak CC, and $t_{cool} > 7.7\ h_{71}^{-1/2}$ Gyr for non-CC clusters).

1.1.4 Mergers in galaxy clusters

In the hierarchical framework of structure formation, galaxy clusters grow by accreting matter from the cosmic-web filaments, the intersection sites of which they primarily reside at. During the accretion process the gravitational potential energy of the infalling matter (gas, galaxy groups, and subclusters) is dissipated, thus heating up the intracluster gas. Often the accretion of matter involves collisions or mergers with other large clusters of galaxies, the most massive of which release gravitational binding energies of as much as $\sim 10^{63-64}$ erg.

Evidence of mergers between galaxy clusters/groups has been found in the optical regime in the form of substructures in the surface density maps and in the line of sight velocity distribution of member galaxies. Presence of a large offset between the brightest cluster galaxy (BCG) and the X-ray surface brightness (SB) peak is also a popular indicator of dynamical activity in a cluster. Substructure observed in the X-ray surface brightness and temperature (hence, pressure and entropy) maps of galaxy clusters is a more definitive indicator of mergers, since X-ray studies are way less susceptible to projection effects which become an important contributor in optical studies. Anisotropic variations of temperature (also, pressure and entropy) in the ICM, in contrast to the azimuthally symmetric thermodynamic profiles expected of a relaxed system, provide a confirmation of mergers in clusters. An example image of a merging galaxy cluster is shown in Figure 1.6

Mergers between galaxy clusters/subclusters produce moderately supersonic shocks (Mach number: $M \lesssim 3$) (Sarazin, 2002) that compress and heat the intracluster gas (Markevitch & Vikhlinin, 2007). These shocks are energetic enough to result in observable phenomenon, and are visible at X-ray and radio wavelengths (e.g., Macario et al., 2011; Dwarakanath et al., 2018; Ge et al., 2019; Hoang et al., 2019). Since the X-ray flux is proportional to the square of gas density, the shock resultant density discontinuities are visible as sharp edges in the SB maps of clusters (Sanders et al., 2016). Detection of shock fronts in X-rays is a key observational tool for studying mergers in galaxy clusters since these can be used to estimate the merger-driven gas bulk flow velocities in the plane of the sky and constrain the merger geometry. Sharp edges in cluster X-ray images can also arise when the rapidly moving dense gas core of an infalling subcluster survives a major merger and forms a prominent contact discontinuity or boundary with the ambient hot gas of the host cluster (e.g. the discontinuity observed in Abell 3667 – Vikhlinin et al., 2001). These contact discontinuities are better known as cold fronts. Cold fronts can also be induced in the cool cores of relaxed galaxy clusters by minor merger events. Such mergers displace the cold central intracluster gas from the centre of the cluster potential and subsequently cause it to slosh around the potential minimum (e.g. the sloshing spiral feature in Abell 2029; Paterno-Mahler et al., 2013). Mergers could also cause metal enrichment of the intracluster gas through enhanced ram-pressure stripping during mergers as seen in simulations (Domainko et al., 2005). Simulations also suggest that merger activity may be responsible for erasing cool cores in galaxy clusters or inhibiting their formation (Sanderson et al., 2006; Burns et al., 2008; Santos et al., 2008; Henning et al., 2009).

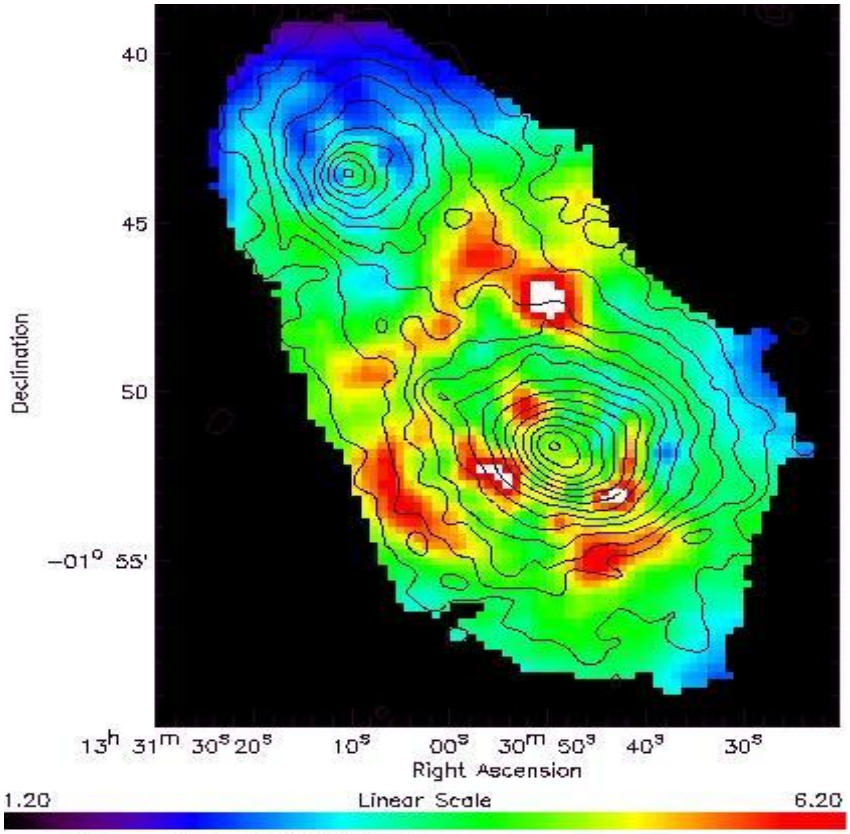

Figure 1.6: Temperature map of galaxy cluster Abell 1750 with contours of X-ray emission overlaid. The two main components of A1750 – A1750N to the north and A1750C to the south are merging. The arc-like hot region in between the two subclusters (seen in *red* color) indicates that the gas is being shocked and compressed as the two subclusters approach each other. The hot regions within A1750C are regions of shocked gas from a past merger event. Credit: ESA/XMM-Newton.

1.1.5 Radio emission from galaxy clusters

Emission from galaxy clusters has also been observed at radio wavelengths. The observed radio emission is synchrotron emission produced by the interaction of a non-thermal population of relativistic electrons (following a power-law energy distribution) with a pervading magnetic field (Sarazin, 1988). It may arise from individual galaxies in the cluster or may be diffuse and extended in nature, i.e., it cannot be ascribed to individual galaxies, but is instead associated with the large-scale ICM (Feretti et al., 2012).

Diffuse and extended radio emission

The diffuse and extended radio emission from galaxy clusters has been broadly classified into

three main classes:

- *Radio halos* are diffuse radio sources of low surface brightness ($0.1 - 1$ μJy arcsec^{-2} at 1.4 GHz) that roughly follow the brightness distribution of the thermal ICM (Feretti et al., 2012). They typically have a smooth and regular morphology and their sizes can range from ∼100–500 kpc (*radio mini halos*) to ∼1–2 Mpc (*giant radio halos*). Radio halos are not localized and occupy a significant volume of the cluster. Giant radio halos are typically found in merging galaxy clusters and are believed to be a consequence of merger induced turbulent particle re-acceleration. Mini halos, on the other hand, are mostly observed in relaxed cool-core clusters, and their origin is attributed to turbulence induced particle re-acceleration caused by gas sloshing motions in the cores of galaxy clusters (van Weeren et al., 2019). Radio halos are almost always characterized by a steep spectrum with integrated spectral index $\alpha^2 > 1.1$.

- *Cluster radio relics/shocks* are diffuse extended sources with low surface brightness, large sizes (∼0.5–2 Mpc), and a more or less elongated morphology. These are mostly located in cluster peripheral regions. Unlike radio halos, cluster radio relics do not trace the ICM baryonic mass distribution. Rather, they can be associated with specific cluster regions where a shock wave is present, or where a shock wave recently passed (van Weeren et al., 2019). The origin of cluster radio relics is, thus, attributed to particles that are accelerated at ICM shock fronts. The integrated radio spectra of relics display power-law shapes, with spectral indices ranging from about 1.0 to 1.5.

- *Radio 'phoenices'* (*revived fossil plasma sources*) are a less widely studied class of diffuse radio sources in galaxy clusters. These are believed to trace fossil AGN radio plasma that has somehow been reenergized through processes in the ICM, unrelated to the radio galaxy itself (van Weeren et al., 2019). Radio phoenices have a range of morphologies, from roundish shapes to elongated and filamentary structures. Their sizes are small (∼300–400 kpc) compared to standard radio relics and they are found at smaller cluster centric distances. Radio phoenices display steep integrated spectra with $\alpha > 1.5$.

An example image of diffuse and extended radio emission from galaxy clusters is shown in Figure 1.7.

[2]In radio astronomy, flux density (S_ν) at frequency ν follows $S_\nu \propto \nu^{-\alpha}$, where α is the spectral index

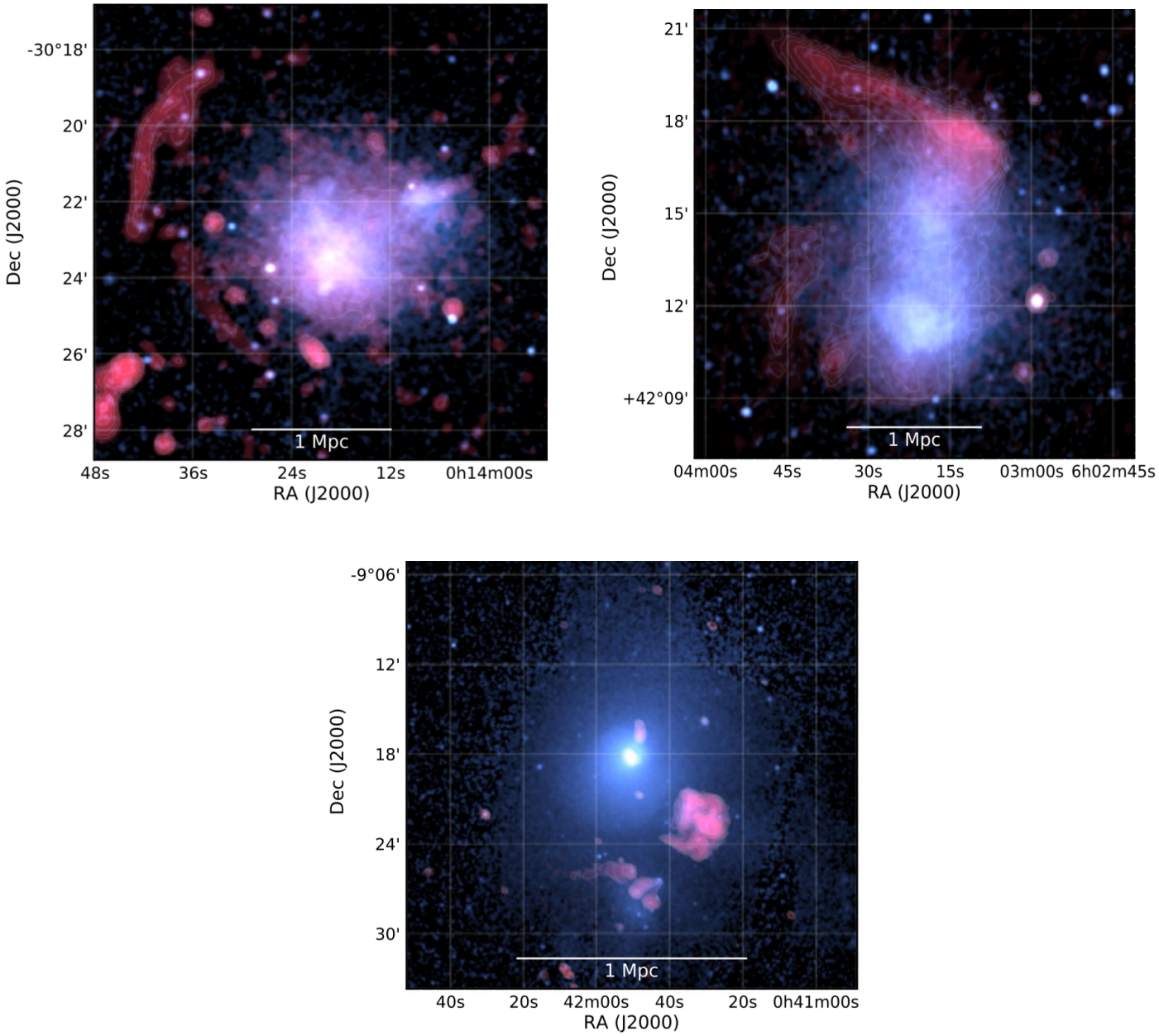

Figure 1.7: Examples of galaxy clusters hosting a giant radio halo (*top left*; Abell 2744), a radio relic/shock (*top right*; Toothbrush Cluster/RX J0603.3+4214), and a radio phoenix (*bottom*; Abell 85), from van Weeren et al. (2019). The X-ray emission is shown in *blue* and the diffuse radio emission in *red*.

Extended radio emission from cluster member galaxies

The member galaxies of clusters and groups more often than not host AGN that emit extended radio synchrotron emission (McNamara & Nulsen, 2007; Fabian, 2012). Radio emission from these galaxies generally extends well beyond the optical boundaries, sometimes out to hundreds

of kiloparsec (Miller & Owen, 2001). The most commonly observed radio galaxy morphology in galaxy clusters is that of a double-lobed galaxy, in which radio energy is emitted from two regions (lobes), one on each side of the galaxy. Double-lobed radio sources are generally divided into two classes – FR I and FR II sources – based on their morphology and radio power (Fanaroff & Riley, 1974). FR I (*edge-darkened*) sources are brighter towards their central host galaxy and become fainter towards the outer extremities of the lobes, while FR II galaxies (*edge-brightened*) have bright hotspots towards the ends of their lobes. The 1.4 GHz radio luminosities of FR I and FR II galaxies are lower and higher than $\sim 10^{24.5}$ W Hz^{-1}, respectively. Cluster galaxies often display more complex radio morphologies, such as the bent-tail (BT) radio sources – a class of radio galaxies in which the jets and tails are significantly bent or distorted from the expected straight line trajectory (Ryle & Windram, 1968; Owen & Rudnick, 1976). Depending on the angle formed between the two bent jets and lobes of the pair, BT sources are classified into wide-angle-tailed (WAT, or C-shaped) sources, where the angle formed is usually very large, and narrow-angle-tailed (NAT, or U-shaped) galaxies, where the jets and lobes form a small angle (Feretti & Venturi, 2002).

Since radio emission from cluster galaxies often extends to large radii ($\sim$few hundred kpc), it is expected that the radio-emitting regions interact with the surrounding hot X-ray emitting intracluster gas. The characteristic shape of BT radio sources is attributed to the weather of the host ICM, and hence, these sources are useful tracers of galaxy clusters (Giacintucci & Venturi, 2009). Relative motion ($\gtrsim$ 1000 km s^{-1}) between the extended radio galaxy and the dense ICM, resulting in significant ram pressure on the radio-emitting material of the jets, is a popularly proposed physical mechanism to explain the observed jet bending. The relative motion can result from the galaxy moving at a high peculiar velocity through the dense gas – as is believed to be the case for NAT galaxies (e.g., O'Dea & Owen, 1985; Venkatesan et al., 1994), or by the intracluster gas itself moving across the galaxy (e.g., bulk flows in the ICM induced by cluster-subcluster mergers) – in case of WAT sources (e.g., Pinkney et al., 1994; Douglass et al., 2011).

Interaction of the jets and lobes of radio galaxies in galaxy clusters (particularly those located in/near the cluster centre) with the surrounding intracluster gas is also observed in the form of deficits in the ICM X-ray emission (Reynolds et al., 2005; Sanders et al., 2009). These deficits dubbed 'cavities' are regions where the radio plasma has displaced the X-ray emitting gas, creating a low-density bubble which rises buoyantly and expands, distributing energy to the surrounding ICM (e.g. Churazov et al., 2002). A number of X-ray observations show cavities in galaxy clusters and groups, coincident with extended radio emission from member galaxies (McNamara et al., 2000; Blanton et al., 2001; Chon et al., 2012). The sizes of the

cavities created by the radio lobes vary widely from a few kpc to tens and hundreds of kpc in diameter (Bîrzan et al., 2004; Blanton et al., 2010). Radio galaxies in clusters are also known to heat the surrounding gas. Although the details of how the radio jets heat the ICM are still not very clear, jet-driven cavity heating (Churazov et al., 2001) and shock heating (Fabian et al., 2003; Nulsen et al., 2005) are two popular mechanisms proposed in the literature. An example of X-ray cavities created by a central radio galaxy in the ICM of the host cluster is shown in Figure 1.8.

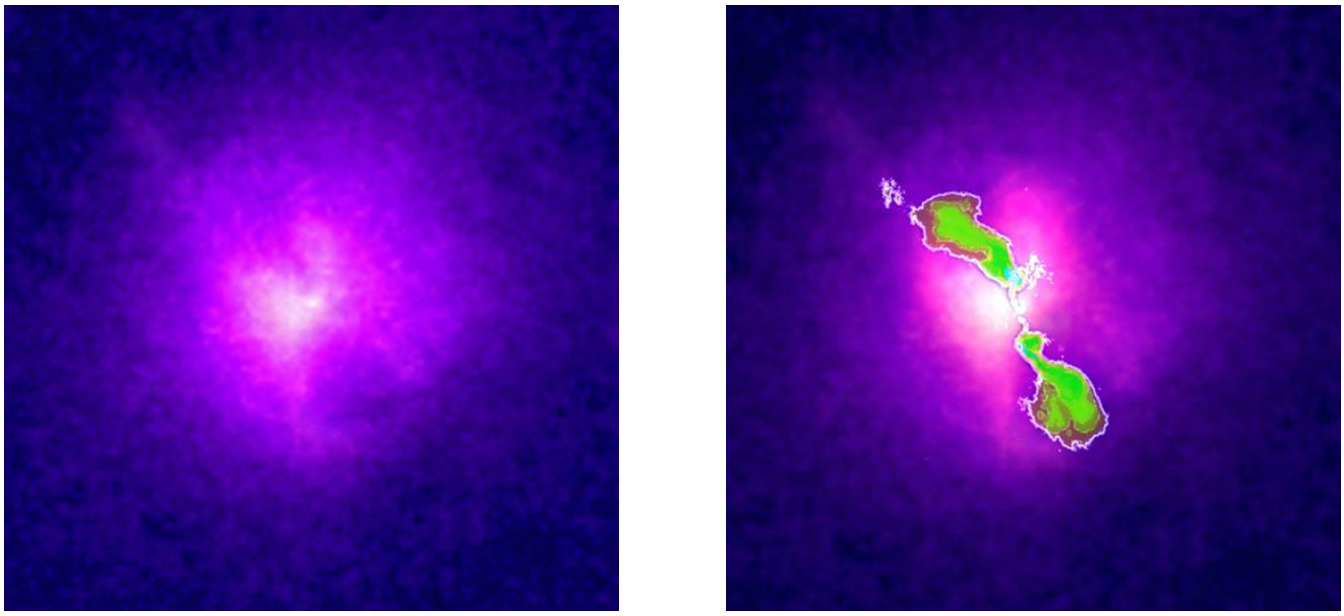

Figure 1.8: *left*: X-ray cavities in the intracluster medium (*pink*) of Hydra A galaxy cluster ($z = 0.054$). *right*: The cavities are coincident with extended emission from the strong radio source, Hydra A (from which the cluster gets its name), near the centre of the galaxy cluster. Radio emission from the galaxy is shown in *green* color. Credit: NASA/CXC/SAO.

1.1.6 Substructures in galaxy clusters

Observations of galaxy clusters, which were once thought of as simple, dynamically relaxed systems, reveal that they contain a significant degree of substructure. This very early view of clusters as fully evolved and spherically symmetric systems changed dramatically about four decades ago when cluster substructures were noticed in the early optical and X-ray images of clusters, indicating that clusters are still growing through infall of galaxies, groups and subclusters. The most extensive evidence of the prevalence of optical substructure in galaxy clusters

was provided by the galaxy surface number density maps of a sample of 65 rich clusters by Geller & Beers (1982). Approximately 40% of the clusters in this sample showed significant substructure on scales $\gtrsim$ 240 kpc.

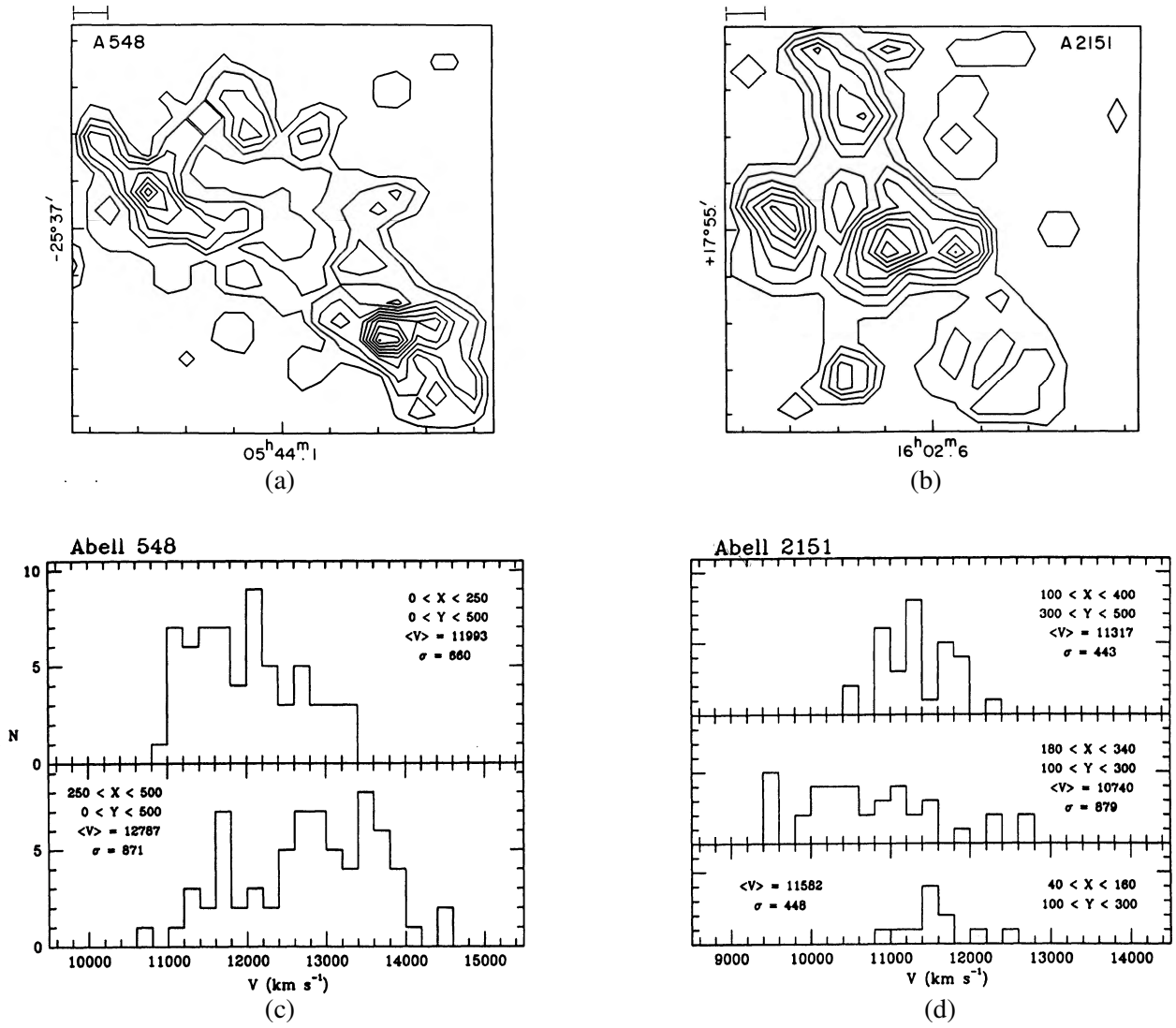

Figure 1.9: (a) and (b): Galaxy surface number density contour diagrams of galaxy clusters Abell 548 and Abell 2151, respectively, from Geller & Beers (1982). The bar shown on the upper left represents 0.24 Mpc at the distance of the clusters. (c) and (d): Velocity histograms of galaxies within different substructures seen in (a) and (b), from Dressler & Shectman (1988). The image coordinates X and Y increase from left to right, and bottom to top, respectively.

Figure 1.9(a) and Figure 1.9(b) show images of optical substructure in two clusters – Abell

548 and Abell 2151 – chosen from this sample. Since galaxy surface density maps can often be affected by projection effects leading to false detections of background/foreground galaxies as cluster members, radial velocity distributions of galaxies serve as a powerful substructure diagnostic to complement these maps. For e.g., Dressler & Shectman (1988) verified the substuctures detected in the number density maps of Geller & Beers (1982) by using radial velocity measurements in a subsample of 15 clusters. The velocity histograms shown in Figure 1.9(c) and Figure 1.9(d) confirm the presence of substructures detected in the optical images of Abell 548 and Abell 2151.

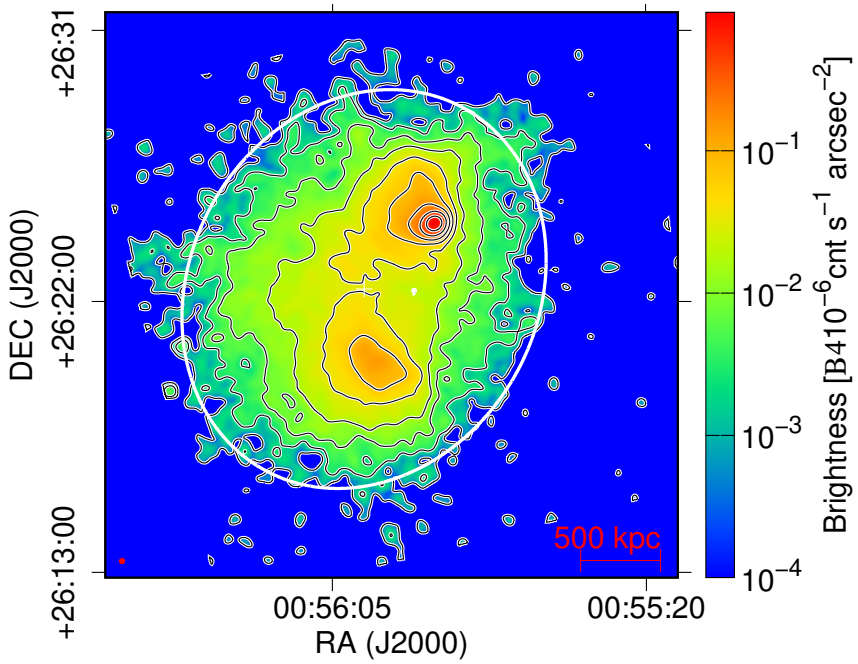

Figure 1.10: Presence of substructure in the *Chandra* X-ray surface brightness image of the galaxy cluster Abell 115 ($z = 0.1918$). Figure from Yuan & Han (2020).

Further supporting evidence for substructuring in galaxy clusters comes from cluster X-ray images which are almost unaffected by projection effects. The earliest X-ray survey of a large sample of 206 clusters with redshifts $z \lesssim 0.15$, indicating the ubiquity of subtructuring, was made with the *Einstein Observatory*. Using this sample, Jones & Forman (1992) found a large fraction ($\sim$40%) of galaxy clusters to contain substantial substructure, in agreement with optical studies of smaller samples. Almost a decade later, a systematic study of substructure in the X-ray surface brightness distributions of 470 *ROSAT* observed clusters, conducted by Schuecker et al. (2001a), found a larger fraction ($\sim$52%) of galaxy clusters to be significantly

substructured. With the advent of new generation telescopes resulting in the growth of observational databases for clusters, including galaxy positions, radial velocities, optical photometry, X-ray maps and radio images, it has now become easier to identify substructure in clusters. The work by Wen & Han (2013), who diagnosed substructure and dynamical state of a very large sample 2092 rich clusters of galaxies using photometric data from the *Sloan Digital Sky Survey*, is one example highlighting the power of modern-day telescopes. Figure 1.10 shows an example of X-ray substructure detected in Abell 115 with the high-resolution *Chandra* telescope. The figure is taken from the work by Yuan & Han (2020), describing the dynamical state of 964 galaxy clusters using *Chandra* X-ray images.

Substructuring indicates the degree of evolution in galaxy clusters, such that in a Universe where structure formation occurs by hierarchical clustering, those with substantial substructure are regarded as dynamically young systems. As a result, clusters with complex morphologies/substructure are useful in constraining the matter density of the Universe. For e.g., the fraction of galaxy clusters which appear unrelaxed at a given epoch will reflect the cluster formation rate (dependent on the cosmological density parameter) at that epoch. A number of studies have tested different models of structure formation by simulating density profiles and morphologies of galaxy clusters by assuming different cosmologies and then comparing them with those observed in the Universe (Evrard et al., 1993; Jing et al., 1995; Beisbart et al., 2001; Jeltema et al., 2005). Cluster substructures are also important because they often coincide with individual groups of galaxies, and therefore, provide the means to study group-scale systems which may not be simply scaled-down versions of their bigger cluster counterparts. Several studies have indicated the steepening of the thermodynamic scaling relations (e.g., the $L_X - kT$ relation) for low temperature (or low mass) systems (< 3 keV), thus, highlighting the enhanced influence of non-gravitational processes (e.g., cooling, AGN feedback, and galactic winds) on these systems (Helsdon & Ponman, 2000a; Magliocchetti & Brüggen, 2007; Eckmiller et al., 2011; Maughan et al., 2012; Lovisari et al., 2015). However, the sample sizes on which these studies are based are rather small due to the difficult detection of galaxy groups owing to their low surface brightness. Substructure detection in both optical and X-rays can help in increasing these sample sizes, eventually leading to a better understanding of the exact differences between clusters and groups of galaxies.

1.2 Galaxy environment and its effect

'Environment' of a galaxy refers to the galaxy's immediate surroundings. It is usually described using the local density field of neighbouring galaxies around the particular galaxy under consideration or may synonymously be defined using the density of the surrounding intergalactic material or by the host halo mass. Depending on where a galaxy is located within the cosmic web (e.g., high density clusters versus extremely low density void regions), its properties (e.g., color, morphology, star formation) may vary.

The most obvious manifestation (and also one of the earliest to be observed) of the effect of environment on galaxy evolution is the morphology-density relation, which relates the density of galaxies in a given region with their typical morphology. Evidence for the existence of such a correlation was first provided by Dressler (1980) in a sample of $\sim$6000 galaxies in 55 rich clusters, indicating an increasing elliptical (E) and lenticular (S0) population and a corresponding decrease in spirals (S) and irregulars (Irr) with increasing density. The presence of the morphology-density relation is reinforced in the local Universe (Goto et al., 2003) with larger galaxy sample sizes ($\sim$few tens of thousands of galaxies) collected from sky surveys conducted using new generation telescopes, e.g., the Sloan Digital Sky Survey (SDSS), and is also observed up to higher redshifts of $\sim$1 (Tasca et al., 2009). The morphology-density relation reexpresses itself in the form of the color-density relation (Blanton et al., 2005b; Bamford et al., 2009), the star formation rate (SFR)-density relation (Hashimoto et al., 1998; Gómez et al., 2003; Kauffmann et al., 2004), or the HI (neutral Hydrogen) gas content-density relation, such that galaxies situated in higher (lower) density regions tend to be redder (bluer), have lower (higher) SFRs, and a lower (higher) HI gas content (Giovanelli & Haynes, 1985; Chung et al., 2009). The existence of these relations clearly indicates that the local environment of a galaxy has an influence on its properties, and that some physical mechanisms triggered in relatively high density environments are responsible for transforming galaxy properties. Several processes associated with environment are thought to play a role in galaxy transformation, viz. single or multiple galaxy-galaxy encounters, tidal interactions between galaxies and the cluster potential well, and the ram-pressure and thermal evaporation effects of the host cluster/group (Boselli & Gavazzi, 2006).

Not only the local environment of galaxies, but also their global environment (or their positions with respect to the Large Scale Structure (LSS) of the Universe) has an effect on their properties. The local density around galaxies alone may not be sufficient to explain the dependence of their properties on the large-scale environment. For e.g., it has recently been observed in the cosmic web structure around the nearby Virgo cluster that at fixed local density, the

fraction of late-type galaxies in filaments is intermediate between those found in the field and cluster regions (Castignani et al., 2021). Over the past few years, wide-field spectroscopic surveys have enabled the study of the role of global environment on galaxy properties through the use of large statistical data sets. A detailed literature review of the LSS environmental effects on galaxies is beyond the scope of this thesis. Nonetheless, in the following text, results from several studies are cited as examples to highlight the effect of the large-scale environment on galaxy properties: Galaxies falling into clusters along cosmic filaments are observed to have an increased SFR compared to those residing in cluster cores and empty voids, likely due to enhanced galaxy-galaxy interactions in the infalling regions (Porter et al., 2008; Biviano et al., 2011; Mahajan et al., 2012; Darvish et al., 2014). The large-scale underdense void regions appear to affect the growth of their member galaxies such that these galaxies tend to have lower values of dynamical mass ($\sim$few times 10^{10} $M_{\odot}$), smaller than average optical stellar disks, and show disturbed HI morphologies, all indicative of ongoing interactions and gas accretion in these pristine regions (van de Weygaert et al., 2011; Kreckel et al., 2012). The environmental imprint of the cosmic web filaments also reflects in the rotation of the member galaxies which have their spins correlated with the host filament axis as found in several studies (Tempel et al., 2013; Rong et al., 2016; Kraljic et al., 2020). More recently, the impact of filaments on the properties of the constituent galaxies has been investigated in greater detail (Alpaslan et al., 2016; Chen et al., 2017; Kuutma et al., 2017; Kraljic et al., 2018; Mahajan et al., 2018). These studies provide observational evidence for a decreasing SFR and an increase in color and stellar mass (M^*) of galaxies on approaching the filament spines, thus, depicting the key role played by the cosmic filaments in shaping the properties of galaxies.

1.2.1 Age and metallicity of galaxies

Age and metallicity[3] (Z) of a galaxy are fundamental attributes which provide clues to its star formation and chemical enrichment histories. Both age and Z, much like other galaxy properties (§1.2), are affected by a galaxy's environment. While older galaxies preferentially inhabit dense regions of space such as cluster cores, younger galaxies are abundantly found in the low-density environment of voids (Sánchez-Blázquez et al., 2006b; Annibali et al., 2007; Collobert et al., 2006; Trager et al., 2008; Pasquali et al., 2010). Several studies of clusters of galaxies have observed a trend of younger mean ages with increasing cluster-centric radius in the Coma ($z = 0.023$; Poggianti et al., 2001; Smith et al., 2008, 2009) and Virgo ($z = 0.0036$; Michielsen et al., 2008; Toloba et al., 2009) clusters. Just like age, the metallicity of galaxies is also found to correlate with their environment. Galaxies in cluster cores are found to be

[3]Metallicity is the abundance of elements heavier than Hydrogen and Helium present in an astronomical object of interest. The term 'metals' is used for *all elements except Hydrogen and Helium*.

more enriched relative to their counterparts in less dense environments (Skillman et al., 1996; Carter et al., 2002; Ellison et al., 2009; Peng & Maiolino, 2014; Wu et al., 2017). The study of a filamentary structure (z ∼0.53) in the COSMOS[4] field by Darvish et al. (2015) revealed that galaxies in the filament region are more metal-enriched (∼0.1–0.15 dex) than a control sample of galaxies in voids. Contrasting results have also been obtained when studying Z as a function of galaxy environment. For e.g., using a sample of ∼38,000 galaxies from the SDSS data release 7, Wu et al. (2017) showed that the gas-phase *Z* is weakly dependent on environment below the turnover stellar mass ($M^*/M_\odot$ $\sim 10^{10.5}$), upto which the metallicity is linearly correlated with environment. Beyond the turnover mass, the metallicity saturates, therefore, becoming independent of environment.

Z is also strongly correlated with the stellar mass of a galaxy (Lequeux et al., 1979). The observed trend is such that Z increases linearly with stellar mass (Caldwell et al., 2003; Ogando et al., 2008; Trager et al., 2008) or luminosity (Skillman et al., 1989; Brodie & Huchra, 1991; Bell & de Jong, 2000) at low masses, but saturates for massive galaxies ($M^*/M_\odot \gtrsim 10^{10.5}$; or beyond the turnover mass). Literature (Panter et al., 2008; Leethochawalit et al., 2018) on the evolution history of Z through cosmic time shows that this trend holds well for stellar (e.g. Gallazzi et al., 2005) as well as gas-phase metallicity (e.g. Tremonti et al., 2004; Cooper et al., 2008) in galaxies. The observed trend is also well established for galaxies at low (z ∼0.1; e.g. Gallazzi et al., 2005) and high redshift (Erb et al., 2006) alike. The mass-metallicity ($M^* - Z$) relation extends across at least three orders of magnitude in stellar mass and a factor of 10 in gas-phase metallicity, though with a significant scatter (Tremonti et al., 2004). Various studies have explored the physical causes of the scatter in the mass-*Z* relation, and the obvious culprit is found to be the observational uncertainty in estimating these quantities. Nevertheless, Cooper et al. (2008), using a sample of more than 57,000 star-forming galaxies from the SDSS data release 4, showed that the environment of galaxies can contribute $\sim 15\%$ of the observed scatter to the mass-*Z* relation. Several other studies provide observational evidence indicative of a slight metallicity enhancement in denser environments, over and above the effect of stellar mass (Mouhcine et al., 2007; Ellison et al., 2009). It is, therefore, unclear as to what factor (galaxy stellar mass, environment, presumably age ?) governs or dominates in governing the metallicity of galaxies. Moreover, the study of age and Z of galaxies poses a further challenge, in that it suffers from the problem of degeneracy, which is described in the following section.

[4]The COSMOS (Cosmic Evolution Survey) is an astronomical survey designed to probe the formation and evolution of galaxies as a function of both redshift and the local galaxy environment. The survey covers a field of 2 square degrees centred at RA = $10^h00^m24^s$ and Dec = $02°10'55''$ with spectroscopy and imaging (X-ray to radio) using a number of large ground-based telescopes and major space-based telescopes.
https://cosmos.astro.caltech.edu/

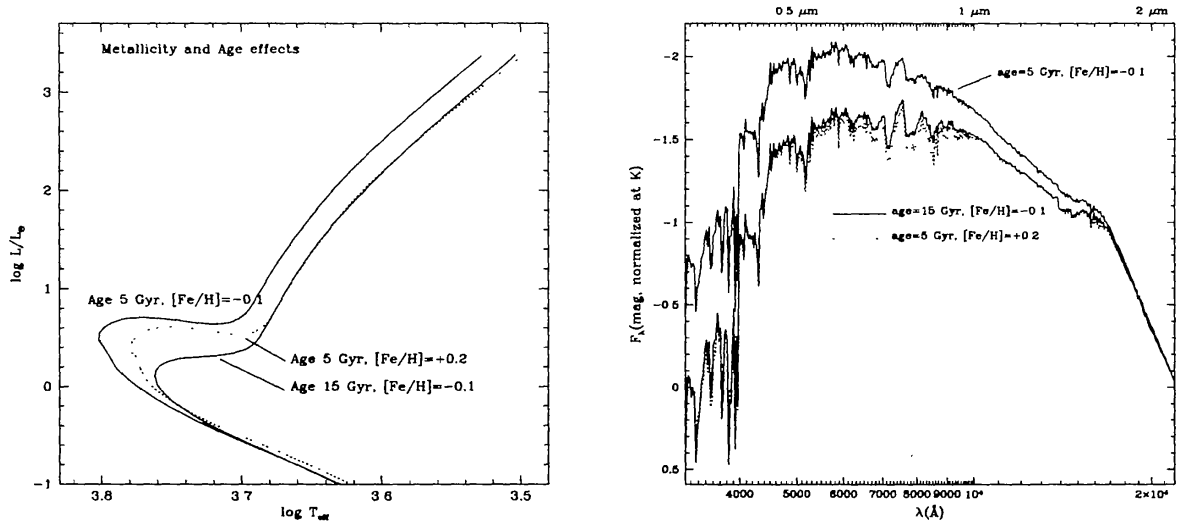

Figure 1.11: The age-metallicity degeneracy – isochrones of three times the age or twice the metallicity have nearly identical spectra. Image from Worthey (1999).

1.2.2 The age-metallicity degeneracy

The study of stellar populations in galaxies, where individual stars cannot be resolved (this is practically impossible today for the vast majority of galaxies, but they often say *times change and nothing is impossible*), is based on their integrated light. This combined light contains contributions from different generations of stars spanning a range in mass, age, and metallicity, and is primarily dominated by the stars which formed during the last episode of significant star formation within the galaxy. Brighter stars contribute more to the observed integrated light, and as a result, an observer essentially measures the luminosity-weighted mean age and metallicity of a galaxy. There is another catch to studying the integrated light from galaxies. Observables such as broad-band colors and stellar absorption line features, used to interpret integrated light from galaxies in terms of age and metallicity, respond in very similar ways to individual changes in age and Z. For instance, colors of the dominant stellar population within the galaxy become redder not only with increasing age but also with an increase in stellar metallicity. As a stellar population ages, more stars move to the giant branch, giving the population a redder color. The increase in metallicity leads to a rise in the stellar opacity which results in an increased absorption of photons in the stellar atmosphere causing it to heat up and expand. Enhanced metallicity may also cause increased line blanketing resulting from the preferential absorption of blue light in the stellar atmospheres due to the build up of a lot of metals there. Both these effects result in stars appearing redder. Since the optical colors may redden due to stellar age or metallicity, or both, two galaxies with significantly different

ages and chemical enrichment may exhibit similar colors and spectral features of comparable strengths. This is famously known as the *age-metallicity degeneracy* (Worthey, 1994, 1999) and is illustrated in Figure 1.11.

1.2.3 Breaking the age-metallicity degeneracy

Broadband optical colors are not very useful at breaking the age-metallicity degeneracy. Several optical absorption line features, however, respond in contrasting ways to changes in age and Z. Some features are more sensitive to changes in age while some others show a marked sensitivity to changes in metallicity. The sensitivity of an absorption feature is gauged using the 'metallicity sensitivity' parameter (Worthey, 1994) which is defined as the ratio of the percentage change in age to the percentage change in metallicity of a stellar population, to keep the strength of the feature of interest constant. Larger values of the parameter indicate a greater metallicity sensitivity. The metallicity sensitivities of several absorption line features are listed in Table 1.1. According to the sensitivity survey undertaken by Worthey (1994), the Balmer absorption line Hβ is the most sensitive age indicator while several Fe lines are promising metallicity indicators.

Table 1.1: Metallicity sensitivities of several absorption line features. Values taken from Worthey (1994).

Line Feature	$\left(\frac{\Delta age/age}{\Delta Z/Z}\right)_I$
G4300	1.0
Hβ	0.6
Fe5270	2.3
Fe5335	2.8
Fe5782	5.1
Ca4227	1.5

The varying sensitivities of the various absorption line features to changes in age and metallicity can be exploited (with limitations) to break the age-metallicity degeneracy. The standard technique is to plot an age-sensitive index against a metallicity-sensitive index to obtain a simultaneous estimate of the luminosity-weighted mean age and metallicity of a stellar population. If

the indices arrayed against each other form a grid-like pattern consisting of well-spaced points, it is an indication that the age-metallicity degeneracy is fairly broken, as opposed to all points on the plot lying on or around a line denoting a degenerate situation. A well-known set of absorption line features popularly used to break the age-metallicity degeneracy (and also the most successful) is the Lick index system which is described below.

1.2.4 The Lick index system

The Lick index system (Worthey et al., 1994; Worthey & Ottaviani, 1997) is a set of twenty-one atomic and molecular stellar absorption features measured in a sample of 460 nearby galactic stars in the 4000–6000 Å waveband. All the stars were observed at the Lick Observatory (Mount Hamilton, California, United States) between 1972 and 1984 using the 3m Shane telescope and spectra obtained with the Cassegrain spectrograph and image dissector scanner (IDS) at moderate resolution (FWHM: full width at half maximum $\sim$9 Å). The first eleven Lick indices were defined using a sample of stars which were primarily K giants and subgiants in the solar-neighborhood (Faber et al., 1985). Gorgas et al. (1993) extended that sample to include dwarf stars (F and G type) in the field and clusters to measure the eleven indices. Worthey (1994) further extended the stellar sample to include M type dwarfs and giants, and several hot stars to span the old, metal-rich populations along with the young stars 0.5–2 Gyr old. The authors also supplemented the original list of eleven absorption line features with ten new features, thus constituting the whole Lick/IDS system.

Absorption Line Measurements: Absorption line strengths are expressed in terms of *indices*, in which a *feature* bandpass is defined centred on the feature of interest, flanked to the blue and red regions by *continuum* bandpasses that are really pseudocontinua[5]. The pseudocontinuum bandpasses are defined by the need to be located near the feature bandpass and to be in regions of less absorption than that of the feature being measured (Worthey et al., 1994). Once the centre of the feature of interest is fixed, two pseudocontinuum bandpasses are defined on either side of the central bandpass. A line is then drawn between the midpoints of the two flanking bandpasses which represents the local continuum. The difference between the local continuum and the central bandpass flux is computed to determine the index strength or the equivalent

[5]At the spectral resolution of the Lick/IDS system ($\sim$8–9 Å FWHM) there is no *true* continuum in the spectra of late-type stars (G, K, and M spectral type) due to excessive absorption. Hence, the term *pseudocontinuum* is used.

width (EW) of the atomic absorption feature of interest.

$$EW(\text{Å}) = \int_{\lambda_1}^{\lambda_2} \left(1 - \frac{F_{I\lambda}}{F_{C\lambda}}\right) d\lambda \tag{1.3}$$

where $F_{I\lambda}$ and $F_{C\lambda}$ are the flux values per unit wavelength in the index passband and the straight-line local continuum flux in the index passband, respectively, and λ_1 and λ_2 are the lower and upper wavelength bounds of the index passband. Part of the Lick absorption feature index system is illustrated for several stellar types in Figure 1.12. The corresponding index definitions, viz. the locations of the index passbands and their flanking pseudocontinua are provided in Table 1.2.

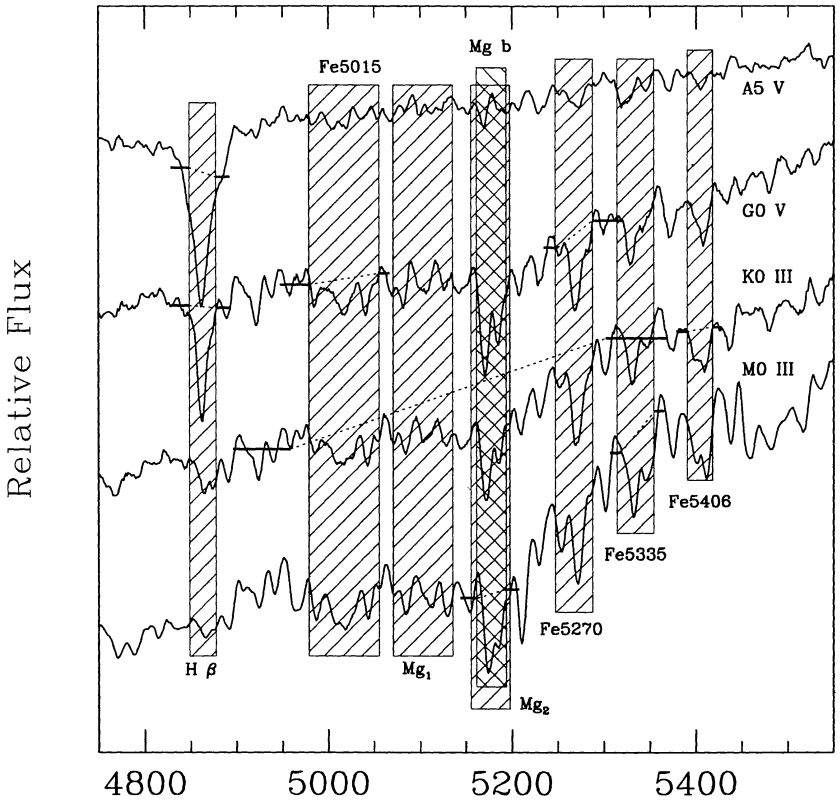

Figure 1.12: Part of the Lick absorption feature index system illustrated for several stellar types. The central index passbands are marked in *hatched rectangles* and the local continua are shown in *dashed lines*. Image from Worthey (1999).

Table 1.2: Definitions of several absorption line indices from the Lick index system. Values taken from Worthey et al. (1994).

Index Name	Index Bandpass (ranges in Å)	Pseudocontinua (ranges in Å)	Line Measures
Hβ	4847.875–4876.625	4827.875–4847.875 (blue) 4876.625–4891.625 (red)	Hβ, Fe I
Fe5015	4977.750–5054.0	4946.500–4977.750 5054.0–5065.250	Fe I, Ni I, Ti I
Mg *b*	5160.125–5192.625	5142.625–5161.375 5191.375–5206.375	Mg *b*
Fe5270	5245.650–5285.650	5233.150–5248.150 5285.650–5318.150	Fe I, Ca I
Fe5335	5312.125–5352.125	5304.625–5315.875 5353.375–5363.375	Fe I
Fe5406	5387.500–5415.0	5376.250–5387.500 5415.0–5425.0	Fe I, Cr I

1.2.5 Stellar Population Synthesis

The interpretation of the observed integrated light (colors and spectra) from a stellar population (e.g. an unresolved galaxy) in terms of meaningful physical parameters (e.g. age, metallicity, mass) describing the population, requires the use of a popular technique called Stellar Population Synthesis (SPS). An SPS model tries to find a combination/synthesis of stars for which the integrated spectral energy distribution (SED) is in close agreement with the observed spectrum of the object under study. The simplest of SPS models is a simple stellar population (SSP) or a single-age, single-metallicity model, where all stars are assumed to have formed at the same time and have an identical chemical composition. There are three basic inputs to any SSP model: an initial mass function (IMF) describing the initial distribution of masses for a population of stars, the stellar evolution tracks of stars of varying masses, and stellar spectral libraries. The SED of an SSP of age t and metallicity Z ($f_{SSP}(t, Z)$) is constructed by combining these components in the following way:

$$f_{SSP}(t, Z) = \int_{M_i^l}^{M_i^u(t)} f_{star}[L(M_i), T(M_i)|t, Z]\phi(M_i)dM_i \tag{1.4}$$

where M_i is the initial (zero-age main sequence) stellar mass, $\phi(M_i)$ is the IMF, f_{star} is a stellar spectrum, L and T are the luminosity and temperature of the star, M_i^l is the Hydrogen burning limit (either 0.07$M_\odot$ or 0.1$M_\odot$ depending on the SPS code), and $M_i^u(t)$, the upper limit of the integration, is dictated by stellar evolution (Conroy, 2013). Using the stellar evolution tracks of stars with masses ranging from the Hydrogen burning limit to the maximum stellar mass of the population ($\sim$100 $M_\odot$), a theoretical isochrone (the loci traced by a stellar population of a given age and Z on the Hertzsprung-Russell diagram, which is a plot of the stellar luminosity versus temperature) is constructed. The isochrone represents a population of stars each having the same age and Z, but different values of stellar luminosity and temperature. A model SED for a particular SSP can then be constructed by using a library of stellar spectra (with a wide stellar parameter coverage) and integrating along the isochrone with appropriate weighting by the adopted IMF, thus allowing a transformation of the age and Z of the stellar population to observables such as color and line indices. By using SSP models, one thus effectively measures the luminosity-weighted mean values of the physical parameters of the stellar population. Detailed information about the star formation history of the population is not obtained with SSP models.

MILES library

MILES[6] is an empirical stellar library developed for stellar population synthesis models. It consists of $\sim$1000 stars spanning a large range in atmospheric parameters. All stellar spectra were obtained at the 2.5m *Isaac Newton Telescope* (Roque de los Muchachos Observatory, La Palma, Spain). The spectra cover the wavelength range 3525–7500 Å (Sánchez-Blázquez et al., 2006a) at a spectral resolution of 2.5 Å (FWHM) (Falcón-Barroso et al., 2011). The number of stars, spectral type coverage, spectral resolution, and flux calibration accuracy in the MILES stellar library is a significant improvement over previous libraries used in population synthesis models.

1.3 This thesis...

This thesis is a compilation of three research works conducted during my doctoral study at the *Indian Institute of Science Education and Research, Mohali, India.* I have carried out the first detailed X-ray studies of two nearby galaxy clusters – Abell 2151 and Abell 1569 – in the first two projects. The main motivation for choosing these two galaxy clusters was that both show

[6]Medium-resolution Isaac Newton Telescope Library of Empirical Spectra; http://miles.iac.es/

interesting substructures and hence, allow for finding evidence of mergers and AGN activity in these systems. Abell 1569, particularly, is a good site to study the interaction between radio galaxies and the host intracluster medium. The third work is a separate study which explores the effect of the large-scale environment on the age and metallicity of galaxies in the Coma supercluster.

The research work presented in this thesis has made use of optical, X-ray, and radio data collected by both ground-based and space-borne instruments, which are described in Chapter 2. The data reduction procedures and subsequent data analyses are described in Chapter 3. The X-ray works on Abell 2151 and Abell 1569 are described in Chapters 4 and 5, respectively. The optical study of the age and Z of galaxies in the Coma supercluster is described in Chapter 6. I summarize the findings of my doctoral research along with prospects for future research in the area in Chapter 7.

Chapter 2

Telescopes and observations

***Outline*:** This chapter describes the different telescopes, their scientific instruments, and the observations used in the research work presented in this thesis. Observations from X-ray space observatories – *XMM-Newton* and *Chandra* – were used in the study of the galaxy clusters Abell 2151 and Abell 1569. A description of these observatories is given in §2.1. The work on Abell 1569 has also made use of radio observations with the ground-based *Very Large Array* (VLA) telescope. A description of the VLA is given in §2.2. The statistical study of age and metallicity of galaxies in the Coma supercluster has employed optical data from the *Sloan Digital Sky Survey* (SDSS) conducted using a dedicated 2.5-m wide-angle ground-based optical telescope. A description of the SDSS is provided in §2.3. Details of the observational data used are provided in each section.

2.1 X-ray

X-rays from astronomical objects are almost completely absorbed by the Earth's atmosphere. Therefore, to observe the different sources that emit X-rays, the X-ray telescopes cannot be based on Earth and have to be placed high above the Earth's surface using balloons and rockets. Additionally, X-rays do not reflect off mirrors in the same way that visible light does. Instead, the X-ray photons penetrate into the mirrors due to their high energy. The only way to capture X-rays, therefore, is to align the mirrors nearly parallel to incoming radiation, which makes these mirrors look more like barrels instead of the more familiar dish-shape of optical telescopes. A schematic illustration of X-ray photons getting focused by an X-ray telescope is given in Figure 2.1.

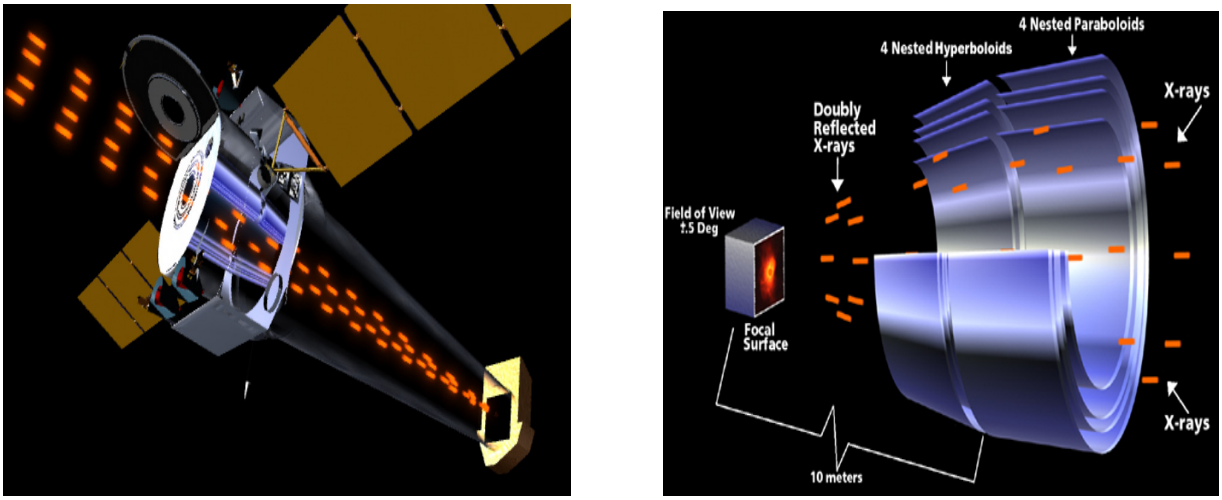

Figure 2.1: *left*: Schematic illustration of an X-ray telescope. X-ray photons (in *red*) entering the telescope at grazing angles are reflected and focused onto an electronic detector placed at the focus to make an image of a cosmic source. *right*: A zoomed in view of the functioning of an assembly of four coaxial and cofocal X-ray mirrors.
Credit: NASA/CXC

2.1.1 XMM-Newton Observatory

The **X**-ray **M**ulti-**M**irror Mission or *XMM-Newton* is a powerful, currently active X-ray observatory launched by the European Space Agency on December 10, 1999, from Kourou, French Guiana, by an Ariane 5 space launch vehicle. The observatory has a highly elliptical orbit with an eccentricity of $\sim$0.67 and an orbital period of $\sim$48 hours. As of May 2021, *XMM-Newton*'s orbit has an apogee height of 105200 km, a perigee height of 15900 km, and an inclination of $70.7°$. The highly eccentric orbit of *XMM-Newton* keeps the satellite outside the radiation belts surrounding the Earth (extending out to $\sim$40000 km from the Earth's surface) for $\sim$40 hours of each orbit, allowing for long and safe observational periods. The total length of *XMM-Newton* is $\sim$10 m, and its solar arrays give the satellite a diametric span of $\sim$16 m. At the time of its launch, the satellite weighed $\sim$3800 kg. The *XMM-Newton* observatory carries four co-aligned telescopes – three X-ray telescopes and a single optical/ultraviolet telescope, giving the mission a multi-wavelength capacity. All data recorded on these telescopes are transmitted to the XMM Mission Operations Centre at the European Space Operations Centre (Darmstadt, Germany) in real time, since the spacecraft does not have onboard data storage capacity. Data are then forwarded to the European Space Astronomy Centre's Science Operations Centre (Villafranca del Castillo, Spain) for processing and distribution.

Each of the three X-ray telescopes onboard the *XMM-Newton* observatory consists of 58 Wolter type I grazing-incidence mirrors which are nested in each other in a coaxial and cofocal configuration. The mirror shells are made of Nickel and are polished with a reflective coating of Gold. The diameters of the innermost and outermost mirror shells are 306 mm and 700 mm, respectively. The innermost mirror has a thickness of 0.47 mm. The mirror thickness increases linearly with shell diameter to guarantee sufficient stiffness giving the outermost mirror shell a thickness of 1.07 mm. The radial separation between adjacent shells varies between 1 mm and 5 mm. The axial length of the mirrors is 600 mm. The nesting of a large number of mirrors gives *XMM-Newton* a large effective collecting area of $\sim$1500 cm^2 at 1 keV and $\sim$900 cm^2 at 7 keV. Each X-ray telescope has a focal length of 7.5 m and contains an X-ray Charge Coupled Device (CCD) camera at its primary focus. The three X-ray CCD cameras together comprise the European Photon Imaging Camera (EPIC). Two of the three telescopes also contain Reflection Grating Assemblies (RGA) for high resolution spectroscopy. The RGAs intercept about 40% of the total light focused by the mirrors and direct it to separate CCD cameras placed at the secondary focii of these telescopes. A schematic illustration of X-rays getting focused at the EPIC and the RGS is shown in Figure 2.2. The work presented in this thesis has made use of data obtained with the EPIC instrument onboard the *XMM-Newton* observatory. The EPIC is described in detail below.

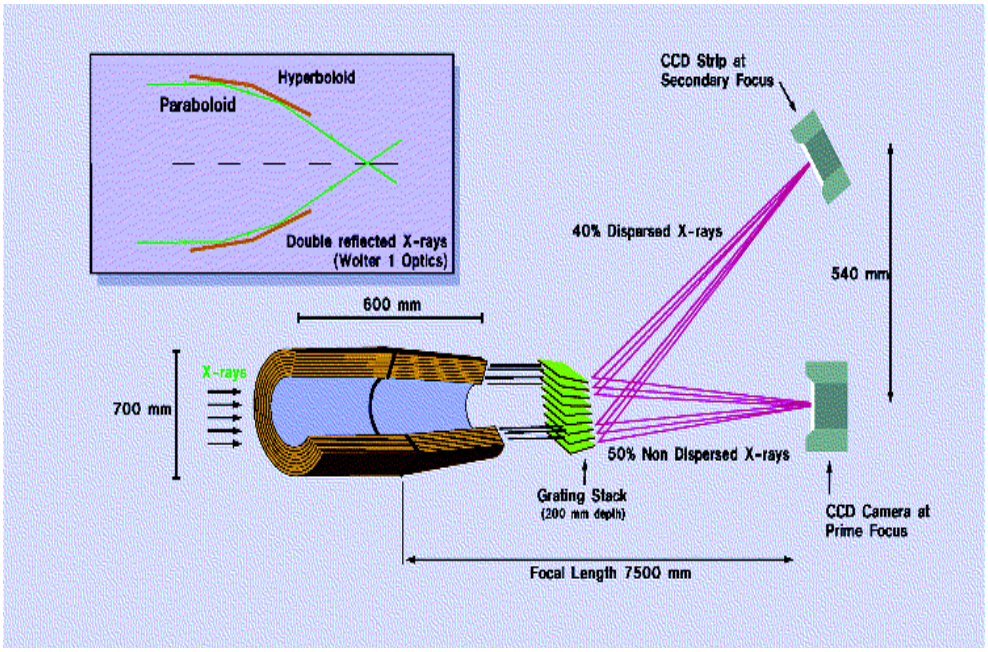

Figure 2.2: X-rays entering two of the three telescopes onboard the *XMM-Newton* observatory get intercepted by the Reflection Grating Assemblies and are directed to separate CCD cameras placed at the secondary focii of these telescopes.
Credit: ESA

The European Photon Imaging Camera

Each of the three X-ray telescopes onboard the *XMM-Newton* observatory carries an X-ray CCD camera. These cameras collectively comprise the European Photon Imaging Camera which is the main spectro-imaging instrument of *XMM-Newton*. One of the EPIC cameras uses pn-type CCDs (EPIC PN) while the other two cameras use Metal-Oxide-Silicon (MOS)-type CCDs (EPIC MOS). Each EPIC camera can perform sensitive imaging observations over a large field of view (FOV) of $\sim$30 arcmin in the energy range 0.2–12.0 keV with a moderate spatial resolution of $\sim$6 arcsec (full width at half maximum). The cameras also provide a moderate spectral resolution of $\sim$150 eV at 6.4 keV.

EPIC PN

The EPIC PN camera is placed at the primary focus of one of the X-ray telescopes onboard the *XMM-Newton* observatory and receives the unobstructed X-ray light focused by the telescope's mirror module. It consists of 12 pn-CCD chips integrated onto a single Silcon wafer and was built by the Max Planck Institute for Extraterrestrial Physics (Garching) and the Institute for Astronomy $\&$ Astrophysics (Tübingen), both located in Germany. Each pn-CCD pixel measures 150 μm on a side (equivalent to 4.1 arcsec on the sky) and each CCD chip consists of 64×200 pixels. The pn CCDs are back-illuminated giving the pn detector a higher quantum efficiency. The pn chip array is slightly offset with respect to the optical axis of its X-ray telescope to avoid the on-axis observing position from coinciding with the central chip boundary. The layout of the EPIC PN camera is shown in Figure 2.3

The pn camera can be operated in six different science modes – Full Frame, Extended Full frame, Large Window, Small Window, Timing, and Burst mode. In the Full Frame and Extended Full Frame modes, all the pixels of all 12 CCDs are read out. Thus, these two modes allow the entire FOV to be covered. The 12 CCDs are read out in a parallel manner. The Full Frame mode has a complete readout cycle of 73.3 ms which includes 4.6 ms needed for the readout itself and the remaining 68.7 ms for the integration of the source image. The Extended Full Frame mode is used for the observation of extended objects and therefore, requires a longer integration time of 199.2 ms (this includes 4.6 ms needed for the readout itself). In the Large Window mode only the inner half of the total area covered by the 12 CCDs is read out. This reduces the FOV in this mode but results in an improved time resolution of 47.7 ms. In the Small Window mode only a part of one of the central four CCDs (CCD number 4) is used to collect data. This results in further reduction in the FOV but provides a finer time resolution of about 5.7 ms. The Timing and Burst modes are two fast modes designed for enhanced time resolution. Only CCD number 4 is operated in these two modes. In the Timing mode the spatial information if preserved only in one dimension but is lost in the other direction due to continu-

ous shifting and collapsing of rows (10 rows at a time here) being read out at a high speed. This mode offers a time resolution of 0.03 ms. In the Burst mode all 179 pixels along one dimension in CCD4 are rapidly read out at a time leading to a high time resolution of 7 μs.

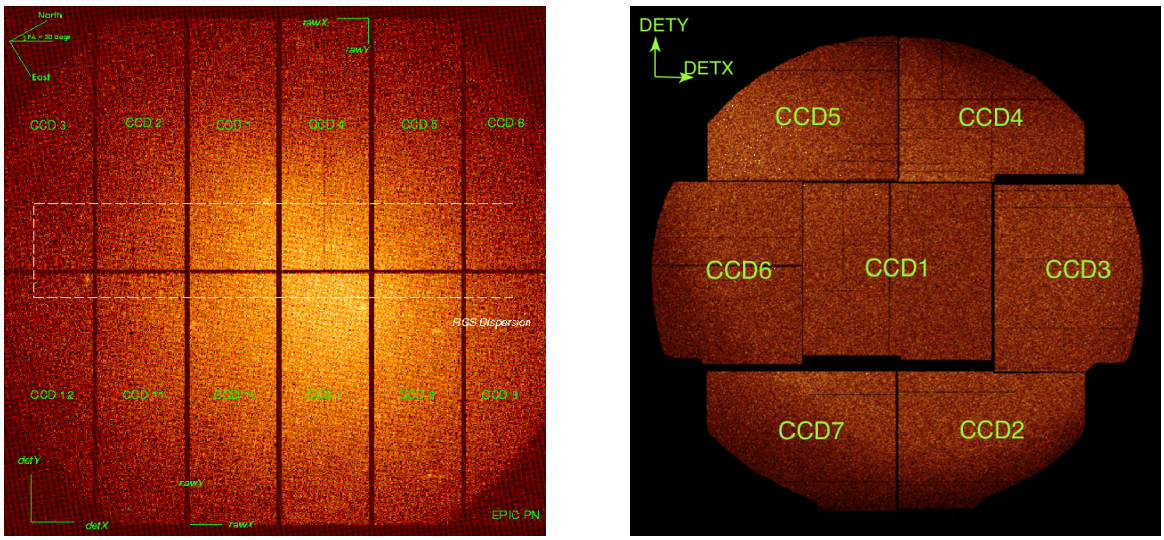

Figure 2.3: The layout of the *XMM-Newton* EPIC PN (*left*) and EPIC MOS (*right*) CCD arrays. Credit: ESA-XMM-Newton SOC

EPIC MOS

The EPIC MOS detectors are placed at the primary focii of the two X-ray telescopes carrying the RGAs. Therefore, these instruments receive only $\sim$44–50$\%$ of the unobstructed incoming light focused by the telescope mirrors. The MOS cameras were developed and built by the University of Leicester (UK) and the English Electric Valve (EEV) Company (now called Teledyne e2v). Each MOS detector consist of an array of 7 individual and identical EEV type 22 front-illuminated CCDs. The central MOS-CCD is located at the focal point on the optical axis of the telescope. The other 6 CCDs surround the central CCD and are moved towards the mirror by 4.5 mm. This is done to follow closely the slight curvature of the focal plane of the telescope. Each MOS-CCD pixel measures 40 μm on a side (equivalent to 1.1 arcsec on the sky) and each CCD chip consists of 600×600 pixels. The layout of the EPIC MOS camera is shown in Figure 2.3

The MOS detector can be operated in four data acquisition modes – Full Frame, Large Window and Small Window (these two are collectively known as the Partial Window mode), and Timing mode. In the Full Frame mode all the pixels of all 7 CCDs are used. This mode offers the full FOV for observations and a time resolution of 2.6 s, which is equal to the basic readout speed of the MOS CCDs. In the Partial Window mode, parts of the central CCD of the MOS camera can be operated independent of the peripheral CCDs, thus, offering faster readout times. The Large Window mode uses 300×300 pixels on the central CCD resulting in a time resolution of 0.9 s while the Small Window mode uses the central 100×100 pixels leading to an integration time of 0.3 s. The Timing mode (also known as Fast mode) is used for timing observations. In this mode a central window of width 100 pixels on the central CCD is used and 100 rows are compressed into one dimension giving a time resolution of 1.75 ms.

The EPIC CCDs not only detect X-ray photons, but are also sensitive to infrared, optical, and ultraviolet light. The detected X-ray signal may, therefore, become contaminated by these unwanted non-X-ray photons. To prevent this, each EPIC camera contains a set of four separate optical blocking filters. These filters are mounted on a six slot filter wheel and are separated from one another by an angular distance of 60 degrees. Two of the filters are *thin* filters, each made of a 40 nm layer of Aluminium followed by a 160 nm polyimide film (directed from the telescope towards the detector). One is a *medium* filter made of an 80 nm Aluminium layer followed by a 160 nm polyimide film. The fourth filter is *thick*. It consists of a 45 nm layer of Tin followed by 55 nm of Aluminium, 330 nm of Polypropylene and a second 55 nm layer of Aluminium. Each filter has a diameter of 76 mm. The remaining two positions on the filter wheel are the fully *closed* and fully *open* positions. The *closed* filter is made of a thick 1.05 mm layer of Aluminium and is used to protect the EPIC CCDs from soft protons. The *open* position is used when the light flux of the source being observed is very low, and no filter is required.

2.1.2 Chandra X-ray Observatory

The *Chandra* X-ray Observatory (CXO), a space mission of the National Aeronautics and Space Administration, was launched on July 23, 1999, from the Kennedy Space Center Launch Complex 39 (Florida, US) by Space Shuttle Columbia. The observatory has a highly elliptical orbit with an eccentricity of $\sim$0.74 which allows it to make uninterrupted observations for as long as 55 hours in its orbital period of $\sim$64 hours. At the time of its launch, *Chandra* had an orbital inclination of 28.5°, an apogee and perigee height of $\sim$140000 km and $\sim$10000 km,

respectively, and weighed ∼4800 kg (Weisskopf et al., 2000). The *Chandra* flight system has a length of 13.8 m and a width of 19.5 m with the solar arrays deployed.

The X-ray telescope onboard the *Chandra* observatory consists of four nested, concentric Wolter type I mirrors having a common focal length of 10 m. These mirrors together with their support structures constitute the High-Resolution Mirror Assembly (HRMA) (van Speybroeck et al., 1997). Each mirror element has a length of ∼0.83 m and diameters approximately 0.63, 0.85, 0.97, and 1.2 m. The mirror thickness ranges from 16 mm for the inner elements to 24 mm for the outer ones. The mirrors are fabricated from Zerodur glass, and polished and coated with Iridium on a binding layer of Chromium. The mirrors have an effective area between 700 and 800 cm^2 at 1 keV and an on-axis angular resolution of ∼0.5 arcsec. The incoming X-rays are focused by the mirror assembly to the focal plane instruments of the observatory – the Advanced CCD Imaging Spectrometer (ACIS) and the High Resolution Camera (HRC). These are the main imaging detectors on *Chandra* and only one out of these two instruments can be used at a given time. There are two additional science instruments available on *Chandra* for high resolution spectroscopy – the High Energy Transmission Grating Spectrometer (HETGS) and the Low Energy Transmission Grating Spectrometer (LETGS). These are grating arrays and can be activated by being flipped into the path of the focused X-rays just behind the mirrors. The science instruments onboard the *Chandra* observatory are controlled by the Operations Control Center (OCC), a part of the Chandra X-ray Center (CXC) hosted by the Smithsonian Astrophysical Observatory in Cambridge, Massachusetts. The data collected by observations with *Chandra* are stored on an onboard recorder and are later transmitted to the ground every eight hours. The data are then processed and analysed by the OCC at the CXC. The work presented in this thesis has made use of X-ray data obtained with the ACIS instrument which is described in detail below.

The Advanced CCD Imaging Spectrometer

The Advanced CCD Imaging Spectrometer (Garmire et al., 2003) is the primary imaging instrument onboard the *Chandra* observatory. It was designed and fabricated by the Pennsylvania State University (Pennsylvania, US) and the Massachusetts Institute of Technology (Cambridge, Massachusetts, US). The ACIS consists of 10 planar CCDs. 4 out of the 10 CCDs are arranged in a 2×2 array (ACIS-I). 6 CCDs are arranged in a 1×6 linear array (ACIS-S). The ACIS-I array is used primarily for imaging. The ACIS-S array can be used either for imaging or in conjunction with the high or low energy grating arrays to obtain high resolution spectra. All of the ACIS-I CCDs (I0–I3) are front-illuminated. 2 out of the 6 ACIS-S CCDs (S1 and S3) are back-illuminated while the others are front-illuminated (S0, S2, S4, S5). Each ACIS CCD consists of 1024×1024 pixels. Each square pixel measures 23.985 μm on a side and subtends

0.492 arcsec on the sky. As a result, the ACIS offers a high on-axis imaging resolution of ∼0.5 arcsec over the energy range 0.2–10 keV. The FOV of ACIS-I is 16.9×16.9 arcmin^2 while that of ACIS-S is 8.3×50.6 arcmin^2. The ACIS is also capable of acquiring moderate resolution spectra. The front-illuminated CCDs provide an energy resolution[1] of ∼130 eV at 1.49 keV and ∼280 eV at 5.9 keV. The back-illuminated S3 chip offers the best spectral resolution[2] of ∼95 eV at 1.49 keV and ∼150 eV at 5.9 keV. The layout of the ACIS-I and ACIS-S CCD arrays is shown in Figure 2.4.

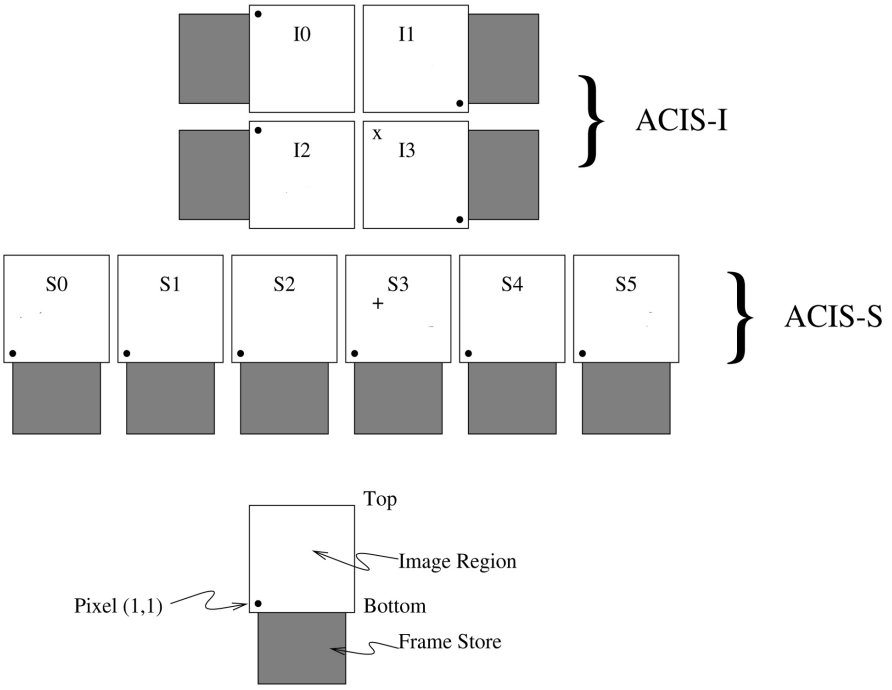

Figure 2.4: The layout of the *Chandra* ACIS-I and ACIS-S CCD arrays. Credit: CXC

The ACIS can be operated in two observing modes – the Timed Exposure (TE) mode, and the Continuous Clocking (CC) mode. In the TE mode, data are collected for a fixed pre-selected period of time, ranging from 0.1 to 10.0 s, in steps of 0.1 s. The integrated data are then transferred from the imaging region to the framestore region which takes ∼41 ms. The framestore read-out process takes ∼3.2 s. The optimal frame time is 3.2 s if data are acquired in the full frame mode, i.e., if data from the entire CCD chip are read. Data acquisition may also be done

[1]The energy resolution listed is measured at the ACIS-I aimpoint on the I3 CCD (x symbol on I3 in Fig. 2.4).

[2]The energy resolution listed is measured at the ACIS-S aimpoint on the S3 CCD (+ symbol on S3 in Fig. 2.4) without using the grating arrays.

from restricted regions of the CCDs, known as subarrays, in order to reduce the frame time. The CC mode is the timing mode of the ACIS which provides a time resolution of 3 ms. In this mode, a 1024×1024 pixel image is collapsed into a 1×1024 pixel image. Data along each column are added together. This results in a faster integration time of 2.85 ms but comes with a loss in details of the spatial distribution in the columns.

Just like the EPIC CCDs of *XMM-Newton*, the *Chandra* ACIS CCDs are also sensitive to optical light. Contamination from optical photons is minimised by placing optical blocking filters between the CCD chips and the HRMA. These filters are composed of a layer of polyimide inserted between two layers of Aluminium (Al–Polyimide–Al). For the ACIS-I array, the thicknesses of the Al–Polyimide–Al layers are 1200Å–2000Å–400Å. For the ACIS-S array, the nominal thicknesses are 1000Å–2000Å–300Å.

2.1.3 Observations

The *XMM-Newton* and *Chandra* X-ray data used in the work presented in this thesis were publicly available and obtained from the HEASARC[3] archive. The observations are listed in Table 2.1. During the *XMM-Newton* observations, the PN detector was operated in Extended Full Frame mode with thin filter while the MOS detectors were set to Full Frame mode and also used thin filter. All *Chandra* observations were made in the Timed Exposure mode.

[3]High Energy Astrophysics Science Archive Research Center; https://heasarc.gsfc.nasa.gov/

Table 2.1: X-ray observations of Abell 2151 and Abell 1569

Cluster	Satellite	Observation ID	Date of Observation	RA (J2000) h:min:s	Dec (J2000) ° : ′ : ″	Detector	Observation Time (ks)
Abell 2151	*XMM-Newton*	0147210201	2003 March 10	16 05 07.08	+17 44 59.00	EPIC	26.20
		0147210101	2003 Aug 9	16 05 07.08	+17 44 59.00	EPIC	29.95
		0147210301	2003 Aug 11	16 05 07.08	+17 44 59.00	EPIC	19.04
	Chandra	4996	2004 July 25	16 04 36.00	+17 43 23.00	ACIS-I	22.12
		17038	2015 Feb 22	16 05 31.80	+17 48 26.20	ACIS-S	7.85
		18171	2016 April 17	16 05 44.60	+17 43 03.50	ACIS-S	15.07
		19592	2017 May 31	16 04 35.80	+17 43 17.30	ACIS-I	16.46
		20086	2017 June 03	16 04 35.80	+17 43 17.30	ACIS-I	30.06
		20087	2017 June 04	16 04 35.80	+17 43 17.30	ACIS-I	35.57
Abell 1569	*Chandra*	6100	2005 April 07	12 36 36.59	+16 36 50.00	ACIS-I	41.75

2.2 Radio

Radio observations of galaxy clusters are vital to study the non-thermal populations of the intracluster medium. They provide the unique opportunity to understand the dynamics of radio galaxies populating galaxy clusters and their interaction with the surrounding intracluster gas. Most radio waves[4] can pass through the Earth's atmosphere without getting absorbed or reflected and reach the surface of the Earth. Hence, most radio telescopes are ground-based. A simple radio telescope designed to collect radio signals from space has three basic components – one or more *antennas* to collect the incoming signal, a *receiver* and *amplifier* to boost the weak signal, and a *recorder* to keep account of the detected signal. The most common type (and the first to be built) of radio telescope is a parabolically shaped reflector, dubbed the 'dish', which focuses the incoming radio waves to a single point above the dish (the *focal* point

[4]The radio window consists of frequencies roughly between 5 MHz and 30 GHz. The upper limit can vary depending upon atmospheric conditions.

of the paraboloid) where a feed[5]/receiver is placed. Alternatively, the focused radio signal may be redirected by a subreflector placed at the focus to a feed (connected to a receiver) placed near the centre of the dish.

To achieve an angular resolution[6] of the order of a few arcseconds with a single radio dish, the size of the dish has to be made extremely large (∼hundreds of metres in diameter). For e.g., the huge 305 m diameter radio dish of the now inoperational Arecibo telescope (Puerto Rico, US) could provide an angular resolution of ∼30 arcsec at an observing wavelength of 21 cm. Since building such large radio dishes is impractical, an array of smaller radio dishes is used to complement the work of a giant, single-dish telescope. Such an array is known as a *radio interferometer*. All the individual dishes in the interferometer simultaneously observe an astronomical source and their observations are added together. A *radio interferometer* is equivalent to a single large telescope of diameter equal to the distance between the two farthest telescopes in the array.

2.2.1 Very Large Array

The *Very Large Array* (VLA) is a radio telescope array located on the plains of San Agustin near Socorro, New Mexico, U.S., and operated by the National Radio Astronomy Observatory. The plains are a flat stretch of desert situated far from cities and are surrounded by mountains which help in keeping out man-made radio interference signals. Construction of the VLA began in 1973 and the array became fully operational in 1980. The VLA underwent a major decade-long technical upgrade (in terms of frequency coverage and resolution, sensitivity, and bandwidth) which was completed in 2012. The VLA was renamed the *Karl G. Jansky Very Large Array* or JVLA thereafter. The interferometer consists of 28 parabolic dishes (27 active and 1 spare), each having a diameter of 25 m and weighing ∼230 tons. The dishes are arranged in a Y-shaped three-arm configuration – the northern, eastern and western arms. Each arm of the VLA contains 9 dishes. Along each arm, the spacing of the 9 dishes is concentrated towards the centre and follows a power law distribution as one moves outwards. The northern arm of the VLA is shorter than the other two arms. The individual dishes are placed on rails and can be moved around with the help of a transporter, making the VLA a reconfigurable array (its angular resolution and maximum angular extent can be varied based on the science requirements).

[5]A feed or a feed horn is a small radio antenna used to observe a specific wavelength range from the many different wavelengths bounced by the dish.

[6]Angular resolution $\theta \sim \lambda/\mathrm{D}$, where, θ is in radians. λ and D are the observing wavelength and the diameter of the dish, respectively, both in the same units.

The VLA can observe sources at declinations between -44° and $+90^\circ$. The observing frequency of the telescope currently ranges from 50 MHz to 50 GHz, and is divided into 9 frequency bands which are listed in Table 2.2. The array can operate in four primary configurations, viz. A, B, C, and D. The four configurations – A, B, C, and D – provide maximum arm lengths of 21 km, 6.4 km, 1.95 km, and 600 m, respectively. The A configuration has the maximum separation between the farthest elements in the array, and hence, offers the best angular resolution at a given observing frequency. The D configuration offers low angular resolution but the largest angular scale of detectable emission (or field of view). The angular resolution and the largest angular scale of observation offered by the different array configurations at different observing frequencies are listed in Table 2.2. As an example, the antenna/dish positions in the VLA B configuration are shown in Figure 2.5. For very high ($> +75^\circ$) and very low ($< -15^\circ$) declination sources, the VLA can be made to operate in hybrid configurations, e.g., the BnA configuration, where the northern arm of the array is in A configuration while the other two arms operate in the B configuration. Figure 2.6 shows the radio galaxy *Hercules A* as observed by the different VLA configurations.

Table 2.2: Frequency bands and configuration properties of the VLA

	Configuration		A		B		C		D	
B_{max}[1] (km)			36.4		11.1		3.4		1.03	
B_{min}[2] (km)			0.68		0.21		0.035		0.035	
Frequency band	Range[3] (GHz)	Central Frequency (GHz)	θ_{SB}[4] (arcsec)	θ_{LAS}[5] (arcsec)	θ_{SB}	θ_{LAS}	θ_{SB}	θ_{LAS}	θ_{SB}	θ_{LAS}
4	0.058–0.084	0.074	24	800	80	2200	260	20000	850	20000
P	0.23–0.47	0.35	5.6	155	18.5	515	60	4150	200	4150
L	1.0–2.0	1.5	1.3	36	4.3	120	14	970	46	970
S	2.0–4.0	3.0	0.65	18	2.1	58	7	490	23	490
C	4.0–8.0	6.0	0.33	8.9	1.0	29	3.5	240	12	240
X	8.0–12.0	10.0	0.20	5.3	0.60	17	2.1	145	7.2	145
Ku	12.0–18.0	15.0	0.13	3.6	0.42	12	1.4	97	4.6	97
K	18.0–26.5	22.0	0.089	2.4	0.28	7.9	0.95	66	3.1	66
Ka	26.5–40.0	33.0	0.059	1.6	0.19	5.3	0.63	44	2.1	44
Q	40.0–50.0	45.0	0.043	1.2	0.14	3.9	0.47	32	1.5	32

Notes:

[1]B_{max} is the maximum antenna separation in the array.

[2]B_{min} is the minimum antenna separation in the array.

[3]The nominal band edges are listed.

[4]θ_{SB} is the synthesized beam width (full width at half maximum) or the angular resolution of the array; The listed resolutions are appropriate for sources with declinations between -15° and $+75^{\circ}$.

[5]θ_{LAS} is the largest angular scale structure visible to the array.

Sources: https://science.nrao.edu/facilities/vla/docs/manuals/oss2013B/performance/bands
https://science.nrao.edu/facilities/vla/docs/manuals/oss/performance/resolution

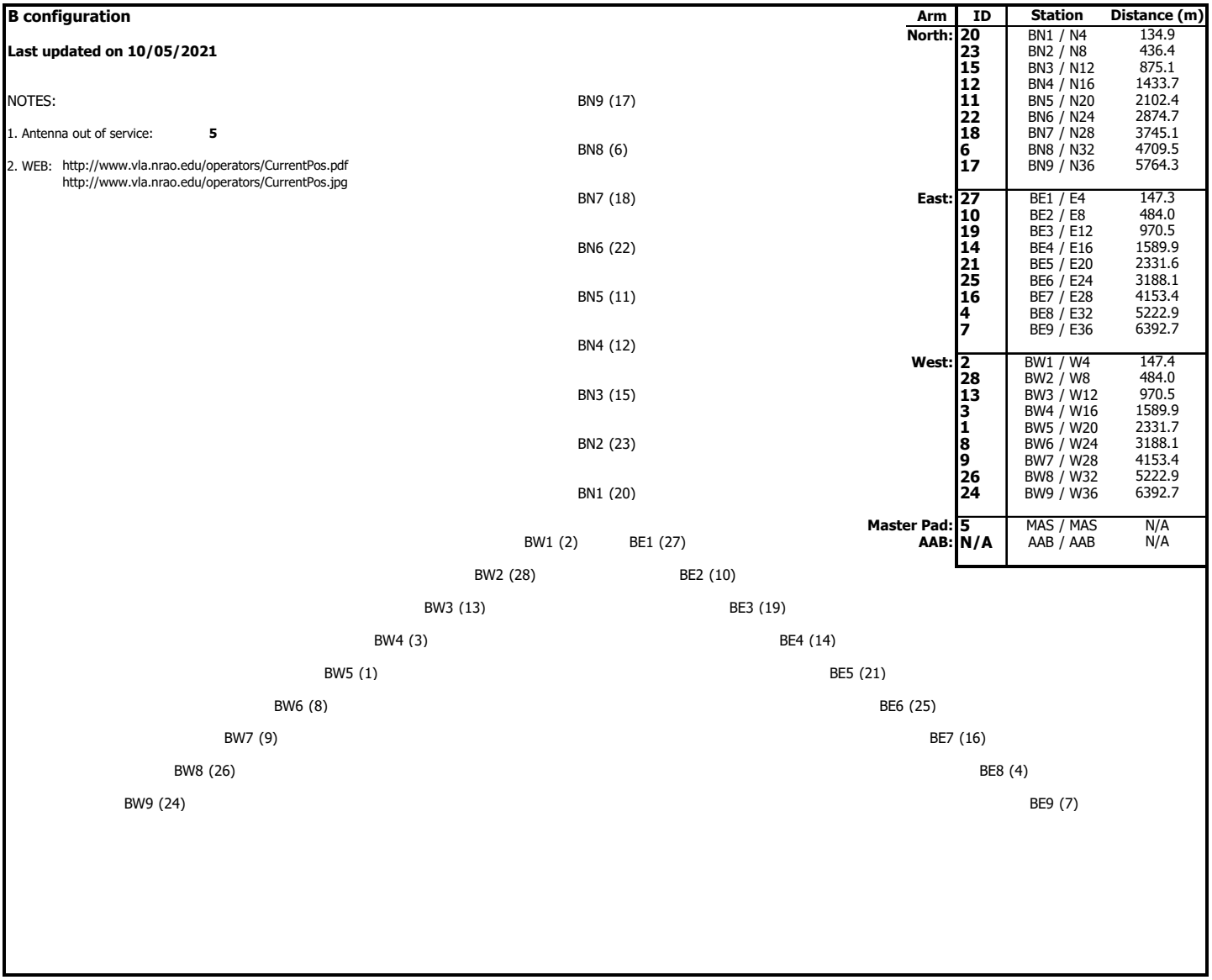

Arm	ID	Station	Distance (m)
North:	20	BN1 / N4	134.9
	23	BN2 / N8	436.4
	15	BN3 / N12	875.1
	12	BN4 / N16	1433.7
	11	BN5 / N20	2102.4
	22	BN6 / N24	2874.7
	18	BN7 / N28	3745.1
	6	BN8 / N32	4709.5
	17	BN9 / N36	5764.3
East:	27	BE1 / E4	147.3
	10	BE2 / E8	484.0
	19	BE3 / E12	970.5
	14	BE4 / E16	1589.9
	21	BE5 / E20	2331.6
	25	BE6 / E24	3188.1
	16	BE7 / E28	4153.4
	4	BE8 / E32	5222.9
	7	BE9 / E36	6392.7
West:	2	BW1 / W4	147.4
	28	BW2 / W8	484.0
	13	BW3 / W12	970.5
	3	BW4 / W16	1589.9
	1	BW5 / W20	2331.7
	8	BW6 / W24	3188.1
	9	BW7 / W28	4153.4
	26	BW8 / W32	5222.9
	24	BW9 / W36	6392.7
Master Pad:	5	MAS / MAS	N/A
AAB:	N/A	AAB / AAB	N/A

Figure 2.5: Positions of the 27 dishes in B configuration of the VLA. The distance listed is the distance of an individual dish from the centre of the array. The maximum arm length in the B configuration is 6.392 km (for the western and eastern arms). The northern arm has a length of 5.764 km and is shorter than the other two arms.
Source: **Antenna positions** in https://science.nrao.edu/facilities/vla

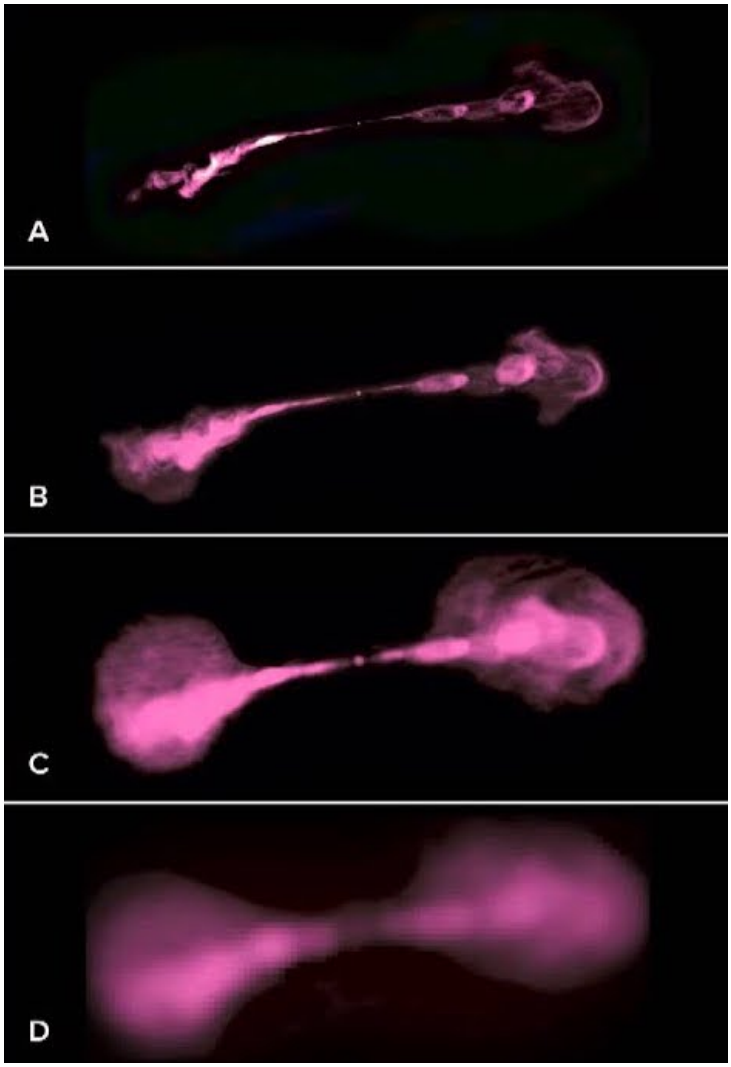

Figure 2.6: Radio galaxy *Hercules A* (also known as 3C 348) as seen by the different array configurations (A, B, C, and D) of the VLA. Finer details of the radio jets can be seen in configuration A whereas the outer, fainter portions (the radio lobes) are best visible when the galaxy is observed in configuration D. Credits: National Radio Astronomy Observatory/Associated Universities, Inc./National Science Foundation. Image retrieved from: https://public.nrao.edu/news/the-very-large-array-astronomical-shapeshifter/

2.2.2 Observations

Archival VLA (prior to the 2012 upgrade) L-band observations of two radio galaxies – 1233+168 and 1233+169 – in Abell 1569 were used in the work presented in this thesis. The two radio galaxies were observed by the VLA in B-configuration on January 12, 1992 (project code: AL252; total integration time: $\sim$16.83 minutes for both 1233+169 and 1233+168), and in C-configuration on January 29, 1991 (project code: AO104; total integration time: $\sim$7 minutes for 1233+169 and $\sim$6.5 minutes for 1233+168). The observational data were obtained from the

NRAO Science Data Archive[7].

2.3 Optical

Astronomical observations at optical wavelengths have been the oldest means to identify and study galaxy clusters. Visible light penetrates the Earth's atmosphere most effectively and hence, simple ground-based observations of galaxy clusters can be made. Using optical imaging and spectroscopy, the properties of individual galaxies inhabiting galaxy clusters can be studied. The spatial distribution of galaxies in clusters can be used to identify potential substructures and anisotropies in the cluster mass distribution. The sky distribution of galaxies obtained from optical observations is also a powerful tracer of the large-scale structure of the Universe, studying whose growth across time can be used to test cosmological models of structure formation.

2.3.1 Sloan Digital Sky Survey

The *Sloan Digital Sky Survey* or the SDSS (York et al., 2000) is a major astronomical imaging and spectroscopic redshift survey conducted using an optical telescope of 2.5-m aperture (also known as the SDSS 2.5-m telescope) and a focal ratio of approximately $f/5$ (Gunn et al., 2006). The SDSS 2.5-m telescope has a field of view of 3° and is located at the *Apache Point Observatory* (New Mexico, United States). The SDSS is named after the *Alfred P. Sloan Foundation*, an American philanthropic nonprofit organization, which contributed significant funding to the development of the project. Currently, the SDSS is carried out by a large international collaboration and receives support from a large number of participating institutions[8].

Imaging

The SDSS collects photometric data using an imaging camera which consists of an array of 30 SITe/Tektronix 2048×2048 pixel square CCDs arranged in six columns of five CCDs each. Each pixel is of size 24 μm which corresponds to 0.396 arcseconds on the sky. Data can be collected at five different wavelengths with the use of color filters, viz., the *u, g, r, i, z* filters,

[7] https://archive.nrao.edu/archive/advquery.jsp
[8] https://www.sdss.org/collaboration/affiliations/

each of which is designed to let in light around a specific wavelength. The central wavelengths, or the wavelengths at which the SDSS filters work the best, are provided in Table 2.3.

Table 2.3: Central wavelengths of the five SDSS filters.
Source: https://www.sdss.org/instruments/camera/

Filter	Wavelength (Å)
u (Ultraviolet)	3551
g (Green)	4686
r (Red)	6166
i (Near Infrared)	7480
z (Infrared)	8932

The SDSS *r, i, u, z,* and *g* filters cover the five rows of the array, in the respective order. Data on an object are collected by each CCD along a column in the array. Therefore, the camera produces five images of a given object in five different colors, all from the same column of CCDs, one from each CCD in that column. The effective exposure time in each filter is 54 seconds since it takes an object 54 seconds to move from the beginning of a CCD to the end. There is some space between the rows of CCDs and therefore, it takes an image 71.7 seconds to move from the beginning of one row to the next. There are 24 additional CCDs placed before and after the main photometric CCDs which are used to collect astrometric data.

Spectroscopy

The SDSS telescope is equipped with two spectrographs to obtain spectra of astronomical objects detected in the imaging surveys. Spectra are collected from multiple astronomical objects in a single spectrographic exposure with the help of an aluminium plate (also known as a plug plate) which has holes drilled at the desired locations to fix the points on the sky field from which spectra are required. The plug plates are individually drilled for each field of observation. The telescope is changed from imaging mode to spectroscopic mode by removing the imaging camera and mounting the plug plate at the focus. Optical fibres are plugged into the holes of the plug plate (hence its name) and the plate is mounted on a fibre cartridge for quick mounting and dismounting from the telescope. The fibres carry the intercepted light from the

focal plane to the two spectrographs through two slitheads, incorporated in the cartridge. Originally (upto 2009) 640 holes could be drilled into the plug plates and each fibre had a diameter of 3 arcsec (180 μm). Each slithead accepted light from 320 of the 640 optical fibres and connected them to the corresponding spectrograph. The number – 320 spectra per spectrograph – was a result of the requirement to place the fibre ends sufficiently far apart (at 390 μm intervals) to prevent crosstalk. Each original SDSS spectrograph collected spectra using 2 SITe/Tektronix 2048$\times$2048 pixel CCDs, one covering a wavelength range of 3800–6150 Å (blue), and the other spanning 5800–9200 Å (red). The original SDSS spectroscopic system contained a total of four 2048$\times$2048 pixel square CCDs. The spectral resolution ranged from 1850 to 2200.

The original SDSS spectrographs were replaced with two identical new spectrographs (*BOSS* spectrographs), still in use, in 2009. In the upgraded system, 1000 holes can be drilled in the plug plate and as a result, spectra of 1000 different objects can be obtained in a single exposure. Each optical fibre plugged into the plate hole has a diameter of 2 arcsec. Each spectrograph obtains spectra of 500 objects (input from 500 fibres) at a time. The fibres send the light collected from each object through a beamsplitter which splits the light spectrum into two parts – blue and red – recorded on two separate cameras in each spectrograph. The red camera uses thick, fully depleted 4Kx4K LBNL CCDs with a pixel size of 15μm that have a high quantum efficiency in the near-infrared. The blue camera uses blue-sensitive 4Kx4K 15μm e2v CCDs (CCD231-84). The upgraded spectrographs have an extended wavelength coverage from 3600 to 10400 Å as compared to the original SDSS spectrographs (3800–9200 Å). The blue camera covers the range 3600–6350 Å while the red camera covers at least 5650–10000 Å. The spectral resolution ranges from 1560–2270 in the blue channel and 1850–2650 in the red channel.

Observation Phases

The SDSS began regular survey observations in 2000. During its first observing phase, SDSS-I (2000–2005), the SDSS carried out deep multi-color imaging over 8000 square degrees of the sky and measured spectra of more than 700,000 celestial objects. The second phase, SDSS-II (2005–2008), imaged half the northern sky and mapped the three-dimensional clustering of about 1,000,000 galaxies and 100,000 quasars. The original SDSS observing plan, which continued from 2000 to 2008, is now known as the SDSS Legacy Survey. Two additional surveys were part of SDSS-II: the *Supernova Survey* which discovered and monitored more than 500 type Ia supernovae, and the original *Sloan Extension for Galactic Understanding and Exploration* (SEGUE-1) which obtained spectra of nearly 230,000 unique stars over a range of spectral types to investigate the structure of the Milky Way. Data collected by the

SDSS are released to the scientific community and the general public as data releases which are cumulative in nature. Data from SDSS-I and SDSS-II were released in seven incremental data releases – data release 1 (DR1) through DR7. The third observing phase of the survey, SDSS-III (2008–2014), consisted of four projects: the *Baryon Oscillation Spectroscopic Survey* (BOSS) which mapped the clustering of galaxies out to a redshift of 0.7; the *Apache Point Observatory Galactic Evolution Experiment 1* (APOGEE-1) which employed high-resolution, high signal-to-noise infrared spectroscopy to survey over 100,000 red giant stars across the full range of the Galactic bulge, bar, disk, and halo; the SEGUE-2 survey which was an extension of SEGUE-1 and spectroscopically observed around 119,000 unique stars in the stellar halo of the Galaxy; and the *Multi-object Apache Point Observatory Radial Velocity Exoplanet Large-area Survey* (MARVELS) which searched 11,040 very nearby stars for evidence of exoplanets surrounding them. Data from SDSS-III were released in four data releases – DR8 through DR12. The fourth and latest phase of the survey, SDSS-IV (2014–2020), extends the infrared spectroscopy of the Milky Way stars to the southern hemisphere (APOGEE-2) using the 2.5-m *du Pont Telescope* (Las Campanas Observatory, Chile). Two additional surveys are part of SDSS-IV: the *Extended Baryon Oscillation Spectroscopic Survey* (eBOSS), an extension of the SDSS-III BOSS, which together with the SDSS-I, SDSS-II, and BOSS, provides galaxy and quasar samples out to a redshift of 3.5; and the *Mapping Nearby Galaxies at Apache Point Observatory* (MaNGA) survey which provides spectral measurements across the face of $\sim$10,000 nearby galaxies to explore their detailed internal structure. Data from SDSS-IV have been released in DR13 through DR16. DR16 is the fourth data release of SDSS-IV and contains all SDSS observations through August 2018. The total imaging area of the sky covered in DR16 is 31,637 square degrees. As an example, the spectroscopic sky coverage of the BOSS and eBOSS from DR16 is shown in the top panel of Figure 2.7. For comparison and with the purpose of highlighting the tremendous progress that the SDSS has made over the years, the spectroscopic sky coverage of its first data release (DR1), covering 1360 square degrees on the sky, is shown in the bottom panel of Figure 2.7. SDSS-V (operations underway since October, 2020) will be the fifth generation of the SDSS and will provide optical and infrared spectroscopy across the entire sky. It will also offer a contiguous integral-field spectroscopic coverage of the Milky Way and Local Volume galaxies.

2.3.2 Observations

Data from release 8 of the SDSS (DR8) were used to study the age and metallicity of galaxies in the Coma Supercluster. The observational data and procedure for galaxy sample selection are described in detail in Chapter 6 of this thesis, to avoid breaking the flow of the content.

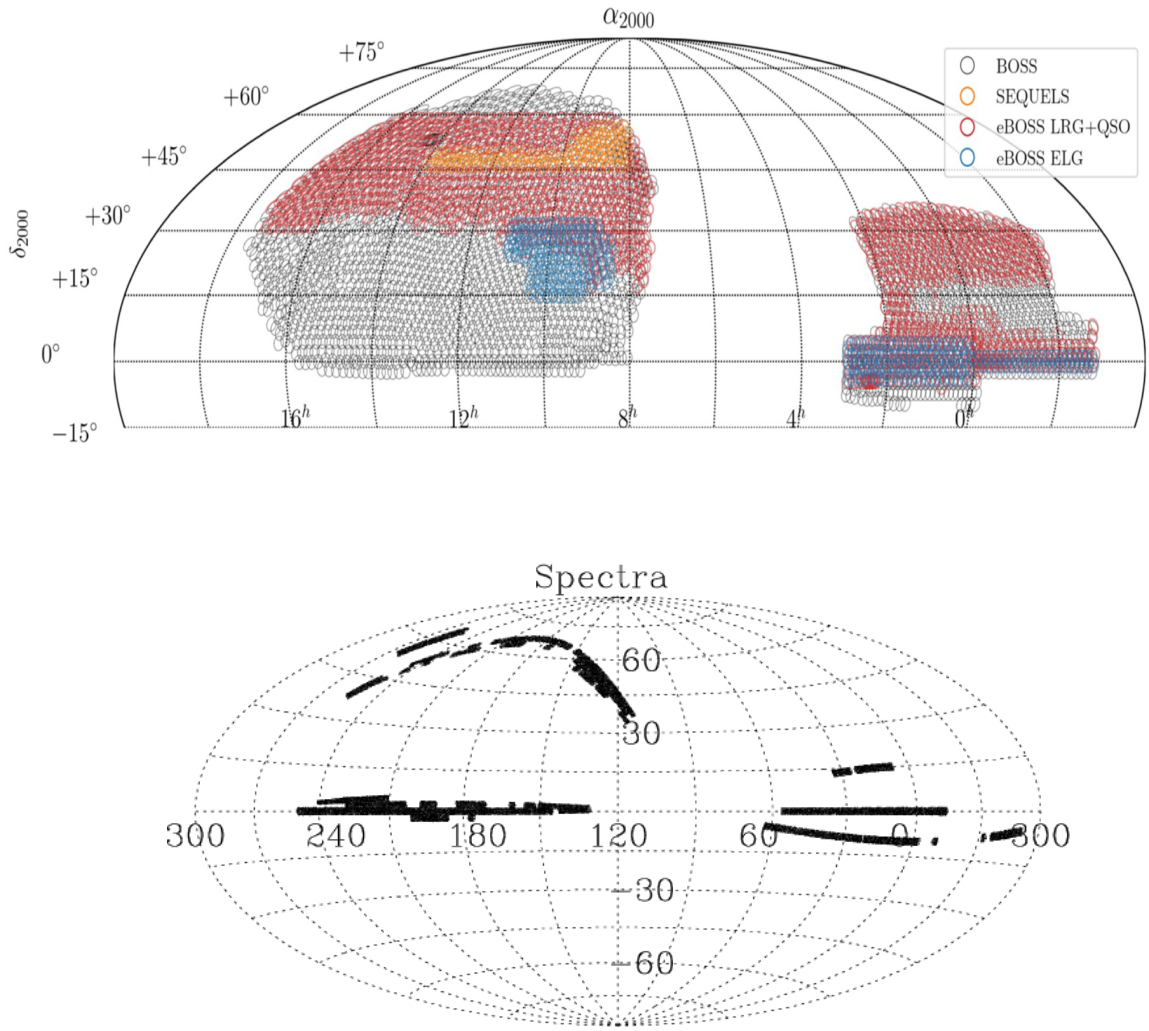

Figure 2.7: *Top*: DR16 eBOSS spectroscopic sky coverage in equatorial coordinates (map centered at RA = 8 hr) from Ahumada et al. (2020). Each symbol represents the location of a completed spectroscopic plate scaled to the approximate field of view. Expansion of acronyms is as follows: ELG - emission line galaxy; LRG - Luminous red galaxy; QSO - Quasi-stellar object or Quasar; SEQUELS – Sloan Extended Quasar, ELG, and LRG Survey – covers several hundred square degrees within the SDSS-III BOSS footprint; *Bottom*: The spectroscopic sky coverage (in equatorial coordinates) of the SDSS first data release (DR1) from Abazajian et al. (2003) is shown for comparison.
Source: Astronomy Image Explorer

Chapter 3

Data reduction and analysis

***Outline*:** This chapter describes the procedures used for the reduction and analyses of data used in the work presented in this thesis. The details of the X-ray data reduction and analyses are provided in §3.1 through §3.3 and are the same for Abell 2151 and Abell 1569 galaxy clusters. Radio data reduction was carried out for the central galaxies in Abell 1569 and its details are provided in §3.5. The optical data analysis is described in §3.6.

3.1 X-ray data screening

The raw data collected by the *XMM-Newton* and *Chandra* X-ray observatories have to be processed along with the designated calibration files to produce calibrated photon event files. These calibrated event files are subsequently filtered to avoid bad time intervals which are contaminated by high particle background activity. The screened photon event files are then processed further for generating X-ray images and spectra.

3.1.1 XMM-Newton

XMM-Newton data were used for studying the intracluster gas properties of Abell 2151.

The *XMM-Newton* Extended Source Analysis Software (XMM-ESAS) package which is integrated into SAS (version 17.0.0) was used for all data reduction. The raw data of each observation (Table 2.1) were processed using the SAS tasks *epchain* and *emchain* along with the latest calibration files to produce the PN and MOS event files, respectively. These event files were then filtered for Soft Proton (SP) flares using the tasks *pn-filter* and *mos-filter*. The useful exposure times obtained as a result of this filtering are given in Table 3.1. The observations 0147210101 and 0147210201 were strongly contaminated with SP flares and had very

low useful exposure time values. These two observations were, therefore, excluded from all further analyses. Out of the three observations of A2151, only 0147210301 was found to be useful. The EPIC PN, MOS1 and MOS2 data of only this observation were used for studying A2151. None of the CCDs in the MOS detectors was found to be in an anomalous state for 0147210301.

3.1.2 Chandra

Chandra data were used for studying the intracluster gas properties of both Abell 2151 and Abell 1569.

The data were analysed with Chandra Interactive Analysis of Observations (CIAO) software version 4.12 and CALDB version 4.9.1. Each dataset (Table 2.1) was reprocessed with the most recently available calibration applied to it using the *chandra_repro* script. The reprocessing created a new *level=2* event file for each dataset which was used in all further processing. The *level=2* event files were then filtered for SP flares by analysing their light curves (LCs) generated in the energy band $0.4-7.0$ keV.

Abell 2151: The LCs of all observations except 4996 were found to be flare free. The observation 4996, strongly affected by SP flares, was found to have residual SP contamination even after a 2.5σ LC filtering using the CIAO task *lc_sigma_clip* that resulted in a useful exposure time value of 14.22 ks for this observation. This residual contamination was found to adversely affect the results of the spectral fits (§3.3), and therefore, 4996 was excluded from all further analyses. The observations – 17038 and 18171 – were found to be useful for the imaging analysis only. The observation 17038 covered the eastern part of the cluster only partially. Therefore, an average or radial spectral analysis of the eastern region with 17038 was not possible. The observation 18171 covered only the far eastern part of the cluster and beyond and was, therefore, not helpful in the spectral analysis. We, therefore, used five *Chandra* observations of A2151, viz., 19592, 20086, 20087, 17038, and 18171 for the imaging analysis and three observations − 19592, 20086, and 20087 for the spectral analysis.

Abell 1569: The observation 6100 was found to be free of SP flares.

The good time intervals of all observations obtained after the LC filtering are listed in Table 3.1.

Table 3.1: The total good time intervals obtained after screening X-ray observations of Abell 2151 and Abell 1569.

Cluster	Satellite	Observation ID	Observation Time (ks)	Detector	Useful Exposure Time (ks)
Abell 2151	*XMM-Newton*	0147210201[a]	26.20	PN	0.72
				MOS1	0.84
				MOS2	1.68
		0147210101[a]	29.95	PN	1.56
				MOS1	3.54
				MOS2	3.72
		0147210301	19.04	PN	4.98
				MOS1	7.74
				MOS2	8.16
	Chandra	4996[b]	22.12	ACIS-I	14.22
		17038[c]	7.85	ACIS-S	7.85
		18171[c]	15.07	ACIS-S	15.07
		19592	16.46	ACIS-I	16.46
		20086	30.06	ACIS-I	30.06
		20087	35.57	ACIS-I	35.57
Abell 1569	*Chandra*	6100	41.75	ACIS-I	41.75

[a]These observations were strongly affected by soft proton flares and were excluded from all imaging and spectral analyses.
[b]The observation was excluded from all imaging and spectral analyses due to strong residual soft proton contamination even after a strict light curve filtering.
[c]These observations were used only in the imaging analysis.

3.2 X-ray imaging analysis

Point sources (e.g., stars and AGN) in the line of sight to galaxy clusters contaminate the X-ray emission from the intracluster medium. High energy particles interacting with the detectors onboard the X-ray telescopes and the structures surrounding them are an additional source of contamination. The removal of these contaminating sources is, therefore, necessary prior to the generation of X-ray images and spectra of galaxy clusters in order to obtain an uncontaminated view of the surface brightness and thermodynamic properties of the intracluster gas.

3.2.1 XMM-Newton

***Quiescent Particle Background treatment*:** The XMM-ESAS package allows neat modelling of the quiescent particle background (QPB) using a combination of the filter-wheel-closed (FWC) data and a database of unexposed-region data based on the methods of Kuntz & Snowden (2008). No blanksky files were used in our analysis.

***Point source detection*:** The XMM-ESAS metatask *cheese* was used to run point source detection on full-field images (it calls the SAS task *edetect_chain*) and create cheese masks from the output point source list. A detection box of size 5×5 pixels was used. The task *edetect_chain* also calculates individual exposure maps for the three EPIC detectors.

***Mosaic making*:** The task *pn_spectra* (*mos_spectra*) followed by *pn_back* (*mos_back*), with parameters *elow=300 and ehigh=4000* and leaving the *region* parameter empty, was used to generate the $0.3-4.0$ keV PN (MOS1/MOS2) image of the entire FOV while masking out the detected point sources (parameter *mask=1*). Running these tasks for the entire FOV also generated the PN, MOS1, and MOS2 model QPB images. The intermediate merged files of the point-source-subtracted observed counts images, the exposure maps, and the model particle background count images in the $0.3-4.0$ keV band, were produced using the ESAS task *comb*. Finally, the task *adapt* was used to generate the combined PN, MOS1, and MOS2, particle-background-subtracted, exposure-corrected image of A2151 in the energy range $0.3-4.0$ keV. A pixel size of 2.5 arcsec was used. The merged image was smoothed using 200 counts.

3.2.2 Chandra

***Particle Background treatment*:** *Chandra* allows the generation of a blanksky background file compatible with a given events file using the task *blanksky*. The task makes use of the instrument-specific background files present in the CALDB which have to be specifically installed. Flare filtering but no energy filtering must be done in order to generate these blanksky files. Matching blanksky background file for each dataset was created using this task *blanksky*.

***Image generation and point source subtraction*:** The flare-free event files were filtered for the energy range $0.4-4.0$ keV using the task *dmcopy* to create images in the same energy band. The task *fluximage* was then used to generate the counts image in the energy range $0.4-4.0$ keV, the exposure map at an effective energy of 2.3 keV, and a psfmap at the same effective energy with an enclosed-count fraction of 0.9 for each dataset. The pixel size used was 0.492 arcsec. The source counts image generated here included point sources which required detection and consequent subtraction. We used the task *wavdetect* with wavelet *scales=2,4* and *ellsigma=5* to identify point sources in each dataset. A background region around each detected point source was required for filling the holes created in the point-source-subtracted image and was

estimated using the task *roi*. The task *dmfilth* was then used to create a point-source-subtracted, hole-filled image for each dataset. Scaled background images were created for each observation given the observation-specific blanksky background files using the task *blanksky_image*. Background subtraction and exposure correction of the image was done using the task *dmimgcalc* and the resulting image was subsequently smoothed using the task *aconvolve*.

***Mosaic generation*:** The point-source-subtracted, hole-filled, unsmoothed images of multiple datasets (in case of A2151) were projected to a common centre and combined using *reproject_image_grid*. We used a pixel size of 0.492 arcsec and a region of 6000×6000 pixels. The individual background images and exposure maps were combined and reprojected according to the combined source image using the task *reproject_image*. Background subtraction and exposure correction of the combined source image was done using the task *dmimgcalc* and the resulting mosaic was smoothed with *aconvolve*.

***Two-dimensional image fitting*:** The *Chandra* images of the galaxy clusters were fitted with a 2D-β model to extract the general characteristics of their large-scale X-ray morphology. CIAO's modelling and fitting application SHERPA was used for this purpose. The 2D-β surface brightness model has the following functional form:

$$f(x,y) = ampl * (1 + r(x,y)^2)^{-\alpha},$$

$$\text{where} \qquad r(x,y)^2 = \frac{x_{off}(x,y)^2 * (1-ellip)^2 + y_{off}(x,y)^2}{r_0^2 * (1-ellip)^2}, \tag{3.1}$$

$$x_{off}(x,y) = (x - x_{pos}) * cos(\theta) + (y - y_{pos}) * sin(\theta),$$

$$\text{and} \qquad y_{off}(x,y) = (y - y_{pos}) * cos(\theta) - (x - x_{pos}) * sin(\theta)$$

The r_0 parameter is the core radius, x_{pos} and y_{pos} are the x and y coordinates of the model centre (position of the brightness peak), $ellip$ is the ellipticity of the model, θ is the angle of the major axis in radians, measured counter-clockwise from the x-axis, $ampl$ is the model value at the peak position (i.e., at [$xpos$, $ypos$]), and $\alpha = 3\beta - 1/2$ is the power-law slope of the surface brightness profile. First, an estimate of the background surface brightness was obtained by modelling the background region with the constant 2D model (*const2d*). Each source region was then fitted with the model *beta2d+const2d*, where *beta2d* is the isotropic 2D-β model (model parameters $ellip$ and θ frozen to 0.0). The background value was fixed when fitting the source regions. An exposure map generated using the task *fluximage* was supplied during the fit. The source regions were also modelled with the elliptical 2D-β model by thawing the paramaters $ellip$ and θ.

3.3 X-ray spectral analysis

3.3.1 Spectral extraction

***XMM-Newton*:** The ESAS tasks *pn_spectra* (*mos_spectra*) and *pn_back* (*mos_back*) were used to generate the source and model background spectra as well the EPIC-PN (MOS) responses from the point-source-subtracted event files. In cases where spectra were desired from a particular region on the detector, a region expression in detector coordinates was input into the tasks *pn_spectra* and *mos_spectra*. We note that the tasks *pn_back* and *mos_back* generate only the model QPB spectra. Therefore, the instrumental background lines, primarily the Al Kα ($\sim$1.49 keV) and Si Kα ($\sim$1.75 keV) for MOS and Al Kα for PN, were explicitly added to the models to fit the data (§3.3.3).

***Chandra*:** The point-source-subtracted event files were used for extraction of spectra and responses with the CIAO task *specextract*. Background spectra were extracted from the scaled blanksky background events files generated using the *blanksky_sample* script.

The extracted spectra were centred on the X-ray emission peaks of the galaxy clusters. All spectra were suitably grouped using the HEASoft FTOOL *grppha*, and analysed using XSPEC version 12.11.0 (Arnaud, 1996). The default χ^2 fit statistic was used.

3.3.2 X-ray background treatment

The X-ray background (XRB) can be separated into two main components. One is the cosmic X-ray background (CXB) which is mainly attributed to point sources of extragalactic origin, mostly believed to be AGN. The CXB dominates the X-ray background in the energy band 2.0–10.0 keV and is well fit by a non-thermal power-law with photon index of $\sim$1.4 (Lumb et al., 2002; De Luca & Molendi, 2004; Hickox & Markevitch, 2006; Cappelluti et al., 2017). The second component is the soft emission from within our Milky Way galaxy. It is the dominant contributor to the XRB at energies below 2.0 keV. We refer to it as the soft X-ray background (SXRB) here. Taking into account the contribution from the SXRB is necessary when studying gas properties of low-temperature clusters ($<$ 2–3 keV). The SXRB mainly consists of three components – an unabsorbed $\sim$0.1 keV thermal emission from the Local Hot Bubble (LHB), an absorbed thermal emission from the cooler ($\sim$0.1 keV) Galactic Halo (GH) and an absorbed thermal emission from the hotter ($\sim$0.26 keV) GH (and/or emission from the Local Group). In some cases, there may be an additional absorbed thermal component ($\sim$0.25-0.35 keV)

associated with the North Polar Spur (NPS) (Willingale et al., 2003; Snowden et al., 2008) contributing to the total observed X-ray emission. The contribution of this component depends on the direction of observation. A2151 lies in the direction of the NPS as seen in Figure 3.1, which shows the *ROSAT* All Sky Survey (RASS) diffuse background image of the NPS in the 3/4 keV band. Therefore, it is very important to take into account the contribution from the NPS in the spectral modelling of A2151. A1569 lies either in the direction of the NPS outskirts or beyond them. The contribution of the NPS to the total SXRB should therefore be very weak (if any). We have included the modelling of the complete X-ray background (CXB+SXRB) in the spectral analysis of the galaxy clusters. In order to constrain the XRB parameters, we have used spectral data from the RASS. For A2151, the RASS diffuse background spectrum and PSPC response were obtained for a circular region of radius 0°.6 (centred on galactic coordinates: l^{II}=32°.47, b^{II}=45°.66) in the vicinity of A2151 using the HEASARC X-ray background tool[1]. The neutral and total hydrogen column densities within this region are similar to those in the A2151 region. For A1569, we obtained the RASS diffuse background spectrum and PSPC response within a circular region of radius 0°.6 (centred on galactic coordinates l^{II}=284°.0; b^{II}=79°.7) in the vicinity of A1569. This region has neutral and total hydrogen column density values similar to those in the A1569 region. The seven channel RASS background spectrum was simultaneously fitted, after proper correction for the observed solid angle, with the *XMM-Newton* and *Chandra* data by a standard model for the XRB (Snowden et al., 2008) (§3.3.3).

3.3.3 Average X-ray spectral analysis

Average X-ray spectra of Abell 2151 and Abell 1569 were extracted for each detector using the methods described in §3.3.1. The PN, MOS1, and MOS2 spectra (for *XMM-Newton* data analysis) were fitted jointly with the RASS diffuse background spectrum (§3.3.2) using a common set of XSPEC models: *constant*(apec+(apec+apec+pegpwrlw)*
**tbabs + apec*tbabs) + gauss* (1.49 keV) + *gauss* (1.75 keV) in the energy range 0.4–7.0 keV. The *Chandra* ACIS-I observations were fitted simultaneously with the RASS diffuse background spectrum using the XSPEC model: *constant*(apec+(apec+apec+*
*pegpwrlw)*tbabs + apec*tbabs)* in the energy ranges 0.5–4.0 keV.

The model component *apec* is the astrophysical plasma emission model of Smith et al. (2001) and *tbabs* is the Tuebingen-Boulder interstellar medium (ISM) absorption model. The *tbabs* model calculates the cross-section for X-ray absorption by the ISM as the sum of the

[1]https://heasarc.gsfc.nasa.gov/cgi-bin/Tools/xraybg/xraybg.pl

cross-sections for X-ray absorption due to the gas-phase ISM, the grain-phase ISM, and the molecules in the ISM. The elemental abundances used by *tbabs* are as given by Wilms et al. (2000). The total hydrogen column densities ($N_{\rm H}$; neutral+molecular) along the line of sight to the clusters, were fixed to values provided by the UK Swift Science Data Centre[2] (Willingale et al., 2013). $N_{\rm H}$ was taken to be 3.91×10^{20} cm^{-2} for A2151, 2.20×10^{20} cm^{-2} for A1569N (the northern subcluster of A1569; see chapter 5 for details), and 2.23×10^{20} cm^{-2} for A1569S (the southern subcluster of A1569). The redshift values of the clusters were also fixed.

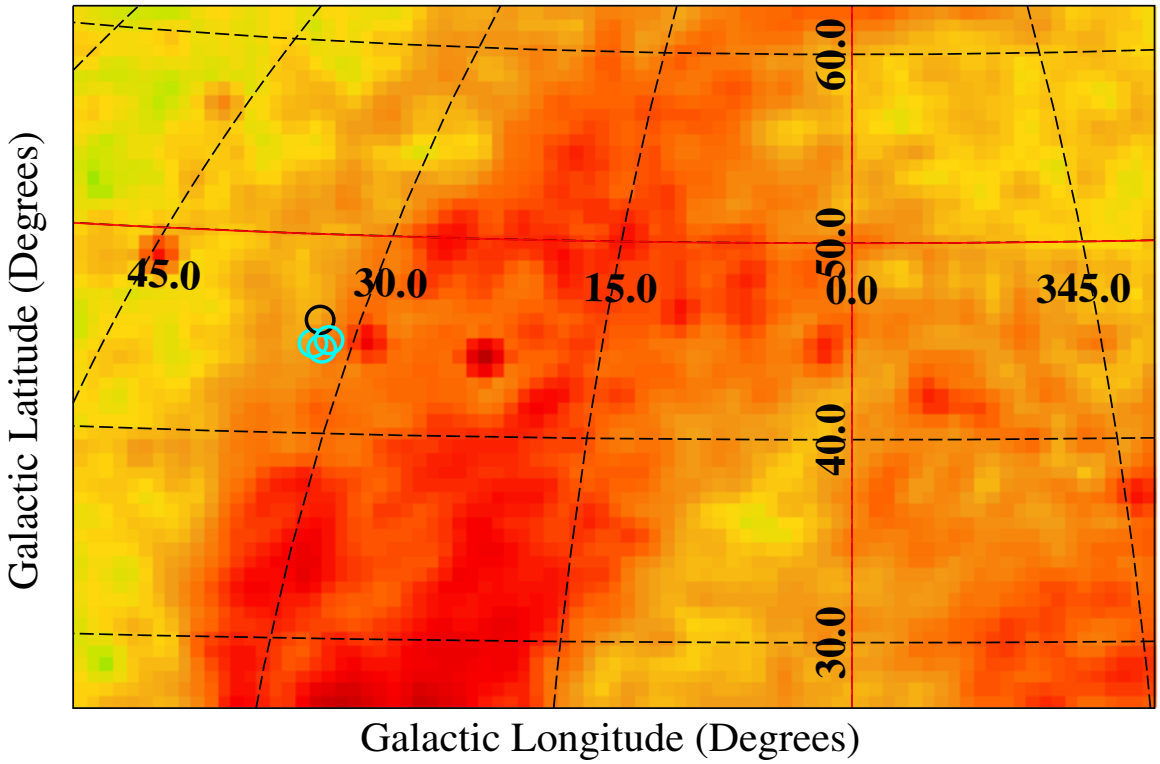

Figure 3.1: RASS 3/4 keV diffuse background image showing part of the North Polar Spur[a] (dominant in orange/red). The cyan circles mark the positions of the three Hercules subclusters – A2151C, A2151N, and A2151E. The black circle in their vicinity indicates the position of the region used to obtain the RASS diffuse background spectrum. The circles are only for representation and do not indicate the actual sizes of the subclusters/background extraction region.

[a]The NASA SkyView service was used to generate the image.

https://skyview.gsfc.nasa.gov/current/cgi/query.pl

The RASS spectral data is in units of cts s^{-1} arcmin^{-2}. Therefore, a *constant* factor was

[2]https://www.swift.ac.uk/analysis/nhtot; The tool returns the neutral, molecular and total galactic column density of Hydrogen.

used to scale down the model normalisation of the PN, MOS1, MOS2 (*XMM-Newton*), and the ACIS (*Chandra*) data. The *constant* factor equals the active sky area available for each detector in arcmin^2 units[3]. The model component *apec+(apec+apec+ pegpwrlw)*tbabs* accounts for the complete XRB (i.e., SXRB+CXB). The three *apec* components here model the SXRB contribution – the unabsorbed thermal emission (kT fixed at 0.1 keV) from the LHB, the absorbed (absorption is accounted for by the multiplicative component *tbabs*) thermal emission (kT fixed at 0.1 keV) from the cooler GH, and the absorbed thermal emission from the NPS or the hotter GH. Contribution from the hotter component of the GH was not found to be significant for A2151. The thermal emission from the NPS, in case of A2151, was found to have kT equal to 0.235 keV[4]. In case of A1569, the temperature of the hotter GH component was fixed at 0.27 keV[4]. A1569 lies either in the direction of the NPS outskirts or beyond them. The contribution of the NPS to the total SXRB should therefore be very weak (if any). We added an extra absorbed *apec* component to the model to account for the thermal emission from the NPS for A1569. This resulted in a very low normalization for the *apec* component representing the NPS emission and left the other best-fitting parameters unchanged. This component was, therefore, left out of the spectral model. The *pegpwrlw* component accounts for the CXB which was approximated by a power-law. For the *XMM-Newton* data, the CXB power-law was given a photon index of 1.42 and had its normalisation fixed based on the 2–10 keV CXB flux value ($2.15 \pm 0.26 \times 10^{-11}$erg cm^{-2}s^{-1}deg^{-2}) obtained by Lumb et al. (2002). For the *Chandra* data, the photon index of the *pegpwrlw* component was set to 1.4 and its normalisation was fixed based on the 2–8 keV CXB flux value ($1.7 \pm 0.2 \times 10^{-11}$erg cm^{-2}s^{-1}deg^{-2}) obtained by Hickox & Markevitch (2006). The component *apec*tbabs* models the absorbed X-ray emission from the cluster. In case of *XMM-Newton* data, the two *Gaussian* terms were used to model the instrumental background lines – the Al Kα line at $\sim$1.49 keV for PN, MOS1 and MOS2, and the Si Kα line at $\sim$1.75 keV for MOS1 and MOS2 detectors. The temperature, abundance and normalisation of the *apec* model describing the cluster emission were allowed to vary freely during the fit. For the RASS background spectrum, the *constant* factor was set equal to 1.0, and the normalisation values of the *apec* model describing the cluster emission and of the gaussian terms were set to 0.0.

[3]This information can be derived from the BACKSCAL keyword in the spectral file header.

[4]This value was obtained from fitting the RASS diffuse background spectrum with the XRB model.

3.3.4 Azimuthally averaged spectral analysis: radial profiles of thermodynamic properties

2D Projected Analysis: X-ray spectra of Abell 2151 and Abell 1569 were extracted from multiple full or partial annular regions for each X-ray detector using the methods described in §3.3.1. The spectral modelling followed the same procedure as described in §3.3.3. Temperature and metallicity profiles were obtained directly from the spectral analysis. In case of A1569, the gas abundance in each annular region was fixed at the average ICM abundance obtained from the average spectral analysis (§3.3.3), since the errors in the abundance value were rather large if it was left free, due to sparse data. The gas electron density was derived from the cluster *apec* normalization, $\mathcal{N}$, defined as:

$$\mathcal{N} = \frac{10^{-14}}{4\pi[D_A(1+z)]^2} \int n_e n_H dV \quad (cm^{-5}) \tag{3.2}$$

where D_A is the angular diameter distance to the source (cm), z is the redshift, V is the volume of the region, and n_e and n_H are the electron and hydrogen densities (cm^{-3}), respectively.

The XSPEC *apec* model takes into account the contribution from the following elements – C, N, O, Ne, Mg, Al, Si, S, Ar, Ca, Fe, Ni, and fixes the H and He contributions to the cosmic value, while determining the metal abundance of the plasma. The trace element abundances (Li, Be, B, F, Na, P, Cl, K, Sc, Ti, V, Cr, Mn, Co, Cu, Zn) are set to the solar value. Including contribution from the elements mentioned above, their relative abundances determined by the abundance table of Wilms et al. (2000), and assuming a fully ionized plasma, such that each atom of an element contributes Z_e (atomic number of the element) electrons, we derived the n_H/n_e ratio for the average value of ICM abundance obtained using the methods of §3.3.3. Assuming that electron density does not vary within a spherical shell, and using the derived n_H/n_e ratios, we obtained the projected electron density profiles of the two clusters. Gas pressure (P) and entropy (K) were calculated using the following relations:

$$\mathrm{P} = \mathrm{n_e kT} \quad (\mathrm{keV\ cm^{-3}}) \tag{3.3}$$

$$\mathrm{K} = \mathrm{n_e^{-2/3} kT} \quad (\mathrm{keV\ cm^{2}}) \tag{3.4}$$

Deprojected Analysis: When performing a spectral analysis in projection, the inner annuli have significant contribution from the outer gas shells. The variation in the thermodynamic quantities may, thus get smoothed out due to these projection effects. We, therefore, carried

out a deprojection analysis on the spectra extracted from the annular regions. The XSPEC model *projct* which estimates parameters in 3D space from the 2D projected annular spectra, was used for this purpose. The model requires all the spectra belonging to the same annulus/sector to be part of the same data group. The model *apec+(apec+apec+pegpwrlw)*tbabs + projct*(tbabs*apec)* was used for fitting the data. The model definitions are the same as described in §3.3.3. The XRB normalisation values in each annulus were kept frozen to the corresponding projected values. The cluster abundance in each annulus was kept frozen to the corresponding projected values in case of A2151 and to the average ICM abundance in case of A1569. The deprojection analysis with *XMM-Newton* data also required two additional *gauss* models to account for the instrumental lines for each data group (§3.3.3). The temperature profiles were obtained directly from the spectral analysis. The electron density, gas pressure and entropy were calculated in the same way as described in the 2D projected analysis.

The results of the deprojection analysis were not affected if partial annuli were used in the spectral analysis (for A2151), since the *projct* model uses a normalised volume (defined as the fraction of the ellipsoidal volume intersected by the elliptical annular cross-section) in its calculations. Therefore, if the volume of the ellipsoid is reduced by some amount (resulting from the use of partial annuli) then the physical volume of intersection also gets reduced by the same factor, thus leaving the normalised volume unchanged. If a combination of complete annuli in the central regions and incomplete annuli towards the outer regions of the cluster was used in the deprojection analysis, we added keywords specifying the start and end angles for the partial annuli to their spectral file extensions. The start and end angles were measured anticlockwise relative to the x-axis.

The following caveats on the use of $projct$ model must be kept in mind, however:

- The model does not account for the effect of missing regions from chip gaps and masked sources.
- The outermost bin always has contribution from all of the emission beyond it. The model effectively puts all the extra emission into the outermost bin. This may result in a higher density value in the outermost shell than in the inner regions. The effect cannot be corrected for since this would require a model for the variation of the emission measure and temperature with radius beyond the outermost annulus. In practice, the temperature and density values obtained for the outermost shell with the deprojection analysis are considered as not useful.

2D Maps of the ICM thermodynamical properties: Azimuthally averaged spectral analysis, although insightful, may not be the best way to study the variation of parameters of the intracluster medium (e.g. temperature and abundance), since these parameters usually change in the direction of surface brightness changes (Sanders, 2006). We implemented the 'contour binning' algorithm of Sanders (2006) which uses the X-ray surface brightness distribution to define spatial bins which cover regions of similar brightness and then performed spectral fitting in each of these bins. This technique was used to obtain the thermodynamic (TD) maps with *Chandra* data. The point-source-subtracted, hole-filled image of the observation with the highest exposure time was used to generate spatial bins. It was accumulatively smoothed with a signal-to-noise ratio (SNR) threshold of 25 and then binned with a minimum SNR of 38. An exposure map and a scaled particle-background image were also supplied to the task *contbin*. Eight spatial bins were obtained for A2151. For *XMM-Newton* data, we extracted spectra from small box/polygon shaped regions in each of the three EPIC detectors. 27 regions were used for A2151. The regions were chosen to have a minimum of 600 counts in each detector. Spectra extracted from different *Chandra* and *XMM-Newton* observations in each of these bins were fitted simultaneously using the model described in §3.3.

The *Chandra contbin* maps were made using the 'contour binning' tool *paint_output_images*. The *XMM-Newton* projected maps were constructed using the FTOOL *ftimgcalc*. Temperature and abundance maps were generated using the best-fitting values obtained as a result of spectral fitting. In order to obtain the projected pressure (P) and entropy (K) maps, we made use of the cluster *apec* normalisation $\mathcal{N}$ (Equation 3.2) and the projected emission measure *EM* defined as follows.

$$EM = \mathcal{N}/A \tag{3.5}$$

where *A* is the area of the spatial bin.
The projected emission measure *EM* is thus, proportional to the square of the electron density integrated along the LOS. Using Equation 3.5, the projected pressure can be computed as

$$\mathrm{P} = \mathrm{kT}(EM)^{1/2} \quad (\mathrm{keV\ cm^{-5/2}\ arcsec^{-1}}) \tag{3.6}$$

and projected entropy as

$$\mathrm{K} = \mathrm{kT}(EM)^{-1/3} \quad (\mathrm{keV\ cm^{5/3}\ arcsec^{-2/3}}) \tag{3.7}$$

A similar method has been adopted in Botteon et al. (2018).

Note: Thermodynamic maps could not be obtained for A1569 due to limited photon statis-

tics of the X-ray observation.

3.4 Derived X-ray properties

In the following calculations, we use H_0 = 67.4 km s^{-1} Mpc^{-1}, Ω_m = 0.315, and Ω_Λ = 0.685, based on the findings of Planck Collaboration et al. (2018).

- **X-ray Luminosity**

  X-ray luminosities (L_X) of the galaxy clusters were estimated by convolving the cluster *apec* model component used in the average spectral analysis (§3.3.3) with the XSPEC model *clumin* for both *XMM-Newton* and *Chandra* data, after freezing the cluster *apec* normalisation. If the global spectral analysis of a cluster made use of regions which were restricted to sectors in the outer parts (as for A2151), luminosities of the excluded regions were estimated from the spectral analysis of the outer annular sectors assuming that each smaller region of equal area within an annulus contributes equally to the total annular luminosity. These values were then added to the luminosity values obtained from the global spectral analysis.

  As an example, consider a partial annulus – a 280° wide sector with inner and outer radii of 210 and 300 arcsec, respectively. The X-ray luminosity of this partial annulus was estimated from the spectral analysis of this region. The luminosity of the missing 80° wide sector (L_{X_80}), with inner and outer radii of 210 and 300 arcsec, respectively, was then estimated as follows:

  $$L_{X\_80} = \frac{80}{280} \times L_{X\_280}$$

  This was done for all partial annuli. The luminosity estimates of all the regions excluded from the global spectral analysis, thus obtained, were added to the luminosity value obtained from the global spectral analysis (L_{X_global}) in order to obtain the total X-ray luminosity (L_{X_total}).

  $$L_{X\_total} = L_{X\_global} + L_{X\_missing\_sectors}$$

  Errors on the total luminosity estimates were obtained using the standard error propagation technique.

- **Gas Mass Estimates**

  The electron gas density profiles obtained using the methods described in §3.3.4 were used

to estimate the gas mass of the clusters. The projected/deprojected gas density profiles of the clusters were fitted using a single-β model given by:

$$n_e(r) = n_e(0)\left(1 + \frac{r^2}{{r_c}^2}\right)^{\frac{-3\beta}{2}} \tag{3.8}$$

where $n_e(0)$ and r_c are the central gas density and projected core radius of the cluster respectively, and β is the ratio of the specific energy in galaxies to the specific energy in hot gas. A double-β model fit to the gas density profiles was also tried but it did not give significant results due to very few data points available.

The gas mass $M_{gas}(R)$ within a certain radius R can be obtained by using the following:

$$M_{gas}(R) = 4\pi\rho_0 \int_0^R \left(1 + \frac{r^2}{{r_c}^2}\right)^{\frac{-3\beta}{2}} r^2 dr \tag{3.9}$$

and

$$\beta = \frac{\mu m_p \sigma^2}{kT} \tag{3.10}$$

where $\rho_0 = \mu n_e(0) m_p$, $m_p = 1.67 \times 10^{-27}$ kg is the mass of proton, μ is the mean molecular weight for a fully ionized gas, σ is the measured optical velocity dispersion of the cluster, and kT is the spectrally determined temperature of the intracluster gas.

Gas mass of the clusters was obtained within a radius upto which significant X-ray emission was observed and also within a projected radius r_{500}, the radius from the adopted cluster centre at which the total mass density is 500 times the critical density of the Universe. r_{500} was estimated using the following relation derived from simulations by Evrard et al. (1996) and adopted by Osmond & Ponman (2004):

$$r_{500} = \frac{124}{H_0}\sqrt{\frac{kT}{10 \text{ keV}}} \text{ Mpc}, \tag{3.11}$$

where kT is the gas temperature in keV obtained from the global spectral analysis of the cluster within the radius up to which X-ray emission is detected and H_0 is the Hubble constant in km s^{-1} Mpc^{-1}.

- **Total Mass Estimates**

The total gravitational mass of a cluster/group within radius r, $M_{grav}(< r)$, under the assumption of hydrostatic equilibrium can be calculated by using the following:

$$M_{grav}(< r) = \frac{-rkT(r)}{G\mu m_p}\left[\frac{dlnT(r)}{dlnr} + \frac{dlnn_e(r)}{dlnr}\right] \tag{3.12}$$

where G is the gravitational constant and the other symbols have the same meaning as defined previously. We used Equation 3.12 to estimate the total gravitational mass of the galaxy clusters within a radius upto which significant X-ray emission was observed and also within r_{500}.

- **Cooling Time Estimates**

  The cooling time in the central regions of the galaxy clusters was calculated using the following relation from Panagoulia et al. (2014):

$$t_{cool} = 0.8 \times 10^{10} \text{ yr} \left(\frac{n_e}{10^{-3}\text{cm}^{-3}}\right)^{-1} \left(\frac{\text{T}}{10^7 \text{ K}}\right)^{1.6} \quad \text{for T} < 3 \times 10^7 \text{ K} \tag{3.13}$$

  The deprojected temperature and electron density (§3.3.4, Deprojected Analysis) were used in calculating the cooling time values.

3.5 Radio data analysis

The individual VLA B-configuration and C-configuration datasets of the two radio galaxies in A1569 were reduced and calibrated using the Astronomical Image Processing System (AIPS) software. Standard steps for the VLA continuum data reduction with AIPS were followed. The source 1328+307[5] (alternatively known as 3C 286) was used as the flux density calibrator. The source 1219+285[6] was used as the phase calibrator. The calibrated B-configuration and C-configuration datasets were then combined using the AIPS task DBCON to generate multi-configuration images of the two radio sources.

Derived Radio Properties

The flux density of each radio galaxy at 1.48 GHz ($S_{1.48GHz}$) was estimated using the AIPS task IMSTAT. The radio luminosity at 1.48 GHz ($L_{1.48GHz}$) was derived using $L_{1.48GHz} = 4\pi D_L^2 S_{1.48GHz}$, where D_L is the luminosity distance to the source. The total radio luminosity of the radio source was obtained by integrating the flux density between $\nu_1 = 10$ MHz and

[5]This name of the source is based on B1950 coordinates. The name of the source in the J2000 coordinate system is 1331+305.

[6]This name of the source is based on B1950 coordinates. The name of the source in the J2000 coordinate system is 1221+282.

$\nu_2 = 10$ GHz as:

$$L_{radio} = 4\pi D_L^2 S_{1.48GHz} \int_{\nu_1}^{\nu_2} (\nu/\nu_{1.48GHz})^{-\alpha} d\nu \tag{3.14}$$

where a power-law spectrum was assumed for the radio source ($S_\nu \sim \nu^{-\alpha}$; α is the spectral index). We assumed a spectral index value $\alpha = 1$, since this value was not available in the literature.

3.6 Optical data analysis

Optical imaging data from the SDSS release 12 (DR12) were used to generate optical mosaics of the galaxy clusters A2151 and A1569. For A2151, forty-two *r-band* images were retrieved from the DR12 Science Archive Server in a field of 18 arcmin centred at RA = 241°.149 and Dec = +17°.72. For A1569, fifty-two *r-band* images were retrieved in a field of 30 arcmin centred at RA = 189°.11 and Dec = +16°.54. These images were mosaicked into a single optical image using SWarp version 2.38.0.

Chapter 4

The Hercules cluster in X-rays

This chapter is based on the research article *The Hercules cluster in X-rays with XMM-Newton and Chandra* published in the *Monthly Notices of the Royal Astronomical Society* by Tiwari & Singh (2021) (MNRAS, 500, 5524).

4.1 Introduction

The Hercules cluster of galaxies, also known as Abell 2151 (hereafter A2151), is located at a redshift of 0.0368 (Zabludoff et al., 1993) and is a significantly substructured system. Its optical centre as determined by Agulli et al. (2017) is at R.A. (J2000) = $16^h05^m23^s.369$; Dec. (J2000) = $17^\circ\ 45'\ 04''.33$, and it has $\sim$360 galaxies belonging to it within a radius of $\sim 1.3 R_{200}$[1]. The cluster contains a high fraction of spiral galaxies ($\gtrsim$ 50 per cent; Giovanelli & Haynes, 1985; Bird et al., 1995; Maccagni et al., 1995) and has a clumpy gas distribution (Magri et al., 1988; Bird et al., 1995). A2151, along with A2147 and A2152, is part of the much larger Hercules supercluster (Barmby & Huchra, 1998).

A2151 has previously been studied in X-rays by Bird et al. (1995) using data from the Position Sensitive Proportional Counter (PSPC) aboard the *Roentgen Satellite* (*ROSAT*), and by Huang & Sarazin (1996) who used the *ROSAT*'s High Resolution Imager (HRI). The PSPC has a field of view (FOV) $\sim 2^\circ$ across while the HRI has a FOV $\sim$38 arcmin across. The PSPC image of Bird et al. (1995) (fig. 1 of their paper) revealed the presence of three subclusters in A2151 – a bright central bimodal gas clump (A2151C), a fainter eastern clump (A2151E), and a northern clump (A2151N) with negligible X-ray emission. The HRI image confirmed the two component X-ray structure of A2151C – a bright central subclump, A2151C(B), and a faint

[1] R_{200} is the radius from the adopted cluster centre at which the density is 200 times the critical density of the universe; It is equal to 1.45 Mpc for A2151 as obtained by Agulli et al. (2017).

subclump, A2151(F). These subclumps were also noticed earlier in an X-ray image observed with the *Einstein Observatory*'s Imaging Proportional Counter (IPC) (Magri et al., 1988). The *ROSAT* PSPC image of A2151 showing its different components is displayed in Figure 4.1.

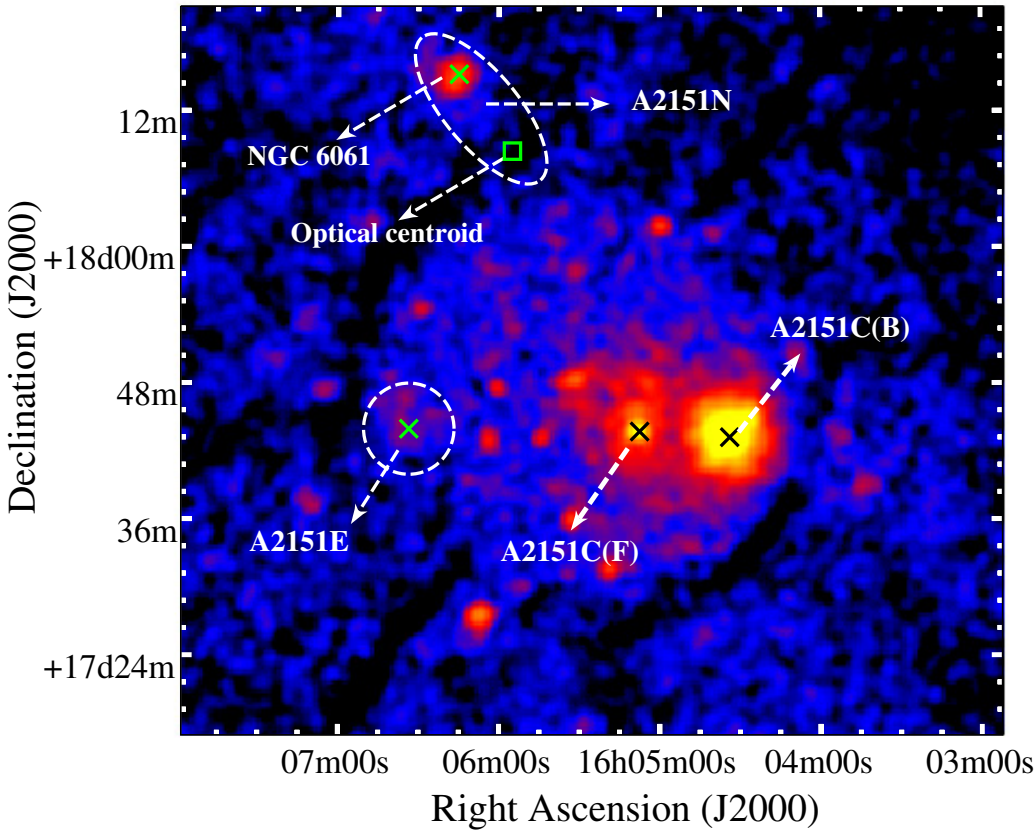

Figure 4.1: The *ROSAT* PSPC image of A2151 showing the different cluster components – A2151C, A2151E, and A2151N. The image was generated using data from the HEASARC archive. The *crosses* mark the positions of the *ROSAT* X-ray peaks obtained for each subcluster by Bird et al. (1995). A2151C is the brightest and has a two-component structure. A2151E towards the east is fainter. A2151N has negligible X-ray emission associated with cluster gas (Bird et al., 1995). The primary source of X-ray emission in A2151N is the galaxy NGC 6061. The *green box* symbol marks the position of the optical centroid of A2151N.

A global X-ray spectral analysis of A2151C(B) (for a radius (r) of 210 h_{75}^{-1} kpc from the X-ray peak), A2151C(F) (r = 200 h_{75}^{-1} kpc), A2151E (r = 130 h_{75}^{-1} kpc), and A2151N (r = 151 h_{75}^{-1} kpc) was performed by Bird et al. (1995) in the energy band 0.1–2.4 keV using low spectral resolution of *ROSAT* PSPC ($\sim$550 eV at 2 keV). The authors found that A2151C(B)

and A2151C(F) have X-ray temperatures of $1.67^{+0.47}_{-0.25}$ keV and $1.03^{+0.60}_{-0.06}$ keV, and overall elemental abundances of $0.56^{+0.31}_{-0.20}$ and $0.32^{+0.15}_{-0.10}$ times solar, respectively. The X-ray luminosities of A2151C(B) and A2151C(F) in the 0.1–2.0 keV band were estimated to be $8.7 \pm 0.7 \times 10^{42}$ erg s^{-1} and $3.6^{+0.68}_{-0.61} \times 10^{42}$ erg s^{-1}, respectively. A spectral analysis of different regions within the individual subclusters was not carried out by Bird et al. (1995). The surface brightness analysis of A2151C(B) by Huang & Sarazin (1996) with the *ROSAT* HRI image revealed the presence of central excess X-ray emission in the subclump, indicating that it contains a cooling flow. The authors estimated a central cooling time of $< 1.9 \times 10^8$ yr within the central 4 arcsec radius of A2151C(B).

Evidence for subclustering in A2151 was also seen in the radial velocity data of 127 galaxies compiled by Bird et al. (1993) (within 0°.9 radius centered at R.A. (J2000) = $16^h03^m11^s$; Dec. (J2000) = 17° 55′ 55″). They found the presence of three galaxy groups or subclusters in their galaxy surface density map. These subclusters were identified as dynamically independent systems by both Bird et al. (1993) and Bird et al. (1995), and coincided with the three X-ray gas clumps. The presence of these three substructures was also seen in the wavelet analysis image of Escalera et al. (1994) whose galaxy sample consisted of 79 galaxies. Huang & Sarazin (1996) used the galaxy list of Bird et al. (1993) and found another galaxy group A2151S to the south of A2151C in their luminosity-weighted galaxy surface density map in addition to the three previously identified subclusters. Moreover, their galaxy density distribution map (fig. 2 of Huang & Sarazin, 1996) showed that the central subcluster further divided into two galaxy groups which coincided with the two components (A2151C(B) and A2151C(F)) seen in the X-ray emission of A2151C. A more recent spectroscopic study of A2151 by Agulli et al. (2017) using data from the *William Herschel Telescope* (WHT) has confirmed the presence of substructure within A2151C (§3.2 and fig. 5 of their paper), identifying 20 members within A2151C(B) and 57 members in A2151C(F). The mean velocity and velocity dispersion were estimated to be 10116 km s^{-1} and 441 km s^{-1}, respectively, for A2151C(B), and 10299 km s^{-1} and 711 km s^{-1}, respectively, for A2151C(F).

In this chapter, we present a study of the hot X-ray emitting gas within the central subcluster of Hercules (A2151C) using all available archival data from observations with the EPIC instrument aboard the *XMM-Newton* observatory and the ACIS instrument aboard the *Chandra* X-ray observatory (§3.1; Table 3.1). We use the superior spatial and energy resolution, and the wider energy bandwidth of *Chandra* ($\sim$0.5 arcsec; $\sim$120 eV; $\sim$0.2$-$10.0 keV) and *XMM-Newton* ($\sim$5 arcsec; $\sim$120 eV; $\sim$0.2$-$10.0 keV) over the *ROSAT* PSPC ($\sim$25 arcsec, $\sim$550 eV; $\sim$0.1$-$2.0 keV) to investigate the thermodynamic properties of the ICM of A2151C by performing a detailed spectral analysis within the two substructures, A2151C(B) and A2151C(F),

which now show optical evidence of being associated with two different galaxy groups (Huang & Sarazin, 1996; Agulli et al., 2017). At redshift z = 0.0368 corresponding to A2151, 1 arcsec equals 0.76 kpc (Wright, 2006).

4.2 X-ray and optical morphologies

An X-ray image of the central subcluster of Hercules, A2151C, in the energy band 0.3–4.0 keV is shown in Figure 4.2(a). The image was made using combined PN+MOS1+MOS2 data from *XMM-Newton*, is corrected for exposures and has the particle-background removed (§3.2). We estimated the average XRB model surface brightness in the energy range 0.3–4.0 keV from the global spectral analysis (§3.3; §4.3). This resulted in XRB surface brightness values of 8.6×10^{-7}, 2.1×10^{-7}, and 2.8×10^{-7} cts s^{-1} arcsec^{-2} for the PN, MOS1, and MOS2 detectors, respectively. The value obtained for PN is naturally higher due to the higher efficiency of the detector. The XRB surface brightness contribution thus obtained has, however, not been subtracted from the combined image, since it was not possible to account for the variation in the efficiency of the three detectors. Nonetheless, these values indicate that the contribution of the XRB to the observed X-ray surface brightness is low. We note that *XMM-Newton* combined PN+MOS1+MOS2 brightness image of A2151C takes the average of the contribution from the three detectors and also corrects for the variation in the detector efficiencies.

Two distinct X-ray clumps are seen in the image shown in Figure 4.2(a). The presence of these two X-ray blobs was first reported in the Einstein IPC image by Magri et al. (1988). They were also identified in the 0.1–2.4 keV *ROSAT* PSPC image of Bird et al. (1995) and the *ROSAT* HRI image of Huang & Sarazin (1996) who confirmed that the X-ray emission in the A2151C divides into two components which correspond to two groups of galaxies. Following the nomenclature of Huang & Sarazin (1996), we refer to the *brighter western* and *fainter eastern* X-ray clumps within A2151C as A2151C(B) (central bright) [X-ray peak: RA = $16^{\rm h}04^{\rm m}35^{\rm s}.73$; Dec = $+17^{\circ}43'17''.31$] and A2151C(F) (central faint) [X-ray peak: RA = $16^{\rm h}05^{\rm m}08^{\rm s}.70$; Dec = $+17^{\circ}43'47''.96$], respectively.

An optical r-band image of A2151C from the *Sloan Digital Sky Survey* is displayed in Figure 4.2(b). The central peak of X-ray emission in A2151C(B) coincides with the brightest cluster galaxy (BCG) NGC 6041 (SIMBAD) while that in A2151C(F) is coincident with a radio galaxy, NGC 6047. Both these galaxies have been classified as giant ellipticals by Baillard et al.

(2011). NGC 6047 has also been designated as a BCG by Liuzzo et al. (2010). Galaxies in A2151C are seen to cluster around the two X-ray peaks. The division of A2151C into two distinct substructures has been observed earlier in the galaxy surface density distribution of Huang & Sarazin (1996) and was confirmed by a more recent optical study by Agulli et al. (2017). Fig. 4.2(b) also shows several pairs of interacting galaxies within A2151C. A few compact galaxy groups (CGGs) have also been identified in the fainter subclump A2151C(F).

The background-subtracted, exposure-corrected, 0.4–4.0 keV combined *Chandra* image of A2151C generated using the five ACIS observations (§3.1; §3.2) is shown in Figure 4.2(c). The image covers A2151C(F) only partially. We note that in addition to the particle-background, the contribution of the XRB has also been subtracted from the mosaic. The 0.4–4.0 keV average surface brightness of the XRB was estimated from the average spectral analysis (§3.3; §4.3) and was found to be equal to 3.51×10^{-10} photons cm^{-2} s^{-1} pixel^{-1} (pixel size=0.492 arcsec). The observation 18171 was included in the imaging analysis for completeness. However, this observation has not contributed much to the image (§3.1.2).

It is evident from both Fig. 4.2(a) and Fig. 4.2(c) that except for a notable departure from circular symmetry in the northwest region, X-ray emission is fairly azimuthally symmetric in A2151C(B). This northwest bump in X-ray emission overlaps with a pair of interacting galaxies NGC 6040 and PGC 56942 (identified as *Arp 122* by Arp, 1966, in his *Atlas of Peculiar Galaxies*; see Fig. 4.2(b)), which are known to be substantially depleted of their neutral Hydrogen content (Giovanelli & Haynes, 1985). The stripping of gas from this galaxy pair has significantly contributed to the intracluster gas in the region (Huang & Sarazin, 1996). In the inner 300 arcsec ($\sim$228 kpc) region of A2151C(F), the X-ray emission is weaker compared to that in A2151C(B) but the surface brightness seems to be similar in the outer parts ($>$ 300 arcsec) of the two subclumps.

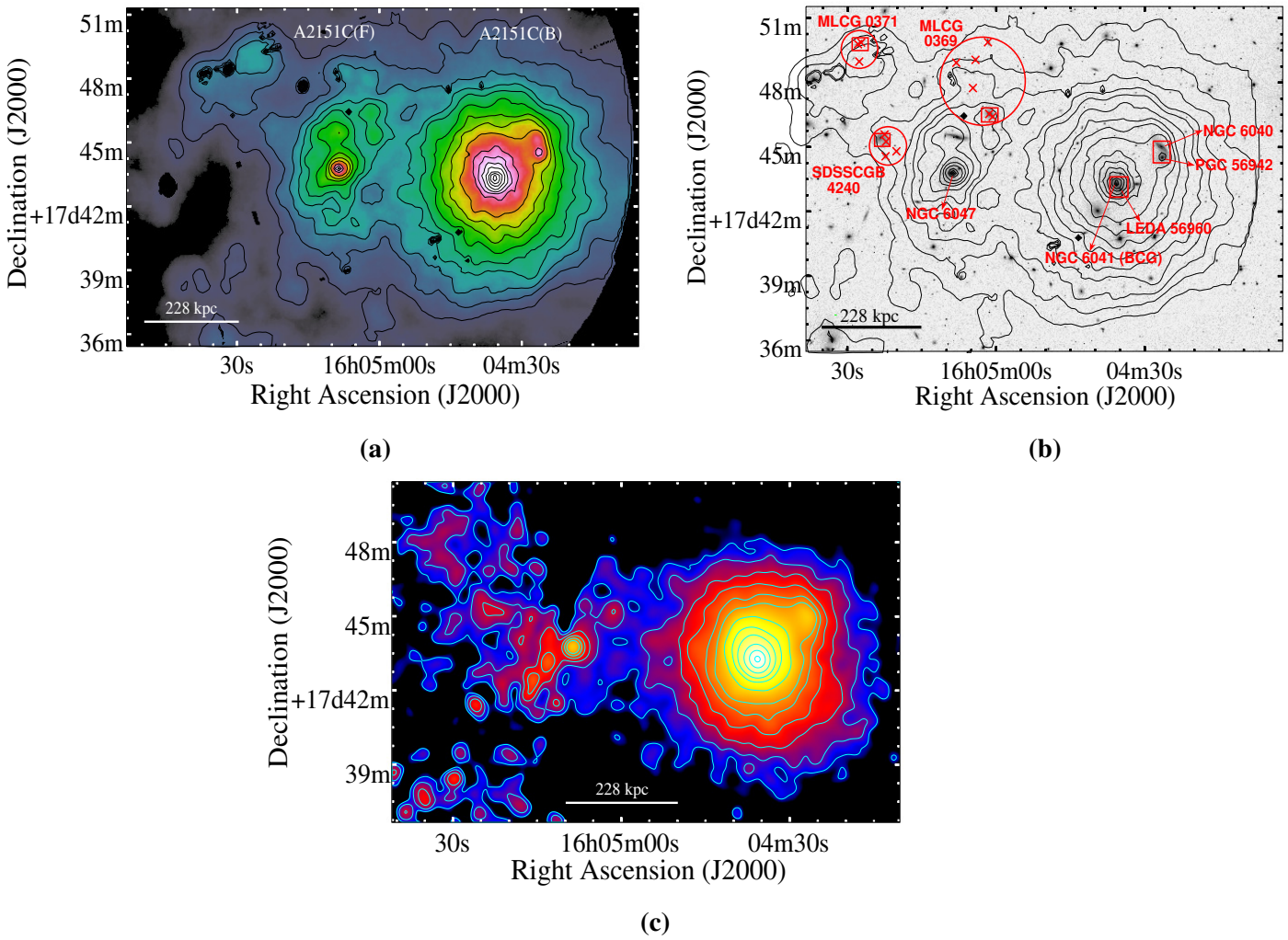

Figure 4.2: **(a)**: The combined PN, MOS1, and MOS2 *XMM-Newton* image in the energy band 0.3–4.0 keV created after subtraction of point sources and particle background, and exposure correction. The image was adaptively smoothed using 200 counts. Both A2151C(B) (bright western subclump) and A2151C(F) (faint eastern subclump) are visible due to the 0°.5 diameter FOV of *XMM-Newton*. Overlaid X-ray surface brightness contours are logarithmically distributed between 9.6 x 10^{-7} and 8.5 x 10^{-5} cts s^{-1} $arcsec^{-2}$. **(b)**: The optical *r*-band image from the *Sloan Digital Sky Survey* with overlaid X-ray contours from the *XMM-Newton* image shown in panel (a). Five pairs of interacting galaxies and three compact galaxy groups within A2151C identified from NED[a] and SIMBAD[b] databases are highlighted in *red boxes* and *red circles* respectively. The circles are used only for representation and do not indicate the actual angular size of the group. The *red crosses* represent the galaxies identified within the individual compact groups. **(c)**: The 0.4–4.0 keV exposure-corrected mosaic created using the five *Chandra* observations after elimination of point sources and subtraction of particle and X-ray background. The image was smoothed using a gaussian kernel with σ = 15 arcsec. Overlaid logarithmic contours range from 1.1 x 10^{-10} to 4.0 x 10^{-8} photons cm^{-2} s^{-1} $pixel^{-1}$.

[a]NASA/IPAC Extragalactic Database: http://ned.ipac.caltech.edu/;

[b]Set of Identifications, Measurements and Bibliography for Astronomical Data:

http://simbad.u-strasbg.fr/

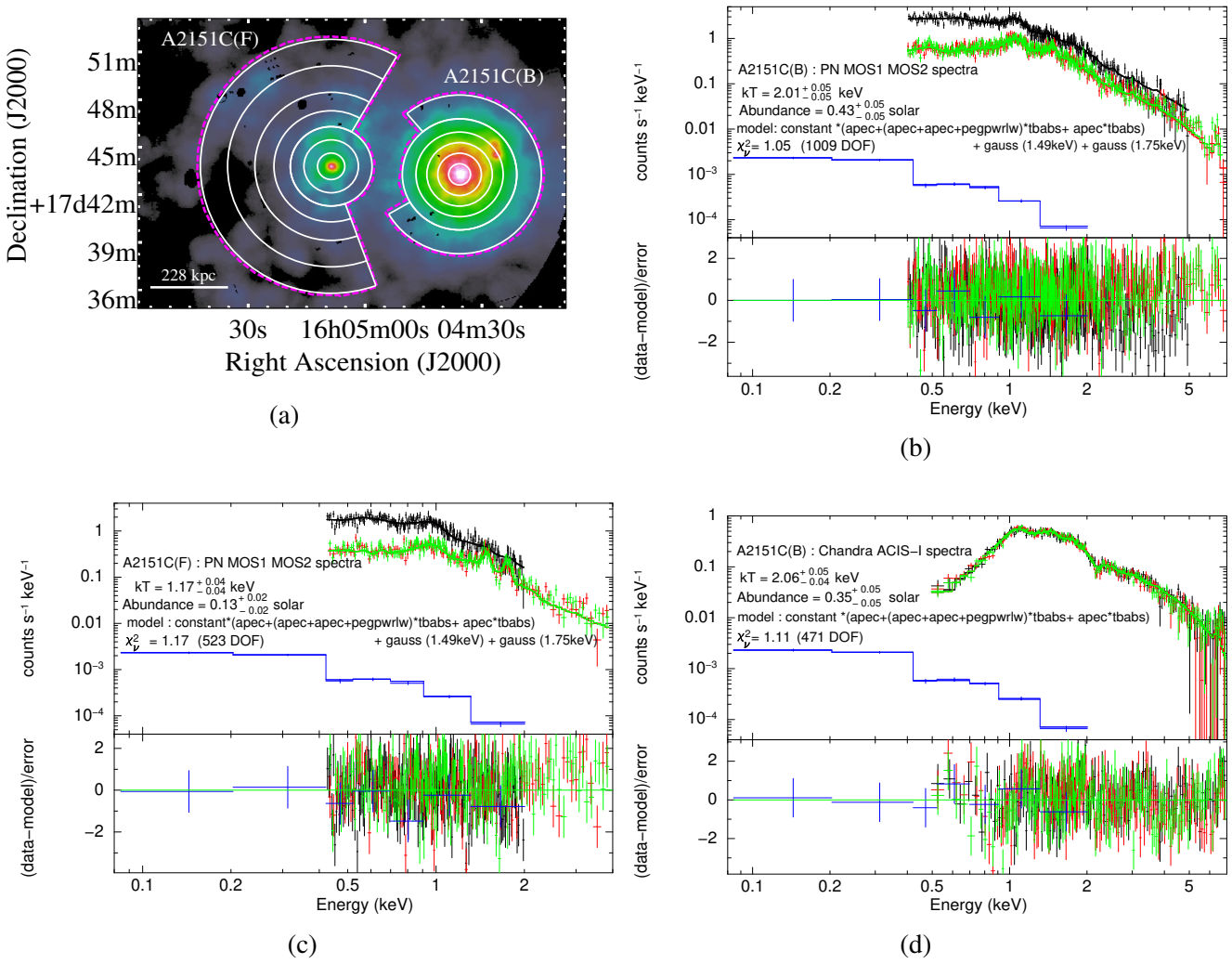

Figure 4.3: **(a)**: Regions used for extraction of spectra are shown. Those outlined in *magenta* color were used for the PN, MOS1, and MOS2 *XMM-Newton* spectral analysis of the full A2151C(B) (*west : circle of radius 210* arcsec + *a 280° wide sector with inner and outer radii of 210 and 300* arcsec, *respectively*) and A2151C(F) (*east : circle of radius 150* arcsec + *a 230° wide sector with inner and outer radii of 150 and 480* arcsec, *respectively*). The same *magenta* region towards the *west* was also used for performing the average spectral analysis of A2151C(B) with *Chandra* data. Regions shown in *white* color were used in the azimuthally averaged spectral analysis of A2151C(B) and A2151C(F) using *XMM-Newton* and *Chandra* data. **(b)**: Average spectra of A2151C(B) obtained from the *XMM-Newton* PN (black), MOS1 (red), and MOS2 (green) detectors. The spectra were fitted simultaneously with the RASS diffuse background spectrum (shown in blue) using the model *constant*(apec+(apec+apec+pegpwrlw)*tbabs + apec*tbabs)* + *gauss* (1.49 keV) + *gauss* (1.75 keV) in the energy range 0.4–5.0 keV for PN and 0.4–7.0 keV for MOS detectors. **(c)**: Average spectra of A2151C(F) obtained from the *XMM-Newton* PN (black), MOS1 (red), and MOS2 (green) detectors. The spectra were fitted simultaneously with the RASS data (shown in blue) using the model *constant*(apec+(apec+apec+pegpwrlw)*tbabs + apec*tbabs)* + *gauss* (1.49 keV) + *gauss* (1.75 keV) model in the energy range 0.4–2.0 keV for PN and 0.4–4.0 keV for MOS detectors. **(d)**: Average spectra of A2151C(B) obtained using the three *Chandra* ACIS-I observations – ObsID 19592 (*black*), ObsID 20086 (*red*), and ObsID 20087 (*green*). The spectra were fitted simultaneously with the RASS spectrum (shown in *blue*) using the model *constant*(apec+(apec+apec+pegpwrlw)*tbabs + apec*tbabs)* in the energy range 0.4–7.0 keV. The lower panels in subplots (b)–(d) show the residuals in terms of sigmas with error bars of size one.

4.3 Average X-ray spectra

The FOV of 0°.5 diameter of *XMM-Newton* EPIC covers both A2151C(B) and A2151C(F) as seen in Fig. 4.2(a). Average X-ray spectra of the two visible X-ray clumps were extracted from regions outlined in *magenta* color in Figure 4.3(a) using the procedure described in §3.3.1. This was done for each of the three EPIC detectors. It can be seen in Fig. 4.2(a) that the X-ray emission from the two groups is not well separated at least in the 2D projected space. We, therefore, selected regions highlighted in *magenta* color in Fig. 4.3(a) in order to avoid contamination of the average X-ray spectral properties of one group due to the other. The extraction region for A2151C(B) was chosen as a circle of radius 210 arcsec plus a 280° wide annular sector of inner and outer radii of 210 and 300 arcsec, respectively, centred at RA = $16^h04^m35^s.73$ and Dec = + 17°43′17″.31. A region comprising a circle of radius 150 arcsec and a sector of angular width 230° with inner and outer radii of 150 and 480 arcsec, respectively, centred at RA = $16^h05^m08^s.70$ and Dec = +17°43′47″.96, was selected for the global spectral extraction of A2151C(F). The region used for the extraction of spectrum for A2151C(B) from *Chandra* data was the same as that used for the average spectral analysis with *XMM-Newton* data.

Table 4.1: Best-fitting parameters – temperature (kT), abundance (Z) and *apec* normalisation ($\mathcal{N}$) – obtained from the X-ray spectral analysis of the full A2151C(B) and A2151C(F) regions (outlined in *magenta* in Fig. 4.3(a), and the derived 0.4−7.0 keV X-ray luminosities (L_X). The minimum reduced χ^2 statistic along with the degrees of freedom (DOF) is also listed. The *XMM-Newton* and *Chandra* global spectra were fitted using the models *constant*(apec+(apec+apec+pegpwrlw)*tbabs + apec*tbabs) + gauss*(1.49 keV) + *gauss*(1.75 keV) and *constant*(apec+(apec+apec+pegpwrlw)*tbabs + apec*tbabs)*, respectively, simultaneously with the RASS diffuse background spectrum. The error bars correspond to 90 per cent confidence intervals.

Region	Data	kT (keV)	Z ($Z_\odot$)	apec norm. ($\mathcal{N}$) (10^{-2} cm^{-5})	L_X (10^{43} erg s^{-1}) (0.4−7.0 keV)	$(\chi^2_\nu)_{\rm min}$ (DOF)
A2151C(B)	*XMM-Newton*	2.01 ± 0.05	0.43 ± 0.05	1.02 ± 0.02	$3.03^{+0.02}_{-0.04}$	1.05 (1009)
A2151C(F)	*XMM-Newton*	1.17 ± 0.04	0.13 ± 0.02	0.43 ± 0.02	1.13 ± 0.02	1.17 (523)
A2151C(B)	*Chandra*	$2.06^{+0.05}_{-0.04}$	0.35 ± 0.05	1.08 ± 0.03	$3.23^{+0.02}_{-0.03}$	1.11 (471)

Spectra and responses were extracted from each *Chandra* and *XMM-Newton* observation as explained in §3.3.1. Background spectra and spectral responses in these regions were also generated as described in §3.3.1. It was not possible to perform the spectral analysis of A2151C(F) (as done with the *XMM-Newton* data) since the *Chandra* observations covered it only partially due to the smaller FOV of ACIS-I. The extracted spectra were fitted using the method and models described in §3.3.3. The data along with the model spectra are shown in Figure 4.3(b)–(d). The best-fitting values of cluster gas temperature, abundance, and *apec* normalisation are provided in Table 4.1. The temperature and abundance values obtained for A2151C(B) with the analysis done using *XMM-Newton* and *Chandra* data agree quite well with each other.

4.4 Azimuthally averaged spectral analysis: radial profiles of gas temperature, abundance and density

2D Projected Profiles

Projected radial profiles of gas temperature (kT), abundance (Z), and electron density (n_e) were obtained for A2151C(B) and A2151C(F) using the procedure described in §3.3.4 by extracting spectra (§3.3.1) in regions shown in *white* color in Fig. 4.3(a). The regions were centred at the peak of X-ray emission for both A2151C(B) and A2151C(F). A2151C(B) was divided into six annular regions with outer radii 40, 80, 120, 160, 210, and 300 arcsec for analysis with *XMM-Newton* data. The outermost region (inner and outer radii of 210 and 300 arcsec respectively) was chosen as a sector (and not a full annulus) with an angular width of 280° to avoid mixing of projected gas properties of the two X-ray groups. The region beyond 300 arcsec was not covered fully by the PN and MOS2 chips. A joint spectral analysis with PN, MOS1 and MOS2 data was, therefore, not possible beyond 300 arcsec. Analysis with *Chandra* data was done using the same regions except the outermost sector which was not included due to poor statistics. A2151C(F) was divided into seven regions with outer radii 50, 100, 150, 210, 280, 380, and 480 arcsec. The four outermost regions with outer radii 210, 280, 380, and 480 arcsec were restricted to sectors with angular width 230°. Since the *Chandra* observations did not cover A2151C(F) fully, only *XMM-Newton* data was used in its analysis. An n_H/n_e ratio of 0.834 derived for an ICM abundance of 0.43 $Z_\odot$ was used. The n_H/n_e values obtained for ICM abundances of 0.35 $Z_\odot$ (average abundance of A2151C(B) from *Chandra*) and 0.13 $Z_\odot$ (average abundance of A2151C(F)) were similar – 0.834 and 0.835, respectively. The results of spectral fitting are provided in Table 4.2. The projected radial profiles are shown in Figure 4.4.

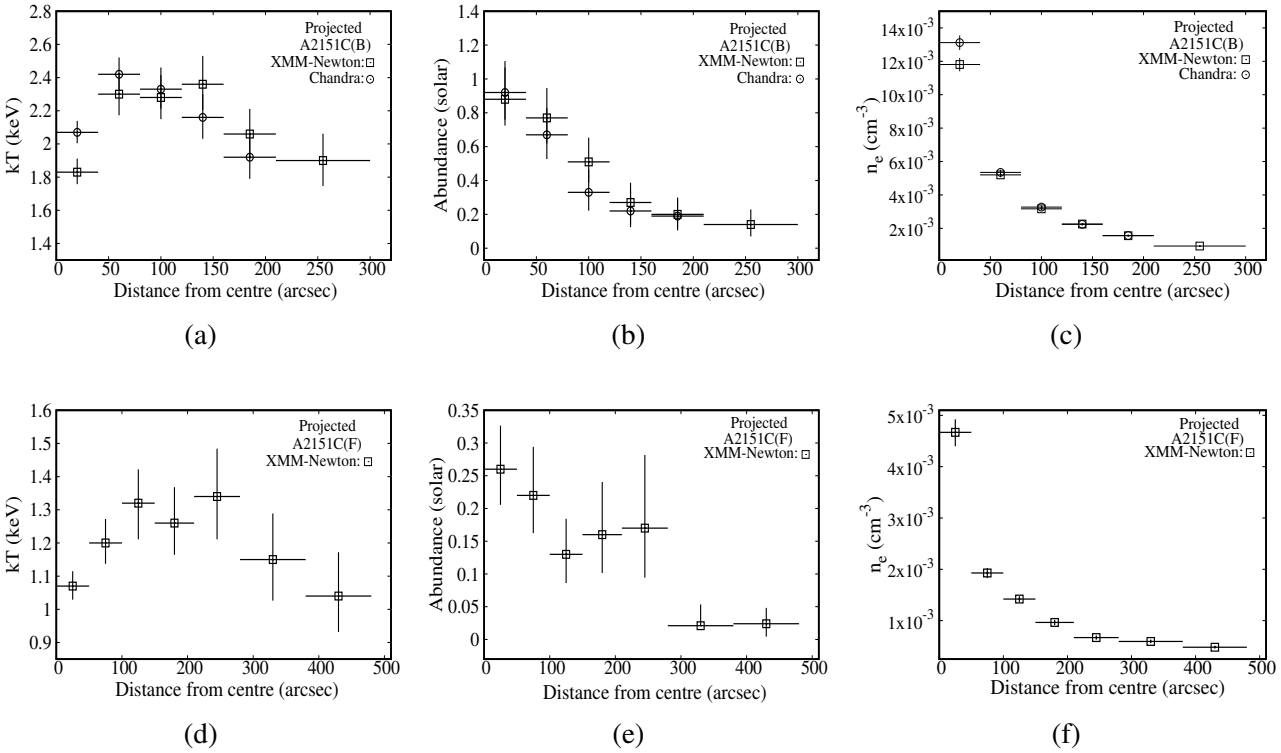

Figure 4.4: Projected temperature (kT), abundance, and electron density (n_e) profiles of A2151C(B) and A2151C(F) obtained from the analysis of spectra extracted in different annuli/sectors (shown in *white* in Fig. 4.3(a)) using *XMM-Newton* (*open box*) and *Chandra* (*open circle*) data. The error bars correspond to a 90 per cent confidence interval.

It can be seen in Fig. 4.4(a) that the temperature in the central 40 arcsec in A2151C(B) is lower than its surroundings by $\sim$0.3 keV. This confirms that A2151C(B) has a cooling core. In contrast, the temperature drop seen towards the inner regions of A2151C(F) is not significant (Fig. 4.4(d)). There is a slight difference between the temperature values obtained with *XMM-Newton* and *Chandra* in the central 40 arcsec region of A2151C(B). This is possibly the effect of the large chip gaps of the PN and MOS1 detectors, falling within the $0-40$ arcsec region in the *XMM-Newton* data, in comparison with the *Chandra* ACIS-I detector where no such gaps are seen to coincide with this region. Fig. 4.4(b) shows that A2151C(B) is fairly metal rich in the inner regions due to chemical enrichment from the BCG NGC 6041. The abundance steadily declines as one goes to the outer parts of the subclump. The abundance of A2151C(F) is much lower than that of A2151C(B). This is an indication of its relatively unevolved nature. Fig. 4.4(e) shows an abrupt rise in the abundance value of A2151C(F) at radii 150–280 arcsec from the centre. Part of this annular region overlaps with the CGG SDSSCGB4240 (Fig. 4.2(b)). The rise in abundance could possibly be due to this galaxy group merging with A2151C(F) (also see §4.5; Fig. 4.7(b) and 4.7(d)).

Table 4.2: Best-fitting parameters obtained from the projected spectral analysis of annuli/sectors in A2151C(B) (0.4–7.0 keV) and A2151C(F) (0.4–4.0 keV) (shown in *white* in Fig. 4.3(a) using *XMM-Newton* and *Chandra* data. The spectra in each region were fitted using the models *constant * (apec+(apec+apec+pegpwrlw)*tbabs + apec*tbabs) + gauss* (1.49 keV) + *gauss* (1.75 keV) and *constant * (apec+(apec+apec+pegpwrlw)*tbabs + apec*tbabs)* for *XMM-Newton* and *Chandra* data, respectively. The *XMM-Newton* and *Chandra* spectra were simultaneously analysed with the RASS diffuse background spectrum. The regions used for spectral extraction and the temperature (kT), abundance (Z), and derived electron density (n_e) values are listed. The errors are quoted at 90 per cent confidence level.

X-ray group	Region	Data	kT (keV)	Z ($Z_\odot$)	n_e (10^{-3} cm^{-3})
A2151C(B)	0–40 arcsec	*XMM-Newton*	$1.83^{+0.08}_{-0.07}$	$0.88^{+0.19}_{-0.16}$	$11.81^{+0.39}_{-0.41}$
		Chandra	2.07 ± 0.07	$0.92^{+0.19}_{-0.16}$	$13.12^{+0.43}_{-0.44}$
	40–80 arcsec	*XMM-Newton*	$2.30^{+0.12}_{-0.13}$	$0.77^{+0.18}_{-0.15}$	5.20 ± 0.14
		Chandra	2.42 ± 0.10	$0.67^{+0.16}_{-0.14}$	$5.35^{+0.16}_{-0.15}$
	80–120 arcsec	*XMM-Newton*	2.28 ± 0.13	$0.51^{+0.14}_{-0.12}$	$3.17^{+0.08}_{-0.09}$
		Chandra	$2.33^{+0.13}_{-0.12}$	$0.33^{+0.13}_{-0.11}$	3.28 ± 0.10
	120–160 arcsec	*XMM-Newton*	$2.36^{+0.17}_{-0.16}$	$0.27^{+0.12}_{-0.13}$	$2.26^{+0.07}_{-0.06}$
		Chandra	$2.16^{+0.14}_{-0.13}$	$0.22^{+0.12}_{-0.10}$	2.24 ± 0.08
	160–210 arcsec	*XMM-Newton*	2.06 ± 0.15	$0.20^{+0.09}_{-0.08}$	1.56 ± 0.04
		Chandra	$1.92^{+0.14}_{-0.13}$	$0.19^{+0.11}_{-0.09}$	1.57 ± 0.06
	210–300 arcsec	*XMM-Newton*	$1.90^{+0.16}_{-0.15}$	$0.14^{+0.09}_{-0.07}$	0.94 ± 0.03
	(280° wide sector)	*Chandra*	-	-	-
A2151C(F)	0–50 arcsec	*XMM-Newton*	1.07 ± 0.04	$0.26^{+0.07}_{-0.05}$	$4.67^{+0.25}_{-0.27}$
	50–100 arcsec		$1.20^{+0.07}_{-0.06}$	$0.22^{+0.07}_{-0.06}$	1.93 ± 0.10
	100–150 arcsec		1.32 ± 0.10	$0.13^{+0.05}_{-0.04}$	1.42 ± 0.06
	150–210 arcsec (230° wide sector)		1.26 ± 0.10	$0.16^{+0.08}_{-0.06}$	0.96 ± 0.05
	210–280 arcsec (230° wide sector)		$1.34^{+0.14}_{-0.13}$	$0.17^{+0.11}_{-0.08}$	0.67 ± 0.04
	280–380 arcsec (230° wide sector)		$1.15^{+0.14}_{-0.12}$	$0.02^{+0.03}_{-0.00}$	0.59 ± 0.04
	380–480 arcsec (230° wide sector)		$1.04^{+0.13}_{-0.11}$	0.02 ± 0.02	0.48 ± 0.03

Deprojected Profiles

Deprojection analysis on the spectra extracted from annular/sector regions shown in Fig. 4.3(a) was performed using the procedure described in §3.3.4. Results of spectral fitting are provided in Table 4.3. The deprojected radial profiles are shown in Figure 4.5. The errors in the best-fitting parameters are rather large in the deprojected case. A low temperature in the core of A2151C(B) is, however, still seen (Fig. 4.5(a)).

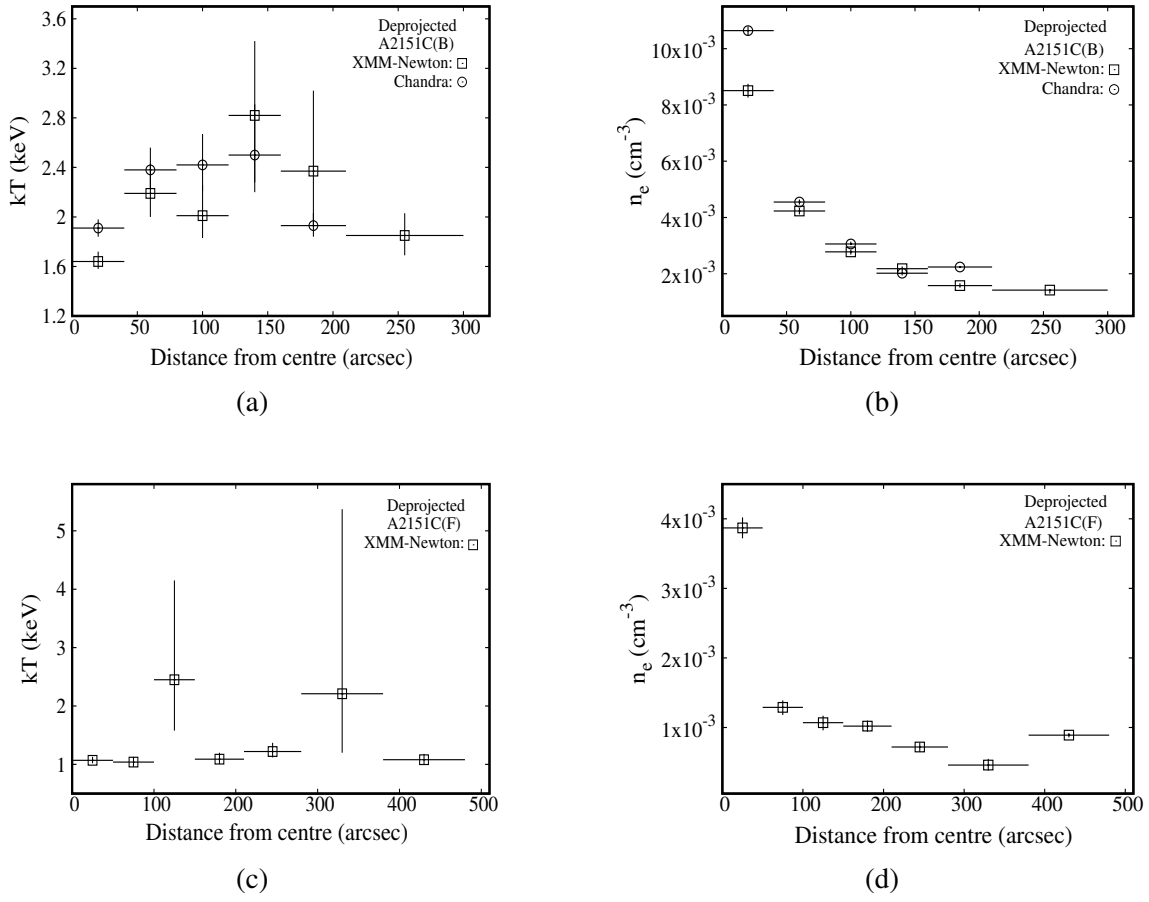

Figure 4.5: Deprojected temperature (kT) and electron density (n_e) profiles of A2151C(B) and A2151C(F) obtained from the spectral analysis with *XMM-Newton* (*open box*) and *Chandra* (*open circle*) data. The abundance value in each annulus/sector was kept frozen to the corresponding projected value. The error bars correspond to a 90 per cent confidence interval.

Table 4.3: Best-fitting parameters obtained from the deprojected spectral analysis of annuli/sectors in A2151C(B) (0.4–7.0 keV) and A2151C(F) (0.4–4.0 keV) (shown in *white* in Fig. 4.3(a)). The spectra were fitted using the models *apec+(apec+apec+pegpwrlw)*tbabs + projct*(apec*tbabs) + gauss* (1.49 keV) + *gauss* (1.75 keV) and *apec+(apec+apec+pegpwrlw)*tbabs + projct*(apec*tbabs)* for *XMM-Newton* and *Chandra* data, respectively. The XRB model normalisations and cluster abundance (Z) within each region were fixed to values obtained from the projected analysis. The regions used for spectral extraction and the temperature (kT) and electron density (n_e) values are listed. The errors are quoted at 90 per cent confidence level.

X-ray group	Region	Data	kT (keV)	n_e (10^{-3}cm^{-3})
A2151C(B)	0–40 arcsec	*XMM-Newton*	$1.64^{+0.08}_{-0.06}$	$8.51^{+0.24}_{-0.25}$
		Chandra	1.91 ± 0.07	$10.64^{+0.15}_{-0.16}$
	40–80 arcsec	*XMM-Newton*	$2.19^{+0.24}_{-0.19}$	$4.23^{+0.11}_{-0.12}$
		Chandra	$2.38^{+0.18}_{-0.15}$	4.55 ± 0.09
	80–120 arcsec	*XMM-Newton*	$2.01^{+0.25}_{-0.18}$	$2.78^{+0.08}_{-0.10}$
		Chandra	$2.42^{+0.25}_{-0.21}$	$3.06^{+0.08}_{-0.04}$
	120–160 arcsec	*XMM-Newton*	$2.82^{+0.60}_{-0.54}$	2.18 ± 0.08
		Chandra	$2.50^{+0.41}_{-0.30}$	2.02 ± 0.08
	160–210 arcsec	*XMM-Newton*	$2.37^{+0.65}_{-0.45}$	$1.58^{+0.08}_{-0.07}$
		Chandra	$1.93^{+0.10}_{-0.09}$	2.24 ± 0.03
	210–300 arcsec	*XMM-Newton*	$1.85^{+0.18}_{-0.16}$	$1.42^{+0.03}_{-0.12}$
	(280° wide sector)	*Chandra*	-	-
A2151C(F)	0–50 arcsec	*XMM-Newton*	$1.07^{+0.06}_{-0.05}$	3.87 ± 0.15
	50–100 arcsec		$1.04^{+0.09}_{-0.08}$	$1.29^{+0.10}_{-0.11}$
	100–150 arcsec		$2.45^{+1.70}_{-0.87}$	$1.07^{+0.10}_{-0.11}$
	150–210 arcsec (230° wide sector)		$1.09^{+0.11}_{-0.08}$	1.02 ± 0.08
	210–280 arcsec (230° wide sector)		$1.22^{+0.15}_{-0.10}$	$0.72^{+0.06}_{-0.07}$
	280–380 arcsec (230° wide sector)		$2.21^{+3.16}_{-1.01}$	$0.46^{+0.09}_{-0.08}$
	380–480 arcsec (230° wide sector)		$1.08^{+0.10}_{-0.08}$	0.89 ± 0.03

4.5 2D maps of the ICM thermodynamical quantities

2D maps of gas temperature, abundance, pressure, and entropy were obtained using the methods described in §3.3.4. The *Chandra* maps of A2151C(B) are shown in Figure 4.6. A drop in the temperature towards the centre of A2151C(B) seen in Fig. 4.6(a) is consistent with the presence of a cool core which was also observed in the temperature profile in Fig. 4.4(a). As we go outwards from this central region, the temperature increases and then again begins to drop in the outskirts of the subclump. The typical error (at 90 per cent confidence level) in the temperature value is $\sim$0.1–0.2 keV. Fig. 4.6(b) indicates that the central regions of the subclump have a higher metallicity as compared to the metallicity in the outer regions. The abundance values, however, are not very well constrained. Typical errors (at 90 per cent confidence level) are $\sim$0.1–0.3 $Z_{\odot}$.

The *XMM-Newton* maps of the full A2151C region are displayed in Figure 4.7. It is to be noted that 2 out of 27 regions used in the *XMM-Newton* analysis (§3.3.4) were not covered by the PN detector or almost completely affected by its chip gaps. These were analysed using MOS1 and MOS2 data only. One region which overlapped with the pair of galaxies NGC 6040 and PGC 56942 (the rightmost red box in Figure 4.2(b)), was fitted with the model *constant*(apec+(apec+apec+pegpwrlw)*tbabs + (apec+powerlaw)*tbabs) + gauss* (1.49 keV) + *gauss* (1.75 keV). The *powerlaw* component was added here to account for the AGN emission from NGC 6040 (Best & Heckman, 2012) which was not subtracted out in the point source detection and removal procedure carried out on the *XMM-Newton* data. Fig. 4.7(a) shows the 2D temperature map of A2151C(B) and A2151C(F). The temperature distribution does not appear to be azimuthally symmetric. A temperature of $\sim$1.7 keV is seen towards the centre of A2151C(B). It rises to $>$ 2 keV as one moves further out from the X-ray peak but begins to drop again towards the outskirts of the subclump. The temperature in regions covering A2151C(F) is lower than that in A2151C(B). The fractional errors in the temperature values are $\sim$6–14 per cent. The abundance map is shown in Fig. 4.7(b). The distribution of metals seems to be fairly symmetric about the X-ray emission peak of A2151C(B). In the inner regions of A2151C(B), the metallicity is close to or as high as the solar value ($Z_{\odot}$) after taking errors of $\sim$30 per cent in these regions into consideration. In contrast, the metallicity value in the interior of A2151C(F) is at most $\sim$0.27 $Z_{\odot}$. The map also reveals that the abundance in the outer regions of both the subclumps is very poor ($\leq$ 0.1 $Z_{\odot}$). The projected maps of pressure and entropy are shown in Fig. 4.7(c) and Fig. 4.7(d), respectively.

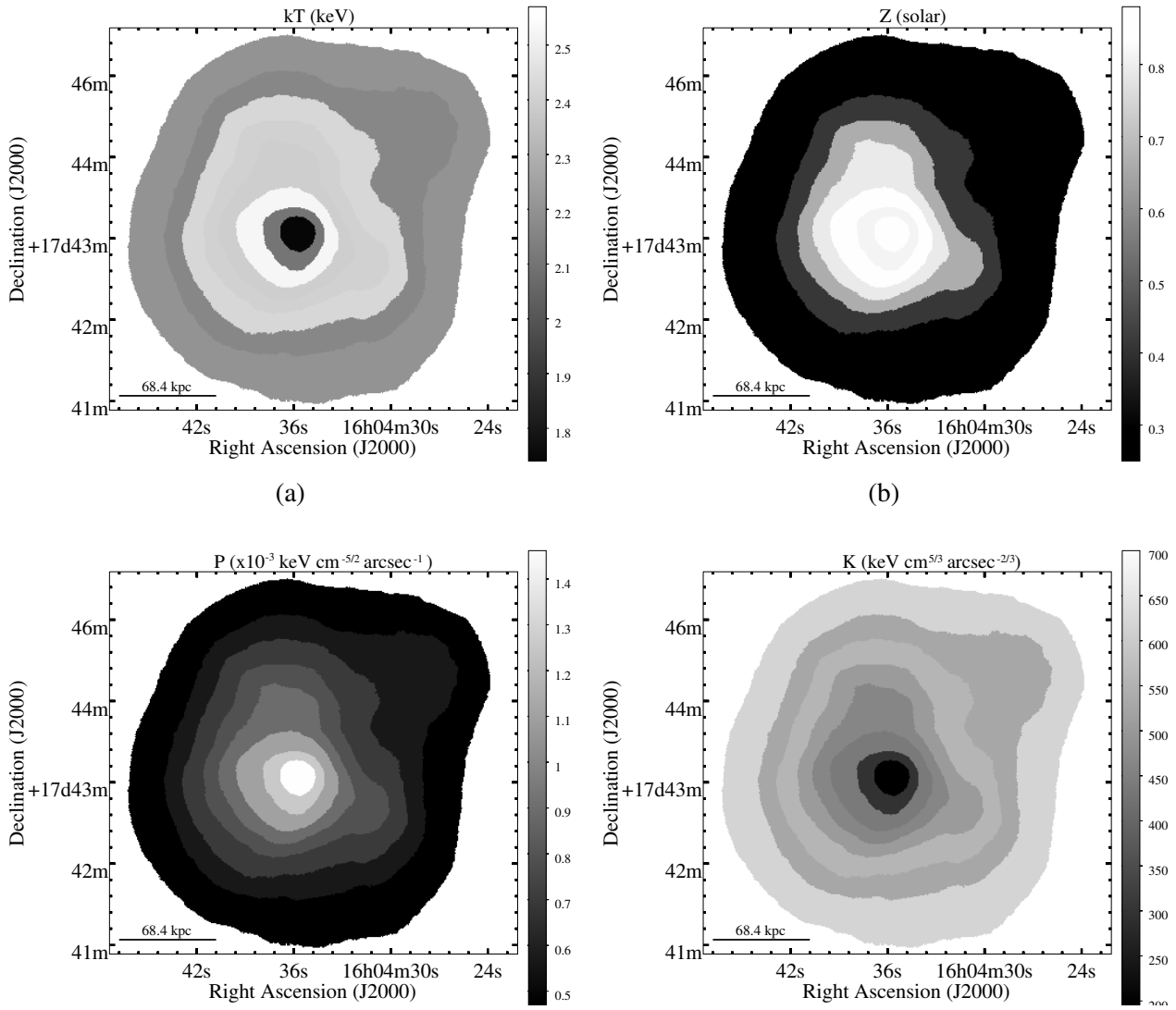

Figure 4.6: 2D maps of A2151C(B) obtained as a result of the application of *contbin* algorithm to *Chandra* data. Panel (a)–(b): Projected temperature (kT) and abundance (Z) obtained directly from spectral fitting; (c)–(d): Projected pressure (P) and entropy (K).

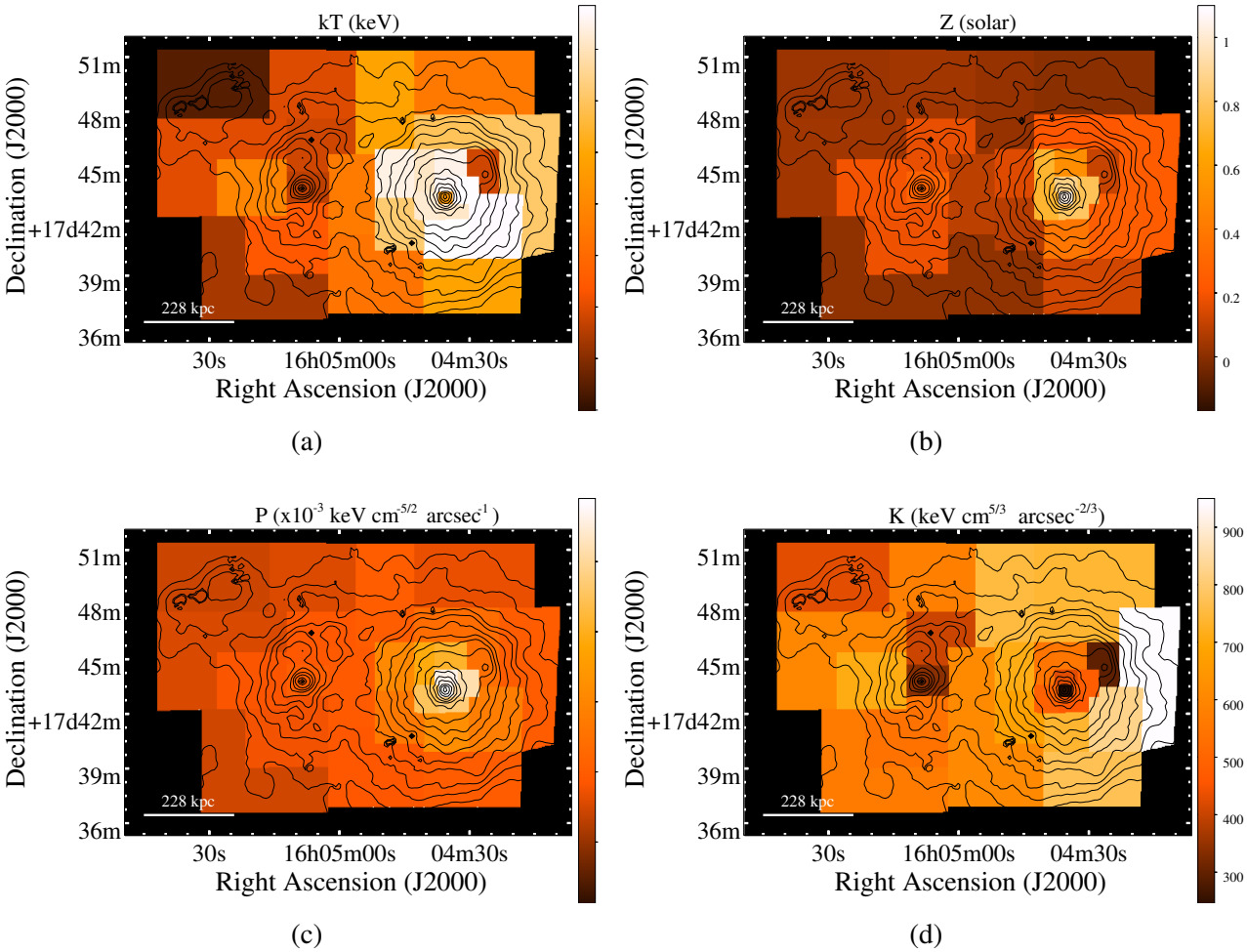

Figure 4.7: Panel (a)–(d): Projected maps of temperature (kT), abundance (Z), pressure (P), and entropy (K), respectively, obtained from the analysis of spectra extracted in 27 box/polygon shaped regions using *XMM-Newton* data.

4.6 Derived physical properties

X-ray Luminosity

X-ray luminosities (L_X) of the two subclumps – A2151C(B) and A2151C(F) – were estimated in the energy range 0.4–7.0 keV using the method explained in §3.4. These are listed in Table 4.1. A2151C(B) is $\sim$3 times more luminous than A2151C(F).

We also obtained X-ray luminosities of the two subclumps in the energy bands $0.1-2.4$ keV and $0.5-2.0$ keV using *XMM-Newton* data to see where they are located with respect to the

L_X-kT relation obtained for groups of galaxies by several authors in the above energy bands. These relations and the associated references are given in Table 4.4. In order to obtain the temperature and luminosity of galaxy groups used in deriving the L_X-kT relations, all authors except Zou et al. (2016) performed a global spectral analysis within the entire FOV or used a circular region of radius R_{spec}, which is the extent up to which X-ray emission from the group was detected. Zou et al. (2016) estimated the ICM properties within the r_{500} aperture.

Table 4.4: Best-fitting L_X–kT relations obtained by different authors for groups of galaxies.

Author	Relation[a]	X-ray Data	Group Sample Size
Helsdon & Ponman (2000b) (fig.1, table 2)	$\log(L_X/h_{50}^{-2}\text{erg s}^{-1}) = 4.30\log(kT/1\text{ keV}) + 42.70$	*ROSAT*	42
Osmond & Ponman (2004) (fig. 12, table 6)	$\log(L_X/h_{70}^{-2}\text{erg s}^{-1}) = 2.75\log(kT/1\text{ keV}) + 42.38$	*ROSAT*	35 (G-sample) [b]
Eckmiller et al. (2011) [c] (fig.3, table 4)	$\log(L_X/0.5\times10^{44}h_{70}^{-2}\text{erg s}^{-1}) = 2.25\log(kT/3\text{ keV}) - 0.02$	*Chandra*	26
Lovisari et al. (2015) (fig. 2, tables 3 and 4)	$\log(L_X/10^{43}h_{70}^{-2}\text{erg s}^{-1}) = 2.86\log(kT/2\text{ keV}) + 0.37$ [d]	*XMM-Newton*	20
Zou et al. (2016) (fig. 3, sec. 4.3)	$\log(L_X/10^{43}h_{70}^{-2}\text{erg s}^{-1}) = 2.79\log(kT/2\text{ keV}) + 0.14$[d]	*Chandra*	23

[a]The X-ray luminosity values used are estimated in the energy range $0.1-2.4$ keV except in Zou et al. (2016) who used the soft X-ray band ($0.5-2.0$ keV) to estimate the luminosity values.

[b] Systems that have group-scale emission.

[c]The X-ray luminosity values in the energy range $0.1-2.4$ keV used by the authors were all taken from the input catalogs and were determined homogeneously from *ROSAT* observations.

[d]This relation by the authors is corrected for the selection bias effects.

Figure 4.8 shows these relations along with the positions of A2151C(B) and A2151C(F) (their L_X values scaled by h_{70}^{-2} for consistency). A2151C(B) follows the group L_X–kT relations very closely, thus, suggesting that its properties are very similar to those of galaxy groups. A2151C(F) lies close to the L_X–kT relations but with a slightly higher X-ray luminosity. We note that the global spectral analysis of A2151C(F) was performed within a region of radius 480 arcsec since significant emission was detected up to this radius (§4.3). The subclump

is, however, fairly regular only up to ∼300 arcsec. Including regions beyond this radius in the global spectral analysis, which may not necessarily be part of the subclump and might correspond to infalling material, may have led to a slight underestimation of temperature and overestimation of luminosity.

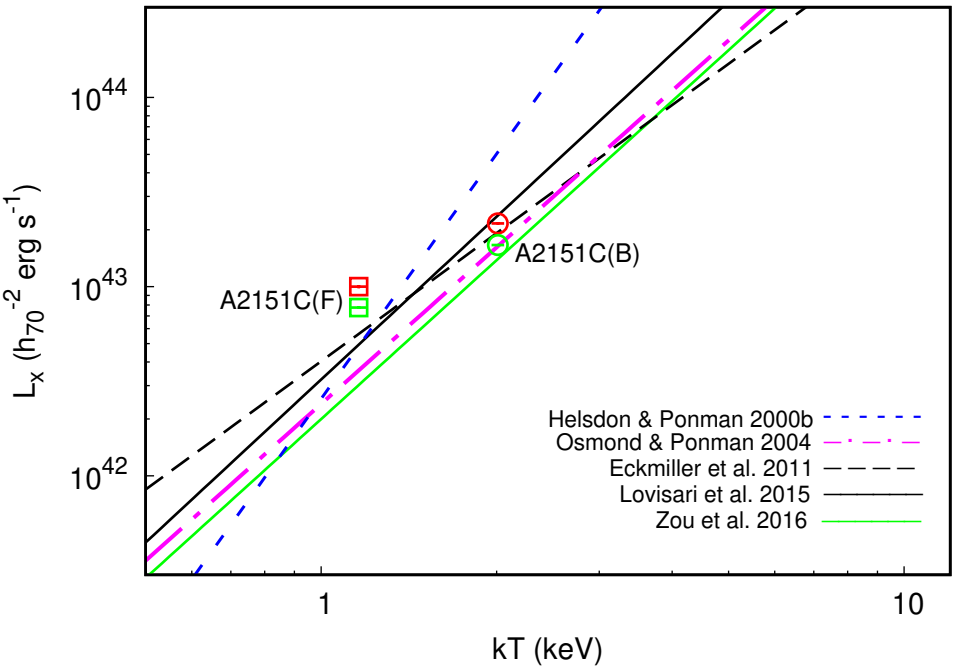

Figure 4.8: L_X–kT relations of galaxy groups obtained by different authors. The *open circle* and *open square* symbols mark the positions of A2151C(B) and A2151C(F) respectively, with the X-ray luminosity estimated in two energy bands $-$ $0.1-2.4$ keV (red symbols; for comparison with all studies except Zou et al. (2016)) and $0.5-2.0$ keV (green symbols; for comparison with Zou et al. (2016)). The errors in L_X and kT are of the size of the symbols or smaller.

Gas Mass Estimates

The gas mass (M_{gas}) of A2151C(B) and A2151C(F) was estimated by fitting a single-β model to the projected electron density profiles as described in §3.4. The results of the deprojection analysis were not used to estimate the gas mass due to the large errors obtained in the best-fitting parameter values. We obtained the gas mass of A2151C(B) and A2151C(F) out to radii 400 arcsec (∼304 kpc) and 430 arcsec (∼326.8 kpc), respectively, from the corresponding X-ray peaks, and also within a projected radius r_{500} (§3.4). We note that for obtaining the r_{500} value of A2151C(B), an average of the temperature values (2.04 keV) obtained from the *XMM-Newton*

and *Chandra* global spectral analysis was used. The results of the single-β model fitting to the projected gas density profiles along with the gas mass estimates are listed in Table 4.5.

Table 4.5: Mass of the intragroup gas obtained by fitting single-β models to the projected gas density profiles of A2151C(B) and A2151C(F). The errors are quoted at 90 per cent confidence level.

Subclump	Data	β	r_c (kpc)	ρ_0 ($10^4 M_\odot$ kpc^{-3})	$(\chi^2_\nu)_{\rm min}$	r (kpc)	$M_{gas}(r)$ ($10^{12} M_\odot$)	r_{500} (kpc)	M_{gas_500} ($10^{12} M_\odot$)
A2151C(B)	*XMM-Newton*	0.38 ± 0.03	$19.35^{+4.04}_{-3.91}$	$23.40^{+3.23}_{-2.42}$	1.46	304	$1.89^{+1.31}_{-0.84}$	830.95	$12.44^{+9.66}_{-6.11}$
	Chandra	0.38 ± 0.03	$16.63^{+3.78}_{-3.85}$	$28.07^{+5.57}_{-3.44}$	1.01	304	$1.92^{+1.60}_{-0.93}$	830.95	$12.60^{+8.71}_{-6.70}$
A2151C(F)	*XMM-Newton*	0.28 ± 0.02	$10.43^{+1.59}_{-1.49}$	13.20 ± 0.44	1.93	326.8	$1.48^{+0.56}_{-0.44}$	629.30	$6.11^{+2.66}_{-1.97}$
						304	$1.27^{+0.47}_{-0.37}$		

We believe that the gas mass value for A2151C(F) may have been overestimated. Fig. 4.2(a) shows that the X-ray emission of A2151C(F) is fairly regular only up to $\sim$300 arcsec. Beyond 300 arcsec radius, several other smaller infalling groups may be merging with the main A2151C(F) group (see Fig. 4.2(b)). The actual extent of A2151C(F) may therefore be $\sim$300 arcsec which is smaller than the 400 or 430 arcsec radii within which the gas mass values are reported in Table 4.5. We also note that spherical symmetry of A2151C(F) has been assumed while calculating the gas mass which may not be a reasonable assumption for radii beyond 300 arcsec. Moreover, the β value obtained for A2151C(F) which has been used in the gas mass estimation is unusually low (discussed further in this subsection). For comparison, we also calculated the gas mass within 300 arcsec ($\sim$228 kpc) radius of each of the two groups which resulted in a value of $1.10^{+0.71}_{-0.47} \times 10^{12} M_\odot$ for A2151C(B) and $6.79^{+2.40}_{-1.90} \times 10^{11} M_\odot$ for A2151C(F). These values indicate that the gas mass within 300 arcsec of A2151C(B) is greater than that of A2151C(F), although the errors are large.

The β value obtained for A2151C(B) is similar to that found in groups of galaxies ($\lesssim 0.5$ Helsdon & Ponman, 2000a; Mulchaey, 2000) but that obtained for A2151C(F) is unusually low. Both β and core radius values of A2151C(B) are comparable to those obtained by Huang & Sarazin (1996). We also compared the β value resulting from fitting the gas density profile (β_{fit}) to that obtained from

$$\beta = \frac{\mu m_p \sigma^2}{kT} \tag{4.1}$$

where σ is the measured optical velocity dispersion of the subclump, m_p is the mass of proton, kT is the spectrally determined temperature of the intragroup gas, and $\mu = 0.613$ is the mean molecular weight for a fully ionized gas with an abundance of 0.43 $Z_\odot$. In case of A2151C(B), Equation 4.1 resulted in a β value $\sim$0.6 using $\sigma = 441$ km s^{-1} from Agulli et al. (2017). This value is quite close to that obtained from fitting the single-β model to the gas density profile. Huang & Sarazin (1996) arrived at $\beta \sim$1.87 on application of Equation 4.1 and β_{fit} $\sim$0.45 resulting from fitting the β model to the surface brightness profile of A2151C(B). They interpreted this large discrepancy between the two β values as a consequence of the dynamically unrelaxed status of the system. This discrepancy seems to be resolved here. In case of A2151C(F), however, Equation 4.1 gave $\beta \sim$3 with $\sigma = 711$ km s^{-1} (Agulli et al., 2017) which is not at all in agreement with the β_{fit} value obtained from the gas density profile fitting ($\sim$0.28). This disagreement may be due to two reasons – either the value of σ for A2151C(F) has been overestimated or A2151C(F) is a dynamically unrelaxed subclump which is itself composed of several small groups of galaxies as can be seen in Fig. 4.2(b).

Total Mass Estimates

Assuming the subclusters to be in hydrostatic equilibrium and using Equation 3.12 in §3.4, we estimated the total gravitational mass of A2151C(B) within a radius of 304 kpc ($\sim$400 arcsec) from the X-ray peak to be $1.60 \pm 0.40 \times 10^{13}$ $M_\odot$. The spectral analysis with *XMM-Newton* data allowed determination of gas temperature and density up to a radius of 300 arcsec (228 kpc). In order to obtain the total gravitational mass within the radius up to which X-ray emission is seen in A2151C(B) ($\sim$400 arcsec; 304 kpc; Fig. 4.2), we assumed the gas temperature and density at this radius to be equal to the best-fitting values obtained for the outermost annular sector (210$-$300 arcsec; Fig. 4.3(a); Table 4.2) in the spectral analysis. The mass estimate based on the *XMM-Newton* data shows that the gas mass is $\sim$12 per cent of the total mass. Calculations by Huang & Sarazin (1996) show a similar value for the gas mass fraction at 400 arcsec ($\sim$15 per cent) in A2151C(B).

The gas temperature and density in the outermost annular sector (210$-$300 arcsec) could not be determined with *Chandra* data due to poor statistics. Hence, *Chandra* data could only give a total mass estimate for a smaller radius. The total mass of A2151C(F) within a radius of 326.8 kpc ($\sim$430 arcsec) was calculated to be $1.44 \pm 0.62 \times 10^{13}$ $M_\odot$ using *XMM-Newton* data. We also estimated the total gravitational mass of the two subclumps within r_{500} (M_{grav_500}) by extrapolating the total mass values obtained at smaller radii. The M_{grav_500} values are $9.08 \pm 5.24 \times 10^{13}$ $M_\odot$ and $3.01 \pm 2.11 \times 10^{13}$ $M_\odot$, for A2151C(B) and A2151C(F), respectively. We note that the results of the projected spectral analysis were used in the above calculations. The

error bars on the mass values correspond to a 90 per cent confidence interval. The total mass values derived here are consistent with the values obtained in a very recent optical study by Monteiro-Oliveira et al. (2022).

Cooling Time Estimates

The thermodynamic maps of A2151C(B) obtained from the spectral analysis of *Chandra* data (§4.5), show a low temperature core of radius ∼15 arcsec (Figure 4.6). We performed a deprojected spectral analysis using *Chandra* spectra extracted from six annular regions with outer radii 15, 50, 80, 120, 160, and 210 arcsec. The resulting deprojected gas temperature and electron number density values within the central 15 arcsec (∼11 kpc) circular region of A2151C(B) are 1.55 ± 0.07 keV and $2.54^{+0.06}_{-0.07} \times 10^{-2}$ cm^{-3}, respectively. Using these values, we calculated the cooling time of A2151C(B) in the central core using Equation 3.13 in §3.4. This resulted in a cooling time of $8.05^{+0.84}_{-0.76} \times 10^{8}$ yr. The estimated cooling time is much smaller than the Hubble time (∼14.5 $\times 10^{9}$ yr in our cosmology), thus confirming the presence of a cool core in A2151C(B).

4.7 Discussion and conclusions

The gas in the two groups of A2151C – A2151C(B) and A2151C(F) – has an average temperature of 2.01 ± 0.05 keV and 1.17 ± 0.04 keV, respectively (Table 4.1). The temperatures obtained are in agreement with the *ROSAT* results of Bird et al. (1995) but with tighter constraints. The X-ray luminosity of A2151C(B) is $3.03^{+0.02}_{-0.04} \times 10^{43}$ erg s^{-1} (0.4 – 7.0 keV) while that of A2151C(F) is $1.13 \pm 0.02 \times 10^{43}$ erg s^{-1} (0.4 – 7.0 keV). The X-ray luminosities are ∼3 times higher than those reported by Bird et al. (1995) due to larger bandwidth and the extent of the gas covered here, though the ratio between the 'bright' and the 'faint' subclumps is similar. The temperature and luminosity values obtained for the two subclumps are representative of groups of galaxies (Bahcall, 1999; Helsdon & Ponman, 2000a; Rasmussen & Ponman, 2007; Lovisari et al., 2015; Zou et al., 2016). The average elemental abundances in A2151C(B) and A2151C(F) are 0.43 ± 0.05 and 0.13 ± 0.02 relative to solar values, respectively (Table 4.1). The abundance of A2151C(B) is consistent with the value obtained by Bird et al. (1995). The average abundance of A2151C(F) is, however, lower than the *ROSAT* value of $0.32^{+0.15}_{-0.10}$. The different values of the temperature and abundance of the gas in the two subclumps corroborate the optical finding that they are indeed two separate galaxy groups. The total gravitational mass of the groups derived under the assumption of hydrostatic equilibrium is estimated to be

$1.60 \pm 0.40 \times 10^{13}$ $M_\odot$ (within a radius of 304 kpc) for A2151C(B) and $1.44 \pm 0.62 \times 10^{13}$ $M_\odot$ (within 326.8 kpc) for A2151C(F) (§4.6). The total mass value obtained for A2151C(B) in this study is found to be consistent with that derived by Huang & Sarazin (1996). The gas mass is derived to be $1.89^{+1.31}_{-0.84} \times 10^{12}$ $M_\odot$ (within a radius of 304 kpc) for A2151C(B) and $1.48^{+0.56}_{-0.44} \times 10^{12}$ $M_\odot$ (within 326.8 kpc) for A2151C(F) (§4.6; Table 4.5). These values are also typical of galaxy groups (Mulchaey, 2000; Lovisari et al., 2015) in contrast to galaxy clusters which have a greater extent and possess higher mass, temperature and luminosity (Böhringer et al., 2002; Reiprich & Böhringer, 2002; Sanderson et al., 2006). The M_{gas_500} and M_{grav_500} values of A2151C(B) are $1.24^{+0.97}_{-0.61} \times 10^{13}$ $M_\odot$ and $9.08 \pm 5.24 \times 10^{13}$ $M_\odot$, respectively, while these values are $6.11^{+2.66}_{-1.97} \times 10^{12}$ $M_\odot$ and $3.01 \pm 2.11 \times 10^{13}$ $M_\odot$ for A2151C(F). Both M_{gas_500} and M_{grav_500} values of the two subclumps are similar to those of galaxy groups (Lovisari et al., 2015).

The combined X-ray image of A2151C(B) and A2151C(F) (Fig. 4.2(a)) shows a region of overlap in X-ray emission between the two groups. The optical analysis of Agulli et al. (2017) indicates that the two groups are located at similar redshifts (radial velocities 10116 km s^{-1} and 10299 km s^{-1}, for A2151C(B) and A2151C(F), respectively). Therefore, the possibility of a group-group merger cannot be completely ignored. The thermodynamic maps in Figure 4.7 do not show an enhancement in temperature, entropy or metallicity in the region between the two groups. The idea of an ongoing group scale merger, thus seems unlikely. We, however, point out that the box size chosen for the spectral analysis in the overlapping region is rather large due to low statistics. Consequently, a rise in the temperature or entropy (which may be visible in a relatively narrower region in projection where the two groups may be interacting) may have been masked out. Higher resolution spectral analysis with better statistics, e.g., from a deep exposure with *Chandra* covering this overlapping region, would be required to shed light on the merger proposition.

A2151C(B) shows evidence of a cool core based on an excess of X-ray emission at the center compared to the single β model fitted to the surface brightness profile obtained from the HRI image (Huang & Sarazin, 1996). The spectral analysis of the 2D projected emission from A2151C(B) presented in this study shows a drop in temperature from 2.31 ± 0.14 keV at radii of $30-120$ kpc to $1.83^{+0.08}_{-0.07}$ keV in the central 30 kpc region (Fig. 4.4(a)) and Table 4.2) thus confirming the result of Huang & Sarazin (1996). The deprojected spectral analysis gives an even lower value of central temperature ($1.64^{+0.08}_{-0.06}$ keV; Fig. 4.5(a) and Table 4.3). The projected maps of temperature in Fig. 4.6(a) and Fig. 4.7(a), and the low central entropy seen in Fig. 4.6(d) and Fig. 4.7(d), indicate the existence of a cool core in A2151C(B). Furthermore, an estimated cooling time of $8.05^{+0.84}_{-0.76} \times 10^8$ yr (significantly smaller than the Hubble time)

in the central 15 arcsec region of A2151C(B) (§4.6) reinforces the presence of a cool core in the subclump. A2151C(F), in contrast, does not show significant evidence of containing a cool core. Although the projected spectral analysis indicates a gradual decrease in temperature from 1.32 ± 0.10 keV at radii of 76−114 kpc to 1.07 ± 0.04 keV in the central 38 kpc region of A2151C(F) (Fig. 4.4(d) and Table 4.2), this trend is not strong enough to classify this subclump as a definitive cool-core group. The deprojected temperature profile of A2151C(F) (Fig. 4.5(c)) does not show a drop in temperature towards the central region. A2151C(F), therefore, comes across as a weak-cool-core or non-cool-core group. Heating from radio sources at the centres of groups and clusters is known to inhibit the central gas from cooling (Mathews & Brighenti, 2003; McNamara & Nulsen, 2007; Gitti et al., 2012; Sun, 2012a) and the presence of the wide-angle tailed (WAT) galaxy NGC 6047 in the centre of A2151C(F) (Huang & Sarazin, 1996) with a total radio luminosity of 7.5×10^{40} erg s^{-1} (integrated from 10 MHz to 10 GHz; Feretti & Giovannini (1988)) may be responsible for arresting the development of a cool core within this group.

The presence of significant clumping of gas seen in A2151 – the bimodality in A2151C seen in Fig. 4.2 in addition to the gas clumps seen towards further east (A2151E) and north (A2151N) in the *ROSAT* PSPC image (fig. 1 of Bird et al., 1995) – contrasts it with relaxed and evolved clusters like Coma (Neumann et al., 2003). The clumped and irregular X-ray morphology observed in A2151C is similar to that observed in the nearby cluster Abell 76 which is believed to be in the early phase of cluster formation (Ota et al., 2013). Similar clumpiness is also found in A2147 (Jones et al., 1979; Reichert et al., 1981) which along with A2151 and A2152 forms the Hercules supercluster, and is also considered to be in its early evolutionary phase. Moreover, the high spiral fraction of galaxies in A2151 ($\gtrsim$ 50 per cent; Giovanelli & Haynes, 1985; Bird et al., 1995; Maccagni et al., 1995) is also indicative of the relatively unevolved state of the cluster as a whole.

The bimodal structure in A2151C seen in X-rays (Magri et al., 1988; Bird et al., 1995; Huang & Sarazin, 1996) as well as in the galaxy distribution (Huang & Sarazin, 1996; Agulli et al., 2017), suggests that A2151C(B) and A2151C(F) are two physically distinct entities. On one hand, A2151C(B) possesses a cool core along with a fairly regular X-ray emission reflecting its relaxed and virialised nature. On the other hand, the irregular X-ray morphology of A2151C(F) together with its low X-ray luminosity, temperature and abundance are indications that this subclump is in the process of formation. The presence of several compact galaxy groups (CGGs) identified within A2151C(F) (Fig. 4.2(b)) lends further support to this idea. We notice an increase in temperature (Fig. 4.7(a)) and entropy (Fig. 4.7(d)) in the eastern region within A2151C(F). The region overlaps with the CGG SDSSCGB 4240 (Fig. 4.2(b))

in the outskirts of A2151C(F), which is probably merging with the subclump and leading to the observed enhancement. The disagreement between the β value obtained from fitting the gas density profile (β_{fit} = 0.28 $\pm$ 0.02) and that derived using Equation 4.1 (β $\sim$3), further suggests the dynamically unrelaxed and evolving status of A2151C(F). Although galaxy groups are known to have $\beta_{fit} \lesssim 0.5$ (Helsdon & Ponman, 2000a; Mulchaey, 2000), the value obtained for A2151C(F) is unusually low.

Bird et al. (1995) did not attribute the bimodality in X-ray emission in A2151C to correspond to two separate features in their galaxy density map (fig. 2 of their paper). Instead, they reported a single galaxy density peak associated with A2151C. Based on this and the presence of the WAT source within A2151C(F) (often associated with clusters mergers; see references in Bird et al., 1995), they postulated that the gas identified with A2151C(F) is the ram-pressure stripped part of A2151E (the gas clump towards further east; not covered in this study but seen in the *ROSAT* PSPC image; see Fig.4.1) which got trapped within the deeper potential well of A2151C(B), when a merger event between A2151C(B) and A2151E took place. Our analysis presents a different scenario, which is also the most interesting outcome of this research work. The X-ray emission in A2151C(F) is now seen to coincide with a definite structure in the spatial distribution of galaxies (fig. 2 of Huang & Sarazin (1996) and fig. 5 of Agulli et al. (2017)). Besides, A2151C(B) appears to be fairly symmetric and undisturbed, and also contains a cool core which seems to be intact even after the supposed occurrence of a merger event. The radio jets associated with NGC 6047 extend $\sim$52 arcsec or $\sim$40 kpc across in a N-S direction and form a small-scale structure (fig. 9 of Huang & Sarazin, 1996). Their extent is comparable to the optical diameter of the galaxy ($\sim$81 arcsec (SDSS r-bandpass; ref: NED) or $\sim$61 kpc). The interstellar medium rather than a merger activity may therefore play a non-negligible role in shaping the tails, as seen in galaxy NGC 4874 within the Coma cluster (Feretti & Giovannini, 1985), in contrast with large-scale WATs ($\gtrsim$ 200 kpc) which are often thought to be created in cluster mergers (Sakelliou & Merrifield, 2000). Nonetheless, if the hypothesis of Bird et al. (1995) is assumed to be true, it may be possible that the merger between A2151C(B) and A2151E was either a minor one or it took place at a time when A2151C(B) had already developed a well defined cool core (simulations show that major mergers tend to disrupt cool cores; Ritchie & Thomas, 2002; ZuHone, 2011), more so if the mergers take place in the early evolutionary stage of the cluster (Burns et al., 2008; Henning et al., 2009). However, to establish the correctness of the tentative post-merger scenario proposed by Bird et al. (1995) or rule it out, deep exposures with *Chandra* as well as radio observations targeting the entire A2151 field (including both A2151C and A2151E), revealing the presence/absence of shocks, are required.

Note: The idea presented in this research work that the subcluster A2151C(F) is in the process of formation is supported by a recent optical study of the full A2151 field by Monteiro-Oliveira et al. (2022). The authors also discard the merger scenario between A2151E and A2151C(B) as proposed by Bird et al. (1995). They also find that A2151C(B) and A2151C(F) are in a pre-merger state and the first encounter between the two subclusters will happen in $\sim$0.4 Gyr.

Chapter 5

X-ray-radio interaction in Abell 1569

This chapter is based on the research article *The complex intracluster medium of Abell 1569 and its interaction with central radio galaxies* published in the *Monthly Notices of the Royal Astronomical Society* by Tiwari & Singh (2022) (MNRAS, 509, 3321).

5.1 Introduction

Abell 1569 (hereafter A1569) is a low-redshift (z = 0.0784) galaxy cluster with richness class 0 (Abell et al., 1989). Its optical centre is at R.A. (J2000) = $12^h36^m18^s$ and Dec. (J2000) = $+16°35'00''$, and it has $\sim$56 member galaxies within a projected radius of 23.5 arcmin measured from this centre (Gomez et al., 1997a). A1569 has been studied in great detail at optical wavelength by Gomez et al. (1997a) using data from the *First Palomar Sky Survey* (*POSS I*) and the 2.3-m *Bok telescope* at the *University of Arizona Steward Observatory*. The authors detected optical substructure in the cluster with the help of one, two, and three-dimensional statistical tests. They detected the presence of two unbound subclusters in A1569, one towards the northwest and the other in the southeast direction. We refer to the former as A1569N and the latter as A1569S in the following text. The subclumps were found to be segregated both spatially and kinematically. The optical centre of A1569N was determined as R.A. (J2000) = $12^h36^m13^s.07$ and Dec. (J2000) = $+16°36'21''.09$, while that of A1569S as R.A. (J2000) = $12^h36^m15^s.65$ and Dec. (J2000) = $+16°31'48''.27$. The estimated number of member galaxies is 25 for A1569N and 29 for A1569S. A1569N is found to have a mean velocity of 23782 km s^{-1} with a velocity dispersion of 622 km s^{-1}, while these values are 20740 km s^{-1} and 433 km s^{-1} respectively, for A1569S.

A1569 was first studied by Abramopoulos & Ku (1983) as part of an X-ray survey of clusters of galaxies using data from the *Einstein Observatory*. The authors did not report the presence

of substructure in the cluster. Substructure in X-ray emission from A1569 was first detected by Gómez et al. (1997b) using the *Roentgen Satellite* (*ROSAT*) position sensitive proportional counter (PSPC) data with an exposure time of 2.85 ks. Their low-resolution ($15'' \times 15''$ pixel size) PSPC image (fig. 1d of their paper) showed the presence of two X-ray clumps – A1569N and A1569S, coinciding with the optically detected subclusters in A1569 (fig. 3f of Gomez et al., 1997a). Analysis of X-ray spectrum of A1569S averaged over a circular region of 4.9 arcmin radius centred on its X-ray peak by Gómez et al. (1997b) found the cluster gas in A1569S to possess an average temperature of $1.4^{+0.9}_{-0.3}$ keV. The fit was performed in the energy range 0.5–2.05 keV, and due to low number of counts (210 ± 16), the elemental abundance of the ICM could not be constrained and was fixed at 0.3 $Z_{\odot}$ during the fit. The X-ray luminosity of A1569S in the energy band 0.5–2.05 keV was estimated to be $1.7 \pm 0.3 \times 10^{43}$ erg s^{-1}. An average spectral analysis of A1569N was not performed due to sparse X-ray data. Furthermore, a spectral analysis of different regions within A1569S was not carried out by Gómez et al. (1997b). The authors calculated a low mass inflow rate of 0.4 $M_{\odot}$ yr^{-1} into the centre of A1569S indicating the absence of a significant cluster-wide cooling flow.

A particularly interesting feature of A1569 is that both its subclusters host extended radio galaxies at their centres. The double-lobed radio source, 1233+169, is hosted by A1569N, whereas A1569S harbours a WAT radio galaxy, 1233+168 (Owen & Ledlow, 1997; Gomez et al., 1997a). Any interaction between 1233+169 and the surrounding gas in A1569N has never been explored. The *ROSAT* study by Gomez et al. (1997a), however, did find some evidence of interplay between 1233+168 and the intracluster gas in A1569S. The authors found that relative velocities of radio sources with respect to the ICM should be in the range 400–2500 km s^{-1} in order to explain the observed bent-tail radio morphology. Radio source 1233+168 was found to exhibit a small peculiar velocity of 215 km s^{-1} which was not sufficient to explain the bending of the WAT according to ram-pressure models. Additionally, the X-ray SB and optical spatial galaxy distributions of A1569S were found to exhibit similar extended morphologies. Direct evidence of merger activity in A1569S was not found due to the low resolution of the PSPC data, but based on the points mentioned above, Gomez et al. (1997a) postulated that a cluster-subcluster merger could provide a reasonable explanation for the observed optical and X-ray properties of A1569S and the WAT morphology.

In this chapter, we present a study of the hot X-ray emitting gas within the two subclusters of A1569 using the superior spatial and energy resolution ($\sim$0.5 arcsec; $\sim$120 eV) of the ACIS aboard the *Chandra* X-ray Observatory over the *ROSAT* PSPC ($\sim$25 arcsec, $\sim$550 eV). We investigate the thermodynamic properties of the ICM of A1569 by performing a detailed spectral analysis within the two substructures, A1569N and A1569S. This work emphasizes

on the interaction of the central radio galaxies with the surrounding cluster gas. The study of Gomez et al. (1997a) is taken a step further to search for cavities and merger signatures in the ICM of A1569N and A1569S. These features enable us to understand the effect of radio mode feedback operating in the subclusters and the influence of the gas environment on the radio galaxies. At the redshift $z = 0.0793$ of A1569N, 1 arcsec = 1.55 kpc, while at redshift $z = 0.0691$ corresponding to A1569S, 1 arcsec = 1.37 kpc (Wright, 2006).

5.2 Imaging analysis

5.2.1 X-ray, optical, and radio images

Figure 5.1a shows the point-source-subtracted, exposure-corrected, and particle-background-subtracted *Chandra* X-ray image of A1569 in the energy range 0.4−4.0 keV, generated using the procedure described in §3.2. Two gas subclumps, one towards the north and the other towards the south, are seen very clearly. As mentioned in §5.1, we refer to the northern subclump as A1569N, and the southern subclump as A1569S. Based on this *Chandra* image of A1569, the X-ray peak of A1569N is located at RA (J2000)=$12^h36^m08^s.14$ and Dec (J2000)=+16°38′29″.19, and that of A1569S is at RA (J2000)=$12^h36^m25^s.97$ and Dec (J2000)=+16°32′19″.40. A1569S appears to be elongated in the E-W direction while the gas in A1569N seems to be extended in the NW-SE direction. The large-scale morphology of the two subclusters is explored in more detail further in this section.

Figure 5.1c and Figure 5.1d show the optical *r*-band images of the central regions of A1569N and A1569S from the SDSS, generated using the procedure described in §3.6. The clustering of galaxies around the X-ray peaks of the subclumps is visible. The presence of two distinct galaxy groups within A1569 coinciding with the locations of the X-ray gas clumps was reported in the detailed optical analysis carried out by Gomez et al. (1997a). The X-ray peak of A1569N coincides with the elliptical galaxy IC 3557 (SIMBAD) shown in Fig.5.1c. IC 3557 along with SDSS J123608.45+163825.2 (Fig.5.1c) constitutes a pair of galaxies. IC 3557 is the brighter member of the pair and is classified as a brightest cluster galaxy (BCG) by Szabo et al. (2011). The X-ray peak of A1569S coincides with the BCG SDSS J123625.78+163218.3 (Fig.5.1d).

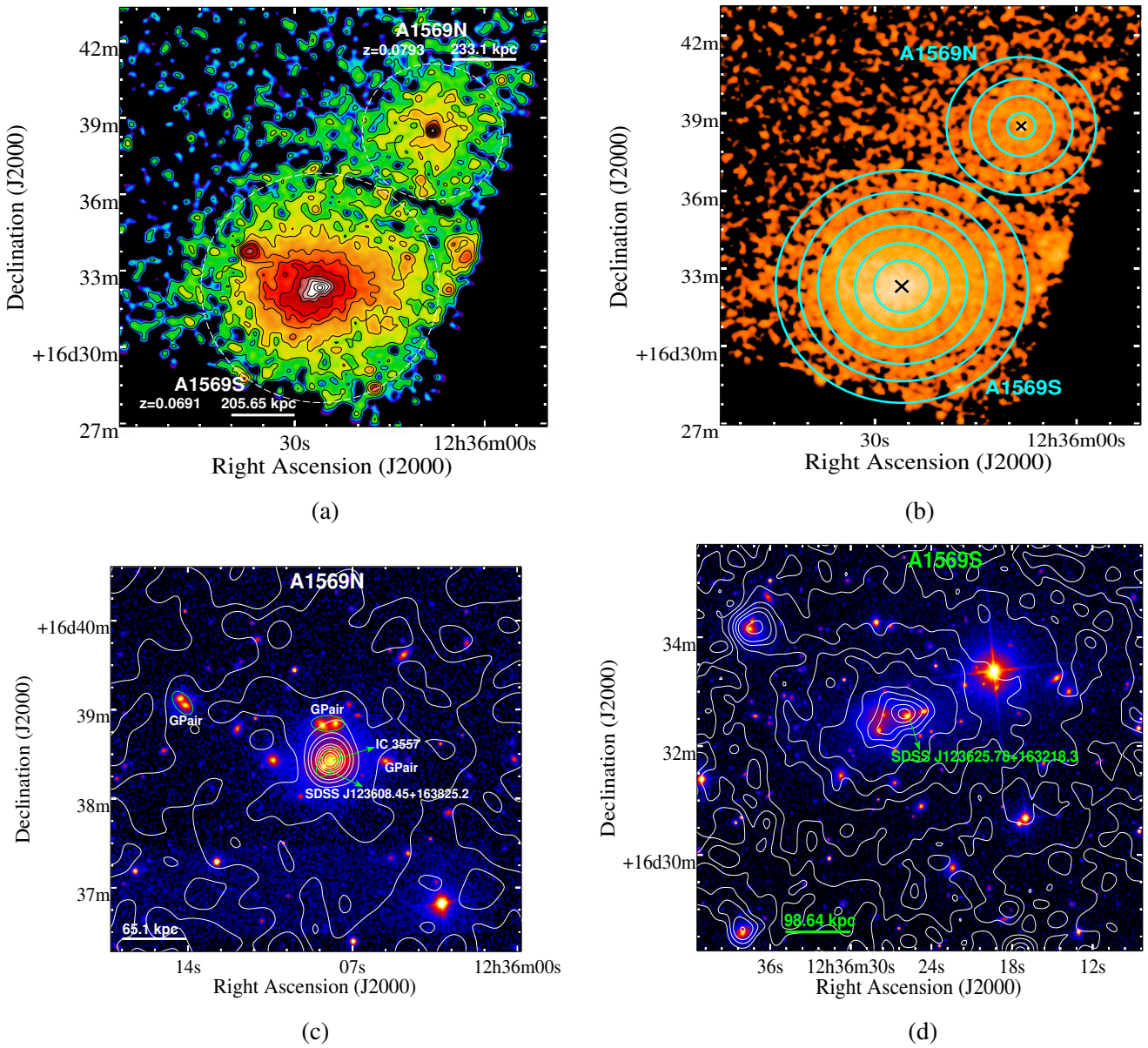

Figure 5.1: **(a)** The 0.4–4.0 keV exposure-corrected *Chandra* image of A1569 obtained after elimination of point sources and subtraction of particle background. The image has a pixel size of 0.492 arcsec and was smoothed using a gaussian kernel with σ = 15 pixels. Overlaid logarithmic contours range from 1.5 x 10^{-10} to 1.0 x 10^{-8} photons cm^{-2} s^{-1} pixel^{-1}. **(b)** Regions used for the azimuthally averaged spectral analysis of A1569N and A1569S. The *black cross* symbols mark the positions of the X-ray peaks. **(c)** and **(d)** Optical *r*-band images of the central regions of A1569N and A1569S, respectively, from the *Sloan Digital Sky Survey* with overlaid X-ray contours from the *Chandra* image shown in panel (a). The brightest cluster galaxy in each subcluster is labelled and few galaxy pairs (Gpair) in A1569N identified from SIMBAD are highlighted in green ellipses.

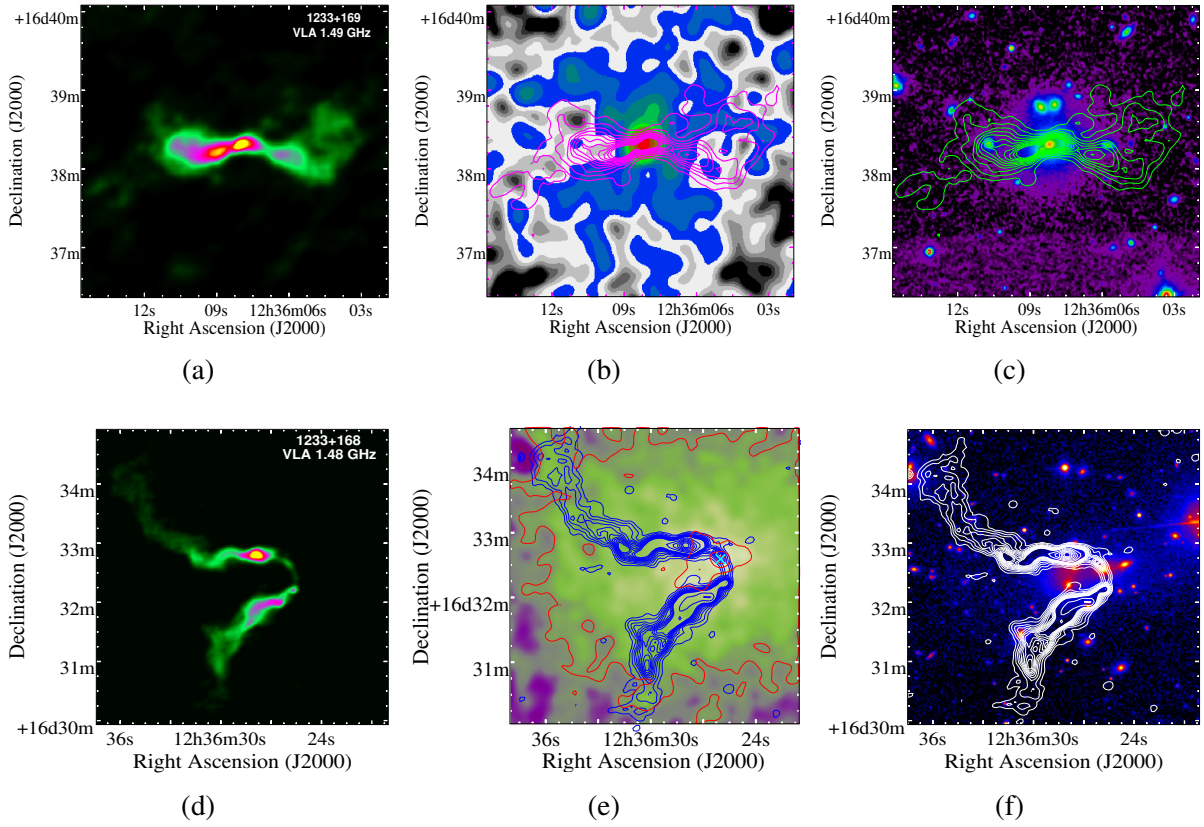

Figure 5.2: ***left:*** The combined B and C-configuration VLA radio image of galaxy 1233+169 (1.49 GHz) in A1569N (*top*) and 1233+168 (1.48 GHz) in A1569S (*bottom*). ***middle:*** *Chandra* zoomed-in images (pixel size: 0.492 arcsec; images smoothed using a gaussian with σ = 8 pixels) around the positions of 1233+169 in A1569N (*top*) and 1233+168 in A1569S (*bottom*), with the VLA radio contours of the galaxies superimposed. In the *bottom* panel, X-ray surface brightness contours are also shown in *red* color, and the *cross* symbol in *cyan* color marks the optical position of the BCG 1233+168. The 1.49 GHz contour levels of 1233+169 are 0.4, 1.4, 2.7, 4.1, 5.5, 6.9, 8.2, 9.6, 11.0, 12.3, and 13.7 mJy beam^{-1} (beam size: 5.00×4.23 arcsec^2). The 1.48 GHz contour levels of 1233+168 are 0.3, 0.7, 1.4, 2.1, 2.8, 3.5, 4.2, 4.9, 5.6, 6.3, 7.0, 14.0, 21.0, 28.0, 35.0, 42.0, and 49.0 mJy beam^{-1} (beam size: 5.00×4.23 arcsec^2). ***right:*** Optical r-band images of the central regions of A1569N (*top*) and A1569S (*bottom*), respectively, with the VLA radio contours of the central galaxies overlaid.

Figure 5.2a and Figure 5.2d display the VLA combined B and C-configuration L-band radio images of the galaxies 1233+169 and 1233+168, respectively, generated using the procedure described in §3.5. 1233+169 in A1569N extends to ∼104 kpc on a side, while the extended features of 1233+168 (∼230 kpc) span almost the entire eastern side of A1569S. The total flux density of 1233+168 at 1.48 GHz is 1360 mJy while that of 1233+169 is 620 mJy. The total radio luminosity of 1233+168 at 1.48 GHz is 1.66×10^{25} W Hz^{-1} while that of 1233+169 is 1.02×10^{25} W Hz^{-1}. High-resolution radio images of these two galaxies have been presented earlier by Owen & Ledlow (1997). However, their interaction with the surrounding intracluster gas has never been explored before. With the aim of investigating this prospect, we searched for

X-ray structure in the vicinity of the extended features of the two radio galaxies. In Figure 5.2b and Figure 5.2e, we present the *Chandra* zoomed-in images of the central regions of A1569N and A1569S respectively, with the radio contours of 1233+169 and 1233+168 overlaid. Fig. 5.2b shows that the X-ray gas distribution in the region around 1233+169 is not azimuthally symmetrical. There appears to be an X-ray deficit in the regions where the extended features of 1233+169 lie, thus, indicating the presence of X-ray substructure adjacent to the radio galaxy in A1569N. Fig. 5.2e, however, does not show obvious X-ray structure around the tails of 1233+168 in A1569S. In the central $\sim$70 kpc region of A1569S, however, the gas distribution clearly deviates from azimuthal symmetry and appears to be elongated. The X-ray extension lies between the tails of 1233+168 and is well beyond its optical light distribution. Figure 5.2c and Figure 5.2f show that the centres of both 1233+169 and 1233+168 coincide with the BCGs of the two subclusters.

5.2.2 Two-dimensional X-ray image fitting

The 0.4-4.0 keV *Chandra* image was fitted with a 2D-β model to extract the general characteristics of the large-scale X-ray morphology of each subcluster, using the method described in §3.2.2. Figure 5.3 shows the image regions used for estimating the background and subcluster properties. Total counts are 7725 for the background, and 7705 and 17552 respectively, for the A1569N and A1569S source regions. We used a binning factor of 8, such that each pixel in the image has a size of 3.936 arcsec.

The model fitting results are listed in Table 5.1. We note that in case of A1569N, a circular region of radius 15 arcsec corresponding to the core of the central galaxy was excluded while modelling the subcluster source emission, since including the central region did not result in physically reasonable parameter values. We also tried fitting the model *gauss2d+beta2d* (the former representing emission from the central galaxy and the latter modelling the cluster gas emission) to A1569N, but this did not result in a good fit.

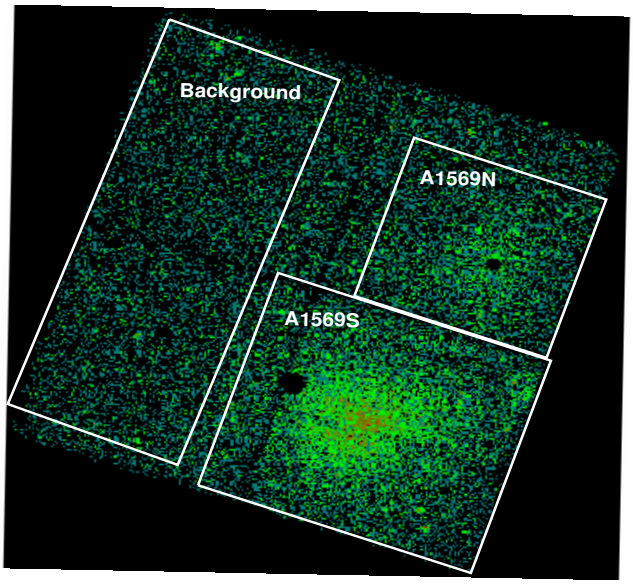

Figure 5.3: Regions used for estimating the background, and subcluster properties of A1569N and A1569S by fitting a two-dimensional β-model to the *Chandra* X-ray image. The image has a pixel size of 3.936 arcsec (8 times the original ACIS pixel size).

The source regions were also modelled with the elliptical 2D-β model by thawing the paramaters $ellip$ and θ. The results are provided in Table 5.1. The position of the subcluster centre thus obtained, along with the core radius and β value for both A1569N and A1569S are consistent with the results of the isotropic 2D-β model. The ellipticity ($ellip$) and position angle (θ) parameters are 0.27 ± 0.02 and $8^{\circ}.6^{+2.9}_{-2.8}$ respectively, for A1569S. Thus, we not only confirm but also robustly quantify the E-W elongation of A1569S previously reported by Gomez et al. (1997a). The ellipticity and position angle values are 0.22 ± 0.09 and $49^{\circ}.2^{+8.5}_{-14.8}$ respectively, for A1569N. These values indicate that A1569N is elongated in the NW-SE direction. The β values obtained for the two subclusters are comparable to those found in groups of galaxies (Helsdon & Ponman, 2000a; Mulchaey, 2000).

Table 5.1: Results of the two-dimensional β-model fitting to the *Chandra* X-ray image of A1569N and A1569S. The errors are quoted at 90 per cent confidence level.

	A1569N		A1569S	
Parameter	Isotropic	Elliptical	Isotropic	Elliptical
Core radius r_c (kpc)	$101.3^{+38.1}_{-28.4}$	$114.5^{+44.8}_{-31.7}$	$40.9^{+4.7}_{-4.4}$	$51.0^{+5.7}_{-5.3}$
Centre position R.A. (J2000)	$12^h36^m08^s.8^{+0.5}_{-0.5}$	$12^h36^m08^s.9^{+0.5}_{-0.5}$	$12^h36^m26^s.6^{+0.1}_{-0.1}$	$12^h36^m26^s.6^{+0.2}_{-0.2}$
Centre position Dec. (J2000)	$+16°38'21''.41 \pm 8''.0$	$+16°38'20''.51^{+8''.6}_{-9''.2}$	$+16°32'17''.9 \pm 1''.7$	$+16°32'18''.4 \pm 1''.5$
Ellipticity $ellip$	–	0.22 ± 0.09	–	0.27 ± 0.02
θ (degree)	–	$49.2^{+8.5}_{-14.8}$	–	$8.6^{+2.9}_{-2.8}$
Amplitude (10^{-9} photon cm^{-2} s^{-1} pixel^{-1})	1.67 ± 0.09	$1.67^{+0.02}_{-0.01}$	10.8 ± 0.08	$10.7^{+0.08}_{-0.07}$
Index β	$0.30^{+0.03}_{-0.01}$	$0.28^{+0.03}_{-0.02}$	0.35 ± 0.01	0.36 ± 0.01
Reduced C-stat	1.03	1.03	1.10	1.09
	Background Estimate			
Constant (10^{-9} photon cm^{-2} s^{-1} pixel^{-1})	0.54 ± 0.01			
Reduced C-stat	0.88			

5.2.3 Search for X-ray deficits around 1233+169

Motivated by the presence of X-ray substructure in the intracluster gas around the radio galaxy 1233+169 in A1569N (Fig. 5.2b), we tested for the existence of potential cavities in the ICM of A1569N. An unsharp-masked image of the central region of A1569N was created by subtracting a heavily smoothed ($\sim$221 arcsec) X-ray image from a lightly smoothed ($\sim$36 arcsec) image. The resulting image with the radio contours of 1233+169 superimposed is shown in Figure 5.4a. The image shows X-ray deficits spatially coincident with the extended features of the radio galaxy 1233+169. The eastern deficit is stronger compared to the western deficit. We note that several smoothing scales were tried to generate the unsharp-masked image and the observed X-ray deficits were best visible with the scales mentioned above, likely because the smaller smoothing scale ($\sim$36 arcsec) is similar to the size of the extended radio features. The X-ray deficits seen in Fig. 5.4a, albeit mild in appearance due to limited photon statistics, are indicative of the presence of potential cavities carved out in the ICM of A1569N by the radio lobes of 1233+169. We note that the unsharp masking technique is highly sensitive to noise

and the smoothing scales used. This, along with the low photon statistics, may have led to the over-sharpening of artefacts (chip gaps, bad pixels, unrecorded pixels) in Fig. 5.4a.

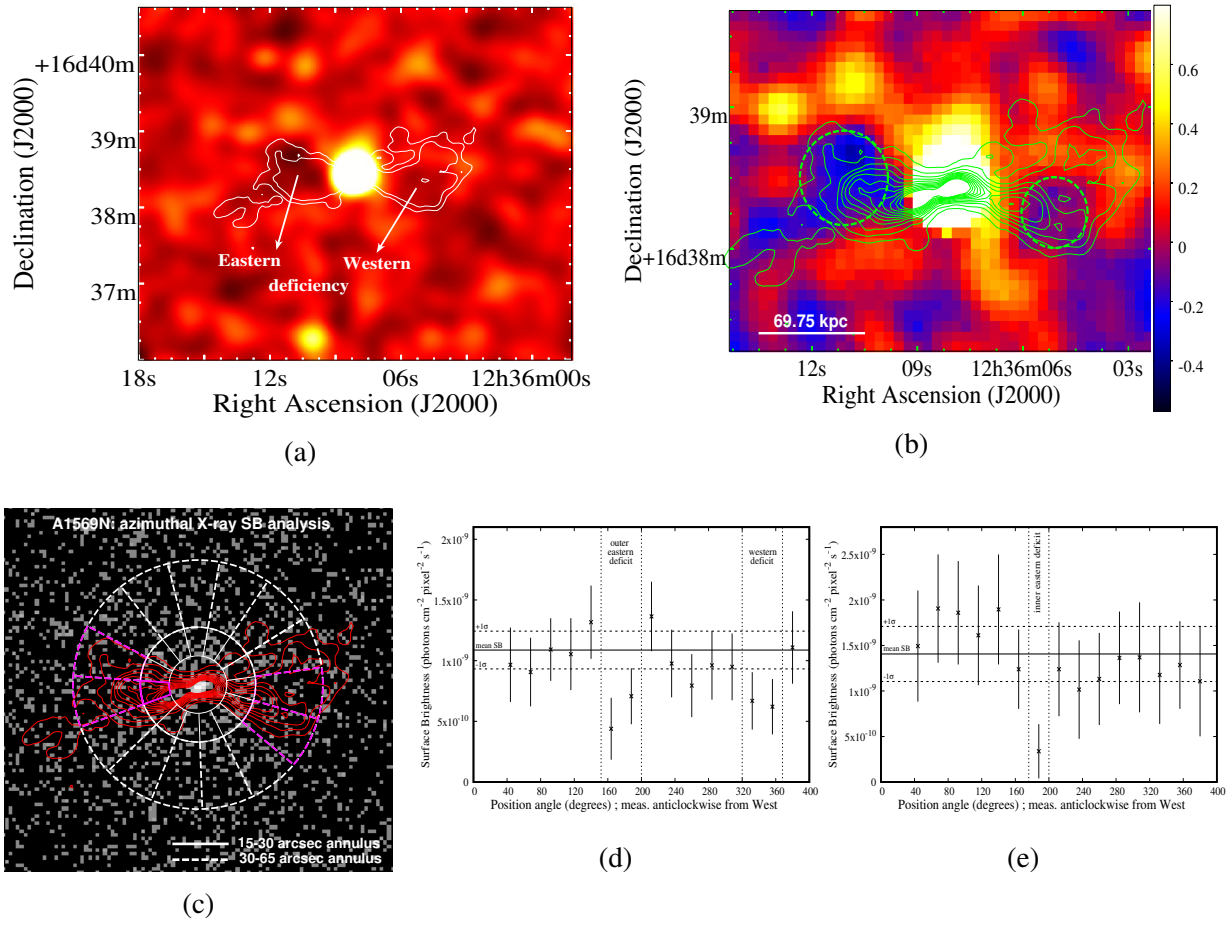

Figure 5.4: **(a)** Unsharp-masked image of the central region of A1569N with the outermost radio SB contours of galaxy 1233+169 superimposed in *white* color. X-ray deficits spatially coincident with the extended features of 1233+169 are seen towards the east and west of the central peak. **(b)** Residual image of the central region of A1569N obtained after subtracting the best-fitting elliptical 2D-β model from the data image. The radio contours of 1233+169 are overlaid in *green*. The dashed *green* circles represent the gas deficient regions. **(c)** The outer (30–65 arcsec) and inner (15–30 arcsec) annular regions used for the azimuthal SB analysis are outlined in *white* dashed and *white* solid line styles, respectively. Both annular regions are divided into fifteen 24° sectors. Radio SB contours of 1233+169 are overlaid in *red* color. The eastern and western sectors within which a significant drop in the SB is observed are highlighted in *magenta* colour. **(d)** 0.5–4.0 keV azimuthal SB profile obtained for the outer annulus (30–65 arcsec) using the fifteen 24° sectors. The solid line marks the mean SB calculated after excluding the 4 lowest data points. Dashed lines show the 1σ uncertainties on the mean. **(e)** 0.5–4.0 keV azimuthal SB profile obtained for the inner annulus (15–30 arcsec) using the fifteen 24° sectors. The solid line marks the mean SB calculated after excluding the lowest data point. Dashed lines show the 1σ uncertainties on the mean; The X-ray deficits highlighted in (d) and (e) correspond to the *magenta* sectors marked in (c).

Additionally, we subtracted the best-fitting elliptical 2D-β model (Table 5.1) from the data image of A1569N. The resulting residual image is shown in Figure 5.4b. Signs of X-ray deficits towards the east and west of the central X-ray peak are more distinctly observed in this image. The gas deficient regions overlap with the radio lobes of 1233+169 and are circled in *green* color in Fig. 5.4b. These regions appear to be surrounded by excess X-ray emission, in the form of bright arms/rims, likely resulting from the displacement and compression of the ICM formerly present in the potential cavities by the radio lobes of 1233+169. We note that in the 2D-β modelling of the gas emission from A1569N, the central galaxy was excluded (§5.2.2). The central region, therefore, shows up as an excess of X-ray emission in the residual image.

To test the statistical significance of the X-ray deficits corresponding to the location of the extended radio features of 1233+169, we compared the X-ray surface brightness in the gas deficient regions with the brightness of other ICM regions at similar radii. We measured the $0.5-4.0$ keV background-subtracted and exposure-corrected azimuthal SB (with point sources removed) using an annulus with inner and outer radii of 30 and 65 arcsec, respectively, divided into sectors with annular width of 24°. The choice of sectors with annular width smaller than 24° made it difficult to assess the significance of the probable cavities, owing to very few photons enclosed. The annular region was centred on the X-ray peak of A1569N and is shown in dashed *white* sectors in Figure 5.4c. The SB profile was constructed using the point-source-subtracted and unsmoothed image of A1569N having a pixel size of 0.492 arcsec, and is shown in Figure 5.4d. The negative features seen in Fig. 5.4d correlate with the X-ray SB deficit towards the east and the west of the central peak of A1569N, and overlap with the position of the radio lobes of 1233+169. These sectors within which the X-ray deficits are observed, are highlighted in *magenta* color in Fig. 5.4c.

We also performed a similar azimuthal SB analysis in a smaller annular region covering the inner part of the potential eastern cavity. This region has inner and outer radii of 15 and 30 arcsec, and is marked in solid *white* line style in Fig. 5.4c. The resulting azimuthal X-ray SB profile is shown in Figure 5.4e. We further estimated the significance of the X-ray deficits, spatially coincident with the radio features of 1233+169, by calculating the mean number of counts in the regions used for the azimuthal SB analysis. We excluded the sectors within which the negative SB features lie in calculating this mean value. The exposure-corrected and particle-background-subtracted mean value for the inner annulus (15–30 arcsec) is 16.7 ± 4.1 counts, whereas this value is 29.7 ± 5.4 counts for the outer annulus (30–65 arcsec). The value in the inner eastern deficit (Fig. 5.4e) is only a mere 3.1 counts, giving a 3.3σ significance. The lowest value in the outer eastern deficit (Fig. 5.4d) is 13.4 counts and that in the western deficit (Fig. 5.4d) is 16.3 counts, giving significance of 3σ and 2.5σ, respectively.

5.3 Average X-ray spectra

Average X-ray spectra of A1569N and A1569S were extracted from regions outlined in white color in Fig.5.1a using the method described in §3.3.1. The regions were centred on the BCGs of the two subclusters. A circular region of radius 160 arcsec was selected for the average spectral extraction of A1569N, whereas a circular region of radius 270 arcsec was chosen for A1569S. Background spectra and responses in these regions were also generated as described in §3.3.1. The extracted spectra were simultaneously fitted with the RASS diffuse background spectrum using the method and models described in §3.3.3. The spectral fitting was done in the energy range 0.5–4.0 keV. The data along with the model spectra are shown in Figure 5.5. The best-fitting values of gas temperature, abundance, and *apec* normalization for the two subclusters are provided in Table 5.2. We note that the X-ray source visible on the eastern outskirts of A1569S (Fig. 5.1a) was removed from the spectral analysis. Additionally, the effect of including the central BCGs on the average and radial ICM thermodynamic properties (§5.4) was tested by excluding the central 15 arcsec region from the spectral analysis. This did not produce a notable change in the derived gas properties.

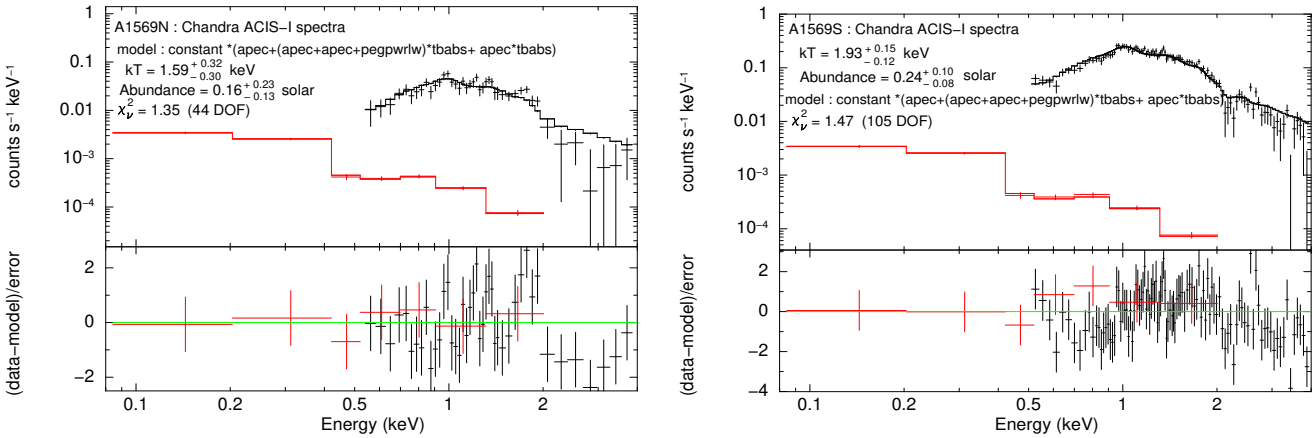

(a) (b)

Figure 5.5: **(a)** Average spectrum of A1569N obtained from the *Chandra* ACIS-I detector. The spectrum was fitted simultaneously with the RASS diffuse background spectrum (shown in *red*) using the model *constant*(apec+(apec+apec+pegpwrlw)*tbabs + apec*tbabs)* in the energy range 0.5–4.0 keV. **(b)** Description same as that in panel (a) but for A1569S. The lower panels in the subplots show the residuals divided by 1σ error bars.

Table 5.2: Best-fitting parameters – subcluster gas temperature (kT), elemental abundance (Z), and *apec* normalization ($\mathcal{N}$) – obtained from the X-ray spectral analysis of the full A1569N and A1569S regions (outlined in *white* circles in Fig.5.1a). The minimum reduced χ^2 statistic along with the degrees of freedom (DOF) is also listed. The *Chandra* global spectra were fitted using the model *constant*(apec+(apec+apec+pegpwrlw)*tbabs + apec*tbabs)*, simultaneously with the RASS diffuse background spectrum. The error bars correspond to 90 per cent confidence intervals based on χ^2_{min}+2.71.

Region	kT (keV)	Z ($Z_\odot$)	apec norm. ($\mathcal{N}$) (10^{-3} cm^{-5})	X-ray Luminosity (L_X) (10^{43} erg s^{-1})	$(\chi^2_\nu)_{\rm min}$ (DOF)
A1569N	$1.6^{+0.3}_{-0.3}$	$0.16^{+0.23}_{-0.13}$	$0.49^{+0.12}_{-0.09}$	0.45 ± 0.04 (0.5−4.0 keV)	1.35(44)
A1569S	$1.9^{+0.2}_{-0.1}$	$0.24^{+0.10}_{-0.08}$	$2.90^{+0.19}_{-0.20}$	2.31 ± 0.06 (0.5−4.0 keV)	1.47(105)

5.4 Azimuthally averaged spectral analysis: radial profiles of gas temperature, electron density, pressure and entropy

2D Projected Profiles

Radial profile of gas temperature was obtained for A1569S by extracting spectra in six annular regions with outer radii 60, 100, 140, 180, 220, and 270 arcsec centred on the X-ray peak mentioned in §5.2.1. The regions are shown in Figure 5.1b. Each of the chosen regions had > 3000 source counts after background subtraction. Details of spectral modelling are the same as for the average spectral analysis (§5.3). The spectral fit was performed in the energy range 0.5–4.0 keV. The gas abundance in each annular region was fixed at the average ICM abundance (0.24 $Z_\odot$) obtained for A1569S (§5.3) since the errors in the abundance value were rather large if it was left free. The best-fitting temperature values are provided in Table 5.3 and the radial temperature profile is shown in Figure 5.6a. Radial profiles of gas electron density, pressure, and entropy were obtained using the procedure described in §3.3.4. The n_H/n_e ratio was derived for an ICM average abundance of 0.24 $Z_\odot$ (§3.3.4) and was found to be equal to 0.835. The derived value of the mean molecular weight (μ) was 0.608. The projected electron density profile of A1569S is shown in Figure 5.6b. The projected pressure and entropy profiles are shown in Figure 5.6c and Figure 5.6d, respectively.

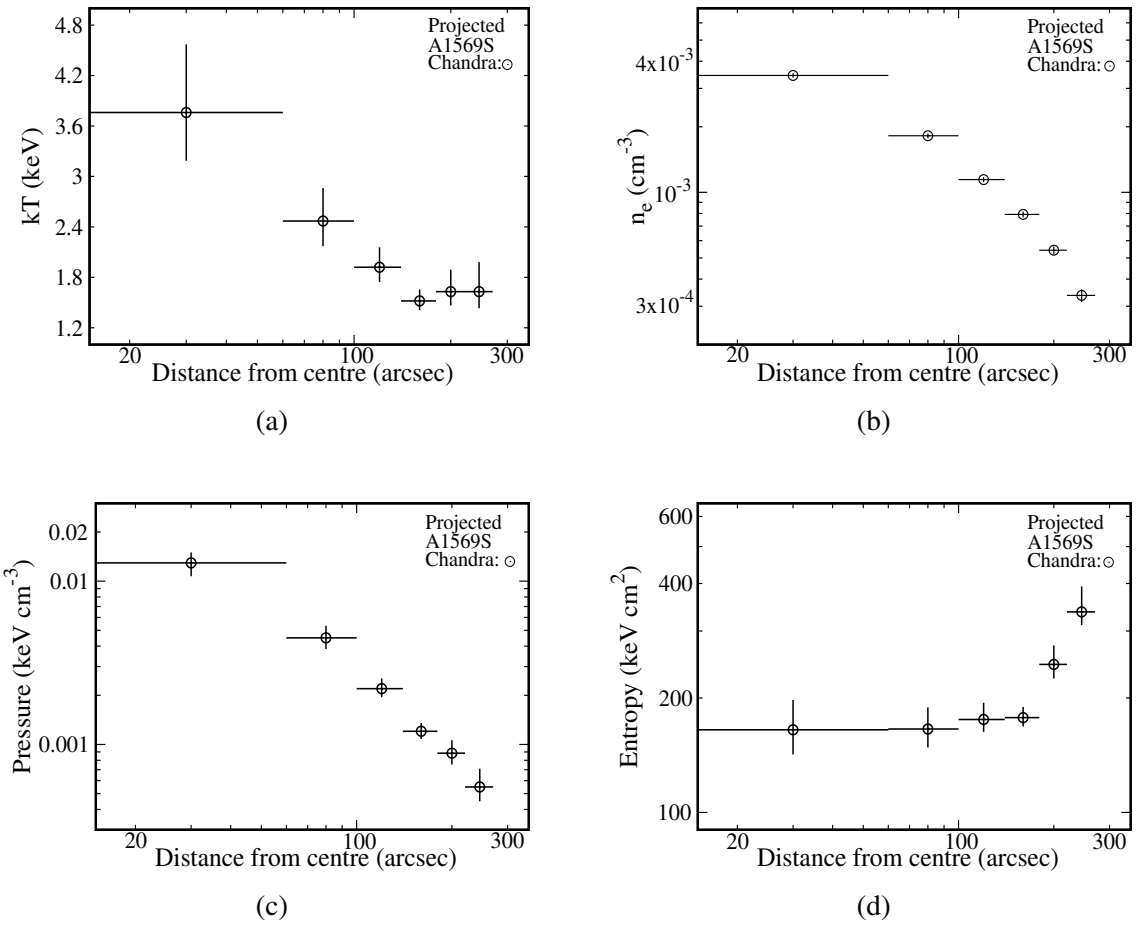

Figure 5.6: Projected temperature (kT), electron density (n_e), pressure, and entropy profiles of A1569S obtained from the azimuthally averaged spectral analysis of *Chandra* data. The abundance value in each annulus was kept frozen to the global abundance value of A1569S (0.24 $Z_\odot$). The error bars correspond to a 90 per cent confidence interval based on χ^2_{min}+2.71.

In order to check for any potential temperature drop towards the central r ∼40 kpc region of A1569S, we additionally performed a projected spectral analysis in two inner radial bins – 0–30 and 30–60 arcsec. The best-fitting temperature value in the inner bin 0–30 arcsec (0–41 kpc) was found to be $6.4^{+5.8}_{-2.1}$ keV corresponding to a derived entropy of 201^{+193}_{-70} keV cm^2. The gas temperature and entropy in the annular bin 30–60 arcsec were found to be $3.0^{+0.7}_{-0.5}$ keV and 144^{+38}_{-27} keV cm^2, respectively. The clear lack of a drop in temperature towards the inner 40 kpc region together with a high central entropy value indicates that A1569S does not possess a large cool core ($\gtrsim$ 40 kpc) associated with the intracluster gas. We note that this analysis was done only to examine the presence of a potential ICM-associated cool core in A1569S. A deprojection analysis (described further in this subsection) including these small inner bins was not workable due to a low number of counts in these regions. For a consistent representation of the projected and deprojected radial profiles of the gas properties of A1569S, we show six

data points (as indicated previously) in Fig. 5.6, with the innermost data point representing the central 0–60 arcsec region.

Table 5.3: Best-fitting temperature and the derived electron density (n_e), pressure (P), and entropy (K) values obtained from the projected spectral analysis of the six annular regions in A1569S (0.5–4.0 keV) (§5.2.1). The regions used for spectral extraction are listed. The *Chandra* spectra were fitted using the model *constant*(apec+(apec+apec+pegpwrlw)*tbabs + apec*tbabs)* and were simultaneously analysed with the RASS diffuse background spectrum. The elemental abundances (Z) in the subcluster were frozen to the average value obtained from the global spectral analysis of A1569S. The errors are quoted at 90 per cent confidence level.

Region	kT (keV)	n_e (10^{-3}cm^{-3})	P (10^{-2} keV cm^{-3})	K (keV cm^2)
0–60 arcsec	$3.8^{+0.8}_{-0.6}$	3.44 ± 0.08	$1.29^{+0.21}_{-0.22}$	165^{+33}_{-23}
60–100 arcsec	$2.5^{+0.4}_{-0.3}$	$1.82^{+0.04}_{-0.05}$	$0.45^{+0.08}_{-0.06}$	166^{+23}_{-18}
100–140 arcsec	$1.9^{+0.2}_{-0.2}$	1.14 ± 0.03	$0.22^{+0.03}_{-0.02}$	176^{+19}_{-13}
140–180 arcsec	$1.5^{+0.1}_{-0.1}$	$0.79^{+0.02}_{-0.03}$	0.12 ± 0.01	178^{+12}_{-9}
180–220 arcsec	$1.6^{+0.3}_{-0.2}$	0.54 ± 0.02	$0.09^{+0.02}_{-0.01}$	245^{+30}_{-20}
220–270 arcsec	$1.6^{+0.4}_{-0.2}$	0.34 ± 0.02	$0.05^{+0.02}_{-0.01}$	337^{+56}_{-26}

We also performed a rather crude spectral analysis in four annular bins of A1569N with outer radii 30, 70, 110, and 160 arcsec centred on the X-ray peak mentioned in §5.2.1 (Fig. 5.1b). The regions were chosen to have a minimum of only 600 background-subtracted counts due to low photon statistics. The gas abundance in each annular region was fixed at the average ICM abundance (0.16 $Z_\odot$) obtained for A1569N (§5.3). The best-fitting temperature values and the derived electron density, pressure, and entropy values are listed in Table 5.4, and the radial profiles are shown in Figure 5.7.

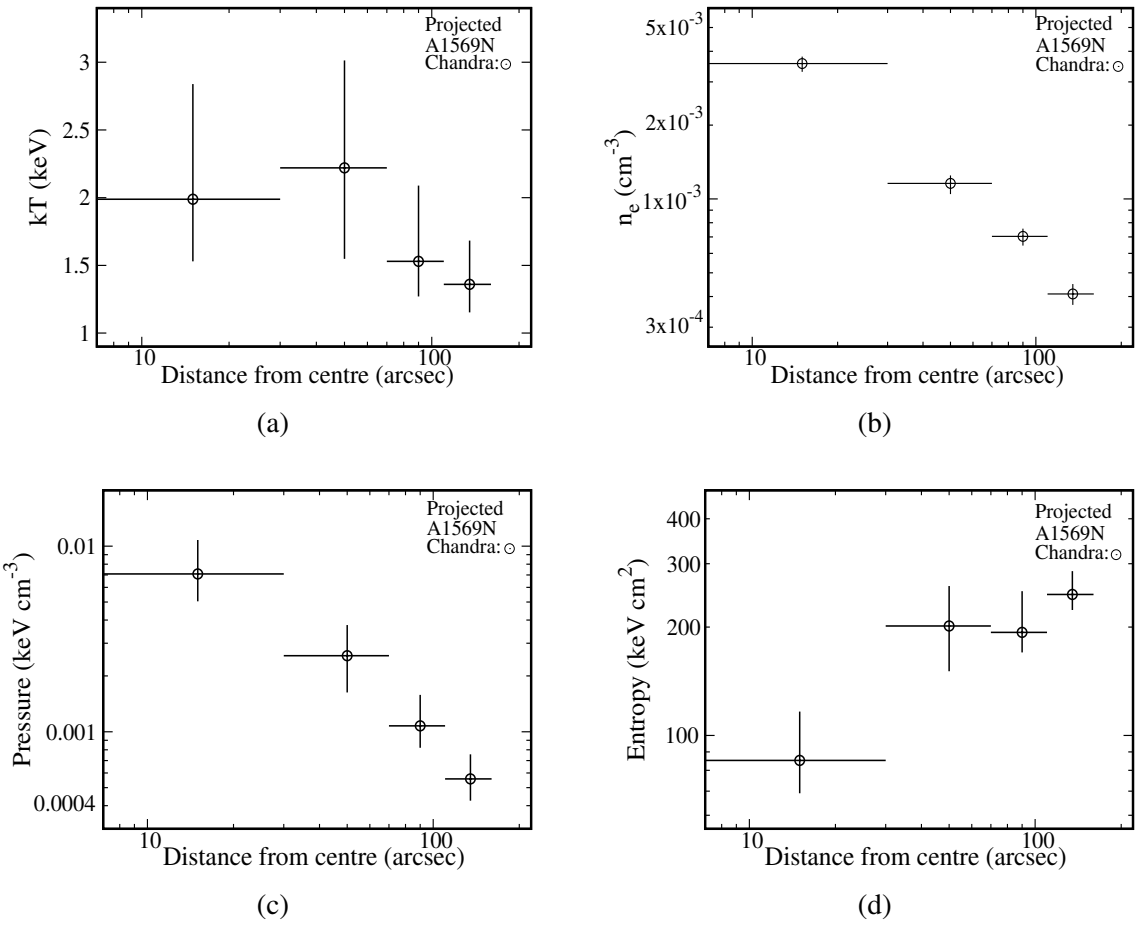

Figure 5.7: Projected temperature (kT), electron density (n_e), pressure, and entropy profiles of A1569N obtained from the azimuthally averaged spectral analysis of *Chandra* data. The abundance value in each annulus was kept frozen to the global abundance value of A1569N (0.16 $Z_\odot$). The error bars correspond to a 90 per cent confidence interval.

Table 5.4: Best-fitting temperature and the derived electron density (n_e), pressure (P), and entropy (K) values obtained from the projected spectral analysis of the four annular regions in A1569N (0.5–4.0 keV) (§5.2.1). The regions used for spectral extraction are listed. The *Chandra* spectra were fitted using the model *constant*(apec+(apec+apec+pegpwrlw)*tbabs + apec*tbabs)* and were simultaneously analysed with the RASS diffuse background spectrum. The cluster abundance (Z) was frozen to the average value obtained from the global spectral analysis of A1569N. The errors are quoted with 90 per cent confidence.

Region	kT (keV)	n_e (10^{-3}cm^{-3})	P (10^{-3} keV cm^{-3})	K (keV cm^2)
0–30 arcsec	$2.0^{+0.9}_{-0.5}$	$3.56^{+0.24}_{-0.27}$	$7.09^{+3.71}_{-2.04}$	85^{+31}_{-16}
30–70 arcsec	$2.2^{+0.8}_{-0.7}$	$1.16^{+0.09}_{-0.11}$	$2.57^{+1.19}_{-0.94}$	201^{+59}_{-51}
70–110 arcsec	$1.5^{+0.6}_{-0.3}$	$0.70^{+0.05}_{-0.06}$	$1.08^{+0.50}_{-0.26}$	193^{+58}_{-23}
110–160 arcsec	$1.4^{+0.3}_{-0.2}$	0.41 ± 0.04	$0.56^{+0.20}_{-0.13}$	246^{+40}_{-23}

Deprojected Profiles

Deprojection analysis on the spectra extracted from the six annular regions of A1569S, shown in Fig.5.1b, was carried out using the same technique as described in §3.3.4. This was done in order to correct for the smoothing of variation in the measured thermodynamic quantities due to projection effects. The energy range 0.5–4.0 keV was used for fitting the data. The cluster abundance value was frozen to 0.24 $Z_\odot$ as before. The best-fitting temperature values and the derived electron density, pressure, and entropy values are listed in Table 5.5. The deprojected profiles of these quantities are shown in Figure 5.8.

Table 5.5: Best-fitting temperature and the derived electron density (n_e), pressure (P), and entropy (K) values obtained from the deprojected spectral analysis of the six annular regions in A1569S (0.5–4.0 keV). The regions used for spectral extraction are listed. The spectra were fitted using the model *apec+(apec+apec+pegpwrlw)*tbabs + projct*(apec*tbabs)*. The XRB model normalizations within each region were fixed to values obtained from the projected spectral analysis, and the cluster abundance (Z) was frozen to the average value obtained from the global spectral analysis of A1569S. The errors are quoted at 90 per cent confidence level.

Region	kT (keV)	n_e (10^{-3}cm^{-3})	P (10^{-2} keV cm^{-3})	K (keV cm^2)
0–60 arcsec	$5.7^{+1.9}_{-1.8}$	2.47 ± 0.11	$1.41^{+0.55}_{-0.50}$	311^{+92}_{-95}
60–100 arcsec	$3.3^{+1.6}_{-0.9}$	1.60 ± 0.09	$0.52^{+0.30}_{-0.16}$	238^{+107}_{-56}
100–140 arcsec	$2.3^{+0.9}_{-0.4}$	1.06 ± 0.07	$0.25^{+0.11}_{-0.06}$	225^{+66}_{-37}
140–180 arcsec	$1.6^{+0.3}_{-0.2}$	0.84 ± 0.06	$0.14^{+0.03}_{-0.02}$	181^{+22}_{-12}
180–220 arcsec	$1.6^{+0.3}_{-0.2}$	$0.63^{+0.05}_{-0.06}$	$0.10^{+0.03}_{-0.02}$	219^{+28}_{-15}
220–270 arcsec	$1.6^{+0.3}_{-0.2}$	0.52 ± 0.03	$0.08^{+0.02}_{-0.01}$	254^{+28}_{-15}

Deprojection was also tried on the four annular spectral bins of A1569N, resulting in $(\chi^2_\nu)_{\rm min}$ = 1.14 (173 DOF). The cluster abundance value was frozen to the average abundance value of A1569N (0.16 $Z_\odot$). The deprojected temperature and electron density in the central 30 arcsec region were found to be $1.82^{+0.66}_{-0.51}$ keV and $3.06^{+0.29}_{-0.33} \times 10^{-3}$ cm^{-3}, respectively. These are not significantly different from the projected temperature and density values. Although the deprojection analysis resulted in a high temperature (5.41 keV) in the second annular bin (30–70 arcsec region where the radio lobes of 1233+169 primarily reside), and an electron density value of $0.86 \pm 0.15 \times 10^{-3}$ cm^{-3}, error limits on the temperature value could not be obtained. For this reason, the deprojected radial profiles of the gas properties of A1569N are not presented, here. The deprojected gas temperature and electron density were found to be $1.62^{+1.20}_{-0.43}$ keV and $0.64^{+0.11}_{-0.13} \times 10^{-3}$ cm^{-3}, respectively for the third annular region (70–110 arcsec), and $1.37^{+0.32}_{-0.17}$ keV and $0.54^{+0.05}_{-0.06} \times 10^{-3}$ cm^{-3} respectively, for the fourth annular bin (110–160 arcsec).

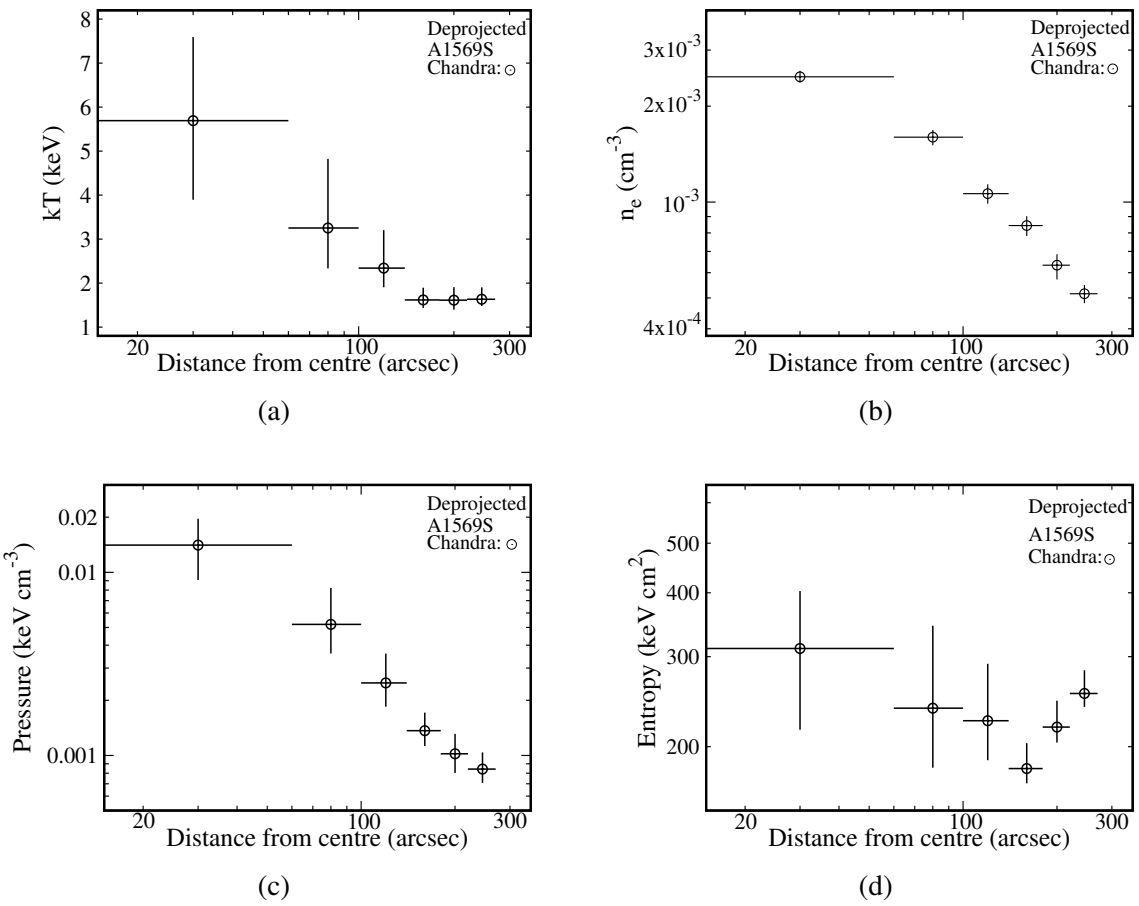

Figure 5.8: Deprojected temperature (kT), electron density (n_e), pressure, and entropy profiles of A1569S obtained from the spectral analysis of *Chandra* data. The abundance value in each annulus was kept frozen to the global abundance value of A1569S (0.24 $Z_\odot$). The error bars correspond to 90 per cent confidence interval.

5.5 Derived physical properties

X-ray Luminosity

The 0.5–4.0 keV luminosities (L_X) of A1569N and A1569S were obtained using the method explained in §3.4 and are listed in Table 5.2.

Gas Mass Estimates

The gas density profiles of A1569N and A1569S obtained in §5.4 were used to estimate the

gas mass of the two subclusters using the procedure described in §3.4. The deprojected electron density profile was used for A1569S, whereas the projected density profile was used for A1569N owing to uncertainty in the reliability of the deprojection analysis in case of A1569N. We obtained the gas mass (M_{gas}) of A1569N and A1569S out to radii 160 arcsec ($\sim$248 kpc) and 270 arcsec ($\sim$370 kpc), respectively, from the corresponding X-ray peaks. The results of the single-β model fitting (β, r_c, and ρ_0) to the gas density profiles along with the gas mass estimates are listed in Table 5.6.

The β values obtained by fitting a single-β model to the electron density profiles of A1569N and A1569S are consistent with those resulting from the 2D-β modelling of the gas surface brightness assuming isotropy (§5.2.2; Table 5.1). The core radius is, however, noticeably different for A1569N in the two cases. This is probably due to the exclusion of the central 15 arcsec region of the galaxy 1233+169 while modelling the 2D surface brightness distribution of the gas in A1569N (§5.2.2), resulting in a large core radius. The electron density profile fitted with a single-β model was, however, derived from the results of the radial spectral analysis of A1569N (§5.4) which included the central 15 arcsec region in the innermost bin.

Table 5.6: Mass of the intra-group gas obtained by fitting single-β models to the gas density profiles of A1569N and A1569S. The errors are quoted at 90 per cent confidence level. Column (1): Subcluster name; Column (2): ratio of the specific energy in galaxies to the specific energy in hot gas; Column (3): projected core radius of the subcluster; Column (4): $\rho_0 = \mu n_e(0) m_p$, where m_p is the mass of proton, μ is the mean molecular weight of the gas, and $n_e(0)$ is the central electron gas density; Column (5): Minimum reduced chi-square statistic and the degrees of freedom; Column (6): Radius within which the gas mass is derived; Column (7): Derived gas mass of the subcluster.

Gas clump	β	r_c (kpc)	ρ_0 (10^4M$_\odot$ kpc^{-3})	$(\chi^2_\nu)_{\rm min}$(DOF)	r (kpc)	$M_{gas}(r)$ (10^{12} M$_\odot$)
(1)	(2)	(3)	(4)	(5)	(6)	(7)
A1569N	$0.34^{+0.03}_{-0.02}$	$15.0^{+0.6}_{-1.4}$	10.3 ± 0.7	1.27 (3)	248	$0.57^{+0.15}_{-0.18}$
A1569S	$0.41^{+0.10}_{-0.07}$	$87.5^{+32.1}_{-26.5}$	$4.2^{+0.5}_{-0.4}$	0.66 (1)	370	$2.3^{+1.8}_{-1.3}$

Total Mass Estimates

Using Equation 3.12, we estimated the total gravitational mass of A1569N within a radius of 248 kpc from the X-ray peak to be $2.0 \pm 1.5 \times 10^{13}$ M$_\odot$. The total mass of A1569S within a

radius of 370 kpc was calculated to be $2.1 \pm 1.6 \times 10^{13}$ $M_{\odot}$. We note that the results of the deprojection spectral analysis were used in the mass calculation of A1569S. In case of A1569N, results of the projection spectral analysis were used owing to uncertainty in the reliability of the deprojection analysis of A1569N. The errors on the mass values correspond to a 90 per cent confidence interval.

Cooling Time Estimates

Using the deprojected temperature and electron density values obtained in §5.4 and Equation 3.13 in §3.4, the cooling time of A1569N in the central 30 arcsec region was found to be $8.6^{+7.2}_{-4.0} \times 10^9$ yr and that of A1569S in the central 60 arcsec region was estimated to be $6.6^{+4.4}_{-3.2} \times 10^{10}$ yr. These values are comparable to/greater than the Hubble time ($\sim$14.5 $\times 10^9$ yr in our cosmology). We note that due to the low number of counts in the observation, these estimates are averages over fairly large central regions. Nonetheless, these large cooling time estimates provide support to the observed lack of drop in gas temperature in the central $\sim$40–50 kpc subcluster regions (§5.4; Fig.5.6a, Fig.5.7a, 5.8a), thus, confirming that large cool cores associated with the intracluster gas are absent in both A1569N and A1569S.

5.6 Radio galaxies and the surrounding gas

5.6.1 Galaxy 1233+169 in A1569N

The apparent gas substructure (Fig. 5.2b) and evident gas deficits (§5.2.3) in A1569N coincident with the extended features of 1233+169, suggest the presence of an ongoing interaction between the radio galaxy 1233+169 and the surrounding ICM. These gas deficient regions appear to be cavities created in the ICM of A1569N by the radio lobes of 1233+169. Approximating the shape of these supposed cavities as spheres (circular regions marked in *green* color in Fig. 5.4b), we estimated the time-averaged mechanical power output of the radio jet creating the cavities. We note that this is a rather crude estimate, since due to limited photon statistics of the X-ray observation, it is not possible to determine the exact shapes of the cavity pair. None the less, it gives an idea about the role that the central radio source can play in affecting the energetics of the surrounding ICM in A1569N. Using the standard procedure adopted in literature (Bîrzan et al., 2004), the total energy associated with a single X-ray cavity (E_{cav}) was calculated as the sum of the work done by the radio jet against the surrounding gas at pressure

P to inflate the cavity with volume V and the internal energy of the fluid within the cavity.

$$E_{cav} = PV + \frac{PV}{\gamma - 1}; \;\; \gamma = C_P/C_V \text{ (ratio of the specific heats)} \tag{5.1}$$

Assuming that the cavity is filled with relativistic fluid ($\gamma = 4/3$), Equation 5.1 translates to:

$$E_{cav} = 4PV \tag{5.2}$$

We derived the surrounding thermal gas pressure (P) at the location of the cavities (midpoint located at ∼43.5 arcsec (67.4 kpc) from the cluster centre) by performing azimuthally averaged spectral analysis within an annulus (inner radius 27 arcsec and outer radius 65 arcsec from the cluster centre) encompassing the two cavities. This resulted in a projected pressure value of 4.23×10^{-12} erg cm^{-3}. The resulting cavity energy values along with the properties of the cavities are given in Table 5.7.

The time-averaged mechanical power associated with each cavity (P_{cav}) was calculated by dividing E_{cav} by the approximate age of the cavity. The latter was calculated by assuming that the cavity bubble has risen from the centre of the cluster to its current radius R at a terminal velocity $v \sim \sqrt{2gV/SC}$, thus giving a buoyancy timescale of $t_{buoy} \sim R\sqrt{SC/2gV}$, where, S is the cross-sectional area of the cavity bubble, V is its volume, R is the distance of the bubble from the cluster nucleus, g is the gravitational acceleration at the location of the cavity, and C is the drag coefficient (taken to be equal to 0.75; Churazov et al., 2001). In order to estimate g at the cavity location, we derived the total gravitational mass enclosed within a sphere of radius 43.5 arcsec from the cluster centre (the midpoint of the cavities) to be 5.2×10^{12} M$_\odot$. This implies a gravitational acceleration of $\sim 1.6 \times 10^{-10}$ m s^{-2} (using $g = GM_{(<R)}/R^2$). The resulting buoyancy timescales and mechanical power associated with the two cavities are listed in Table 5.7. The total mechanical power of the two cavities is $\sim 2.1 \times 10^{43}$ erg s^{-1}. The $0.4 - 8.0$ keV X-ray luminosity of the ICM in A1569N measured within a radius of 65 arcsec (radius within which the extended radio features of 1233+169 and the cavities are seen) from the centre is $2.2 \pm 0.2 \times 10^{42}$ erg s^{-1}. The total mechanical power associated with the cavities is an order of magnitude larger than the observed X-ray luminosity in the central region of A1569N. This indicates that the radio galaxy 1233+169 can have a substantial impact on the energetics of the ICM in the core of A1569N. We note that the circular regions chosen as cavities are based entirely on visual inspection. The errors on the cavity volume estimates can, therefore, be large due to smoothing and projection effects. In order to check how the errors in gas pressure and cavity volume affect the cavity energetics, we recalculated the total power associated with the cavity pair by assuming an upper cap of 50 per cent error in the cavity radii and 40 per cent error in the surrounding gas pressure (the actual relative error in gas pressure). The estimated total cavity power is still larger than the X-ray radiative loss by a factor of 2,

indicating that accounting for errors does not significantly change the effect that the cavities have on the surrounding gas.

Table 5.7: Physical properties and energetics of the two cavities carved out by 1233+169 in the ICM of A1569N.

Cavity parameters	Eastern cavity	Western Cavity
Radius (kpc)	28	21
Volume (V) (m^3)	2.7×10^{63}	1.1×10^{63}
E_{cav} (erg)	4.5×10^{58}	1.9×10^{58}
Distance from centre (R) (kpc)	67.4	67.4
t_{buoy} (yr)	0.95×10^{8}	1.1×10^{8}
P_{cav} (erg s^{-1})	1.5×10^{43}	0.56×10^{43}

We also compared the energetics of 1233+169 with the jet (cavity) power – radio power ($P_{cav} - -L_{radio}$) relation obtained by O'Sullivan et al. (2011) for a sample of galaxy groups and clusters harbouring radio sources, as shown in Figure 5.9. The radio power used in this relation is the integrated 10 MHz–10 GHz power of the radio source. We calculated the total radio luminosity of 1233+169 by integrating the flux density between $\nu_1 = 10$ MHz and $\nu_2 = 10$ GHz using Equation 3.14. A luminosity distance (D_L) of 371.6 Mpc, and 1.48 GHz flux density (S_{ν_0}) of 620 mJy obtained from the VLA data was used. This resulted in $L_{radio} = 1.42 \times 10^{42}$ erg s^{-1}. The derived P_{cav} and L_{radio} values place 1233+169 well within the scatter observed in the $P_{cav} - L_{radio}$ plot of O'Sullivan et al. (2011) (Fig. 5.9), indicating that the radio source contains adequate mechanical energy to create cavities in the ICM of A1569N.

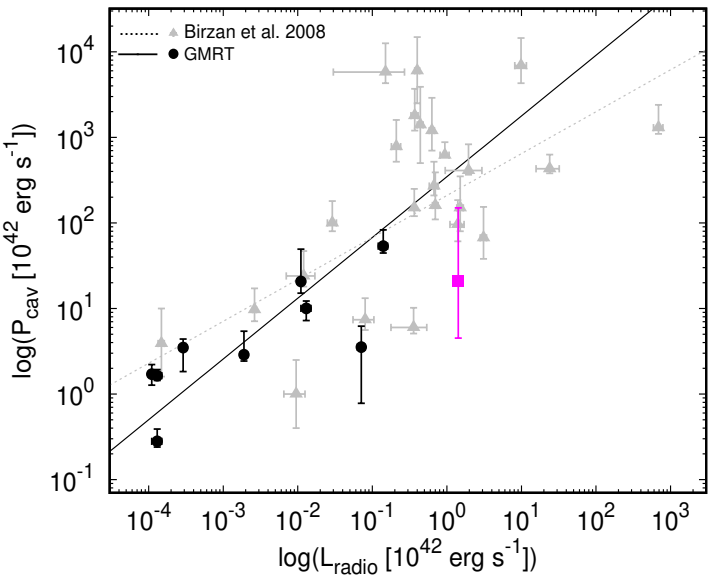

Figure 5.9: Cavity power vs. integrated 10 MHz−10 GHz radio power relation plot reproduced from O'Sullivan et al. (2011). The *solid black* line indicates the fit to all the data points. The *dotted grey* line indicates the relation found by Bîrzan et al. (2008). The *filled box* symbol in *magenta* color represents the A1569N cavity system energetics.

5.6.2 A subcluster–cluster merger in A1569S?

The gas distribution in A1569S clearly deviates from azimuthal symmetry and appears to be elongated in the central ∼70 kpc region (Fig. 5.2e). The direction of the observed X-ray elongation is along the line that bisects the radio tails of 1233+168. A1569S clearly lacks a large cool core as indicated by the spectral analysis presented in §5.4. The presence of central X-ray substructure, elongation of cluster gas distribution in the vicinity of extended radio galaxies, and absence of a cool core are often considered as common indicators of mergers in galaxy clusters (Pinkney et al., 1993; Burns et al., 1994, 1996; Roettiger et al., 1996; Gómez et al., 1997b).

Based on the above mentioned observational facts, we performed a systematic search for discontinuities in the surface brightness distribution of the intracluster medium of A1569S that could be indicative of any previous merger activity in the cluster. The python package *Pyproffit*[1] (version 0.6.0) was used for this purpose (Eckert et al., 2020). A point-source-subtracted image of the cluster (0.5–4.0 keV energy range), an exposure map, and a scaled background image were supplied to *Pyproffit*. Surface brightness profiles centred at R.A. (J2000) = $12^h36^m25^s.86$

[1] https://github.com/domeckert/pyproffit

and Dec. (J2000) = +16°32′19″.94 were initially extracted in the eastern and western directions corresponding to sectors 90–270° and 270–450° (angles measured anticlockwise with respect to the horizontal), respectively. The azimuthal span of the sectors was then gradually decreased until a surface brightness discontinuity started to become visible in the eastern sector spanning 110–250°. No evident signs of discontinuities were noticed in the western direction. The discontinuity in the eastern direction was best visible in the sector 145–237° which is highlighted in *magenta* color in Figure 5.10a. The surface brightness profile along this sector is shown in Figure 5.10b where a discontinuity is apparent at ∼1 arcmin. This is consistent with the abrupt drop in the surface brightness noticed across the *yellow* arc shown in Fig. 5.10a.

In order to check if the observed surface brightness discontinuity corresponds to a gas density jump in the ICM of A1569S, we fitted a broken power-law 3D density model projected along the line of sight to the 2D surface brightness profile extracted in the eastern sector 145–237°, in the vicinity of the observed discontinuity. The broken power-law 3D density model (*BknPow* in *Pyproffit*) is described as:

$$\begin{aligned} n(r) &= n_0 \left(\frac{r}{r_{jump}}\right)^{-\alpha_1} \quad \text{for } r < r_{jump} \\ n(r) &= \frac{1}{C} n_0 \left(\frac{r}{r_{jump}}\right)^{-\alpha_2} \quad \text{for } r \geq r_{jump} \end{aligned} \tag{5.3}$$

where α_1 and α_2 are the power-law indices, n_0 is the normalization factor, r is the radius from the centre of the sector, r_{jump} is the radius at which the density jump is observed, and C is the density compression factor or the magnitude of the density jump. A detailed description of the 2D surface brightness projection of the broken power-law 3D density model is given in the Appendix of Owers et al. (2009). The radial range was restricted to 0.01–1.7 arcmin for fitting the broken power-law density model since the density profile beyond the apparent surface brightness edge could be approximated by a power-law only till ∼1.7 arcmin. A radial bin size of 3 arcsec was used. Initially, all parameters were left free during the fit. A background value of 1.18×10^{-5} cts s^{-1} arcmin^{-2} was obtained. The model was fitted again with the background fixed to this value, which did not cause the other model parameters to change. A $(\chi^2_\nu)_{\text{min}}$ value of 0.51 was obtained for 54 DOF. The best–fitting model is shown in Figure 5.10c,d and its parameters are listed in Table 5.8. The surface brightness edge is located at 1.01 arcmin and corresponds to a gas density jump of 2.3 ± 0.6.

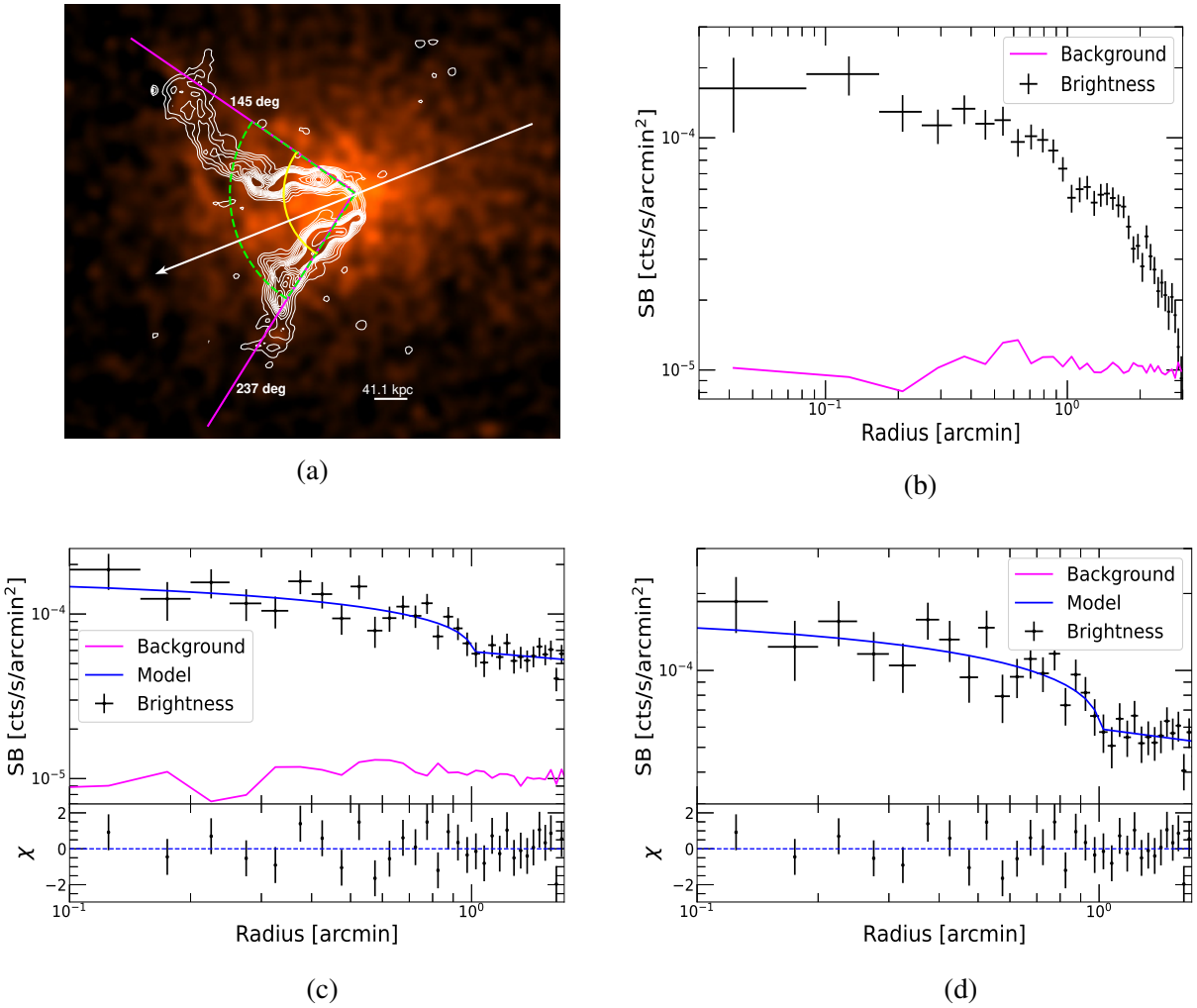

Figure 5.10: **(a)** The point-source subtracted, particle-background-subtracted, and exposure-corrected image of the central region of A1569S in the energy range 0.5–4.0 keV. The extended radio features of 1233+168 are shown in *white* color. The *solid white* line bisects the angle between the bent radio tails of 1233+168 which is the direction along which local X-ray gas elongation is observed. The 145–237° eastern wedge used for extracting the X-ray surface brightness profile is highlighted using *solid magenta* lines. The *solid yellow* arc marks the position of the surface brightness edge at 1 arcmin. The sector highlighted in *dotted green* is used for fitting the broken power-law 3D density model. **(b)** The 0.5–4.0 keV X-ray surface brightness profile extracted in the eastern sector 145–237°. An edge is apparent at ∼1 arcmin. **(c)** The best-fitting broken power-law density model (*blue*) fitted in the radial range 0.01–1.7 arcmin to the X-ray surface brightness profile extracted in the sector 145–237°. **(d)** Same as (c) except that the background has been removed from the figure for better representation.

Table 5.8: Best–fitting parameters of the broken power-law 3D density model fitted to the X-ray surface brightness profile of A1569S extracted in the sector 145–237°. The errors are quoted at 68 per cent (1σ) confidence level.

α_1	α_2	r_{jump} (arcmin)	SB Normalization (10^{-5} cts s^{-1} arcmin^{-2})	C (density jump magnitude)
0.29 ± 0.15	0.62 ± 0.12	1.01 ± 0.07	5.49 ± 1.32	2.3 ± 0.6

In order to assess the nature of this density discontinuity, we performed a projected spectral analysis along the sector 145–237° in four radial bins ranging 0–60.6, 60.6–110, 110-180, and 180-270 arcsec. Each of these regions was chosen to have a minimum of 800 counts. The best-fitting temperature, and the derived electron pressure and density values obtained for each region are provided in Table 5.9, and the profiles shown in Figure 5.11. A deprojection analysis was also attempted but the errors on the model parameters could not be constrained due to low number statistics.

Table 5.9: Best-fitting temperature (kT) and the derived electron density (n_e), and pressure (P) values obtained from the projected spectral analysis performed along the eastern sector 145–237° in A1569S. The regions used for spectral extraction are listed. The errors are quoted at 90 per cent confidence level.

Region	kT (keV)	n_e (10^{-3} cm^{-3})	P (10^{-2} keV cm^{-3})
0–60.6 arcsec	$3.3^{+1.5}_{-0.9}$	$3.91^{+0.18}_{-0.17}$	$1.30^{+0.69}_{-0.38}$
60.6–110 arcsec	$2.6^{+0.7}_{-0.5}$	1.96 ± 0.08	$0.51^{+0.16}_{-0.11}$
110–180 arcsec	$1.8^{+0.4}_{-0.2}$	$1.04^{+0.03}_{-0.04}$	$0.19^{+0.05}_{-0.03}$
180–270 arcsec	$1.4^{+0.3}_{-0.2}$	0.43 ± 0.03	$0.06^{+0.02}_{-0.01}$

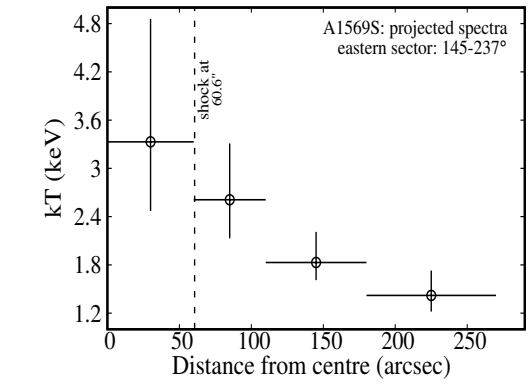

(a)

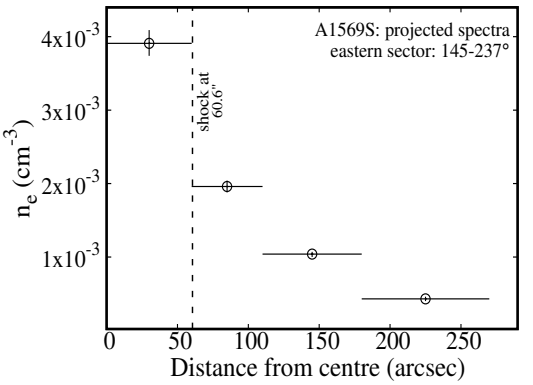

(b)

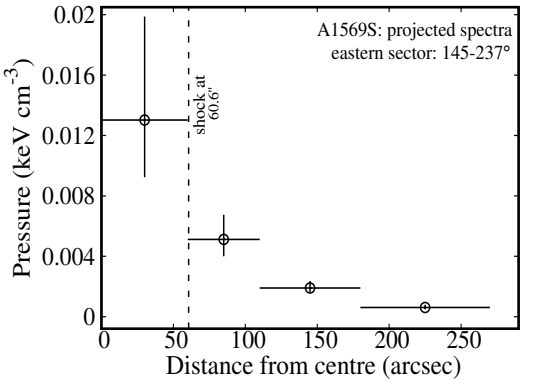

(c)

Figure 5.11: **(a)** Gas temperature (kT), **(b)** electron density (n_e), **(c)** pressure profiles obtained as a result of the projected spectral analysis performed in four radial bins along the eastern sector 145–237° in A1569S. The *dashed* vertical line at 60.6 arcsec marks the position of the putative shock.

It can be seen in Figure 5.11a that the gas temperature inside (0–60.6 arcsec region) the surface brightness edge (located at 1.01 arcmin) is indicated to be slightly higher ($\sim 3.3^{+1.5}_{-0.9}$

keV) than the gas temperature outside the edge (60.6–110 arcsec region; $2.6^{+0.7}_{-0.5}$ keV), although the errors are large. Across the edge, the gas density jump derived from the spectral analysis is however, very significant with a value of 2.0 ± 0.2 (Figure 5.11b). This is consistent with the value obtained by fitting the surface brightness profile with the broken power-law density model (2.3 ± 0.6). The gas pressure across the edge drops by a factor of $2.5^{+2.4}_{-1.2}$ (Figure 5.11c). The gas density jump observed at 1.01 arcmin, along with an indication of a drop in both the gas temperature and pressure across it, is indicative of the presence of a shock front at this location (*yellow* arc in Figure 5.10a). Additionally, we also checked for the presence of substructures resulting from any sloshing motions of the gas (e.g., spiral patterns) in the 2D-β model subtracted image of A1569S. We did not find evidence of any such structures in the residual image, thus, supporting the argument that the observed edge is indeed a shock and not a cold front. The shock is plausibly the result of a merger between A1569S and a subcluster that has fallen in from the west along the direction indicated by the *white* arrow line shown in Figure 5.10a, which is likely responsible for the local X-ray gas elongation observed in the inner region of A1569S. Under this scenario, the region 0–60.6 arcsec in the sector 145-237° is already affected by passage of the shock (post-shock) and the region 60.6–110 arcsec is yet to experience it (pre-shock). We note that the choice of the radial size of these regions is influenced by the photon statistics, and a deeper X-ray observation of A1569S will be immensely helpful in better constraining the thermodynamic properties of the gas across the discontinuity. Several other studies (Owers et al. (2009); Bourdin et al. (2013); Ubertosi et al. (2021) to name a few) have performed a similar analysis in relatively large (> 70 kpc) spectral bins to confirm whether a discontinuity is a potential shock or a cold front.

The Mach number of the shock (M) was calculated from the gas pressure (P) and density (n) values obtained spectrally in the post-shock (0–60.6 arcsec) and pre-shock (60.6–110 arcsec) regions using the following equations:

$$\frac{P_{post}}{P_{pre}} = \frac{10M^2 - 2}{8} \tag{5.4}$$

resulting in $M = 1.5^{+0.6}_{-0.3}$, and

$$\frac{n_{post}}{n_{pre}} = \frac{4M^2}{3 + M^2} = C \tag{5.5}$$

resulting in $M = 1.7^{+0.2}_{-0.1}$.

The gas was assumed to be monoatomic with an adiabatic index $\gamma = 5/3$ in these calculations. The shock Mach number was not estimated from the gas temperature jump due to the large uncertainty in the temperature values. Using equation (5.5) and a density jump $C = 2.3 \pm 0.6$ obtained from fitting the surface brightness profile with a broken power-law density model, we estimated $M = 2.0^{+0.8}_{-0.5}$.

The shock Mach number was then used to calculate the shock velocity (v) using

$$M = \frac{v}{c_s} \tag{5.6}$$

where c_s is the speed of sound in a gas of temperature 2.61 keV (temperature of the pre-shock region), which was calculated using,

$$c_s = \sqrt{\frac{\gamma kT}{\mu m_p}} \tag{5.7}$$

Using $M = 1.7$ (this value, estimated using the spectrally derived gas density jump, was chosen because it has the tightest constraints), $\gamma = 5/3$, $\mu = 0.608$, and $m_p = 1.67 \times 10^{-27}$ kg, we estimated $c_s = 831.7$ km s^{-1} for a 2.61 keV gas, and a shock velocity $v = 1413.9$ km s^{-1}.

5.7 Discussion and conclusions

The imaging analysis of the *Chandra* X-ray data (§5.2) shows clear presence of two gas clumps in A1569 (Fig. 5.1a) as noticed earlier in the *ROSAT* PSPC image of the cluster by Gomez et al. (1997a). The northern clump – A1569N – is smaller (radial extent ∼248 kpc), and appears to be extended in the NW-SE direction (Fig. 5.1a) which is confirmed by the 2D-β modelling of its gas surface brightness presented in §5.2.2 (Table 5.1). The southern gas clump – A1569S – is larger (radial extent ∼370 kpc) (Fig. 5.1a) and is elongated in the E-W direction with an ellipticity of 0.27 ± 0.02 (§5.2.2; Table 5.1) consistent with the value obtained by Gómez et al. (1997b). A global spectral analysis of A1569N results in a gas temperature of $1.6^{+0.3}_{-0.3}$ keV and an average elemental abundance of $0.16^{+0.23}_{-0.13}$ Z$_\odot$ (Table 5.2). The spectral analysis of A1569N has been performed for the first time in this study. We find that the gas in A1569S has an average temperature of $1.9^{+0.2}_{-0.1}$ keV which is in agreement with the *ROSAT* result of Gómez

et al. (1997b) but has much tighter constraints. The average abundance of metals in A1569S is $0.24^{+0.10}_{-0.08}$ $Z_{\odot}$ and is reported for the first time here. The X-ray luminosity of A1569N is $4.5 \pm 0.4 \times 10^{42}$ erg s^{-1} (0.5–4.0 keV) while that of A1569S is $2.31 \pm 0.06 \times 10^{43}$ erg s^{-1} (0.5–4.0 keV), making it ∼five times more luminous than A1569N. The temperature and luminosity values obtained for the two gas clumps are representative of groups of galaxies (Bahcall, 1999; Helsdon & Ponman, 2000a; Rasmussen & Ponman, 2007; Lovisari et al., 2015; Zou et al., 2016). The derived gas mass (§5.5) of A1569N within a radius of 248 kpc is $5.7^{+1.5}_{-1.8} \times 10^{11}$ $M_{\odot}$ and that of A1569S (within 370 kpc) is $2.3^{+1.8}_{-1.3} \times 10^{12}$ $M_{\odot}$ (Table 5.6). The total gravitational mass of A1569N within a radius of 248 kpc is $2.0 \pm 1.5 \times 10^{13}$ $M_{\odot}$ and that of A1569S within a radius of 370 kpc is $2.1 \pm 1.6 \times 10^{13}$ $M_{\odot}$ (§5.5). These values are also typical of galaxy groups (Mulchaey, 2000; Lovisari et al., 2015) in contrast to galaxy clusters which have a greater extent and possess higher mass, temperature and luminosity (Böhringer et al., 2002; Reiprich & Böhringer, 2002; Sanderson et al., 2006).

A pair of X-ray cavities has been discovered within the central ∼100 kpc (∼65 arcsec radius) region of A1569N, consistent with a clear deviation found in the X-ray isophotes from azimuthal symmetry in the same region of A1569N (Fig. 5.1a, c). The presence of the cavity pair is confirmed by the unsharp-masked image (Fig. 5.4a) and the elliptical 2D-β model subtracted residual image (Fig. 5.4b) presented in §5.2.3. These X-ray cavities are very likely to have been excavated in the ICM by the displacement of hot gas by the radio lobes of the central elliptical galaxy 1233+169, as indicated by the spatial coincidence of the X-ray deficits with the presence of radio emission from 1233+169 (Fig. 5.2b). The eastern and western deficits have about 3σ and 2.5σ significance, respectively. Calculation of the energetics of the cavities (§5.6.1) shows that the total mechanical power associated with the cavity pair is $\sim 2.1 \times 10^{43}$erg s^{-1}, which is an order of magnitude larger than the X-ray luminosity of ($2.2 \pm 0.2 \times 10^{42}$ erg s^{-1}) observed in the central region of A1569N. These values indicate that the radio galaxy 1233+169 can play a significant role in affecting the properties of the intragroup gas in A1569N.

We find evidence for heating of the intragroup gas in A1569N by the central radio source 1233+169. This is apparent from the temperature and entropy rise observed in the second annular spectral bin (30-70 arcsec) where the radio lobes of 1233+169 lie (Fig.5.7a, d) and also from the location of A1569N with respect to the $L_X - T_X$ relation obtained for a sample of 13 radio-quiet galaxy groups by Croston et al. (2005) (top right panel of fig. 2 of their paper) as displayed in Figure 5.12. For a sample of 30 $ROSAT$-observed galaxy groups, Croston et al. (2005) obtained the X-ray luminosity (0.1–2.4 keV) and temperature by performing a spectral analysis within a circular region of radius r_{cut}, which is the extent up to which X-ray emission from the group was detected. Galaxy groups were classified as radio-loud and radio-

quiet based on a radio-luminosity cutoff value ($L_{1.4\,GHz} = c1 = 1.2 \times 10^{21}$ W Hz^{-1} used in Fig. 5.12). The authors found that the radio-loud groups are likely to be hotter at a given X-ray luminosity than the radio-quiet groups. They tested different models and attributed the observed effect to the heating of the host group gas by the central radio source. The location of A1569N, a radio-loud group, clearly on the hotter side of the radio-quiet relation (*black* line) in Fig. 5.12 indicates that the central radio source 1233+169 is responsible for heating the gas in A1569N. Analogous results suggesting that radio-loud groups are likely to have a higher temperature than radio-quiet groups of the same luminosity have been reported by Croston et al. (2008) in an *XMM-Newton* study of galaxy groups hosting low-power radio galaxies. Another similar study by Magliocchetti & Brüggen (2007) finds that the $L_X - T_X$ relation steepens for low-temperature clusters ($\lesssim$ 3 keV) hosting central radio objects with extended jets and/or lobe structures, and attribute this effect to overheating of the intracluster gas, likely caused by the interplay between the extended radio structures and the intracluster medium. There is a marginal indication that the gas temperature in A1569N is on the higher side of the correlation shown (Fig. 5.12), pointing towards the possibility of some heating by the central radio source.

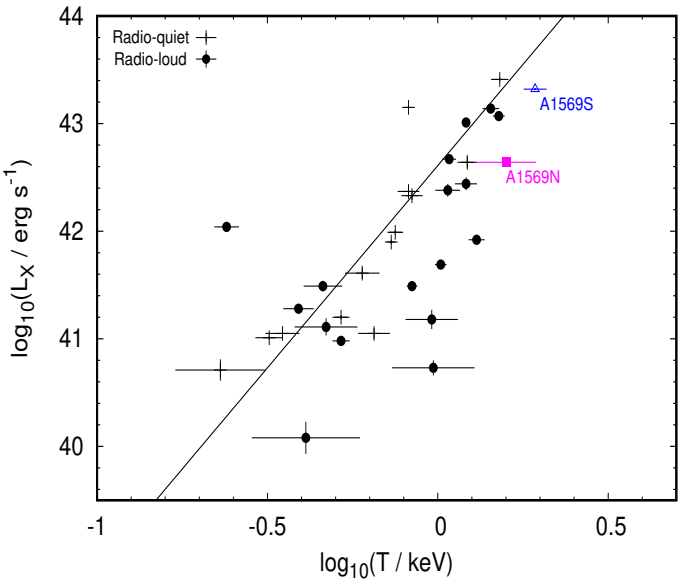

Figure 5.12: $L_X - T_X$ plot for a sample of radio-loud (*filled circles*) and radio-quiet (*plus* symbols) groups adopted from Croston et al. (2005). The overplotted *black* line is the best-fitting radio-quiet relation. The *filled magenta box* and *filled blue triangle* symbols represent A1569N and A1569S, respectively. There is a clear tendency for radio-loud groups to be on the hotter side of the radio-quiet relation.

The lack of signatures of large-scale ($\gtrsim$ 46 kpc) cooling in the central region of A1569N

further corroborates the radio-source heating proposition. The projected spectral analysis presented in §5.4 does not show a central drop in temperature (Fig. 5.7a) or a sharply peaked electron density profile (Fig. 5.7b). Low temperature in the central region of A1569N is not observed even after taking projection effects into account. A single $\beta-$model fit to the projected electron density radial profile of A1569N gives a central density value of $6.85 \pm 0.44 \times 10^{-3}$ cm^{-3} unlike the high densities found in the central regions of cool-core galaxy groups/clusters. Absence of observed cooling is also supported by a cooling time of $8.6^{+7.2}_{-4.0}$ Gyr within the central 46.5 kpc (30 arcsec) region of A1569N which is comparable to the Hubble time (§5.5). Radiative losses from the thermal ICM are believed to be balanced by feedback from the central radio source in massive galaxy clusters. This picture has not been explored as much in the case of galaxy groups. However, due to shallower gravitational potential of galaxy groups, and hence, lower binding energy per particle, the same non-gravitational heating energy (supplied by the central radio source) per particle has a greater effect in groups than clusters (McNamara & Nulsen, 2007; Gitti et al., 2012). Sun (2012b) report that almost all galaxy groups with a large-scale cool core do not host a central radio source. For groups which have a cool core along with a central radio source, the cool core is a coronal cool core corresponding to that of the central galaxy and not the group. Best et al. (2007) point out that radio-heating probably overcompensates the radiative cooling losses in groups of galaxies. The increased importance of overheating of the intracluster gas by central radio sources in low-mass clusters (kT $\lesssim$ 3 keV) has also been highlighted by Magliocchetti & Brüggen (2007). Jetha et al. (2007) suggest that energy injection from central radio sources is sufficient to balance cooling in the core of the galaxy groups. Based on the facts that the lobes of 1233+169 are confined to the very central region of A1569N and that the jet power is an order of magnitude larger than the X-ray radiative loss in the region, together with evidence for heating of the intragroup gas highlighted previously, we attribute the lack of a large, ICM-associated cool core in A1569N likely to cavity heating caused by 1233+169. A1569N may, however, possess a small-scale (r $\sim$few kpc) coronal cool core associated with the central BCG. This is indicated by the two-dimensional image fitting of A1569N presented in §5.2.2, where a single 2D-β model could well describe the cluster emission, only if the central 15 arcsec ($\sim$23 kpc) region corresponding to the central galaxy was excluded from the modelling. We note that it has not been possible to confirm the presence of a coronal cool core in A1569N in this work via a spectral analysis in smaller radial bins within the central 30 arcsec ($<$ 46 kpc) region or through double-β image modelling due to a low number of counts.

The gas distribution within the southern subcluster, A1569S, is not azimuthally symmetric (Fig. 5.1a). Local elongation of the intracluster gas is observed in between the radio tails of the central source 1233+168 (Fig. 5.2e). These properties are typical of dynamically disturbed systems which have undergone mergers or are in the process of formation (Burns et al., 1996;

Roettiger et al., 1996; Schuecker et al., 2001b; Sarazin, 2002). We detect an X-ray surface brightness discontinuity at 1.01 arcmin ($\sim$83 kpc) to the east (sector spanning 145–237°) from the subcluster centre (Fig. 5.10b). The discontinuity corresponds to a gas density jump of 2.3 ± 0.6 (Table 5.8, Fig. 5.10c, d) and lies perpendicular to the line bisecting the angle between the radio tails of 1233+168 (Fig. 5.10a). Projected spectral analysis carried out along the eastern sector containing the SB edge indicates a drop in both the gas temperature and pressure across the discontinuity, indicative of the presence of a shock in the subcluster (§5.6.2; Fig. 5.11). The observed pressure drop across the edge is $2.5^{+2.4}_{-1.2}$ and the estimated shock Mach value is $\sim$1.7, suggesting that the putative shock is a weak shock resulting from a small-scale merger between A1569S and another subcluster. The proposed merger scenario is also supported by the absence of a cool core in A1569S as indicated by the spectral analysis presented in §5.4, and a cooling time of $6.6^{+4.4}_{-3.2} \times 10^{10}$ yr within the central 60 arcsec ($\sim$82 kpc) region of A1569S (§5.5), since merger activity in galaxy clusters tends to disrupt and inhibit the formation of cool cores (Ritchie & Thomas, 2002; ZuHone, 2011), particularly if the merger takes place in the early evolutionary stage of the cluster (Burns et al., 2008; Henning et al., 2009). Shocks associated with mergers increase the entropy of the gas (Markevitch et al., 1996; Sarazin, 2004). Merger activity can disperse the low-entropy gas in the cluster centre and mix it with the high-entropy ICM at larger radii, which leads to high central entropy and flattening of the entropy profile in the inner regions of galaxy clusters (Planelles & Quilis, 2009; ZuHone, 2011). The entropy profile of A1569S is flat (Fig. 5.6d) that is consistent with the absence of a large-scale ($\gtrsim$ 40 kpc) cool core. Deprojection spectral analysis shows high entropy (311^{+92}_{-95} keV cm^2) in the central 60 arcsec ($\sim$82 kpc) region of A1569S (Fig. 5.8d), lending further support for the merger scenario. Similar high central entropy values ($\gtrsim$300 keV cm^2) have been found in other low surface brightness clusters undergoing mergers (e.g., Abell 1631 – Babazaki et al. (2018); Abell 2399 – Mitsuishi et al. (2018)).

Relative motions between extended radio galaxies and the dense host ICM, result in significant ram pressure on the radio-emitting material of the jets, which leads to the observed jet bending. Gomez et al. (1997a) estimated $400 - 2500$ km s^{-1} as the range of relative velocities of radio sources with respect to the ICM that is responsible for the observed WAT radio morphology. The central WAT source 1233+168 in A1569S, however, has a peculiar velocity of 215 km s^{-1} with respect to the subcluster dynamical centre. This velocity is insufficient to account for the bending of the jets (Gomez et al., 1997a). The relative motion between the radio galaxy and the host ICM required for ram pressure exertion can very well arise from the gas itself moving across the galaxy. Simulations show that bulk flow motions of gas with high velocities of $\gtrsim$1000 km s^{-1} are generated in cluster mergers (Roettiger et al., 1993; Loken et al., 1995; Roettiger et al., 1996). Within the central regions of galaxy clusters ($r \sim$200 kpc), these motions may remain above 1000 km s^{-1} for timescales of $\sim$2 Gyr which are much

longer than the typical lifetimes of radio galaxies ($\sim 10^7 - 10^8$ yr) (Loken et al., 1995; Roettiger et al., 1996). This bulk flow of the ICM (relative to the central extended radio galaxy) arising in cluster mergers has been invoked as the primary reason for the observed bending of central WAT sources (Burns et al., 1994; Pinkney et al., 1994; Loken et al., 1995; Gomez et al., 1997a; Gómez et al., 1997b; Douglass et al., 2011). The overall E-W morphology of A1569S, the direction of local elongation of the ICM in between the radio tails of 1233+168, and the presence of gas density discontinuity perpendicular to the line bisecting the angle between the radio tails of 1233+168, suggest that the most plausible geometry of the ongoing interaction is a head-on merger between A1569S and a subcluster falling in from the west along the line bisecting the WAT tails in the plane of the sky. Using a pre-shock gas temperature of 2.6 keV and a merger shock Mach value equal to 1.7, we estimate the ICM bulk flow velocity to have an upper limit of $\sim$1414 km s^{-1} (equal to the shock velocity) (§5.6.2). The proposed merger geometry and the estimated flow velocity is the most likely explanation for the observed bending of the WAT source 1233+168, thus supporting the merger hypothesis of Gomez et al. (1997a).

We do not detect cavities in the substructure maps of A1569S. This is in support of the calculation of Gomez et al. (1997a) who found the radio tails of 1233+168 to be underpressured by more than a factor of 10 with respect to the surrounding ICM, likely due to the entrainment of the ICM into the radio tails. As a result, we attribute the temperature excess observed in A1569S (Fig. 5.12), a radio-loud group, to be the heating effect of the above-mentioned merger. Deeper X-ray observations are, however, required to confirm the presence/absence of cavities in A1569S, and the presence of any AGN driven shocks in the ICM of both A1569N and A1569S. These observations will also enable us to produce high resolution thermodynamic maps of the two subclusters, detect any metallicity substructure around the radio lobes and visually identify SB edges in the X-ray images. The study of X-ray cavities and mergers in small-scale galaxy clusters and groups has been sparse due to the low surface brightness of these objects, and should benefit greatly from deeper exposures or larger X-ray telescopes. Future radio observations of A1569S will prove helpful in confirming the observed merger activity in A1569S.

Chapter 6

Large-scale environment of galaxies in the Coma supercluster: their age and metallicity

This chapter is based on the research article *Age and metallicity of galaxies in different environments of the Coma supercluster* published in *New Astronomy* by Tiwari et al. (2020) (New Astronomy, 81:101417).

6.1 Introduction

The Coma supercluster (170° $\leq$ RA (J2000) $\leq$ 200°, 17° $\leq$ Dec (J2000) $\leq$ 33°, and 0.0142 $\leq z \leq$ 0.0328) is one of the largest structures in the nearby Universe (Chincarini & Rood, 1976) comprising two rich galaxy clusters: Coma (Abell 1656) and Abell 1367, connected by a network of large-scale ($\sim$30–40 Mpc h^{-1}) filaments (Fontanelli, 1984) and several small galaxy groups. The supercluster was one of the first large-scale structures to be discovered and a definite map of its structure was provided by Gregory & Thompson (1978). In the work presented in this chapter, the trends in luminosity-weighted age and stellar metallicity (*Z*) of galaxies with stellar mass (M^*) and environment, for the Coma supercluster which spans 480 square degrees (Mahajan et al., 2010, 2018) on the sky, have been explored. The large size, richness, and the proximity of the Coma supercluster makes it an excellent site to investigate the age and *Z* of its constituent galaxies. Throughout this work, the Λ cold dark matter concordance cosmology parameterised by Ω_m=0.3, Ω_Λ=0.7 and, H_0=70 km s^{-1} Mpc^{-1} has been used for determining distances and magnitudes.

6.2 Data

The data used in this work are drawn from the data release 8 (DR8) of the *Sloan Digital Sky Survey* Data (York et al., 2000; Aihara et al., 2011). The spectroscopic catalogue of the SDSS galaxies is complete to $r^1 \leq 17.77$ mag. We, therefore, implement this criteria together with the following to select galaxies for our sample:

- $170^\circ \leq$ RA $\leq 200^\circ$,
- $17^\circ \leq$ Dec $\leq 33^\circ$, and
- radial velocity, cz such that $4260 \leq cz \leq 9844$ km s^{-1} ($0.0142 \leq z \leq 0.0328$).

The latter is chosen so as to include all galaxies within $\pm 3\sigma$ of the mean redshift of the Coma and the Abell 1367 clusters (central velocities of 6973 and 6495 km s^{-1}, respectively; Rines et al., 2003). For this sample, we adopt the stellar mass completeness limit of $\log M^*/M_\odot = 9.05$ (following fig. 8 of Weigel et al., 2016).

6.2.1 Properties of galaxies

The physical properties of galaxies in the sample used in this work are drawn from the catalogues provided by the Max Planck Institute for Astrophysics (MPA) and Johns Hopkins University (JHU) group. The MPA-JHU catalogues make use of the spectra obtained using the $3''$ diameter fibre. Model spectra are fitted to the emission-line free regions of the observed spectrum. The residuals obtained after subtracting the fitted spectrum from the observed spectrum are then modelled as gaussians giving emission line measurements (Tremonti et al., 2004). In order to produce an absorption-line only spectrum, the fitted emission lines are subtracted from the observed spectrum. This work makes use of absorption line data only. The stellar masses in the MPA-JHU catalogue are calculated based on the methodology described in Kauffmann et al. (2003), with the difference that the MPA-JHU pipeline makes use of the *ugriz* galaxy photometry instead of spectral indices. A Kroupa IMF is assumed. The output is provided as 2.5, 16, 50, 84, and 97.5 percentiles of the probability distribution function (PDF) of the logarithm of the stellar mass. In this work, the median value of the stellar mass PDF has been used. SDSS photometry catalogues list several different measures of magnitudes. Of these, model magnitudes, which are estimated by fitting a surface brightness profile to the two-dimensional image of a galaxy, usually provide the best available color for extended objects. In this work, the extinction corrected g and r band model magnitudes have been used.

[1]The petrosian r-band magnitude limit of the SDSS.

6.2.2 Environment

Environment of galaxies can be broadly classified into two regimes: 'local environment' ($\lesssim 1$ Mpc), which is often well quantified by measuring the local projected density using nearest neighbours, and the 'large-scale' environment which quantifies the > 1 Mpc density field around galaxies. Using a large sample of clusters, Rines et al. (2005) showed that beyond the virial radius, the local density at a given projected distance from the centre of the cluster can vary by as much as two orders of magnitude (their fig. 12). Muldrew et al. (2012) showed that environment metrics based on nearest neighbour density are well suited to measure the local environment in large halos, where as aperture-based methods are better representations of the large-scale environment of galaxies. Since this work is about exploring the relation between galaxy properties and their large-scale environment, a method based on the latter methodology is adopted to quantify environment.

Here, the scheme described in Mahajan et al. (2018) is used to classify galaxies in the Coma supercluster into three distinct environments: clusters/groups, filaments or voids[2]. The number of galaxies inhabiting different environments for the giant and dwarf galaxies are presented in Table 6.1. For completeness, the definition of different environments is summarised below:

- *Cluster/group galaxies*: all galaxies identified to lie in groups or clusters.
- *Filament galaxies*: all galaxies that are within a radius of 1 Mpc of the filamentary spine.
- *Void galaxies*: all other galaxies in the sample which are not selected in either of the above two categories.

Table 6.1: Environment segregation of the samples

Environment	Red sample	Complete sample
Cluster/group	837	1810
Filament	364	963
Voids	57	161

The distribution of galaxies in different environments in the Coma Supercluster is shown in Fig. 6.1.

[2]Since the data used here are sampled from DR8 unlike Mahajan et al. (2018), environment information is missing for 19 galaxies of which 5 belong to the red sample.

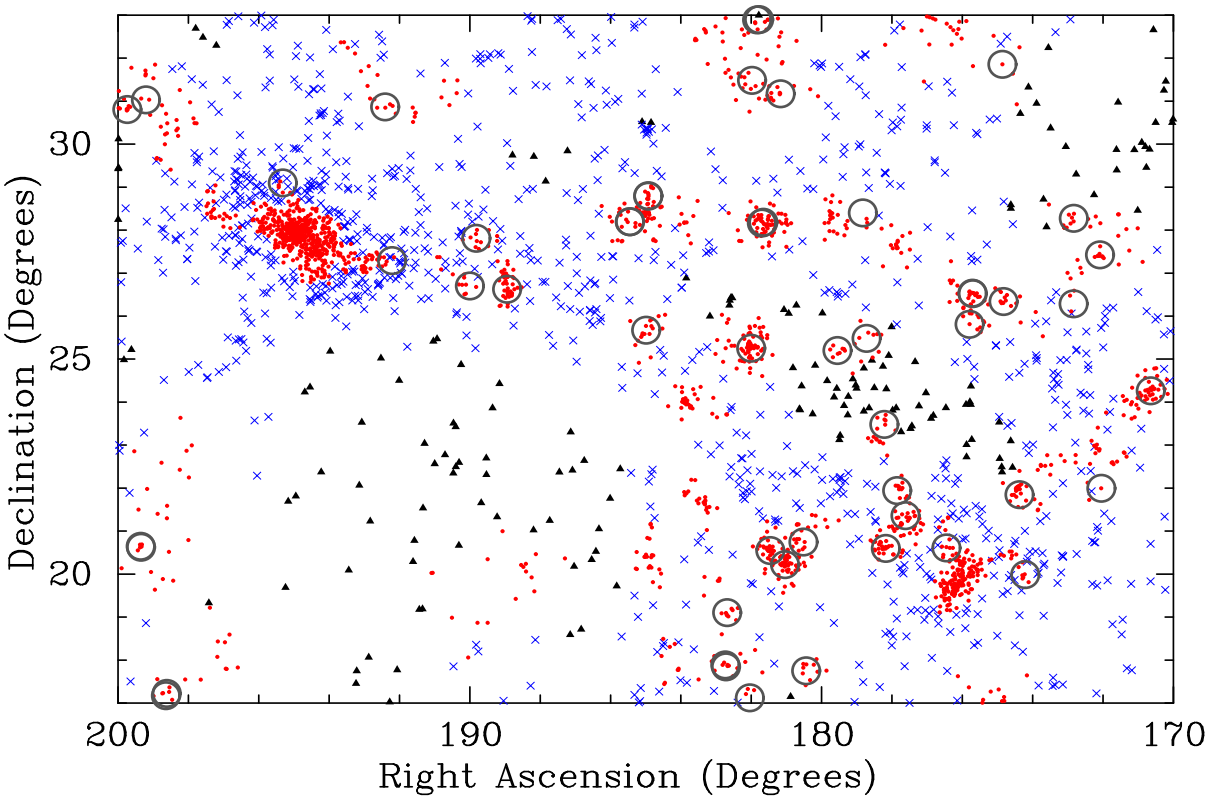

Figure 6.1: A 2-d sky representation of Coma Supercluster. 2,934 galaxies out of 2,953 galaxies in the complete sample, for which environment information is available are shown. *Red points, blue crosses*, and *black triangles* represent galaxies in clusters/groups, filaments, and void regions, respectively. The *dark grey circles* represent galaxy groups identified in the NASA/IPAC Extragalactic Database (NED).

6.2.3 Age and Z of galaxies

In this work, three spectral line indices defined on the Lick system (§1.2.4) have been adopted, viz. Hβ (4847.875 Å–4876.625 Å) is used as an indicator of age, and the mean of Fe5270 (5245.650 Å–5285.650 Å) and Fe5335 (5312.125 Å–5352.125 Å) indices, $\langle Fe \rangle$, is adopted as an indicator for Z of galaxies in our sample. The Hβ index is a widely adopted age-sensitive spectral index (Kuntschner & Davies, 1998; Kuntschner, 2000; Poggianti et al., 2001; Caldwell et al., 2003), while $\langle Fe \rangle$ is commonly used as a proxy for stellar Z (Jørgensen, 1997, 1999; Poggianti et al., 2001; Proctor et al., 2004; Sánchez-Blázquez et al., 2006c). We note that all absorption line indices are measured from galaxy spectra after subtracting all emission lines with signal-to-noise ratio (SNR) $\geq 3\sigma$. A detailed description of the methodology adopted for the measurement of spectral indices from the SDSS spectra is described in Brinchmann et al. (2004) and Tremonti et al. (2004).

Although these indices have been used in the literature to analyse populations of galaxies, especially in the passively evolving galaxies in galaxy clusters, the work described in this chapter is distinguishable because we have analysed 'all' types of galaxies i.e., emission-line and absorption-line systems, spanning a wide range in stellar mass and environmental density homogeneously. This uniform treatment of data allows one to get an insight into the evolution of galaxies not just in dense clusters, but in the much larger supercluster. In order to meet our science goals it is, therefore, essential to include all types of galaxies even if some of them may have high uncertainties. However, in order to test for biases in our results arising due to high observational uncertainties, we have performed the analysis by segregating our data into two sub-samples:

- **Complete sample** of 2,953 galaxies, and
- **Red sample**: A reduced subset of the complete sample comprising 1,263 galaxies with < 20 *per cent uncertainty in all the three absorption line indices* used in this work.

The distribution of all galaxies used for analysis in this study in the colour-magnitude plane is shown in Figure 6.2. As expected, most of the galaxies on the red sequence are strong absorption line systems, and therefore, belong to the lower-uncertainty red sub-sample.

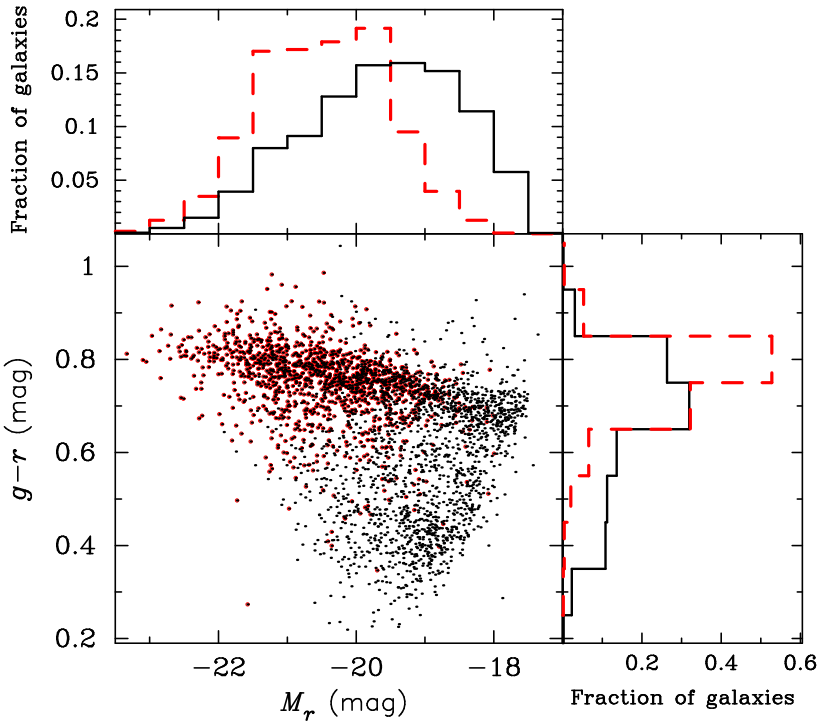

Figure 6.2: This figure shows the distribution of all galaxies in the colour-magnitude plane, and the respective distributions of the $(g - r)$ colour and M_r magnitude for the complete *(black points, solid lines)* and red *(red points, dashed lines)* sub-samples.

In Figure 6.3 we show that the smaller 'red' sub-sample is dominated by massive red galaxies, which are passively-evolving systems with low uncertainty in absorption line measurements. A corollary of this observation is that the star-forming galaxies with spectra dominated by emission lines are found to have the highest uncertainty in the absorption line indices required to estimate their age and metallicity. Specifically, the typical uncertainty in the Hβ and $\langle Fe \rangle$ indices are 0.4 Å (0.25 Å) and 0.3 Å (0.2 Å) in the complete (red) sub-samples, respectively. Furthermore, 90 per cent of the galaxies in the complete (red) sub-sample have $<$ 29 per cent ($<$ 16 per cent) and $<$ 34 per cent ($<$ 11 per cent) uncertainty in the Hβ and $\langle Fe \rangle$ indices, respectively.

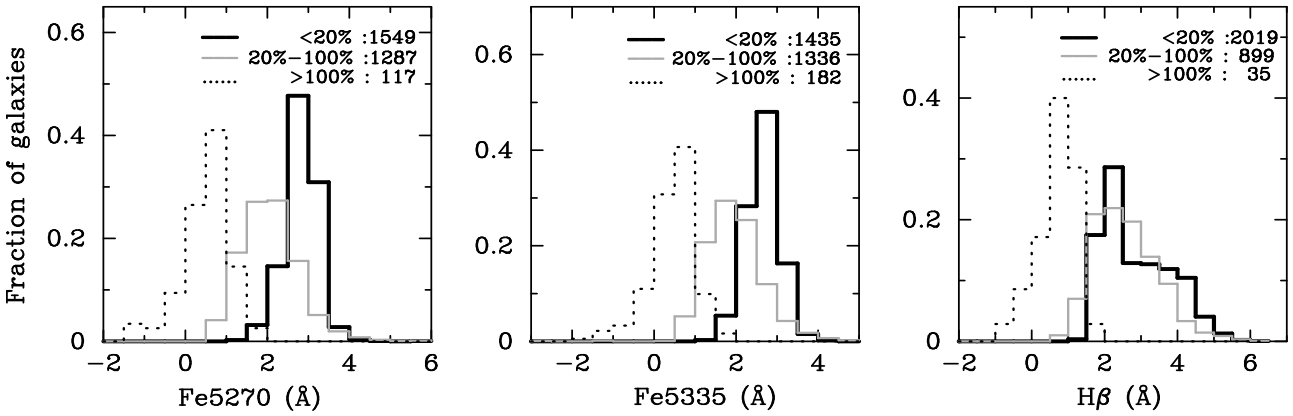

Figure 6.3: This figure shows the distributions of absorption line indices for the complete sample of 2,953 galaxies segregated according to the relative measurement errors as indicated in the legend. The number of galaxies contributing to each distribution is also mentioned. In general, larger absorption line equivalent width is synonymous with lower measurement error.

6.3 Estimation of age and metallicity

In this work, we use Single Stellar Population (SSP) models which transform the observed line indices into luminosity-weighted mean age and mean metal content of galaxies (§1.2.5). In particular, we use the SSP models described in Vazdekis et al. (2010, hereafter V10). V10 make use of the solar-scaled theoretical isochrones of Girardi et al. (2000, hereafter Padova isochrones) and cover a wide range of parameters and initial mass functions. The Padova isochrones are based on theoretical stellar evolutionary tracks for many low and intermediate mass stars (0.15–7 $M_{\odot}$) covering a wide range in metallicity ($0.0004 \leq Z \leq 0.03$). The stellar

tracks are presented at very small mass intervals and hence, allow for a detailed mapping of the Hertzsprung-Russell Diagram, which results in a detailed derivation of isochrones (Girardi et al., 2000).

V10 compute the SSP spectral energy distributions (SED) by integrating the spectra of stars along the isochrone taking into account their number per mass bin in accordance with the adopted IMF. They make use of stars in the Medium-resolution Isaac Newton Telescope Library of Empirical Spectra (MILES) database (§1.2.5), which have a good stellar atmospheric parameter coverage, and compute their predictions for different IMFs.

Here, we use the predicted line strengths based on the work of V10 from the MILES database. We have employed fourteen constant age (0.79, 0.89, 1.00, 1.12, 1.78, 2.82, 3.16, 4.47, 5.01, 5.62, 6.31, 7.08, 7.94, and 14.12 Gyr) and six constant metallicity isochrones (-1.71, -1.31, -0.71, -0.4, 0.0, 0.22 [M/H][3]). The bimodal IMF (slope $= 1.3$) closely resembles the Kroupa IMF (Kroupa, 2001), and the SSP SEDs obtained for these IMFs do not show significant differences (V10). Furthermore, the effects of varying the slope of the IMF on the SSP SEDs are far less significant for the bimodal IMF relative to those arising from varying the slope of the unimodal IMF (V10). We therefore adopt the bimodal IMF (Vazdekis et al., 1996) in this work.

The distribution of galaxies for the red and complete sub-samples in the Hβ-$\langle$Fe$\rangle$ plane, along with the constant age and *Z* isochrones mentioned above, is shown in Figure 6.4. The age and *Z* of galaxies are estimated by interpolating from the nearest model points. However, for 98 (503) galaxies in the red (complete) sub-sample which lie outside the model grid, the age and metallicity of galaxies are estimated by extrapolating the constant age and *Z* isochrones. In regions where the isochrones cannot be extended, i.e. $<$ 0.7943 Gyr and $>$ 14.1254 Gyr in age, and $Z <$ -1.71 and $Z >$ +0.22 for metallicity, galaxies are assigned an age of 0.05 Gyr and 20 Gyr, and a metallicity value of $\pm$4, respectively. In order to draw statistically valid results, these galaxies are excluded from further analysis.

In order to compute the uncertainty in the age and *Z* due to the measurement error in the Hβ and $\langle Fe \rangle$ indices, the index values are perturbed with their uncertainties and age and *Z* are recomputed. This gives the upper and lower bounds in both the quantities for each galaxy. We

[3][M/H] is the 'abundance ratio'. It is defined as the logarithm of the ratio of the amount of a metallic element (commonly Fe) and Hydrogen in an astronomical object of interest relative to the corresponding ratio in the Sun. The value is 0.0 for the Sun.

note that several perturbed index values fall outside the model grid, either due to the measured value being very close to the grid boundary or having a large uncertainty associated with it. In such cases, age and Z bounds are estimated via extrapolation by extending the model isochrones where possible. The galaxies for which the isochrones can not be extended, are excluded from further error analysis. Following Jørgensen (1999) and Poggianti et al. (2001), the uncertainties in age and Z are then calculated by taking half of the difference between the upper and lower limits for each galaxy. In the complete (red) sub-sample, age and Z bounds are well estimated for 62 per cent (74 per cent) and 69 per cent (85 per cent) of the galaxies, respectively. The fractions are naturally higher for the red sub-sample, owing to smaller uncertainty in the indices and the sub-sample consisting mainly of those galaxies which lie well within the model grid. Based on these galaxy fractions, the median absolute uncertainty in age is found to be 1.7 Gyr (2.4 Gyr), and in Z is 0.26 dex (0.2 dex) for the complete (red) sub-sample, respectively. These uncertainties are comparable to those found by Poggianti et al. (2001) for the central region of the Coma cluster using data from the William Herschel Telescope. We present the age and Z , and the respective uncertainties obtained for them for all the galaxies in our sample in Table 6.2, which is provided in Table A.1 of Appendix A in its entirety. The columns are: (i) Right Ascension (J2000), (ii) Declination (J2000), (iii) redshift, (iv) age (Gyr), (v) and (vi) upper and lower limits of age (Gyr), (vii) Z (dex), (viii) and (ix) upper and lower limits of Z (dex), respectively.

Table 6.2: The position, age and Z for all the galaxies in the sample analysed in this work. The full table is provided in Table A.1.

Right Ascension (J2000)	Declination (J2000)	Redshift	Age (Gyr)	Age Upper limit (Gyr)	Age lower limit (Gyr)	Z (dex)	Z upper limit (dex)	Z lower limit (dex)
178.312	20.736	0.0252	2.2	3.1	1.4	-0.12	-	-0.39
191.190	27.500	0.0314	1.8	2.6	1.2	-0.25	-	-0.55
197.003	28.081	0.0192	2.7	5.1	1.9	-0.36	-0.07	-0.64
189.744	27.564	0.0224	2.1	2.9	1.4	-0.16	-	-0.45
179.050	21.394	0.0255	2.1	2.9	1.5	-0.34	0.04	-0.61
180.642	20.815	0.0223	1.7	2.7	1.1	-0.07	-	-0.44
195.960	28.054	0.0210	2.4	4.1	1.5	-0.12	-	-0.42
181.856	28.530	0.0303	1.9	2.9	1.2	0.04	-	-0.31
181.500	27.639	0.0285	2.4	4.1	1.6	-0.31	0.08	-0.61
177.888	27.669	0.0290	1.8	3.1	1.1	0.20	-	-0.23
182.909	19.845	0.0223	2.5	4.0	1.8	-1.12	-0.85	-1.34

It is to be noted that the uncertainty in age varies with the age of the population, due to the logarithmic nature of the grid used to compute the ages and Z (Fig. 6.4; also see fig. 8 of Poggianti et al., 2001). The typical uncertainty in age is found to be 1 Gyr (0.7 Gyr) for galaxies < 3 Gyr old for the complete (red) sub-sample. For older populations, the uncertainty is $\sim$3.4 Gyr for both the sub-samples. The red sub-sample, chosen to have lesser uncertainty in the indices, is largely dominated by older systems with age > 3 Gyr (Fig. 6.4). On the other hand, $\sim$65 per cent of the galaxies in the complete sub-sample are < 3 Gyr old, consequently giving slightly higher age uncertainty of 2.4 Gyr for the red sub-sample when all galaxy populations are taken into account.

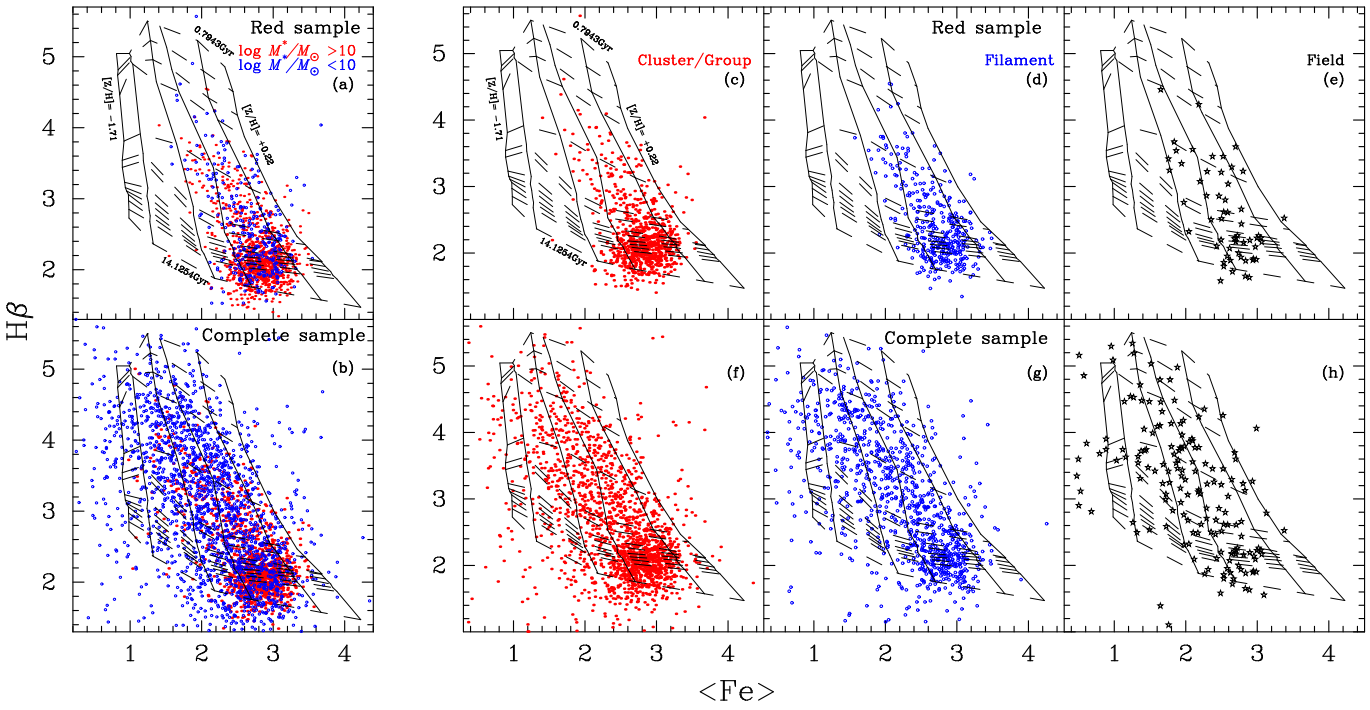

Figure 6.4: Distribution of galaxies in the Hβ-$\langle$Fe$\rangle$ plane for the red *(top)* and complete *(bottom)* sub-samples. The *blue circles* and *red points* in panels (a) and (b) represent the dwarf and giant galaxies in the two sub-samples, respectively. Overplotted are constant age *(dashed)* and constant metallicity *(solid)* isochrones. The age and metallicity values corresponding to the extreme contour levels are marked. Panels (c) to (h) represent the distribution of galaxies in clusters, filaments and voids in the red *(panels c-e)* and complete *(panels f-h)* samples, respectively.

6.4 Analysis and results

It is well known that massive, passively-evolving galaxies reside in dense environments. Therefore, in order to analyse the trends in age and metallicity with environment and stellar mass, it is essential to decouple the latter two properties of galaxies. In this work, we accomplish this by splitting each sub-sample into bins of M^* and environment, assuming insignificant evolution of galaxies within each sub-sample.

We split our data into two bins of M^*, viz. defining galaxies having $\log M^*/M_\odot < 10$ and > 10 as 'dwarfs' and 'giant' galaxies, respectively. While 24 per cent of galaxies in the red sample are classified as dwarfs, almost 62 per cent of galaxies in the complete sample appear in this class. Fig. 6.2 shows the distributions of the $g - r$ colour for the complete and the red sub-sample, respectively. As expected, galaxies in both the sub-samples become redder with increasing r-band luminosity, which is a good proxy for M^*. In particular, the lack of low-mass, blue galaxies, especially in the red sub-sample is evident, once again justifying the need to analyse the complete sample including galaxies with higher measurement uncertainties in the spectral indices.

The distribution of galaxies in the Hβ-$\langle$Fe$\rangle$ plane in Fig. 6.4 shows that most of the passively-evolving giant systems have large absorption in $\langle$Fe$\rangle$ and lower absorption in Hβ, indicating high metallicity and lower star formation in the recent past, respectively. The dwarfs in the red sample follow the giants. However, the dwarfs in the complete sample span the entire Hβ-$\langle$Fe$\rangle$ plane, suggesting a wide range of star formation histories.

Segregation with environment (panels (c)-(h) in Fig. 6.4) shows that most of the cluster galaxies are concentrated in the bottom-right quadrant dominated by massive, passively-evolving systems with a small but non-negligible fraction of the remaining galaxies spanning the rest of the Hβ-$\langle$Fe$\rangle$ plane. In filaments and voids however, galaxies span the entire Hβ-$\langle$Fe$\rangle$ plane with some traces of an excess in the bottom-right quadrant in the filaments. The consequence of such a distribution in the context of the M^* distribution and environment of galaxies is discussed in the following sections.

6.4.1 Disentangling the effects of age and M^* on Z

In this section the metallicity of galaxies as a function of their stellar mass and luminosity-weighted age is studied. In Figure 6.5 we show the distributions of age and Z for the dwarf and giant galaxies along with the median for each distribution. Both samples show statistically significant differences in the distribution of the age of the dwarf and giant galaxies, but negligible differences in the distribution of their Z. These inferences are drawn on the basis of the outcome of the Kolmogorov-Smirnov (KS) statistical test, which tests for the likelihood that the two samples being compared originate from the same parent distribution. The KS test probabilities in favour of the hypothesis for the red and the complete samples for age and Z of galaxies in different mass bins and environments are shown in Tables 6.3 and 6.4, respectively.

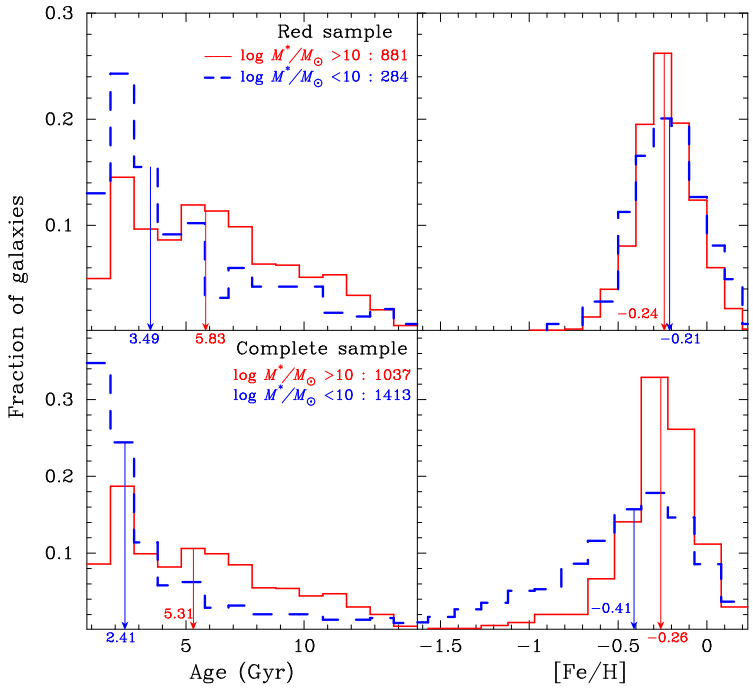

Figure 6.5: The age *(left)* and metallicity *(right)* distributions of galaxies in the red *(top)* and complete *(bottom)* sub-samples, respectively. Each sub-sample is further split into dwarfs and giants. The bottom-pointing arrows in each panel represent the median age and metallicity of the distributions.

Table 6.3: KS test probabilities for age and metallicity distributions of galaxies in different mass range and environments in the red sub-sample.

M^*	Age	[Fe/H]
Dwarfs & Giants	2.3E-12	8.0E-02
Environment		
Cluster/Group & Filament	5.9E-05	8.8E-01
Cluster/Group & voids	3.0E-03	8.0E-02
Filaments & voids	2.5E-01	1.9E-01

Table 6.4: KS test probabilities for age and metallicity distributions of galaxies in different mass range and environments in the complete sample.

M^*	Age	[Fe/H]
Dwarfs & Giants	4.8E-62	5.8E-47
Environment		
Cluster/Group & Filament	3.2E-14	7.7E-05
Cluster/Group & voids	6.3E-07	1.3E-05
Filaments & voids	3.0E-01	2.0E-02

Taking inspiration from Poggianti et al. (2001), we split our sample into four bins in age: < 3 Gyr (very young galaxies), 3–6 Gyr (intermediate), 6–9 Gyr (intermediate old) and > 9 Gyr (very old). In Figure 6.6 we show the median trend in metallicity as a function of stellar mass for the dwarf and giant galaxies in each bin of age for the red and the complete sub-samples, respectively. For the dwarf galaxies we have combined the intermediate-old and very old galaxy populations due to low number statistics. Both the dwarf and giant galaxies show a continuous decline in metallicity with increasing age. Although counter-intuitive, this result is explainable in a scenario where galaxies grow by accreting smaller satellites and cold gas from the large-scale structure in which they are embedded. Such cold-mode accretion will feed low metallicity gas, thereby reducing the mean metallicity of the progenitor galaxy (e.g. D'Souza & Bell, 2018). Furthermore, stars in younger populations benefit from previous generations' metal enrichment (Rakos et al., 2001).

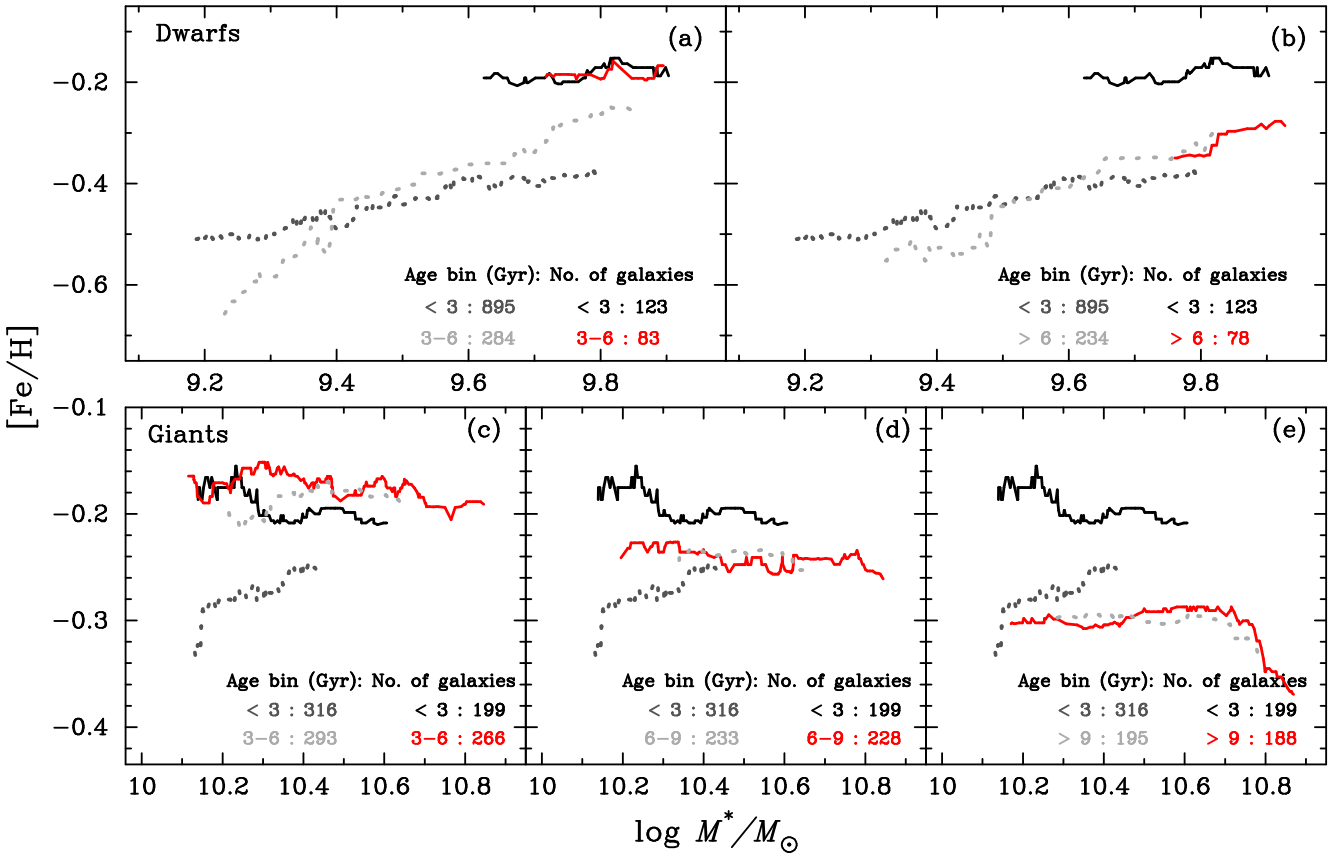

Figure 6.6: The median trend in the metallicity of *(top)* dwarf and *(bottom)* giant galaxies as a function of M^*. The solid lines represent the red sub-sample, while the complete sample is shown using the dotted lines. The *black lines (solid for red sub-sample and dotted for complete sample)* in each panel represent the metallicity distribution of the youngest galaxies in the specified mass bin, which is compared to the sub-sample of older galaxies *(solid red for red sub-sample and dotted grey line for complete sample)*. The age of the sample to be compared with the youngest galaxies increases from left to right as indicated by the age range mentioned in each panel along with the number of galaxies contributing to each curve.

Galaxies can lose enriched inter-stellar medium (ISM) via galactic outflows, for instance, in supernovae explosion, resulting in a decline of the mean metallicity of galaxies (Chisholm et al., 2018). This hypothesis is clearly observed for the red sub-sample, where the Z of galaxies is found to decline with increasing age, irrespective of their M^*. This trend is duplicated for the complete sample of giant galaxies, and albeit with some scatter, also for the complete sample of dwarf galaxies. At fixed age however, Z is mostly independent of M^* for the dwarf and giant galaxies alike, except for the most-massive, oldest galaxies which show a sharp decline in their Z, likely caused by excessive cold-mode accretion in the central dominant galaxies in clusters and groups.

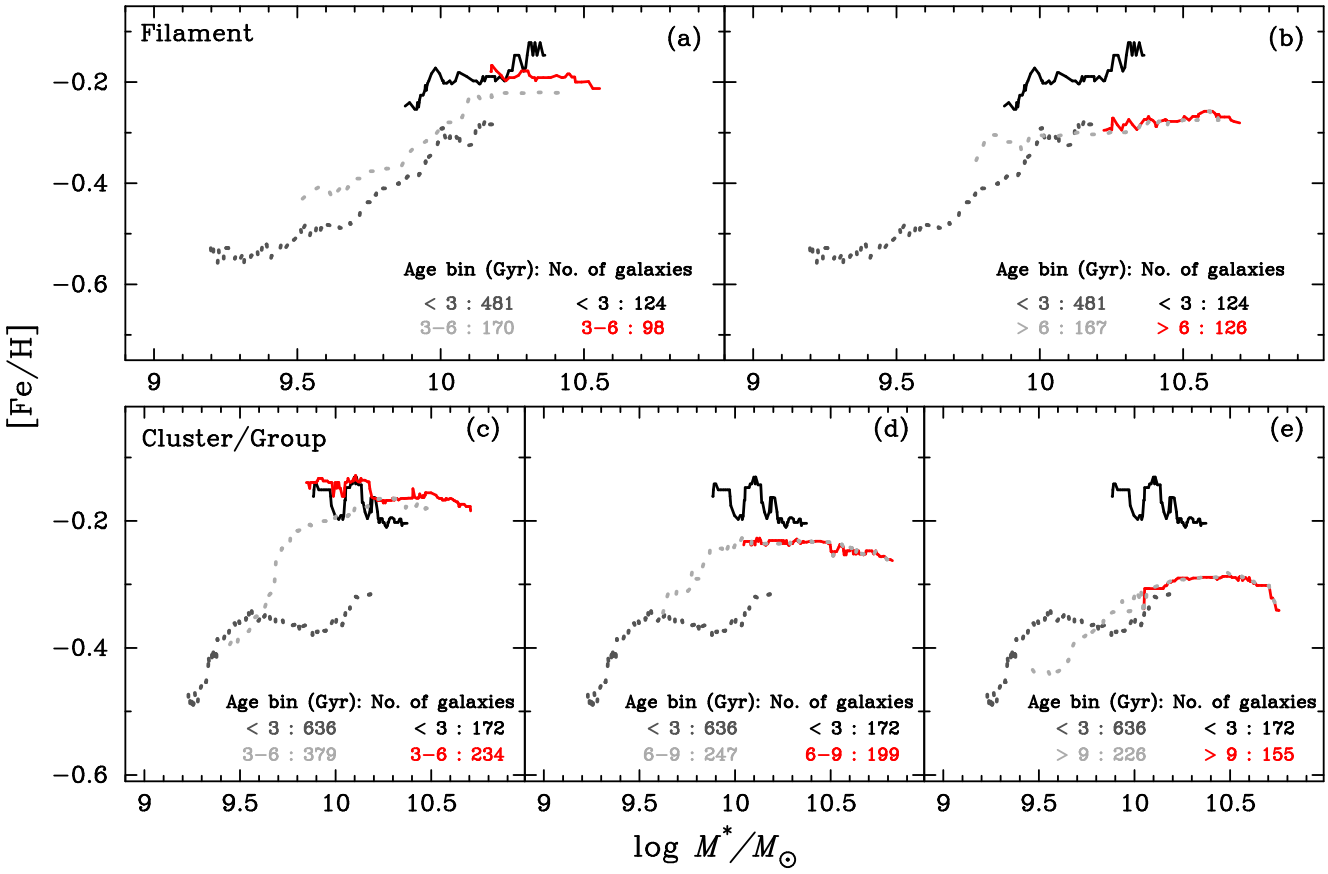

Figure 6.7: The median trend in the metallicity for galaxies in *(top)* filaments and *(bottom)* clusters or groups. The line styles are same as in Fig. 6.6. Void galaxies are not shown due to low number statistics.

6.4.2 Age and Z of dwarfs and giants in different environments

In Figure 6.7 we show the median trend in metallicity as a function of stellar mass for galaxies in clusters and filaments in each bin of age for both red and complete sub-samples. The void galaxies could not be shown here due to low number statistics. Just like Fig. 6.6, the intermediate-old and very old populations are combined together for the filament galaxies due to low number of galaxies in these bins. Fig. 6.8 shows the distribution of age and Z of galaxies in different environments for the two sub-samples. The previously observed trend of decreasing Z with increasing age is seen in all sub-samples, except the complete sub-sample of filament galaxies. Specifically, while 56 per cent of galaxies in voids are metal-rich ([Fe/H] $>$ -0.3), the fraction increases to 65 per cent for filaments, and further to 68 per cent for the cluster galaxies in the red sub-sample, suggesting that dense environments rich in passively-evolving galaxies also have more metal-rich galaxies. However, we must also consider the fact that dense environments comprise of more massive galaxies. In order to test the effect of environment on Z of galaxies independent of stellar mass, we create sub-samples of galaxies in two stellar

mass ranges for different environments. For massive galaxies ($M^*/M_\odot > 10^{10.5}$) the median Z is found to be -0.26 (-0.26), -0.25 (-0.24) and -0.28 (-0.28) in clusters, filaments and field for the complete (red) sub-samples, respectively. Similarly, for the intermediate mass galaxies ($10^{10} \leq M^*/M_\odot < 10^{10.5}$) the same is -0.24 (-0.22), -0.26 (-0.22) and -0.36 (-0.27), respectively. This analysis implies that the Z of void galaxies is statistically different from the Z of galaxies in clusters or filaments.

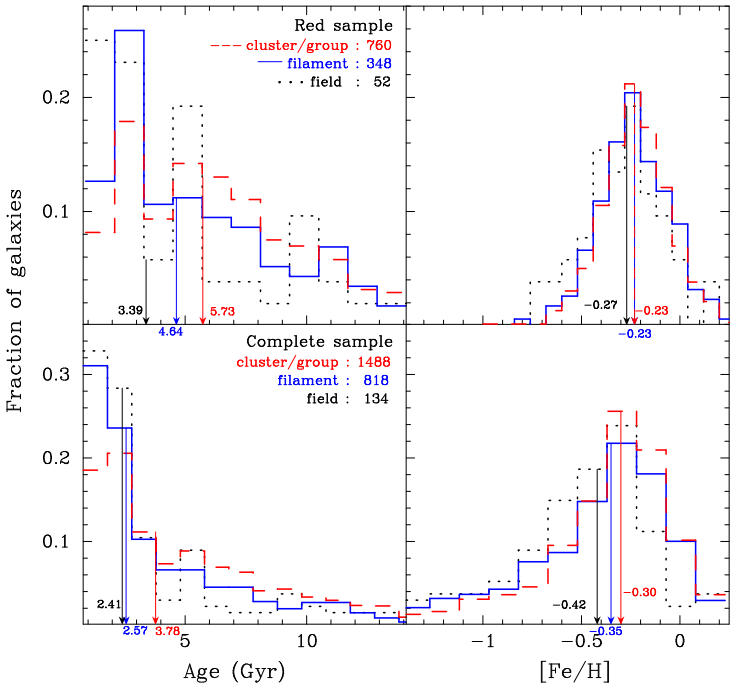

Figure 6.8: Same as Fig. 6.5, but for each sample divided on the basis of environment as classified in Mahajan et al. (2018). Galaxies become older and metal-rich as the density of environment increases from field to filaments to clusters or groups.

Together with these analyses and Figs. 6.6 and 6.7, we conclude that the Z of galaxies in the Coma supercluster is primarily dictated by their age, and that M^* and environment seem to have a second order effect on the Z of galaxies.

We also performed a similar analysis for the age of galaxies in different environments in the two mass-matched sub-samples. The median age for galaxies in clusters, filaments and voids is found to be 6.79 (6.91), 6.01 (6.17) and 5.58 (5.28) Gyr for the massive galaxies, and 4.74 (5.45), 3.31 (4.55) and 2.76 (2.55) Gyr for the intermediate mass galaxies in the complete (red)

sub-samples, respectively. Based on these data, the massive galaxies in clusters are older than the filaments galaxies by ∼0.7–0.8 Gyr, while their counterparts in the voids are younger than filament galaxies by ∼0.5–0.7 Gyr. The less massive galaxies show a clearer difference in their age, such that the cluster galaxies are older than the filament galaxies by 1-1.5 Gyr, which in turn are older than their counterparts in the voids by $\lesssim$ 1 Gyr. In general, we find that about two-thirds of all giant and dwarf galaxies have [Fe/H]> -0.3, but even though 64 per cent of the dwarfs are younger than 5 Gyr, the same applies to 40 per cent of the giant galaxies only (Table 6.5).

Table 6.5: The fraction of young/old and metal-rich/metal-poor galaxies among each category of galaxies in the two samples.

Red sub-sample		
	%Old (> 5 Gyr)	%Metal rich ([Fe/H] > -0.3)
Dwarfs	36.3	65.8
Giants	59.8	66.6
Galaxy Cluster/Group	58.3	67.6
Filament	47.1	65.2
Field	40.4	55.8
Complete sample		
	%Old (> 5 Gyr)	%Metal rich ([Fe/H] > -0.3)
Dwarfs	22.6	36.4
Giants	52.6	59.8
Galaxy Cluster/Group	40.7	49.5
Filament	27.5	42.7
Field	23.9	32.8

6.5 Discussion

In the work presented in this chapter, we use the Lick indices' measurements for galaxies to study the correlation between age, stellar *Z*, stellar mass, and environment of galaxies in the Coma supercluster. While the giant galaxies are mostly old and metal-rich, their dwarf coun-

terparts are relatively younger and metal-poor (Table 6.5, Fig. 6.5 and 6.9). These observations are a manifestation of the downsizing scenario observed elsewhere (Heavens et al., 2004; Gallazzi et al., 2005; Jimenez et al., 2005; Thomas et al., 2005; Neistein et al., 2006; Cid Fernandes et al., 2007; Panter et al., 2007; Fontanot et al., 2009; Thomas et al., 2010), viz. the stars in more massive galaxies tend to form earlier and over a shorter time-span. In the following, we analyse our results in the light of information from the existing literature, also describing the shortcomings of the analyses presented in this study.

6.5.1 Age-Z anticorrelation

In agreement with the literature (e.g. Jørgensen, 1999; Poggianti et al., 2001; Kuntschner, 2000; Price et al., 2011), we find that the (luminosity-weighted) age and stellar Z of galaxies are anti-correlated, such that the younger galaxies tend to be more metal-rich than their older counterparts. These trends are observed in all environments (Fig. 6.7), and for the dwarf ($M^* < 10^{10} M_{\odot}$) and giant galaxies ($M^* > 10^{10} M_{\odot}$; Fig. 6.5) alike. This trend was previously observed for the passively-evolving elliptical and S0s in clusters. In the work presented here, we observe the same even after incorporating the late-type galaxies and sampling a continuous range of environments present in the Coma supercluster.

Such an anticorrelation where errors in both age and Z are correlated (Kuntschner et al., 2001), is difficult to assess because an underestimation in one leads to an overestimation of the other (Trager et al., 2000). Hence this trend may conspire to give a tight correlation between age or Z sensitive indices and other global properties such as the stellar mass (Fig. 6.5; Tremonti et al., 2004; Gallazzi et al., 2005) or luminosity of galaxies (Bell & de Jong, 2000; Poggianti et al., 2001). Although it is worth noting that if correlated errors were the only cause, such a relation would have been more apparent in low S/N galaxies, i.e. the ones with the highest errors. But the fact that the anticorrelation is unambiguously observed for the red sub-sample (i.e. high S/N galaxies), at all masses and environments implies that for our sample the age-Z anticorrelation is not an artefact, in agreement with Poggianti et al. (2001) who employed data for two physically separated regions in the Coma cluster.

6.5.2 The mass-Z relation

In Figure 6.9 the *Z* of galaxies as a function of their M^* for the complete and red sub-samples, along with 1-σ deviations in the relation of running median, is shown. The observed trend is similar to that observed elsewhere (e.g. Bell & de Jong, 2000; Tremonti et al., 2004; Gallazzi et al., 2005), i.e., the metallicity increases with stellar mass or luminosity, and then saturates for the massive galaxies ($M^*/M_\odot \gtrsim 10^{10.5}$). This relation reflects the importance of stellar mass in determining the composition of galaxies. Also, the scatter in the M^*-*Z* relation decreases with increasing mass. The large scatter in the lower mass galaxies is partly due to the larger uncertainties in the age and *Z* of low-mass galaxies. However, even at fixed stellar mass the scatter is larger than the uncertainties in *Z* (Gallazzi et al., 2005).

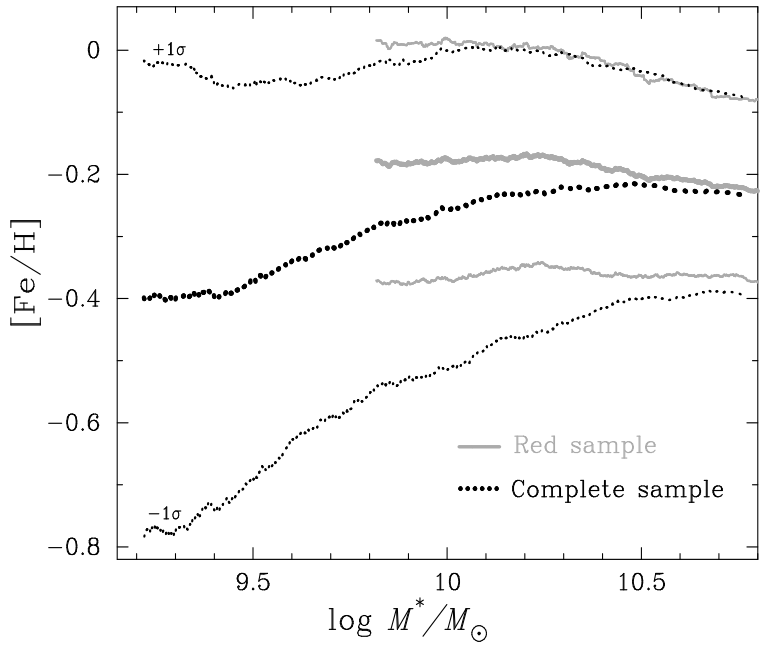

Figure 6.9: The median [Fe/H] ratio as a function of M^* for the complete *(black)* and red *(grey)* sub-samples, respectively. The lines representing the $\pm 1\sigma$ limit are shown on either side of the median relation. Notice that the high S/N (red) sub-sample comprises mainly of massive galaxies.

In a sample which spans a range of environments, such scatter is expected due to the variety of galaxies contributing to the relation (Cooper et al., 2008). For instance, despite having very different metallicities, dwarf elliptical galaxies and irregulars will both contribute to the M^*-*Z* relation at log $M^*/M_\odot \sim 9$, thereby adding to the scatter caused by the variations in the intrinsic properties of galaxies (at fixed mass).

The mass-*Z* relation also has a strong dependence on the star formation rate (SFR) of galaxies. These quantities form the "fundamental metallicity relation (FMR)" (Lara-López et al., 2010; Mannucci et al., 2010). Furthermore, using data from the ALFALFA atomic gas survey, Bothwell et al. (2013) showed that galaxies in the nearby Universe obey an HI FMR, between stellar mass, gas-phase metallicity and the HI mass. Bothwell et al. (2013) hypothesize that the HI FMR relation is more fundamental and drives the relation between SFR, M^* and metallicity because the dependence of *Z* on HI mass does not saturate like it does for the SFR. Bothwell et al. (2013) also find that at fixed stellar mass, galaxies with higher atomic gas mass have relatively lower gas-phase *Z*.

6.5.3 Metallicity of galaxies in different environments

In Sec. 6.4.2 we observed that environment and stellar mass play a secondary role in determining the *Z* of galaxies. The *Z* of galaxies is primarily determined by their age, such that the older galaxies have lower *Z* than their younger counterparts. We now explore the impact of environment on the metallicity of galaxies.

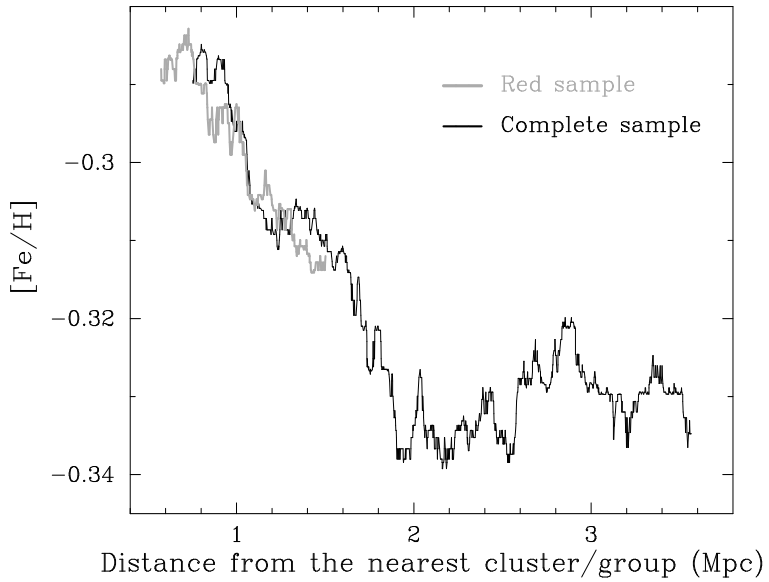

Figure 6.10: This figure shows the median [Fe/H] ratio for cluster galaxies as a function of their distance from the centre of the nearest cluster for the complete *(black)* and red *(grey)* sub-samples, respectively. In the complete sample, *Z* decreases with increasing cluster-centric distance saturating to [Fe/H]~ -0.33 at $\gtrsim 2$ Mpc from the cluster centre.

In Fig. 6.10 the variation in the [Fe/H] ratio as a function of distance from the centre of the nearest cluster for the red and complete sub-samples, is shown. The median [Fe/H] ratio of galaxies decreases $\sim$0.05 dex between the centre and the virial radius (1-2 Mpc) of a typical galaxy cluster at $z \sim 0$. Thereafter, the [Fe/H] assumes a constant value of -0.34 to upto twice that radius.

With the general knowledge that galaxies in dense environments are more evolved (Blanton et al., 2005a), it is not surprising to see that on an average the [Fe/H] ratio declines moving away from the cluster centre. Analogous results have previously been obtained for general samples of star-forming galaxies from the SDSS. For instance, Cooper et al. (2008) not only observed the metallicity-density relation, but showed that it was as strong as the colour-density and luminosity-density relation observed for galaxies in the nearby Universe. These authors also suggest that as much as 15 per cent of the scatter found in the mass-metallicity relation discussed in the previous section can be contributed by differences in the environment.

Using optical spectroscopic data from the SDSS and UV photometric data from the Galaxy Evolution (GALEX) surveys we have shown that broadband colours (*g-r, FUV-NUV*) and equivalent width of Hα emission line varies as a function of the distance from centre of the filaments in the Coma supercluster (Mahajan et al., 2018). These observations imply the critical role played by large-scale cosmic filaments in the evolution of galaxies much before they encounter the hostile cluster-related environmental processes. We now provide further support to these observations in Fig. 6.11. This figure shows the observed trend in the [Fe/H] ratio of filament galaxies as a function of the distance from the spine of the filament, where spine is the central axis of the filament assuming they are uniform cylinders[4]. The observed trends although mild, suggests that the [Fe/H] ratio is 0.02–0.03 dex lower for galaxies at the spine of the filament relative to their counterparts $\gtrsim$ 1 Mpc away from it.

[4]A detailed description of the procedure used to define filaments is describe in sec. 3 of Mahajan et al. (2018)

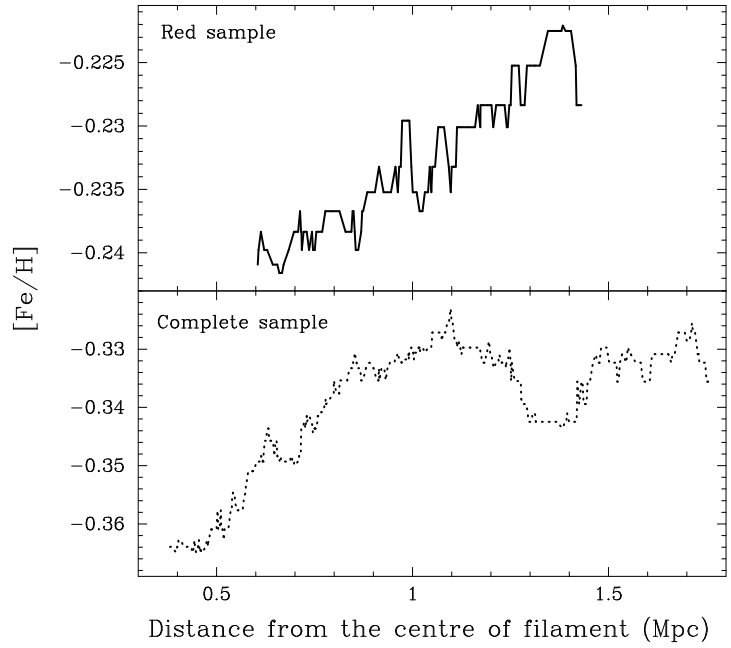

Figure 6.11: Same as Fig. 6.10, but showing median [Fe/H] ratio shown as a function of their distance from the spine of large-scale filaments for the red and complete sub-samples. Assuming filaments to be cylinders, the *Z* of galaxies seems to drop towards the central axis of the filament. These observations are in agreement with those presented in Mahajan et al. (2018).

In line with the literature (Alpaslan et al., 2015; Chen et al., 2015; Mahajan et al., 2018), these observations also suggest that galaxies closer to the spine of the filaments either experience greater infall of gas due to the depth of the potential well, or accrete more smaller satellites which aide in lowering the [Fe/H] value. The former scenario seems to be in agreement with the studies of galaxies in galaxy groups (Janowiecki et al., 2017), where environment is similar to filaments. Janowiecki et al. (2017) found that low-mass ($M^*/M_\odot \leq 10^{10.2}$) central galaxies in small groups have higher atomic gas fraction, molecular gas content and star formation activity relative to similar galaxies in isolation. In particular, Janowiecki et al. (2017) found that the atomic gas fraction in low-mass centrals is $\sim$0.3 dex higher than their counterparts in isolation. These authors attribute their findings to the inflow of cold gas from the cosmic web and gas-rich mergers.

Our results are also in broad agreement with the work of Liao & Gao (2019), who used simulations to show that the gas accreted at high redshift ($z = 2.5, 4$) on the cosmic-web gets shock heated and then cools at the centre of the filaments. These authors find that $\sim$30 per cent of this gas gets accreted on to the halos on the filaments. Thereafter, this accreted gas will not only lower the metallicity of the halos, but also provide fuel for star formation.

6.5.4 Caveats

In this section, some shortcomings of the data and analyses presented in this work are described.

- *Fibre-spectroscopy*: In SDSS, galaxy spectra are obtained by observing each galaxy through a $3''$ diameter fibre. This means that at the distance of Coma we are essentially receiving light from the central $\sim$1.4 kpc of a galaxy and the line indices are measured for the core region of the galaxy only. The SDSS Lick indices are not corrected for this aperture bias. Therefore, ages and Z estimated using these indices, may not be representative of the whole galaxy. The effects of such an aperture bias are described in Gallazzi et al. (2005). In the context of the work presented here it is particularly important that even though the age and Z may be overestimated for some galaxies, the mean trends in age and Z observed as a function of stellar mass are not significantly affected (Gallazzi et al., 2005).

- *Completeness*: SDSS being a fibre-based survey is limited by the physical size of fibres, such that no two fibres can be closer than $55''$ or within $100''$ of the plate centre. As a consequence, repeated observations of each region on the sky are essential in order to obtain high completeness.

- *Luminosity-weighted age and Z*: When interpreting trends in luminosity-weighted, model-based age and Z it is important to remember that averaging over all stellar populations masks the true complexities in both these quantities. For instance, even a small fraction of a very young population together with very old populations can dramatically change the strength of Balmer lines, thus making the galaxy appear much younger than its mass-weighted age (Worthey et al., 1995, their fig. 1).

- *Sample and data*: Given the limitations of the sample size, data quality, and methodology adopted to estimate the age and metallicity of galaxies in this work, it has not been possible to disentangle the effect of stellar mass and environment completely by refining bin sizes (e.g. Peng et al., 2010), or splitting our sample into mass bins every where (e.g. Figs. 6.10 and 6.11). Despite these drawbacks, we present our complete analysis in this work in the hope that future studies on galaxy properties in the cosmic-web will draw inspiration from this work and better constrain the statistical observational trends seen here.

6.6 Summary

The observed trends of age and metallicity of galaxies in the Coma supercluster presented in this work support a scenario where galaxies are born in the voids, and then assemble into

clusters through filaments. During the course of their passage, as these galaxies evolve, they accumulate metals as well as stellar mass, thus explaining the observed mass-density, age-density and metallicity-density correlations, along with the trends observed for the *Z* and age of galaxies as a function of their M^* and environment. It would be interesting to explore this hypothesis in simulations and test its impact on the observed properties of galaxies at $z \sim 0$. In our knowledge, this is the first study of the age and *Z* of galaxies in a supercluster providing a continuous range of environments. If confirmed, the statistical trends observed here would help refine recipes for the evolution of galaxies in different environments in simulations.

We believe deeper spectroscopic data for a range of environments is critical to confirm the observations made in this work. Although the Coma supercluster provides a unique laboratory where galaxies spanning almost three orders of magnitude in stellar mass could be explored in a continuous range of environments, it may not be a fair representative of the nearby Universe because it is $\sim$3 times denser than the surrounding space (Hogg et al., 2004; Gavazzi et al., 2010). Future large facilities such as the Large Synoptic Survey Telescope (LSST), combined with spectroscopic follow-up and 21-cm data, will be a key to confirming such trends and understanding their origin. Large radio surveys planned for the near future may be able to confirm how, and how much of the cold gas is accreted by galaxies from the cosmic-web.

Chapter 7

Summary

In the work presented in this thesis, I have carried out the first detailed studies of the hot X-ray emitting gas within two nearby galaxy clusters – Abell 2151 (z = 0.0368) and Abell 1569 (z = 0.0784) – using data from the *XMM-Newton* and *Chandra* space observatories. X-ray surface brightness images of the clusters have been obtained to analyze their X-ray morphology and detect the presence of small and large-scale substructures. The brightness images show the presence of significant substructure in both A2151 and A1569. I have investigated the thermodynamic properties of the intracluster medium by performing a detailed spectral analysis within each subcluster of the two clusters. Radial profiles and 2D maps of metallicity and thermodynamic properties of the gas have been presented to test for the presence of cool cores and to examine the merger dynamics of the systems. Estimates for various physical properties of the clusters, for e.g., the X-ray luminosity, gas mass, total mass, central cooling time, have been obtained. The subclusters in A1569 host extended radio galaxies at their centres. Radio observations of these galaxies with the *Very Large Array* have been used to take a closer look at their interaction with the surrounding intracluster gas. I have searched for cavities and merger signatures in the ICM of A1569 to understand the effect of radio-mode feedback operating in the subclusters and the influence of the gas environment on radio galaxies. In addition to the above, I have used spectroscopic data from the *Sloan Digital Sky Survey* to explore the statistical trends in the luminosity-weighted age and metallicity of galaxies in the Coma supercluster ($170^\circ \leq$ RA (J2000) $\leq 200^\circ$, $17^\circ \leq$ Dec (J2000) $\leq 33^\circ$, and $0.0142 \leq z \leq 0.0328$) as a function of their stellar mass and large-scale environment, viz. clusters/groups, filaments, and voids. Three spectral absorption line indices defined on the Lick system have been used in this statistical study; Hβ (4847.875 Å- 4876.625 Å) is used as an indicator of age, and the mean of Fe5270 (5245.650 Å- 5285.650 Å) and Fe5335 (5312.125 Å- 5352.125 Å) indices, $\langle$Fe$\rangle$, is adopted as an indicator of the metallicity of galaxies. The observed line indices are transformed into luminosity-weighted mean age and mean metal content of galaxies using Single Stellar Population models. The trends of age and Z have been obtained for two samples: a *complete* sample of 2,953 galaxies, many of which have large errors in the absorption line indices, and a *red* sample which is a reduced subset of the complete sample comprising 1,263 galaxies where

every absorption line index is subject to an error of < 20 per cent. I report the main findings of my research in the following sections.

7.1 Abell 2151

- The two-component X-ray structure of the central subcluster in Abell 2151, A2151C, is confirmed. The western subclump within A2151C, A2151C(B), is brighter and has $L_{X\,(0.4-7.0\,\mathrm{keV})} = 3.03^{+0.02}_{-0.04} \times 10^{43}$ erg s^{-1}, while the eastern component, A2151C(F), is fainter with $L_{X\,(0.4-7.0\,\mathrm{keV})} = 1.13 \pm 0.02 \times 10^{43}$ erg s^{-1}.

- A2151C(B) displays a fairly regular X-ray morphology, whereas A2151C(F) is quite irregular. Several compact groups of galaxies are also seen within A2151C(F).

- Low average temperature, 2.01 ± 0.05 keV for A2151C(B) and 1.17 ± 0.04 keV for A2151C(F), representative of galaxy groups rather than clusters is confirmed.

- A2151C(B) has a higher elemental abundance of 0.43 ± 0.05 Z$_\odot$ than A2151C(F) which has an abundance of only 0.13 ± 0.02 Z$_\odot$.

- Low temperature (1.55 ± 0.07 keV) in the central 15 arcsec region in addition to a short cooling time of $\sim$0.81 Gyr confirms the presence of a cool core in A2151C(B). There is no convincing evidence for a cool core in A2151C(F), however.

- An enhancement of temperature or entropy in the overlapping region between A2151C(B) and A2151C(F) is not found, thus making the possibility of an ongoing merger between the two groups seem unlikely.

- A2151C(B) is identified as a rich and relaxed group, while A2151C(F) appears to be in the process of formation.

- A past merger event between A2151C and A2151E (the eastern subcluster of Hercules cluster) seems unlikely.

7.2 Abell 1569

- Abell 1569 consists of two subclusters, one towards the north and the other towards the south. The northern subcluster – A1569N – has $L_{X(0.5\text{–}4.0\text{ keV})} = 4.5 \pm 0.4 \times 10^{42}$ erg s^{-1}, and is $\sim$5 times fainter than the southern subcluster – A1569S – that has $L_{X(0.5\text{–}4.0\text{ keV})} = 2.31 \pm 0.06 \times 10^{43}$ erg s^{-1}.
- The average temperature of A1569N is $1.6^{+0.3}_{-0.3}$ keV while that of A1569S is $1.9^{+0.2}_{-0.1}$ keV.
- X-ray emission from A1569N and A1569S extends to radius $r \sim$248 kpc and $r \sim$370 kpc respectively, which along with the low temperature and luminosity values confirms that the two subclusters are indeed galaxy groups.
- A1569N has an average elemental abundance of $0.16^{+0.23}_{-0.13}$ Z$_\odot$ while this value is $0.24^{+0.10}_{-0.08}$ Z$_\odot$ for A1569S.
- Both A1569N and A1569S lack the presence of a large ($\gtrsim$ 40–50 kpc) cool core associated with the intracluster gas.
- A pair of cavities coincident with extended radio emission from the central galaxy 1233+169 in A1569N is detected.
- The mechanical power associated with the cavity pair ($\sim 2.1 \times 10^{43}$ erg s^{-1}) is an order of magnitude larger than the X-ray radiative loss in the central region of A1569N ($2.2 \pm 0.2 \times 10^{42}$ erg s^{-1}), pointing towards cavity-induced heating of the gas in A1569N.
- A surface brightness edge is detected at 1.01 arcmin along the eastern sector 145–237° in A1569S. The edge corresponds to a gas density jump of 2.3 ± 0.6 and a pressure drop of $2.5^{+2.4}_{-1.2}$.
- The detected density discontinuity is perpendicular to the line bisecting the angle between the tails of the central WAT galaxy, 1233+168, in A1569S, which is indicative of a head-on merger occurring between A1569S and a subcluster falling in from the west along the line bisecting the WAT tails.
- The shock associated with the merger is a weak shock with Mach number $\sim$1.7 and velocity equal to 1414 km s^{-1}.
- The proposed merger scenario and the accompanying ICM bulk flow is likely responsible for the bending of the WAT source 1233+168 in A1569S.

7.3 Age and metallicity of galaxies in the Coma supercluster

- The stellar metallicity (Z) of galaxies declines with increasing age in cluster and filament environments alike. Similar trends are observed for the dwarf and giant galaxies.
- At fixed luminosity-weighted age, stellar metallicity of all galaxies, dwarfs and giants, is independent of stellar mass except the most massive ($M^*/M_\odot \gtrsim 10^{10.7}$), oldest galaxies ($\gtrsim$ 9 Gyr) for which the Z declines sharply with M^*. This trend is best observed in the low uncertainty sub-sample.
- Massive galaxies ($M^*/M_\odot > 10^{10.5}$) in clusters are older than the filaments galaxies by $\sim$0.7–0.8 Gyr, while their counterparts in the voids are younger than filament galaxies by $\sim$0.5–0.7 Gyr. The age distributions for the intermediate mass galaxies ($10^{10} < M^*/M_\odot < 10^{10.5}$) are similar but more significant, such that the galaxies in clusters are older than the filament galaxies by 1–1.5 Gyr, while their counterparts in the voids are younger than filament galaxies by $\sim$1 Gyr.
- The Z of intermediate mass galaxies ($10^{10} < M^*/M_\odot < 10^{10.5}$) in void environment is $\sim$0.1 dex lower than their counterparts in clusters or filaments.
- The median stellar Z of filament galaxies declines towards the central spine of the cylinder. This result indicates that some mechanism, most likely the infall of new unenriched gas on the cosmic web being accreted by the filament galaxies, is leading to a lower Z.

7.4 Future goals and interests

Several future goals stem from the research works I have carried out during my Ph.D. My work on the intracluster medium of A2151C has paved the way for future work targeting the entire Abell 2151 field (including all subclusters), using radio and deeper X-ray observations. As mentioned in Chapter 4, a previous study of A2151 by Bird et al. (1995) did not attribute the bimodality in X-ray emission in A2151C to correspond to two separate features in their galaxy density map. Instead, the authors reported a single galaxy density peak associated with A2151C. Based on this and the presence of the WAT source (often associated with clusters mergers) NGC 6047 within A2151C(F), they postulated that the gas identified with A2151C(F) is the ram-pressure stripped part of A2151E (the gas clump towards further east)

which got trapped within the deeper potential well of A2151C(B), when a merger event between A2151C(B) and A2151E took place. The analysis presented in Chapter 4 points towards a different scenario. The X-ray emission in A2151C(F) is now seen to coincide with a definite structure in the spatial distribution of galaxies. Besides, A2151C(B) appears to be fairly symmetric and undisturbed, and also contains a cool core which seems to be intact even after the supposed occurrence of a merger event. The radio jets associated with NGC 6047 extend $\sim$52 arcsec or $\sim$40 kpc across in a N-S direction and form a small-scale structure. Their extent is comparable to the optical diameter of the galaxy ($\sim$81 arcsec or $\sim$61 kpc). The interstellar medium rather than a merger activity may therefore play a non-negligible role in shaping the tails of NGC 6047 in contrast with large-scale WATs ($\gtrsim$ 200 kpc) which are often thought to be created in cluster mergers. Nonetheless, if the hypothesis of Bird et al. (1995) is assumed to be true, it may be possible that the merger between A2151C(B) and A2151E was either a minor one or it took place at a time when A2151C(B) had already developed a well defined cool core (major mergers often tend to disrupt cool cores, more so if the mergers take place in the early evolutionary stage of the cluster). It is, therefore, imperative to propose deeper X-ray as well as radio observations of A2151 to establish the correctness of the tentative post-merger scenario proposed by Bird et al. (1995) or rule it out. An immediate research plan with regard to Abell 2151 is to observe the entire cluster at low radio frequencies using the upgraded Giant Metrewave Radio Telescope (uGMRT), which can reveal the presence/absence of shocks in this region.

My interest in radio-mode feedback operating in small-scale galaxy clusters and groups has stemmed from the X-ray study of Abell 1569. There is possible evidence for a small-scale cluster-subcluster merger in the southern subcluster of Abell 1569, A1569S, as indicated by its high central entropy and the presence of local gas elongation, and a density discontinuity in between the bent radio tails of 1233+168. As future work, it would be interesting to investigate the existence of a radio halo in a low mass system such as A1569S which shows typical signatures of merging in X-rays. I would also like to propose deeper X-ray observations of A1569 which will prove helpful in confirming the presence/absence of cavities in A1569S and the presence of any AGN driven shocks in the ICM of both A1569N and A1569S. These observations will also enable us to produce high-resolution thermodynamic maps of the two subclusters, detect any metallicity substructure around the radio lobes and visually identify SB edges in the X-ray images. The work on Abell 1569 has also encouraged me to explore the formation of bent-tail radio galaxies, particularly WAT sources, that are usually associated with the brightest cluster galaxies. To this end, I wrote a successful proposal to observe the central radio galaxies in Abell 1569 at low-frequency (650 MHz) with the uGMRT (Observation Cycle 40, January 2021). I plan to use the collected data for a spectral index study of the two galaxies. Another future goal stemming from this work is to investigate the effects of AGN-feedback in

galaxy groups and low-mass galaxy clusters, where this phenomenon has not been explored as much as in massive galaxy clusters. This is crucial to understand the exact differences between galaxy clusters and groups. I believe this is also necessary for a better interpretation of the observed thermodynamic scaling relations of clusters and groups of galaxies.

My work on the Coma supercluster, coupled with the X-ray works conducted as part of this thesis, has sparked my interest in the study of large-scale filamentary structures emitting in the far-ultraviolet and X-rays, better known as the Warm-Hot Intergalactic Medium (WHIM). Probing the WHIM (indirectly or directly) is essential to resolve the missing baryon problem in the local Universe. The WHIM has been indirectly detected by studying the absorption line features in the spectrum of a bright source (e.g., a quasar) in the background of the presumed WHIM and more recently by dispersion measurements of the fast radio bursts (to name a few methods). In recent years, several direct detections of the diffuse X-ray emitting gas associated with filaments (hot-phase WHIM) have been made. These are, however, limited to short (< 10 Mpc) and dense filaments, mainly those between nearby pairs of clusters or individually extending beyond the virial radii of clusters. It is only now that direct detection of the low-density WHIM and characterisation of its properties are becoming possible with the new *eROSITA* telescope, which shows a promising prospect for mapping out the large-scale cosmic web in X-rays. In the context of galaxy clusters, characterisation of the soft X-ray background – the emission from the Milky Way halo in particular – is another research area that draws my attention. Correctly accounting for the galactic foreground contribution is imperative for an accurate estimation of the temperature (and other derived thermodynamic properties) of galaxy clusters, particularly in case of low-temperature systems such as galaxy groups. Recent studies conducted in this active area of research indicate that the Galactic Halo may contain several discrete gas components, with the hottest gas component approaching temperature $\gtrsim 10^7$ K. These results are, however, limited by X-ray observations along several lines of sight. Deeper observations along as many sightlines as possible can test these results and impact our current understanding of galaxy cluster/group properties.

Bibliography

Abazajian K., et al., 2003, The Astronomical Journal, 126, 2081

Abell G. O., 1958, The Astrophysical Journal Supplement, 3, 211

Abell G. O., Corwin Harold G. J., Olowin R. P., 1989, The Astrophysical Journal Supplement, 70, 1

Abramopoulos F., Ku W. H. M., 1983, The Astrophysical Journal, 271, 446

Agulli I., Aguerri J. A. L., Diaferio A., Dominguez Palmero L., Sánchez-Janssen R., 2017, Monthly Notices of the Royal Astronomical Society, 467, 4410

Ahumada R., et al., 2020, The Astrophysical Journal Supplement, 249, 3

Aihara H., et al., 2011, ApJS, 193, 29

Allen S. W., Evrard A. E., Mantz A. B., 2011, Annual Review of Astronomy and Astrophysics, 49, 409

Alpaslan M., et al., 2015, MNRAS, 451, 3249

Alpaslan M., et al., 2016, Monthly Notices of the Royal Astronomical Society, 457, 2287

Annibali F., Bressan A., Rampazzo R., Zeilinger W., Danese L., 2007, in Vallenari A., Tantalo R., Portinari L., Moretti A., eds, Astronomical Society of the Pacific Conference Series Vol. 374, From Stars to Galaxies: Building the Pieces to Build Up the Universe. p. 469 (arXiv:astro-ph/0702451)

Arnaud K. A., 1996, in Jacoby G. H., Barnes J., eds, Astronomical Society of the Pacific Conference Series Vol. 101, Astronomical Data Analysis Software and Systems V. p. 17

Arp H., 1966, The Astrophysical Journal Supplement, 14, 1

Babazaki Y., Mitsuishi I., Ota N., Sasaki S., Böhringer H., Chon G., Pratt G. W., Matsumoto H., 2018, Publications of the Astronomical Society of Japan, 70, 46

Babyk I., Melnyk O., Elyiv A., 2012, Advances in Astronomy and Space Physics, 2, 56

Bahcall N. A., 1999, in Dekel A., Ostriker J. P., eds, Formation of Structure in the Universe. p. 135

Baillard A., et al., 2011, Astronomy & Astrophysics, 532, A74

Bamford S. P., et al., 2009, Monthly Notices of the Royal Astronomical Society, 393, 1324

Barmby P., Huchra J. P., 1998, The Astronomical Journal, 115, 6

Bauer F. E., Fabian A. C., Sanders J. S., Allen S. W., Johnstone R. M., 2005, Monthly Notices of the Royal Astronomical Society, 359, 1481

Beisbart C., Valdarnini R., Buchert T., 2001, Astronomy & Astrophysics, 379, 412

Bell E. F., de Jong R. S., 2000, MNRAS, 312, 497

Best P. N., Heckman T. M., 2012, Monthly Notices of the Royal Astronomical Society, 421, 1569

Best P. N., von der Linden A., Kauffmann G., Heckman T. M., Kaiser C. R., 2007, Monthly Notices of the Royal Astronomical Society, 379, 894

Bird C. M., Dickey J. M., Salpeter E. E., 1993, The Astrophysical Journal, 404, 81

Bird C. M., Davis D. S., Beers T. C., 1995, The Astronomical Journal, 109, 920

Bîrzan L., Rafferty D. A., McNamara B. R., Wise M. W., Nulsen P. E. J., 2004, The Astrophysical Journal, 607, 800

Bîrzan L., McNamara B. R., Nulsen P. E. J., Carilli C. L., Wise M. W., 2008, The Astrophysical Journal, 686, 859

Biviano A., Fadda D., Durret F., Edwards L. O. V., Marleau F., 2011, Astronomy & Astrophysics, 532, A77

Blanton E. L., Sarazin C. L., McNamara B. R., Wise M. W., 2001, The Astrophysical Journal Letters, 558, L15

Blanton M. R., Eisenstein D., Hogg D. W., Schlegel D. J., Brinkmann J., 2005a, ApJ, 629, 143

Blanton M. R., Eisenstein D., Hogg D. W., Schlegel D. J., Brinkmann J., 2005b, The Astrophysical Journal, 629, 143

Blanton E. L., Clarke T. E., Sarazin C. L., Randall S. W., McNamara B. R., 2010, Proceedings of the National Academy of Science, 107, 7174

Böhringer H., 1999, in Aschenbach B., Freyberg M. J., eds, Vol. 272, Highlights in X-ray Astronomy. p. 248

Böhringer H., Werner N., 2010, Astronomy & Astrophysics Reviews, 18, 127

Böhringer H., Matsushita K., Churazov E., Ikebe Y., Chen Y., 2002, Astronomy & Astrophysics, 382, 804

Boselli A., Gavazzi G., 2006, Publications of the Astronomical Society of the Pacific, 118, 517

Bothwell M. S., Maiolino R., Kennicutt R., Cresci G., Mannucci F., Marconi A., Cicone C., 2013, MNRAS, 433, 1425

Botteon A., Gastaldello F., Brunetti G., 2018, Monthly Notices of the Royal Astronomical Society, 476, 5591

Bourdin H., Mazzotta P., Markevitch M., Giacintucci S., Brunetti G., 2013, The Astrophysical Journal, 764, 82

Bradt H., 2008, Astrophysics Processes

Brinchmann J., Charlot S., White S. D. M., Tremonti C., Kauffmann G., Heckman T., Brinkmann J., 2004, MNRAS, 351, 1151

Brodie J. P., Huchra J. P., 1991, ApJ, 379, 157

Burns J. O., Rhee G., Owen F. N., Pinkney J., 1994, The Astrophysical Journal, 423, 94

Burns J. O., Gomez P., Pinkney S., Roettiger K., Loken C., 1996, in Trimble V., Reisenegger A., eds, Astronomical Society of the Pacific Conference Series Vol. 88, Clusters, Lensing, and the Future of the Universe. p. 184

Burns J. O., Hallman E. J., Gantner B., Motl P. M., Norman M. L., 2008, The Astrophysical Journal, 675, 1125

Byram E. T., Chubb T. A., Friedman H., 1969, in Quasars and high-energy astronomy. p. 245

Caldwell N., Rose J. A., Concannon K. D., 2003, AJ, 125, 2891

Cappelluti N., et al., 2017, The Astrophysical Journal, 837, 19

Carter D., et al., 2002, ApJ, 567, 772

Castignani G., et al., 2021, arXiv e-prints, p. arXiv:2110.13797

Chen Y., Reiprich T. H., Böhringer H., Ikebe Y., Zhang Y. Y., 2007, Astronomy & Astrophysics, 466, 805

Chen Y.-C., Ho S., Freeman P. E., Genovese C. R., Wasserman L., 2015, MNRAS, 454, 1140

Chen Y.-C., et al., 2017, Monthly Notices of the Royal Astronomical Society, 466, 1880

Chincarini G., Rood H. J., 1976, The Astrophysical Journal, 206, 30

Chisholm J., Tremonti C., Leitherer C., 2018, MNRAS, 481, 1690

Chon G., Böhringer H., Krause M., Trümper J., 2012, Astronomy & Astrophysics, 545, L3

Chung A., van Gorkom J. H., Kenney J. D. P., Crowl H., Vollmer B., 2009, The Astronomical Journal, 138, 1741

Churazov E., Brüggen M., Kaiser C. R., Böhringer H., Forman W., 2001, The Astrophysical Journal, 554, 261

Churazov E., Sunyaev R., Forman W., Böhringer H., 2002, Monthly Notices of the Royal Astronomical Society, 332, 729

Cid Fernandes R., Asari N. V., Sodré L., Stasińska G., Mateus A., Torres-Papaqui J. P., Schoenell W., 2007, MNRAS, 375, L16

Collobert M., Sarzi M., Davies R. L., Kuntschner H., Colless M., 2006, MNRAS, 370, 1213

Conroy C., 2013, Annual Review of Astronomy and Astrophysics, 51, 393

Cooper M. C., Tremonti C. A., Newman J. A., Zabludoff A. I., 2008, MNRAS, 390, 245

Croston J. H., Hardcastle M. J., Birkinshaw M., 2005, Monthly Notices of the Royal Astronomical Society, 357, 279

Croston J. H., Hardcastle M. J., Birkinshaw M., Worrall D. M., Laing R. A., 2008, Monthly Notices of the Royal Astronomical Society, 386, 1709

D'Souza R., Bell E. F., 2018, MNRAS, 474, 5300

Darvish B., Sobral D., Mobasher B., Scoville N. Z., Best P., Sales L. V., Smail I., 2014, The Astrophysical Journal, 796, 51

De Luca A., Molendi S., 2004, Astronomy & Astrophysics, 419, 837

Domainko W., et al., 2005, Advances in Space Research, 36, 685

Douglass E. M., Blanton E. L., Clarke T. E., Randall S. W., Wing J. D., 2011, The Astrophysical Journal, 743, 199

Dressler A., 1980, ApJ, 236, 351

Dressler A., Shectman S. A., 1988, The Astronomical Journal, 95, 985

Dwarakanath K. S., Parekh V., Kale R., George L. T., 2018, Monthly Notices of the Royal Astronomical Society, 477, 957

Eckert D., Finoguenov A., Ghirardini V., Grandis S., Kaefer F., Sanders J., Ramos-Ceja M., 2020, The Open Journal of Astrophysics, 3, 12

Eckmiller H. J., Hudson D. S., Reiprich T. H., 2011, Astronomy & Astrophysics, 535, A105

Edge A. C., Stewart G. C., 1991, Monthly Notices of the Royal Astronomical Society, 252, 414

Ellison S. L., Simard L., Cowan N. B., Baldry I. K., Patton D. R., McConnachie A. W., 2009, MNRAS, 396, 1257

Erb D. K., Shapley A. E., Pettini M., Steidel C. C., Reddy N. A., Adelberger K. L., 2006, ApJ, 644, 813

Escalera E., Biviano A., Girardi M., Giuricin G., Mardirossian F., Mazure A., Mezzetti M., 1994, The Astrophysical Journal, 423, 539

Evrard A. E., Mohr J. J., Fabricant D. G., Geller M. J., 1993, The Astrophysical Journal Letters, 419, L9

Evrard A. E., Metzler C. A., Navarro J. F., 1996, The Astrophysical Journal, 469, 494

Faber S. M., Friel E. D., Burstein D., Gaskell C. M., 1985, ApJS, 57, 711

Fabian A. C., 1994, Annual Review of Astronomy and Astrophysics, 32, 277

Fabian A. C., 2012, Annual Review of Astronomy and Astrophysics, 50, 455

Fabian A. C., Sanders J. S., Allen S. W., Crawford C. S., Iwasawa K., Johnstone R. M., Schmidt R. W., Taylor G. B., 2003, Monthly Notices of the Royal Astronomical Society, 344, L43

Falcón-Barroso J., Sánchez-Blázquez P., Vazdekis A., Ricciardelli E., Cardiel N., Cenarro A. J., Gorgas J., Peletier R. F., 2011, Astronomy & Astrophysics, 532, A95

Fanaroff B. L., Riley J. M., 1974, Monthly Notices of the Royal Astronomical Society, 167, 31P

Feretti L., Giovannini G., 1985, Astronomy & Astrophysics, 147, L13

Feretti L., Giovannini G., 1988, Astronomy & Astrophysics, 191, 21

Feretti L., Venturi T., 2002, Radio Galaxies and Their Environment. Springer Netherlands, Dordrecht, pp 163–195, doi:10.1007/0-306-48096-4˙6, https://doi.org/10.1007/0-306-48096-4_6

Feretti L., Giovannini G., Govoni F., Murgia M., 2012, Astronomy & Astrophysics Reviews, 20, 54

Fontanelli P., 1984, A&A, 138, 85

Fontanot F., De Lucia G., Monaco P., Somerville R. S., Santini P., 2009, MNRAS, 397, 1776

Forman W., Jones C., 1982, Annual Review of Astronomy and Astrophysics, 20, 547

Forman W., Jones C., Cominsky L., Julien P., Murray S., Peters G., Tananbaum H., Giacconi R., 1978, The Astrophysical Journal Supplement, 38, 357

Gallazzi A., Charlot S., Brinchmann J., White S. D. M., Tremonti C. A., 2005, MNRAS, 362, 41

Garmire G. P., Bautz M. W., Ford P. G., Nousek J. A., Ricker George R. J., 2003, in Truemper J. E., Tananbaum H. D., eds, Society of Photo-Optical Instrumentation Engineers (SPIE) Conference Series Vol. 4851, X-Ray and Gamma-Ray Telescopes and Instruments for Astronomy.. pp 28–44, doi:10.1117/12.461599

Gavazzi G., Fumagalli M., Cucciati O., Boselli A., 2010, A&A, 517, A73

Ge C., et al., 2019, Monthly Notices of the Royal Astronomical Society, 486, L36

Geller M. J., Beers T. C., 1982, Publications of the Astronomical Society of the Pacific, 94, 421

Giacconi R., Murray S., Gursky H., Kellogg E., Schreier E., Tananbaum H., 1972, The Astrophysical Journal, 178, 281

Giacintucci S., Venturi T., 2009, Astronomy & Astrophysics, 505, 55

Giacintucci S., Markevitch M., Brunetti G., Cassano R., Venturi T., 2011, Astronomy & Astrophysics, 525, L10

Giovanelli R., Haynes M. P., 1985, The Astrophysical Journal, 292, 404

Girardi L., Bressan A., Bertelli G., Chiosi C., 2000, A&AS, 141, 371

Gitti M., Brighenti F., McNamara B. R., 2012, Advances in Astronomy, 2012, 950641

Gomez P. L., Ledlow M. J., Burns J. O., Pinkey J., Hill J. M., 1997a, The Astronomical Journal, 114, 1711

Gómez P. L., Pinkney J., Burns J. O., Wang Q., Owen F. N., Voges W., 1997b, The Astrophysical Journal, 474, 580

Gómez P. L., et al., 2003, The Astrophysical Journal, 584, 210

Gorgas J., Faber S. M., Burstein D., Gonzalez J. J., Courteau S., Prosser C., 1993, ApJS, 86, 153

Goto T., Yamauchi C., Fujita Y., Okamura S., Sekiguchi M., Smail I., Bernardi M., Gomez P. L., 2003, Monthly Notices of the Royal Astronomical Society, 346, 601

Gregory S. A., Thompson L. A., 1978, The Astrophysical Journal, 222, 784

Gunn J. E., et al., 2006, The Astronomical Journal, 131, 2332

Hashimoto Y., Oemler Augustus J., Lin H., Tucker D. L., 1998, The Astrophysical Journal, 499, 589

Heavens A., Panter B., Jimenez R., Dunlop J., 2004, Nature, 428, 625

Helsdon S. F., Ponman T. J., 2000a, Monthly Notices of the Royal Astronomical Society, 315, 356

Helsdon S. F., Ponman T. J., 2000b, Monthly Notices of the Royal Astronomical Society, 319, 933

Henning J. W., Gantner B., Burns J. O., Hallman E. J., 2009, The Astrophysical Journal, 697, 1597

Hickox R. C., Markevitch M., 2006, The Astrophysical Journal, 645, 95

Hoang D. N., et al., 2019, Astronomy & Astrophysics, 622, A20

Hogg D. W., et al., 2004, ApJL, 601, L29

Huang Z., Sarazin C. L., 1996, The Astrophysical Journal, 461, 622

Hubble E. P., 1925, The Astrophysical Journal, 62, 409

Hubble E. P., 1926, The Astrophysical Journal, 63, 236

Hudson D. S., Mittal R., Reiprich T. H., Nulsen P. E. J., Andernach H., Sarazin C. L., 2010, Astronomy & Astrophysics, 513, A37

Janowiecki S., Catinella B., Cortese L., Saintonge A., Brown T., Wang J., 2017, MNRAS, 466, 4795

Jeltema T. E., Canizares C. R., Bautz M. W., Buote D. A., 2005, The Astrophysical Journal, 624, 606

Jetha N. N., Ponman T. J., Hardcastle M. J., Croston J. H., 2007, Monthly Notices of the Royal Astronomical Society, 376, 193

Jimenez R., Panter B., Heavens A. F., Verde L., 2005, MNRAS, 356, 495

Jing Y. P., Mo H. J., Borner G., Fang L. Z., 1995, Monthly Notices of the Royal Astronomical Society, 276, 417

Jones C., Forman W., 1992, in Fabian A. C., ed., NATO Advanced Study Institute (ASI) Series C Vol. 366, Clusters and Superclusters of Galaxies. p. 49, doi:10.1007/978-94-011-2482-9_4

Jones C., Mandel E., Schwarz J., Forman W., Murray S. S., Harnden F. R. J., 1979, The Astrophysical Journal Letters, 234, L21

Jørgensen I., 1997, MNRAS, 288, 161

Jørgensen I., 1999, MNRAS, 306, 607

Kauffmann G., et al., 2003, MNRAS, 346, 1055

Kauffmann G., White S. D. M., Heckman T. M., Ménard B., Brinchmann J., Charlot S., Tremonti C., Brinkmann J., 2004, Monthly Notices of the Royal Astronomical Society, 353, 713

Klemola A. R., 1969, The Astronomical Journal, 74, 804

Kraljic K., et al., 2018, Monthly Notices of the Royal Astronomical Society, 474, 547

Kraljic K., Davé R., Pichon C., 2020, Monthly Notices of the Royal Astronomical Society, 493, 362

Kravtsov A. V., Borgani S., 2012, Annual Review of Astronomy and Astrophysics, 50, 353

Kreckel K., Platen E., Aragón-Calvo M. A., van Gorkom J. H., van de Weygaert R., van der Hulst J. M., Beygu B., 2012, The Astronomical Journal, 144, 16

Kroupa P., 2001, MNRAS, 322, 231

Kuntschner H., 2000, MNRAS, 315, 184

Kuntschner H., Davies R. L., 1998, MNRAS, 295, L29

Kuntschner H., Lucey J. R., Smith R. J., Hudson M. J., Davies R. L., 2001, MNRAS, 323, 615

Kuntz K. D., Snowden S. L., 2008, Astronomy & Astrophysics, 478, 575

Kuutma T., Tamm A., Tempel E., 2017, Astronomy & Astrophysics, 600, L6

Lara-López M. A., et al., 2010, A&A, 521, L53

Leethochawalit N., Kirby E. N., Moran S. M., Ellis R. S., Treu T., 2018, ApJ, 856, 15

Lequeux J., Peimbert M., Rayo J. F., Serrano A., Torres-Peimbert S., 1979, A&A, 80, 155

Liao S., Gao L., 2019, MNRAS, 485, 464

Lima Neto G. B., Capelato H. V., Sodré L. J., Proust D., 2003, Astronomy & Astrophysics, 398, 31

Liuzzo E., Giovannini G., Giroletti M., 2010, in 10th European VLBI Network Symposium and EVN Users Meeting: VLBI and the New Generation of Radio Arrays. p. 28

Loken C., Roettiger K., Burns J. O., Norman M., 1995, The Astrophysical Journal, 445, 80

Lovisari L., Reiprich T. H., Schellenberger G., 2015, Astronomy & Astrophysics, 573, A118

Lumb D. H., Warwick R. S., Page M., De Luca A., 2002, Astronomy & Astrophysics, 389, 93

Macario G., Markevitch M., Giacintucci S., Brunetti G., Venturi T., Murray S. S., 2011, The Astrophysical Journal, 728, 82

Maccagni D., Garilli B., Tarenghi M., 1995, The Astronomical Journal, 109, 465

Magliocchetti M., Brüggen M., 2007, Monthly Notices of the Royal Astronomical Society, 379, 260

Magri C., Haynes M. P., Forman W., Jones C., Giovanelli R., 1988, The Astrophysical Journal, 333, 136

Mahajan S., Haines C. P., Raychaudhury S., 2010, MNRAS, 404, 1745

Mahajan S., Raychaudhury S., Pimbblet K. A., 2012, Monthly Notices of the Royal Astronomical Society, 427, 1252

Mahajan S., Singh A., Shobhana D., 2018, MNRAS, 478, 4336

Mannucci F., Cresci G., Maiolino R., Marconi A., Gnerucci A., 2010, MNRAS, 408, 2115

Markevitch M., Vikhlinin A., 2007, Physics Reports, 443, 1

Markevitch M. L., Sarazin C. L., Irwin J. A., 1996, The Astrophysical Journal Letters, 472, L17

Mathews W. G., Brighenti F., 2003, Annual Review of Astronomy and Astrophysics, 41, 191

Maughan B. J., Giles P. A., Randall S. W., Jones C., Forman W. R., 2012, Monthly Notices of the Royal Astronomical Society, 421, 1583

McNamara B. R., Nulsen P. E. J., 2007, Annual Review of Astronomy and Astrophysics, 45, 117

McNamara B. R., et al., 2000, The Astrophysical Journal Letters, 534, L135

Michielsen D., et al., 2008, MNRAS, 385, 1374

Miller N. A., Owen F. N., 2001, The Astrophysical Journal Supplement, 134, 355

Mitchell R. J., Culhane J. L., Davison P. J. N., Ives J. C., 1976, Monthly Notices of the Royal Astronomical Society, 175, 29P

Mitchell R. J., Dickens R. J., Burnell S. J. B., Culhane J. L., 1979, Monthly Notices of the Royal Astronomical Society, 189, 329

Mitsuishi I., Babazaki Y., Ota N., Sasaki S., Böhringer H., Chon G., Pratt G. W., 2018, Publications of the Astronomical Society of Japan, 70, 112

Monteiro-Oliveira R., Morell D. F., Sampaio V. M., Ribeiro A. L. B., de Carvalho R. R., 2022, Monthly Notices of the Royal Astronomical Society, 509, 3470

Mouhcine M., Baldry I. K., Bamford S. P., 2007, MNRAS, 382, 801

Mulchaey J. S., 2000, Annual Review of Astronomy and Astrophysics, 38, 289

Muldrew S. I., et al., 2012, MNRAS, 419, 2670

Mushotzky R. F., Serlemitsos P. J., Smith B. W., Boldt E. A., Holt S. S., 1978, The Astrophysical Journal, 225, 21

Mushotzky R. F., Holt S. S., Boldt E. A., Serlemitsos P. J., Smith B. W., 1981, The Astrophysical Journal Letters, 244, L47

Neistein E., van den Bosch F. C., Dekel A., 2006, MNRAS, 372, 933

Neumann D. M., Lumb D. H., Pratt G. W., Briel U. G., 2003, Astronomy & Astrophysics, 400, 811

Nulsen P. E. J., Stewart G. C., Fabian A. C., Mushotzky R. F., Holt S. S., Ku W. H. M., Malin D. F., 1982, Monthly Notices of the Royal Astronomical Society, 199, 1089

Nulsen P. E. J., McNamara B. R., Wise M. W., David L. P., 2005, The Astrophysical Journal, 628, 629

O'Dea C. P., Owen F. N., 1985, The Astronomical Journal, 90, 954

O'Sullivan E., Giacintucci S., David L. P., Gitti M., Vrtilek J. M., Raychaudhury S., Ponman T. J., 2011, The Astrophysical Journal, 735, 11

Ogando R. L. C., Maia M. A. G., Pellegrini P. S., da Costa L. N., 2008, AJ, 135, 2424

Osmond J. P. F., Ponman T. J., 2004, Monthly Notices of the Royal Astronomical Society, 350, 1511

Osterbrock D. E., 1974, Astrophysics of gaseous nebulae

Ota N., Fujino Y., Ibaraki Y., Böhringer H., Chon G., 2013, Astronomy & Astrophysics, 556, A21

Owen F. N., Ledlow M. J., 1997, The Astrophysical Journal Supplement, 108, 41

Owen F. N., Rudnick L., 1976, The Astrophysical Journal Letters, 205, L1

Owers M. S., Nulsen P. E. J., Couch W. J., Markevitch M., 2009, The Astrophysical Journal, 704, 1349

Panagoulia E. K., Fabian A. C., Sanders J. S., 2014, Monthly Notices of the Royal Astronomical Society, 438, 2341

Panter B., Jimenez R., Heavens A. F., Charlot S., 2007, MNRAS, 378, 1550

Panter B., Jimenez R., Heavens A. F., Charlot S., 2008, MNRAS, 391, 1117

Pasquali A., Gallazzi A., Fontanot F., van den Bosch F. C., De Lucia G., Mo H. J., Yang X., 2010, MNRAS, 407, 937

Paterno-Mahler R., Blanton E. L., Randall S. W., Clarke T. E., 2013, The Astrophysical Journal, 773, 114

Peng Y.-j., Maiolino R., 2014, MNRAS, 438, 262

Peng Y.-j., et al., 2010, ApJ, 721, 193

Peres C. B., Fabian A. C., Edge A. C., Allen S. W., Johnstone R. M., White D. A., 1998, Monthly Notices of the Royal Astronomical Society, 298, 416

Peterson J. R., Fabian A. C., 2006, Physics Reports, 427, 1

Peterson J. R., et al., 2001, Astronomy & Astrophysics, 365, L104

Peterson J. R., Kahn S. M., Paerels F. B. S., Kaastra J. S., Tamura T., Bleeker J. A. M., Ferrigno C., Jernigan J. G., 2003, The Astrophysical Journal, 590, 207

Pinkney J., Rhee G., Burns J. O., Hill J. M., Oegerle W., Batuski D., Hintzen P., 1993, The Astrophysical Journal, 416, 36

Pinkney J., Burns J. O., Hill J. M., 1994, The Astronomical Journal, 108, 2031

Planck Collaboration et al., 2018, arXiv e-prints, p. arXiv:1807.06209

Planelles S., Quilis V., 2009, Monthly Notices of the Royal Astronomical Society, 399, 410

Poggianti B. M., et al., 2001, ApJ, 562, 689

Porter S. C., Raychaudhury S., Pimbblet K. A., Drinkwater M. J., 2008, Monthly Notices of the Royal Astronomical Society, 388, 1152

Price J., Phillipps S., Huxor A., Smith R. J., Lucey J. R., 2011, MNRAS, 411, 2558

Proctor R. N., Forbes D. A., Hau G. K. T., Beasley M. A., De Silva G. M., Contreras R., Terlevich A. I., 2004, MNRAS, 349, 1381

Rakos K., Schombert J., Maitzen H. M., Prugovecki S., Odell A., 2001, The Astronomical Journal, 121, 1974

Rasmussen J., Ponman T. J., 2007, Monthly Notices of the Royal Astronomical Society, 380, 1554

Reichert G., Mason K. O., Lea S. M., Charles P. A., Bowyer S., Pravdo S., 1981, The Astrophysical Journal, 247, 803

Reiprich T. H., Böhringer H., 2002, The Astrophysical Journal, 567, 716

Reynolds C. S., Brenneman L. W., Stocke J. T., 2005, Monthly Notices of the Royal Astronomical Society, 357, 381

Rines K., Geller M. J., Kurtz M. J., Diaferio A., 2003, AJ, 126, 2152

Rines K., Geller M. J., Kurtz M. J., Diaferio A., 2005, AJ, 130, 1482

Ritchie B. W., Thomas P. A., 2002, Monthly Notices of the Royal Astronomical Society, 329, 675

Roettiger K., Burns J., Loken C., 1993, The Astrophysical Journal Letters, 407, L53

Roettiger K., Burns J. O., Loken C., 1996, The Astrophysical Journal, 473, 651

Rong Y., Liu Y., Zhang S.-N., 2016, Monthly Notices of the Royal Astronomical Society, 455, 2267

Rose J. A., 1976, Astronomy & Astrophysics, Supplement, 23, 109

Rothenflug R., Vigroux L., Mushotzky R. F., Holt S. S., 1984, The Astrophysical Journal, 279, 53

Ryle M., Windram M. D., 1968, Monthly Notices of the Royal Astronomical Society, 138, 1

Sakelliou I., Merrifield M. R., 2000, Monthly Notices of the Royal Astronomical Society, 311, 649

Sánchez-Blázquez P., et al., 2006a, Monthly Notices of the Royal Astronomical Society, 371, 703

Sánchez-Blázquez P., Gorgas J., Cardiel N., González J. J., 2006b, A&A, 457, 787

Sánchez-Blázquez P., Gorgas J., Cardiel N., González J. J., 2006c, A&A, 457, 809

Sanders J. S., 2006, Monthly Notices of the Royal Astronomical Society, 371, 829

Sanders J. S., Fabian A. C., Taylor G. B., 2009, Monthly Notices of the Royal Astronomical Society, 393, 71

Sanders J. S., Fabian A. C., Russell H. R., Walker S. A., Blundell K. M., 2016, Monthly Notices of the Royal Astronomical Society, 460, 1898

Sanderson A. J. R., Ponman T. J., O'Sullivan E., 2006, Monthly Notices of the Royal Astronomical Society, 372, 1496

Santos J. S., Rosati P., Tozzi P., Böhringer H., Ettori S., Bignamini A., 2008, Astronomy & Astrophysics, 483, 35

Sarazin C. L., 1988, X-ray emission from clusters of galaxies. Cambridge University Press

Sarazin C. L., 2002, The Physics of Cluster Mergers. Springer Dordrecht, pp 1–38, doi:10.1007/0-306-48096-4_1

Sarazin C. L., 2004, Journal of Korean Astronomical Society, 37, 433

Schuecker P., Böhringer H., Reiprich T. H., Feretti L., 2001a, Astronomy & Astrophysics, 378, 408

Schuecker P., Böhringer H., Reiprich T. H., Feretti L., 2001b, Astronomy & Astrophysics, 378, 408

Serlemitsos P. J., Smith B. W., Boldt E. A., Holt S. S., Swank J. H., 1977, The Astrophysical Journal Letters, 211, L63

Shectman S. A., 1985, The Astrophysical Journal Supplement, 57, 77

Singh K. P., Westergaard N. J., Schnopper H. W., 1986, The Astrophysical Journal Letters, 308, L51

Singh K. P., Westergaard N. J., Schnopper H. W., 1988, The Astrophysical Journal, 331, 672

Skillman E. D., Kennicutt R. C., Hodge P. W., 1989, ApJ, 347, 875

Skillman E. D., Kennicutt Jr. R. C., Shields G. A., Zaritsky D., 1996, ApJ, 462, 147

Smith R. K., Brickhouse N. S., Liedahl D. A., Raymond J. C., 2001, The Astrophysical Journal Letters, 556, L91

Smith R. J., et al., 2008, MNRAS, 386, L96

Smith R. J., Lucey J. R., Hudson M. J., Allanson S. P., Bridges T. J., Hornschemeier A. E., Marzke R. O., Miller N. A., 2009, MNRAS, 392, 1265

Snow T. P. J., 1970, The Astronomical Journal, 75, 237

Snowden S. L., Mushotzky R. F., Kuntz K. D., Davis D. S., 2008, Astronomy & Astrophysics, 478, 615

Springel V., Frenk C. S., White S. D. M., 2006, Nature, 440, 1137

Stewart G. C., Fabian A. C., Jones C., Forman W., 1984, The Astrophysical Journal, 285, 1

Sun M., 2012a, New Journal of Physics, 14, 045004

Sun M., 2012b, New Journal of Physics, 14, 045004

Szabo T., Pierpaoli E., Dong F., Pipino A., Gunn J., 2011, The Astrophysical Journal, 736, 21

Tamura T., et al., 2001, Astronomy & Astrophysics, 365, L87

Tasca L. A. M., et al., 2009, Astronomy & Astrophysics, 503, 379

Tempel E., Stoica R. S., Saar E., 2013, Monthly Notices of the Royal Astronomical Society, 428, 1827

Thomas D., Maraston C., Bender R., Mendes de Oliveira C., 2005, ApJ, 621, 673

Thomas D., Maraston C., Schawinski K., Sarzi M., Silk J., 2010, MNRAS, 404, 1775

Tiwari J., Singh K. P., 2021, Monthly Notices of the Royal Astronomical Society, 500, 5524

Tiwari J., Singh K. P., 2022, Monthly Notices of the Royal Astronomical Society, 509, 3321

Tiwari J., Mahajan S., Singh K. P., 2020, New Astronomy, 81, 101417

Toloba E., et al., 2009, ApJL, 707, L17

Trager S. C., Faber S. M., Worthey G., González J. J., 2000, AJ, 120, 165

Trager S. C., Faber S. M., Dressler A., 2008, MNRAS, 386, 715

Tremonti C. A., et al., 2004, ApJ, 613, 898

Ubertosi F., Gitti M., Torresi E., Brighenti F., Grandi P., 2021, Monthly Notices of the Royal Astronomical Society, 503, 4627

Vazdekis A., Casuso E., Peletier R. F., Beckman J. E., 1996, ApJS, 106, 307

Vazdekis A., Sánchez-Blázquez P., Falcón-Barroso J., Cenarro A. J., Beasley M. A., Cardiel N., Gorgas J., Peletier R. F., 2010, MNRAS, 404, 1639

Venkatesan T. C. A., Batuski D. J., Hanisch R. J., Burns J. O., 1994, The Astrophysical Journal, 436, 67

Vikhlinin A., Markevitch M., Murray S. S., 2001, The Astrophysical Journal, 551, 160

Weigel A. K., Schawinski K., Bruderer C., 2016, MNRAS, 459, 2150

Weisskopf M. C., Tananbaum H. D., Van Speybroeck L. P., O'Dell S. L., 2000, in Truemper J. E., Aschenbach B., eds, Society of Photo-Optical Instrumentation Engineers (SPIE) Conference Series Vol. 4012, X-Ray Optics, Instruments, and Missions III. pp 2–16 (arXiv:astro-ph/0004127), doi:10.1117/12.391545

Wen Z. L., Han J. L., 2013, Monthly Notices of the Royal Astronomical Society, 436, 275

Willingale R., Hands A. D. P., Warwick R. S., Snowden S. L., Burrows D. N., 2003, Monthly Notices of the Royal Astronomical Society, 343, 995

Willingale R., Starling R. L. C., Beardmore A. P., Tanvir N. R., O'Brien P. T., 2013, Monthly Notices of the Royal Astronomical Society, 431, 394

Wilms J., Allen A., McCray R., 2000, The Astrophysical Journal, 542, 914

Worthey G., 1994, ApJS, 95, 107

Worthey G., 1999, in Hubeny I., Heap S., Cornett R., eds, Astronomical Society of the Pacific Conference Series Vol. 192, Spectrophotometric Dating of Stars and Galaxies. p. 283

Worthey G., Ottaviani D. L., 1997, ApJS, 111, 377

Worthey G., Faber S. M., Gonzalez J. J., Burstein D., 1994, The Astrophysical Journal Supplement, 94, 687

Worthey G., Trager S. C., Faber S. M., 1995, in Buzzoni A., Renzini A., Serrano A., eds, Astronomical Society of the Pacific Conference Series Vol. 86, Fresh Views of Elliptical Galaxies. p. 203

Wright E. L., 2006, Publications of the Astronomical Society of the Pacific, 118, 1711

Wu P.-F., Zahid H. J., Hwang H. S., Geller M. J., 2017, MNRAS, 468, 1881

York D. G., et al., 2000, AJ, 120, 1579

Yuan Z. S., Han J. L., 2020, Monthly Notices of the Royal Astronomical Society, 497, 5485

Zabludoff A. I., Geller M. J., Huchra J. P., Vogeley M. S., 1993, The Astronomical Journal, 106, 1273

Zou S., Maughan B. J., Giles P. A., Vikhlinin A., Pacaud F., Burenin R., Hornstrup A., 2016, Monthly Notices of the Royal Astronomical Society, 463, 820

ZuHone J. A., 2011, The Astrophysical Journal, 728, 54

Zwicky F., 1937, The Astrophysical Journal, 86, 217

Zwicky F., Herzog E., Wild P., Karpowicz M., Kowal C. T., 1961, Catalogue of galaxies and of clusters of galaxies, Vol. I

Zwicky F., Herzog E., Wild P., 1963, Catalogue of galaxies and of clusters of galaxies, Vol. 2

Zwicky F., Karpowicz M., Kowal C. T., 1965, "Catalogue of Galaxies and of Clusters of Galaxies", Vol. V

Zwicky F., Herzog E., Wild P., 1966, Catalogue of galaxies and of clusters of galaxies, Vol. 3

van Speybroeck L. P., Jerius D., Edgar R. J., Gaetz T. J., Zhao P., Reid P. B., 1997, in Hoover R. B., Walker A. B., eds, Society of Photo-Optical Instrumentation Engineers (SPIE) Conference Series Vol. 3113, Grazing Incidence and Multilayer X-Ray Optical Systems. pp 89–104, doi:10.1117/12.278890

van Weeren R. J., de Gasperin F., Akamatsu H., Brüggen M., Feretti L., Kang H., Stroe A., Zandanel F., 2019, Space Science Reviews, 215, 16

van de Weygaert R., et al., 2011, in Environment and the Formation of Galaxies: 30 years later. p. 17 (arXiv:1101.4187), doi:10.1007/978-3-642-20285-8_3

Appendix A

Additional Information

Table A.1: Position, redshift, and derived age and metallicity values along with their upper and lower limits for all galaxies analyzed in the Coma supercluster sample (Chapter 6; §6.3; Table 6.2). Right Ascension and Declination are listed in degrees.

RA (J2000)	Dec (J2000)	z	Age (Gyr)	Age upper (Gyr)	Age lower (Gyr)	Z (dex)	Z upper (dex)	Z lower (dex)
195.313	27.669	0.0236	4.6	13.9	2.2	-0.13	-	-0.46
178.312	20.736	0.0252	2.2	3.1	1.4	-0.12	-	-0.39
191.190	27.500	0.0314	1.8	2.6	1.2	-0.25	-	-0.55
197.003	28.081	0.0192	2.7	5.1	1.9	-0.36	-0.07	-0.64
189.744	27.564	0.0224	2.1	2.9	1.4	-0.16	-	-0.45
179.050	21.394	0.0255	2.1	2.9	1.5	-0.34	0.04	-0.61
180.642	20.815	0.0223	1.7	2.7	1.1	-0.07	-	-0.44
195.960	28.054	0.0210	2.4	4.1	1.5	-0.12	-	-0.42
181.856	28.530	0.0303	1.9	2.9	1.2	0.04	-	-0.31
181.500	27.639	0.0285	2.4	4.1	1.6	-0.31	0.08	-0.61
177.888	27.669	0.0290	1.8	3.1	1.1	0.20	-	-0.23
182.909	19.845	0.0223	2.5	4.0	1.8	-1.12	-0.85	-1.34
178.010	30.320	0.0220	2.3	3.7	1.8	-0.71	-0.50	-1.01
182.309	18.149	0.0232	3.6	11.9	2.3	-0.50	-0.21	-0.89
184.793	28.557	0.0264	2.6	4.9	1.7	-0.25	0.13	-0.56
183.327	19.937	0.0278	2.9	6.4	2.2	-0.44	-0.18	-0.73
174.845	22.119	0.0230	1.4	1.8	1.0	-0.45	-0.06	-0.76
171.016	28.459	0.0232	2.8	5.6	1.9	-0.32	-0.01	-0.61
194.848	27.920	0.0231	4.5	13.6	2.4	-0.30	0.05	-0.64
183.019	32.735	0.0251	2.6	5.1	1.8	-0.36	-0.03	-0.66
196.655	28.338	0.0217	4.4	12.8	2.0	0.14	-	-0.19
170.464	27.540	0.0326	3.8	11.1	2.3	-0.37	-0.08	-0.72
194.402	28.077	0.0225	1.9	3.4	1.1	0.19	-	-0.25
182.822	32.594	0.0232	2.7	5.7	1.9	-0.38	-0.07	-0.69
183.737	23.869	0.0238	2.2	3.5	1.4	-0.23	-	-0.55
184.038	28.130	0.0271	2.7	5.9	1.8	-0.35	-0.04	-0.66
180.716	20.726	0.0232	2.8	6.0	2.1	-0.54	-0.29	-0.82
178.896	32.020	0.0312	1.1	1.6	0.9	-0.10	0.21	-0.58
170.799	24.270	0.0270	1.9	3.3	1.1	0.18	-	-0.25
178.005	20.659	0.0202	1.7	2.4	1.2	-0.42	0.03	-0.69
183.842	23.994	0.0250	2.4	3.7	1.6	-0.43	-0.09	-0.71
188.924	26.222	0.0214	2.8	6.4	1.7	-0.18	-	-0.52
195.533	27.648	0.0230	1.3	1.6	1.0	-0.64	-0.32	-1.04
182.726	25.253	0.0229	1.7	2.4	1.2	-0.54	-0.13	-0.85
197.826	29.794	0.0242	2.3	4.3	1.5	-0.24	0.22	-0.57

continued on next page..

Table A.1 – continued from previous page

RA (J2000)	Dec (J2000)	z	Age (Gyr)	Age upper (Gyr)	Age lower (Gyr)	Z (dex)	Z upper (dex)	Z lower (dex)
176.152	19.752	0.0191	2.4	4.3	1.5	-0.25	0.20	-0.59
176.739	32.654	0.0328	1.0	1.3	0.9	-0.33	-0.06	-0.69
188.850	29.492	0.0152	1.1	1.6	0.8	0.07	-	-0.43
178.458	21.219	0.0230	1.1	1.4	0.9	-0.33	-0.04	-0.70
194.060	30.200	0.0250	3.0	9.8	1.6	-0.01	-	-0.39
193.968	25.183	0.0229	1.3	1.6	1.0	-0.78	-0.41	-1.23
193.074	27.086	0.0210	2.7	5.5	1.9	-0.77	-0.49	-1.10
187.036	20.180	0.0226	2.4	4.4	1.7	-0.62	-0.32	-0.97
198.784	30.404	0.0232	1.7	2.3	1.4	-0.80	-0.49	-1.13
172.764	25.198	0.0320	1.7	2.5	1.4	-0.97	-0.63	-1.28
196.118	23.575	0.0314	2.4	4.8	1.4	-0.16	-	-0.54
185.326	32.711	0.0230	1.3	1.7	1.0	-0.48	-0.10	-0.87
175.575	30.230	0.0322	2.8	7.6	1.8	-0.31	0.08	-0.68
181.464	24.356	0.0234	2.3	4.4	1.4	-0.09	-	-0.44
193.667	32.367	0.0242	1.6	2.4	1.1	-0.27	0.19	-0.62
196.563	25.461	0.0242	1.5	1.8	1.2	-0.95	-0.56	-1.30
184.071	18.413	0.0299	1.6	2.5	1.1	-0.20	-	-0.59
177.909	21.463	0.0265	2.6	5.9	1.6	-0.29	0.14	-0.64
194.856	27.934	0.0253	2.0	3.1	1.2	-0.08	-	-0.41
183.076	27.530	0.0279	2.9	10.7	1.6	-0.10	-	-0.54
186.271	25.958	0.0222	2.4	5.0	1.6	-0.55	-0.18	-0.91
197.458	24.578	0.0236	1.9	3.0	1.5	-0.80	-0.51	-1.14
192.873	31.815	0.0245	2.8	8.6	1.8	-0.41	-0.06	-0.80
196.581	28.053	0.0241	3.0	10.0	1.6	-0.10	-	-0.50
177.850	21.068	0.0264	3.8	13.1	2.1	-0.31	0.08	-0.71
187.502	32.880	0.0308	2.1	3.7	1.4	-0.51	-0.03	-0.90
195.038	27.866	0.0177	1.4	1.7	1.1	-0.70	-0.35	-1.13
181.490	31.348	0.0232	2.2	4.1	1.3	-0.26	-	-0.64
197.997	20.794	0.0225	2.3	3.7	1.7	-0.83	-0.56	-1.14
189.555	28.937	0.0244	2.4	4.4	1.6	-0.47	-0.11	-0.79
194.734	28.464	0.0197	1.0	1.4	0.8	-0.22	0.09	-0.67
182.653	19.016	0.0266	1.6	2.4	1.1	-0.32	0.15	-0.63
175.738	26.060	0.0306	2.7	7.5	1.5	-0.03	-	-0.45
195.402	27.708	0.0264	3.0	10.9	1.7	-0.22	-	-0.65
184.880	20.186	0.0294	1.5	2.3	1.0	-0.15	-	-0.58
199.867	27.749	0.0232	1.5	2.0	1.1	-0.59	-0.19	-0.96
185.015	20.408	0.0308	2.2	3.2	1.4	-0.25	0.19	-0.55
194.529	26.787	0.0240	1.8	2.8	1.4	-0.63	-0.25	-1.01
192.448	32.080	0.0318	3.0	10.2	2.1	-0.52	-0.21	-0.92
175.621	21.587	0.0224	2.5	6.6	1.5	-0.43	0.04	-0.86
177.773	20.147	0.0208	3.0	8.6	2.1	-0.46	-0.18	-0.83
182.795	24.546	0.0254	2.2	4.2	1.3	-0.21	-	-0.58
171.334	22.733	0.0238	1.7	3.0	1.0	0.00	-	-0.47
195.307	28.083	0.0194	2.9	12.0	1.4	-0.04	-	-0.52
173.608	28.076	0.0303	1.5	2.0	1.1	-0.66	-0.27	-1.08
191.614	20.289	0.0292	2.3	3.5	1.6	-0.44	-0.07	-0.73
187.266	27.779	0.0234	1.8	3.0	1.5	-1.08	-0.67	-1.41
194.906	27.336	0.0233	2.7	9.8	1.5	-0.14	-	-0.59
191.624	30.849	0.0288	1.3	1.9	0.9	-0.14	-	-0.59
199.437	20.553	0.0227	2.9	11.4	1.7	-0.38	0.04	-0.84
193.153	30.417	0.0231	1.3	1.6	1.0	-0.78	-0.37	-1.26
174.621	28.587	0.0235	1.9	2.9	1.2	-0.24	-	-0.61
180.225	17.894	0.0235	1.6	2.3	1.1	-0.30	0.15	-0.65
192.765	27.370	0.0277	2.5	4.8	1.7	-0.86	-0.53	-1.19
196.473	28.112	0.0246	1.6	2.6	1.0	-0.21	-	-0.64

continued on next page..

Table A.1 – continued from previous page

RA (J2000)	Dec (J2000)	z	Age (Gyr)	Age upper (Gyr)	Age lower (Gyr)	Z (dex)	Z upper (dex)	Z lower (dex)
179.361	25.233	0.0149	1.4	2.2	1.0	-0.30	0.17	-0.76
178.944	20.821	0.0223	1.1	1.6	0.8	-0.25	0.10	-0.74
174.508	18.341	0.0295	1.6	2.4	1.1	-0.51	-0.02	-0.91
172.253	22.986	0.0322	1.8	3.0	1.1	-0.01	-	-0.41
181.403	20.477	0.0234	2.3	5.3	1.2	-0.06	-	-0.48
193.699	30.545	0.0208	1.5	2.3	0.9	-0.17	-	-0.67
175.576	19.838	0.0213	1.4	2.1	0.9	0.02	-	-0.50
177.232	23.910	0.0315	3.5	12.9	2.1	-0.36	-0.01	-0.78
175.879	25.398	0.0313	2.6	6.2	1.7	-0.62	-0.26	-1.02
198.759	28.036	0.0218	1.3	1.7	1.0	-0.40	-0.00	-0.78
194.934	28.176	0.0277	2.5	8.3	1.1	0.08	-	-0.41
178.878	24.944	0.0284	1.5	2.0	1.1	-0.65	-0.27	-1.04
180.730	20.202	0.0243	2.9	8.6	2.0	-0.62	-0.32	-1.00
182.530	20.452	0.0308	2.4	4.9	1.5	-0.19	-	-0.56
191.613	30.516	0.0221	1.4	2.2	1.0	-0.20	-	-0.64
186.918	30.931	0.0304	2.3	4.3	1.6	-0.72	-0.40	-1.12
181.570	32.664	0.0274	2.8	6.8	2.0	-0.57	-0.28	-0.91
186.417	20.528	0.0183	1.7	3.3	1.0	0.11	-	-0.36
175.430	17.008	0.0225	1.3	2.1	0.9	-0.16	-	-0.65
181.844	27.852	0.0257	2.0	3.9	1.4	-0.68	-0.25	-1.14
185.142	17.352	0.0312	1.6	3.0	0.9	-0.10	-	-0.62
178.177	23.704	0.0220	1.9	4.4	1.1	-0.37	-	-0.86
182.813	17.888	0.0234	1.8	2.7	1.4	-0.79	-0.47	-1.16
194.119	27.291	0.0251	1.6	2.3	1.1	-0.38	0.11	-0.74
184.892	20.823	0.0314	1.2	1.7	0.9	-0.29	0.09	-0.72
175.964	19.862	0.0231	2.1	3.7	1.3	-0.35	0.18	-0.72
189.825	27.909	0.0216	1.7	2.9	1.1	-0.57	-0.03	-1.00
180.744	20.085	0.0237	3.0	11.0	1.9	-0.38	-0.04	-0.80
194.976	26.820	0.0267	1.3	1.8	0.9	-0.26	0.13	-0.70
199.211	31.631	0.0303	1.1	1.6	0.9	-0.37	0.00	-0.91
176.241	30.440	0.0313	1.7	2.3	1.3	-1.07	-0.64	-1.42
175.700	31.812	0.0321	1.4	2.1	1.0	-0.59	-0.07	-1.15
180.472	20.188	0.0237	1.5	2.3	1.0	-0.23	-	-0.69
181.069	26.149	0.0325	1.5	2.5	1.0	-0.29	-	-0.78
170.948	24.102	0.0259	3.7	13.4	2.1	-0.33	0.05	-0.75
176.599	20.039	0.0247	1.5	2.2	1.0	-0.20	-	-0.59
197.699	29.710	0.0212	1.7	2.8	1.2	-0.70	-0.24	-1.18
183.324	21.654	0.0239	1.4	2.1	1.0	-0.38	0.10	-0.82
174.460	22.013	0.0302	3.1	12.7	2.0	-0.39	-0.05	-0.84
172.238	27.375	0.0321	2.4	5.5	1.6	-0.83	-0.44	-1.22
182.246	31.301	0.0234	2.1	3.1	1.5	-0.68	-0.39	-1.03
184.277	27.193	0.0254	1.7	2.8	1.1	-0.44	0.14	-0.88
177.820	21.314	0.0231	1.7	2.4	1.2	-0.43	0.05	-0.75
181.720	25.197	0.0219	1.8	2.9	1.1	-0.44	0.13	-0.83
174.222	21.004	0.0300	2.0	2.9	1.4	-0.49	-0.07	-0.82
181.436	19.599	0.0231	1.1	1.6	0.8	-0.03	-	-0.57
194.655	27.177	0.0256	1.2	1.5	1.0	-0.79	-0.39	-1.30
198.723	27.008	0.0154	2.7	6.2	1.8	-0.30	0.06	-0.62
170.081	25.650	0.0265	1.1	1.7	0.0	-0.28	0.17	-0.97
174.563	28.137	0.0304	1.1	1.7	0.8	-0.24	0.15	-0.80
175.949	20.363	0.0224	1.5	2.1	1.1	-0.46	-0.02	-0.82
172.186	17.227	0.0207	1.9	2.9	1.4	-0.67	-0.28	-1.07
194.362	26.694	0.0243	2.4	5.3	1.5	-0.41	0.04	-0.80
183.980	26.662	0.0255	1.7	2.7	1.3	-1.01	-0.59	-1.37
188.982	26.422	0.0211	2.6	8.2	1.3	-0.11	-	-0.59

continued on next page..

Table A.1 – continued from previous page

RA (J2000)	Dec (J2000)	z	Age (Gyr)	Age upper (Gyr)	Age lower (Gyr)	Z (dex)	Z upper (dex)	Z lower (dex)
180.508	20.265	0.0226	2.8	7.3	1.9	-0.63	-0.33	-0.99
181.659	25.750	0.0242	3.0	7.7	2.2	-0.54	-0.28	-0.88
173.588	22.766	0.0311	1.6	2.3	1.0	-0.42	0.09	-0.81
178.936	17.888	0.0212	1.6	2.6	1.0	-0.16	-	-0.58
181.153	20.419	0.0248	2.1	4.8	1.1	-0.22	-	-0.70
198.946	31.846	0.0170	1.5	2.2	1.0	-0.53	-0.03	-1.00
175.805	20.132	0.0183	2.0	3.7	1.1	-0.14	-	-0.56
193.233	17.454	0.0222	1.6	2.5	1.0	-0.43	0.12	-0.88
172.885	28.288	0.0238	1.8	3.0	1.1	0.00	-	-0.38
180.920	20.396	0.0234	2.8	9.4	1.7	-0.31	0.12	-0.73
183.790	21.924	0.0221	1.6	2.2	1.3	-0.96	-0.60	-1.28
181.001	28.250	0.0275	2.9	9.9	1.6	-0.14	-	-0.56
194.269	27.773	0.0251	2.1	3.1	1.5	-0.44	-0.05	-0.73
176.813	19.176	0.0201	2.0	3.1	1.2	-0.11	-	-0.45
181.550	20.985	0.0308	1.4	1.8	1.0	-0.45	-0.01	-0.85
199.339	31.059	0.0186	1.4	1.8	1.0	-0.60	-0.17	-1.07
182.253	22.688	0.0226	1.4	1.7	1.0	-0.84	-0.29	-1.43
183.423	20.881	0.0225	1.7	3.1	1.2	-0.76	-0.27	-1.25
175.856	25.005	0.0206	2.8	7.5	1.9	-0.67	-0.36	-1.05
185.320	32.782	0.0228	1.1	2.2	0.0	0.13	-	-0.65
172.927	32.899	0.0308	1.7	2.7	1.1	-0.30	-	-0.66
194.441	27.429	0.0278	1.4	2.2	1.0	-0.18	-	-0.63
182.589	23.812	0.0227	1.9	3.5	1.1	-0.46	0.13	-0.88
181.898	25.772	0.0234	1.5	2.4	1.0	-0.34	0.18	-0.80
176.452	22.648	0.0230	2.8	11.8	1.5	-0.13	-	-0.60
195.189	27.835	0.0293	2.9	10.9	1.7	-0.38	0.03	-0.84
173.723	20.488	0.0228	2.3	4.3	1.5	-0.53	-0.13	-0.90
180.702	20.815	0.0238	2.8	7.1	2.0	-0.54	-0.26	-0.88
192.937	27.018	0.0213	1.3	1.8	0.9	-0.25	0.13	-0.70
196.045	22.290	0.0238	4.8	8.6	2.8	-1.12	-0.90	-1.31
191.719	26.709	0.0203	1.6	2.2	1.2	-0.62	-0.23	-1.01
184.806	22.431	0.0223	1.7	2.6	1.1	-0.54	-0.03	-0.96
184.091	31.212	0.0263	2.5	4.5	1.7	-0.57	-0.29	-0.88
195.960	28.179	0.0213	2.2	4.8	1.2	-0.24	-	-0.67
183.653	24.301	0.0209	1.7	2.8	1.2	-0.54	-0.02	-0.94
179.284	28.042	0.0272	1.6	2.6	1.0	-0.06	-	-0.56
188.948	26.755	0.0235	1.6	2.9	0.9	0.04	-	-0.54
173.612	21.352	0.0212	2.2	4.7	1.4	-0.58	-0.10	-1.02
172.171	19.731	0.0195	3.0	11.3	1.9	-0.68	-0.35	-1.11
194.658	27.464	0.0209	2.7	7.9	1.7	-0.76	-0.33	-1.20
183.251	25.282	0.0244	1.9	3.9	1.2	-0.56	0.00	-1.01
182.820	28.519	0.0289	1.5	2.6	0.9	-0.14	-	-0.69
197.441	28.621	0.0226	1.3	2.1	0.9	-0.11	-	-0.62
173.056	23.938	0.0314	2.6	7.7	1.3	-0.14	-	-0.59
174.368	21.977	0.0311	1.3	2.0	0.9	-0.24	0.20	-0.77
194.177	27.548	0.0253	2.0	3.0	1.3	-0.14	-	-0.47
172.402	23.732	0.0246	3.0	6.1	2.0	-0.97	-0.64	-1.26
195.774	25.475	0.0243	1.7	3.1	1.3	-0.99	-0.52	-1.40
180.951	20.416	0.0213	2.9	12.2	1.8	-0.58	-0.20	-1.05
191.172	26.420	0.0152	1.3	1.7	1.0	-0.60	-0.22	-1.03
174.230	24.890	0.0326	1.2	1.5	1.0	-0.80	-0.44	-1.24
199.221	31.711	0.0170	1.1	1.3	0.9	-0.91	-0.52	-1.36
182.623	26.253	0.0226	2.2	7.5	1.0	0.21	-	-0.37
191.581	27.537	0.0200	1.8	3.0	1.2	-0.61	-0.11	-1.05
187.261	27.641	0.0233	1.7	2.8	1.0	0.00	-	-0.45

continued on next page..

Table A.1 – continued from previous page

RA (J2000)	Dec (J2000)	z	Age (Gyr)	Age upper (Gyr)	Age lower (Gyr)	Z (dex)	Z upper (dex)	Z lower (dex)
171.901	26.179	0.0239	1.0	1.4	0.9	-0.22	0.06	-0.62
190.246	24.871	0.0214	1.6	2.1	1.3	-0.77	-0.44	-1.13
183.441	24.356	0.0209	1.1	1.6	0.9	-0.36	0.01	-0.88
194.680	28.910	0.0278	1.2	1.7	0.9	-0.27	0.08	-0.67
195.880	28.092	0.0211	2.9	10.5	1.7	-0.29	0.17	-0.71
174.123	31.325	0.0235	1.4	1.9	1.0	-0.45	0.03	-0.94
194.538	28.709	0.0254	1.7	2.6	1.1	-0.41	0.15	-0.82
178.272	20.583	0.0223	3.1	12.6	2.0	-0.41	-0.07	-0.86
191.574	20.783	0.0233	2.8	8.3	1.8	-0.41	-0.04	-0.80
175.795	26.493	0.0319	2.0	13.2	0.0	-0.04	-	-0.83
198.789	29.636	0.0225	2.3	4.6	1.5	-0.72	-0.34	-1.15
185.514	28.186	0.0253	2.2	3.8	1.5	-0.52	-0.08	-0.89
198.292	30.191	0.0233	1.7	2.9	1.2	-1.01	-0.50	-1.45
191.542	30.732	0.0219	1.1	1.6	0.0	-0.33	0.11	-1.01
170.899	30.038	0.0237	2.4	4.7	1.6	-0.92	-0.55	-1.26
185.742	28.494	0.0254	1.5	2.7	0.8	-0.10	-	-0.69
194.759	28.116	0.0314	2.2	3.6	1.6	-1.14	-0.73	-1.46
189.751	28.315	0.0251	1.8	3.0	1.4	-1.13	-0.71	-1.46
198.884	17.556	0.0233	1.7	2.7	1.1	0.04	-	-0.37
194.889	32.291	0.0314	1.9	4.2	1.0	-0.22	-	-0.70
183.677	24.981	0.0221	2.1	2.9	1.6	-1.27	-0.98	-1.54
176.138	26.523	0.0298	2.5	5.0	1.6	-0.96	-0.55	-1.30
185.928	26.849	0.0218	1.6	3.8	0.9	-0.48	0.19	-1.13
195.664	25.384	0.0242	1.8	2.5	1.5	-1.28	-0.89	-1.63
184.316	18.309	0.0327	1.9	2.8	1.3	-0.52	-0.09	-0.86
172.053	25.727	0.0234	1.3	1.8	0.9	-0.16	0.20	-0.61
192.175	26.417	0.0230	1.4	1.8	1.0	-0.64	-0.20	-1.17
172.753	20.469	0.0205	1.5	1.9	1.2	-0.86	-0.46	-1.25
195.149	27.574	0.0170	2.1	3.9	1.4	-0.51	-0.06	-0.89
170.365	24.405	0.0228	1.4	2.3	0.9	-0.10	-	-0.56
197.803	26.814	0.0212	2.4	5.6	1.5	-0.67	-0.24	-1.12
197.972	27.594	0.0205	1.5	2.6	0.0	-0.09	-	-0.71
177.735	21.973	0.0259	2.9	3.9	1.8	-1.35	-1.04	-1.68
193.204	27.402	0.0258	1.2	1.4	1.0	-0.89	-0.49	-1.33
174.360	26.456	0.0307	2.7	6.3	1.8	-0.38	-0.04	-0.71
183.648	28.327	0.0256	2.5	7.3	1.4	-0.31	-	-0.76
171.054	23.934	0.0263	1.6	2.7	1.0	-0.04	-	-0.48
193.603	27.364	0.0261	2.8	7.3	1.9	-0.59	-0.27	-0.97
181.523	32.893	0.0270	1.5	1.8	1.1	-0.89	-0.38	-1.37
190.510	18.988	0.0270	1.6	2.5	1.0	-0.04	-	-0.49
176.154	32.565	0.0318	2.2	5.3	1.1	-0.25	-	-0.72
179.265	21.407	0.0312	1.3	1.7	1.0	-0.72	-0.31	-1.22
181.662	31.401	0.0227	2.3	3.2	1.7	-0.60	-0.36	-0.87
174.731	26.491	0.0305	2.7	9.2	1.8	-0.71	-0.34	-1.15
189.078	27.754	0.0246	3.0	13.7	1.4	-0.09	-	-0.59
181.112	20.592	0.0224	1.6	2.9	0.9	0.05	-	-0.50
187.223	29.841	0.0270	1.6	2.6	1.0	-0.47	0.09	-0.92
185.115	31.172	0.0224	2.1	3.5	1.5	-0.70	-0.40	-1.07
194.144	27.228	0.0240	2.6	7.3	1.6	-0.82	-0.35	-1.27
180.117	17.727	0.0233	1.2	1.8	0.8	-0.01	-	-0.56
174.646	21.696	0.0315	2.3	5.6	1.3	-0.37	0.21	-0.81
194.365	27.636	0.0268	2.6	5.5	1.6	-0.12	-	-0.47
190.371	31.186	0.0307	1.5	1.9	1.2	-0.95	-0.49	-1.35
190.772	27.714	0.0250	1.2	1.7	0.9	-0.40	0.02	-0.95
181.374	29.196	0.0282	1.5	2.1	1.1	-0.74	-0.28	-1.23

continued on next page..

Table A.1 – continued from previous page

RA (J2000)	Dec (J2000)	z	Age (Gyr)	Age upper (Gyr)	Age lower (Gyr)	Z (dex)	Z upper (dex)	Z lower (dex)
199.642	17.503	0.0236	1.4	1.8	1.0	-0.72	-0.24	-1.29
195.926	32.990	0.0324	1.5	2.5	1.0	-0.33	0.22	-0.83
198.664	30.225	0.0236	2.6	4.9	1.7	-1.07	-0.65	-1.40
181.039	20.185	0.0254	3.8	11.1	2.3	-0.84	-0.52	-1.18
186.131	31.248	0.0284	2.6	5.6	1.6	-0.44	0.01	-0.82
197.215	28.629	0.0227	1.3	1.9	0.9	-0.59	-0.07	-1.21
196.583	32.974	0.0261	1.2	1.6	1.0	-0.63	-0.26	-1.10
176.266	19.859	0.0211	2.7	6.9	1.6	-0.20	-	-0.57
181.820	32.669	0.0310	2.6	5.8	1.6	-1.02	-0.53	-1.47
176.537	20.447	0.0238	1.6	2.7	1.0	-0.58	0.01	-1.12
185.591	29.581	0.0263	1.4	1.9	1.0	-0.43	0.02	-0.89
171.188	22.872	0.0193	2.6	9.0	1.6	-0.63	-0.16	-1.12
186.821	30.623	0.0303	2.4	6.4	1.5	-0.62	-0.12	-1.11
172.365	24.165	0.0327	1.9	6.2	1.0	-0.51	-	-1.17
176.199	19.773	0.0282	2.3	4.8	1.6	-0.88	-0.48	-1.26
193.575	32.369	0.0225	1.6	2.8	0.9	-0.19	-	-0.73
181.093	19.567	0.0228	1.0	1.6	0.0	-0.31	0.11	-0.96
184.010	17.531	0.0254	1.6	3.6	0.0	0.03	-	-0.59
190.579	30.906	0.0285	1.6	2.4	1.2	-1.00	-0.52	-1.41
174.670	24.585	0.0229	1.4	2.1	0.9	-0.35	0.13	-0.86
184.525	25.711	0.0237	1.8	3.1	1.1	-0.51	0.06	-0.96
184.483	18.399	0.0254	3.9	6.5	2.2	-1.31	-1.00	-1.70
181.531	32.895	0.0274	1.8	3.1	1.3	-0.65	-0.20	-1.08
181.189	31.158	0.0267	1.1	1.6	0.9	-0.48	-0.03	-1.15
181.363	28.575	0.0282	1.3	1.7	1.1	-0.66	-0.30	-1.10
173.196	20.038	0.0204	2.6	6.0	1.7	-0.62	-0.27	-1.01
195.560	28.102	0.0198	1.5	2.5	1.0	-0.17	-	-0.65
195.553	28.215	0.0273	1.6	2.1	1.2	-1.04	-0.56	-1.45
177.757	29.030	0.0284	1.6	3.0	1.0	-0.49	0.14	-1.11
194.542	24.349	0.0226	0.8	0.8	0.0	-0.73	-0.33	-1.18
172.438	22.127	0.0217	3.1	8.9	2.0	-0.83	-0.48	-1.20
178.011	25.751	0.0189	1.1	1.6	0.8	-0.25	0.16	-0.85
178.258	24.830	0.0227	1.0	1.3	0.8	-0.35	-0.02	-0.88
173.848	21.502	0.0297	1.4	2.3	0.9	-0.52	0.06	-1.20
170.509	25.921	0.0211	2.3	5.4	1.2	-0.21	-	-0.65
177.490	27.548	0.0293	3.3	13.8	1.7	-0.17	-	-0.62
194.736	27.822	0.0290	1.7	2.6	1.0	-0.19	-	-0.60
197.769	30.483	0.0210	1.5	2.3	1.1	-0.61	-0.12	-1.09
197.360	28.416	0.0206	2.3	4.7	1.4	-0.31	0.19	-0.67
181.713	28.351	0.0304	2.8	12.8	1.4	-0.20	-	-0.73
189.838	25.255	0.0300	1.9	3.1	1.4	-0.85	-0.47	-1.21
182.532	19.161	0.0247	2.1	4.9	1.2	-0.56	0.07	-1.09
173.833	17.409	0.0272	1.2	1.9	0.9	-0.19	0.20	-0.70
185.603	28.616	0.0273	1.0	1.7	0.0	0.04	-	-0.68
174.377	22.400	0.0229	2.3	5.3	1.4	-0.44	0.11	-0.87
177.984	23.812	0.0221	2.2	4.0	1.4	-0.55	-0.11	-0.93
190.857	27.373	0.0245	1.4	1.8	1.0	-0.62	-0.19	-1.09
173.425	21.865	0.0228	0.8	1.0	0.0	-0.14	0.21	-0.52
175.574	27.316	0.0312	1.3	2.2	0.8	0.05	-	-0.51
175.411	17.077	0.0222	1.9	3.6	1.3	-0.66	-0.21	-1.12
172.821	26.590	0.0315	2.1	5.5	1.0	0.04	-	-0.48
181.440	31.059	0.0231	2.3	4.6	1.6	-0.73	-0.41	-1.10
181.526	20.370	0.0256	1.5	1.8	1.2	-0.95	-0.56	-1.30
177.342	24.938	0.0199	1.2	1.8	0.9	-0.26	0.14	-0.72
189.833	27.605	0.0265	2.1	4.2	1.3	-0.56	-0.05	-1.01

continued on next page..

Table A.1 – continued from previous page

RA (J2000)	Dec (J2000)	z	Age (Gyr)	Age upper (Gyr)	Age lower (Gyr)	Z (dex)	Z upper (dex)	Z lower (dex)
176.453	20.629	0.0234	4.1	14.0	2.3	-0.86	-0.53	-1.20
194.300	27.103	0.0245	2.4	5.2	1.5	-0.34	0.16	-0.72
181.168	20.233	0.0208	1.7	4.1	0.9	-0.27	-	-0.82
176.784	29.624	0.0221	0.9	1.1	0.0	-0.61	-0.25	-1.12
184.430	30.378	0.0280	1.9	3.6	1.1	-0.31	-	-0.76
195.844	28.797	0.0263	2.6	13.7	1.4	-0.41	0.21	-1.01
193.174	28.960	0.0327	1.3	1.7	1.0	-0.56	-0.15	-1.03
189.226	21.329	0.0316	1.4	2.3	0.9	-0.26	-	-0.81
180.848	19.774	0.0234	2.5	5.2	1.6	-0.44	-0.03	-0.81
182.048	30.753	0.0235	1.3	1.6	1.0	-0.92	-0.36	-1.49
176.023	32.453	0.0310	1.6	2.5	1.0	-0.27	-	-0.74
182.699	19.064	0.0255	2.6	11.4	1.5	-0.36	-	-0.89
194.524	28.371	0.0254	2.2	4.0	1.4	-0.22	-	-0.57
196.436	25.385	0.0246	1.2	2.2	0.0	-0.06	-	-0.69
191.284	27.577	0.0270	2.2	8.3	1.0	0.05	-	-0.54
193.455	28.943	0.0237	2.0	4.4	1.1	-0.12	-	-0.55
173.645	22.518	0.0310	2.1	3.6	1.5	-1.18	-0.68	-1.60
196.652	27.873	0.0209	1.0	1.4	0.8	-0.39	-0.04	-0.95
178.605	20.785	0.0223	1.0	1.4	0.0	-0.36	0.05	-1.10
193.096	31.697	0.0308	1.1	1.9	0.0	-0.09	-	-0.70
170.590	24.363	0.0282	1.3	3.5	0.0	-0.09	-	-0.98
184.597	19.696	0.0305	1.7	2.9	1.2	-0.65	-0.16	-1.11
178.254	23.040	0.0226	0.9	1.3	0.0	0.04	-	-0.57
184.802	25.715	0.0248	2.5	10.4	1.3	-0.50	0.14	-1.08
176.476	22.456	0.0227	2.1	5.2	1.1	-0.50	0.14	-1.00
177.720	21.169	0.0256	2.1	3.7	1.5	-0.56	-0.15	-0.93
176.580	20.640	0.0219	2.3	6.5	1.4	-0.78	-0.19	-1.32
194.083	32.655	0.0231	2.7	13.5	1.5	-0.48	0.09	-1.05
198.434	19.847	0.0227	2.1	3.4	1.5	-0.61	-0.25	-0.96
197.011	27.311	0.0196	1.8	3.2	1.3	-0.96	-0.51	-1.35
182.812	29.158	0.0220	1.4	2.1	1.0	-0.67	-0.16	-1.25
173.144	17.431	0.0259	1.0	1.5	0.0	-0.21	-	-0.92
193.439	20.093	0.0224	2.8	10.8	1.5	-0.15	-	-0.60
198.216	27.880	0.0214	1.6	3.1	1.0	-0.48	0.15	-1.08
178.060	18.651	0.0261	1.5	3.0	0.9	-0.24	-	-0.89
174.165	20.290	0.0319	1.8	4.0	1.0	-0.43	-	-0.94
178.379	20.591	0.0228	1.7	4.2	0.9	-0.12	-	-0.68
182.082	32.592	0.0297	1.3	2.0	0.9	-0.30	0.18	-0.87
178.419	25.581	0.0288	1.4	2.5	0.8	-0.27	-	-0.94
187.933	26.800	0.0226	2.2	6.7	1.1	-0.39	-	-0.91
198.598	30.484	0.0201	2.3	4.9	1.4	-0.42	0.09	-0.83
192.538	32.007	0.0236	1.3	1.9	0.9	-0.38	0.07	-0.86
177.847	26.784	0.0222	1.8	3.9	1.1	-0.54	0.11	-1.07
194.539	26.664	0.0243	1.0	1.6	0.0	0.10	-	-0.53
196.805	28.047	0.0244	2.3	4.2	1.5	-1.20	-0.65	-1.68
181.107	20.264	0.0238	2.4	5.7	1.5	-0.52	-0.02	-0.96
175.565	20.049	0.0204	1.1	1.6	0.8	-0.39	0.03	-1.04
180.966	20.395	0.0232	1.7	4.4	0.9	-0.26	-	-0.85
180.813	24.796	0.0213	0.9	1.1	0.0	-0.73	-0.24	-1.40
178.802	23.790	0.0314	1.8	3.7	1.1	-0.57	0.03	-1.04
184.509	18.328	0.0321	1.6	2.5	1.1	-0.36	0.16	-0.73
180.575	21.011	0.0256	2.3	3.9	1.7	-1.13	-0.74	-1.44
180.172	21.360	0.0246	2.4	5.6	1.3	-0.30	-	-0.74
176.257	20.852	0.0229	0.8	2.0	0.0	0.15	-	-0.94
175.570	26.028	0.0312	2.5	4.9	1.7	-0.94	-0.58	-1.26

continued on next page..

Table A.1 – continued from previous page

RA (J2000)	Dec (J2000)	z	Age (Gyr)	Age upper (Gyr)	Age lower (Gyr)	Z (dex)	Z upper (dex)	Z lower (dex)
183.016	25.119	0.0236	1.2	2.2	0.0	0.08	-	-0.56
186.961	27.381	0.0255	1.8	3.9	1.0	-0.51	0.14	-1.04
195.270	27.892	0.0194	1.7	3.8	0.9	-0.03	-	-0.56
179.487	25.144	0.0151	1.7	2.7	1.1	-0.53	0.01	-0.97
175.400	25.887	0.0244	2.5	4.9	1.7	-1.00	-0.61	-1.30
170.798	24.745	0.0210	1.6	3.0	1.0	-0.68	-0.12	-1.24
174.835	26.306	0.0229	1.1	1.8	0.0	0.01	-	-0.57
184.864	21.155	0.0319	1.6	2.8	0.9	-0.19	-	-0.76
186.263	27.374	0.0242	1.6	2.7	1.1	-0.70	-0.22	-1.20
175.562	19.977	0.0261	1.7	2.6	1.4	-1.13	-0.66	-1.52
175.760	26.139	0.0230	2.3	9.1	1.2	-0.55	0.16	-1.15
193.014	27.166	0.0252	2.4	5.4	1.4	-0.24	-	-0.63
176.307	19.756	0.0275	1.1	1.7	0.8	-0.16	0.21	-0.70
197.341	30.923	0.0168	1.4	2.1	1.0	-0.50	0.00	-0.96
187.247	28.862	0.0267	2.7	12.6	1.6	-0.60	-0.09	-1.12
172.604	27.002	0.0320	1.7	3.1	1.3	-0.98	-0.50	-1.42
190.202	27.776	0.0222	2.2	7.3	1.2	-0.89	-0.16	-1.55
177.227	21.471	0.0264	1.4	2.6	0.0	0.18	-	-0.46
171.806	23.770	0.0215	1.0	1.2	0.8	-0.50	-0.16	-1.02
183.238	31.863	0.0323	1.7	3.4	1.0	-0.18	-	-0.68
180.702	21.146	0.0234	2.7	8.1	1.7	-0.60	-0.22	-1.03
183.970	24.231	0.0286	1.3	2.0	0.9	-0.33	0.15	-0.93
172.168	21.097	0.0204	2.4	5.4	1.5	-0.85	-0.42	-1.26
176.063	19.511	0.0219	2.7	9.3	1.5	-0.23	-	-0.70
192.525	25.022	0.0215	1.0	1.3	0.0	-0.22	0.08	-0.66
184.823	20.443	0.0322	1.7	3.0	1.1	-0.48	0.10	-0.92
175.733	23.129	0.0289	3.1	10.5	1.8	-0.85	-0.46	-1.26
176.986	28.069	0.0296	1.9	3.9	1.1	-0.55	0.06	-1.05
181.731	25.624	0.0230	2.1	5.9	1.1	-0.62	0.06	-1.20
192.788	27.407	0.0228	3.4	13.8	2.1	-0.73	-0.37	-1.18
185.664	24.330	0.0228	2.4	6.7	1.4	-0.76	-0.22	-1.26
177.970	20.456	0.0229	2.2	7.2	1.0	-0.13	-	-0.70
194.846	28.489	0.0233	1.4	2.0	0.9	-0.29	0.16	-0.74
176.167	19.211	0.0195	2.1	7.1	1.0	-0.21	-	-0.80
179.917	26.546	0.0224	2.0	5.6	1.1	-0.44	-	-1.01
172.647	27.123	0.0323	1.6	2.5	1.1	-0.61	-0.14	-1.05
172.560	23.802	0.0249	1.9	3.9	1.3	-0.98	-0.47	-1.44
193.465	28.979	0.0265	1.5	2.4	1.0	-0.91	-0.23	-1.58
171.443	18.940	0.0178	2.2	3.7	1.4	-0.28	0.18	-0.60
192.908	31.353	0.0206	1.8	3.6	1.0	-0.26	-	-0.73
182.708	23.714	0.0226	1.5	2.9	0.9	-0.46	0.15	-1.14
179.952	29.641	0.0290	1.6	2.7	1.1	-0.66	-0.17	-1.14
176.140	19.627	0.0241	2.7	11.5	1.6	-0.56	-0.11	-1.04
189.492	20.346	0.0222	2.9	10.2	1.6	-0.96	-0.43	-1.45
192.624	31.607	0.0298	1.0	1.4	0.8	-0.39	-0.06	-0.88
185.197	17.016	0.0259	1.7	2.9	1.4	-1.02	-0.63	-1.34
187.411	26.231	0.0226	1.9	4.5	1.0	-0.06	-	-0.58
185.823	19.724	0.0305	2.1	3.7	1.5	-1.07	-0.64	-1.43
185.217	19.004	0.0232	1.2	2.8	0.0	0.02	-	-0.90
180.451	17.418	0.0217	1.6	2.6	1.0	-0.69	-0.17	-1.23
189.192	32.116	0.0236	1.5	2.0	1.1	-0.95	-0.36	-1.52
180.908	20.253	0.0234	1.5	2.7	1.0	-0.49	0.10	-1.06
195.647	27.439	0.0181	2.1	4.7	1.3	-0.75	-0.24	-1.26
174.862	31.854	0.0278	1.0	1.1	0.8	-0.88	-0.27	-1.65
184.912	30.284	0.0292	2.1	6.2	1.1	-0.32	-	-0.86

continued on next page..

Table A.1 – continued from previous page

RA (J2000)	Dec (J2000)	z	Age (Gyr)	Age upper (Gyr)	Age lower (Gyr)	Z (dex)	Z upper (dex)	Z lower (dex)
176.128	17.626	0.0224	1.4	1.9	0.9	-0.49	-0.01	-0.98
174.166	17.643	0.0273	0.9	1.0	0.9	-1.20	-0.71	-1.66
170.875	27.262	0.0327	2.5	7.6	1.6	-0.69	-0.22	-1.18
193.346	27.033	0.0235	2.6	10.9	1.3	-0.31	-	-0.86
176.436	20.031	0.0177	1.6	3.3	0.9	-0.33	-	-0.92
180.817	22.390	0.0278	1.9	4.4	1.0	-0.48	0.21	-1.04
183.610	24.182	0.0227	1.9	3.9	1.1	-0.49	0.12	-0.96
198.243	31.259	0.0204	1.1	1.8	0.0	-0.30	-	-1.09
180.880	17.150	0.0219	1.6	2.3	1.3	-0.93	-0.52	-1.28
192.265	30.926	0.0271	1.0	1.6	0.0	-0.12	-	-0.93
191.778	25.287	0.0316	1.6	3.7	0.8	-0.17	-	-0.81
193.213	17.749	0.0216	1.3	1.5	0.9	-0.97	-0.35	-1.62
175.536	25.974	0.0228	1.0	1.3	0.0	-0.61	-0.10	-1.43
179.862	17.757	0.0216	1.8	2.8	1.2	-0.44	0.10	-0.81
186.437	26.767	0.0229	1.2	1.6	0.9	-0.73	-0.20	-1.49
181.393	20.638	0.0240	2.6	12.5	1.4	-0.36	-	-0.93
199.724	30.804	0.0305	2.2	4.7	1.3	-0.29	-	-0.69
195.213	27.743	0.0271	2.1	5.3	1.1	-0.47	0.20	-1.01
177.608	21.765	0.0256	2.3	8.2	1.1	-0.39	-	-0.96
178.570	24.973	0.0287	1.6	2.7	1.0	-0.48	0.09	-0.98
187.297	20.367	0.0226	2.7	6.6	1.6	-1.12	-0.57	-1.65
174.293	19.972	0.0212	1.1	1.7	0.8	-0.40	0.10	-1.15
179.323	28.119	0.0221	1.9	4.7	1.1	-0.45	-	-0.97
179.651	18.863	0.0228	3.3	10.5	1.9	-0.90	-0.51	-1.29
190.471	22.349	0.0232	1.2	1.7	0.9	-0.64	-0.20	-1.22
195.140	27.638	0.0250	1.5	1.8	1.1	-1.03	-0.48	-1.51
180.921	27.548	0.0302	1.9	4.9	1.1	-0.83	-0.10	-1.50
179.567	26.559	0.0224	1.1	2.9	0.0	0.00	-	-0.99
173.138	20.417	0.0227	2.5	4.9	1.6	-1.07	-0.63	-1.44
191.835	27.247	0.0258	1.4	2.4	0.9	-0.53	0.04	-1.18
171.950	25.841	0.0328	2.3	5.3	1.2	-0.22	-	-0.67
173.093	22.626	0.0315	0.9	1.2	0.0	-0.14	-	-0.63
180.928	29.639	0.0284	1.3	1.7	1.0	-0.61	-0.20	-1.09
184.076	17.770	0.0298	2.6	7.1	1.6	-0.89	-0.40	-1.33
194.025	27.678	0.0165	1.3	1.3	1.0	-1.24	-0.69	-1.69
182.061	25.410	0.0231	2.2	4.9	1.1	-0.20	-	-0.62
175.735	19.966	0.0243	1.5	3.1	0.9	-0.30	-	-0.95
177.049	19.157	0.0206	2.5	14.0	1.1	-0.28	-	-0.91
181.827	20.584	0.0245	2.4	4.7	1.7	-0.95	-0.57	-1.28
195.158	28.058	0.0255	1.6	2.4	1.1	-0.76	-0.31	-1.23
193.527	29.243	0.0246	1.4	2.7	0.0	0.01	-	-0.74
175.104	19.963	0.0225	1.5	2.3	1.1	-0.68	-0.21	-1.20
198.996	31.531	0.0320	1.4	2.5	0.9	-0.49	0.10	-1.18
196.973	28.383	0.0214	1.8	4.3	1.0	-0.35	-	-0.90
181.311	21.082	0.0234	2.7	10.9	1.6	-0.71	-0.26	-1.20
175.110	32.520	0.0328	2.4	4.7	1.6	-0.63	-0.30	-1.00
176.876	21.821	0.0277	1.5	3.9	0.0	-0.04	-	-0.78
197.584	32.483	0.0176	1.4	2.4	0.9	-0.38	0.16	-0.94
178.658	28.978	0.0282	1.4	2.7	0.0	0.01	-	-0.68
194.984	27.746	0.0298	1.3	1.8	0.9	-0.49	0.00	-1.04
187.853	26.796	0.0231	1.4	3.2	0.0	-0.32	-	-1.13
171.764	21.233	0.0156	1.7	2.9	1.3	-1.06	-0.61	-1.45
170.164	24.190	0.0264	1.6	2.6	1.0	-0.51	0.05	-0.99
170.697	24.472	0.0277	1.4	2.8	0.0	-0.22	-	-0.97
181.150	32.597	0.0251	2.5	7.9	1.5	-0.52	0.02	-1.01

continued on next page..

Table A.1 – continued from previous page

RA (J2000)	Dec (J2000)	z	Age (Gyr)	Age upper (Gyr)	Age lower (Gyr)	Z (dex)	Z upper (dex)	Z lower (dex)
183.905	20.344	0.0313	1.5	2.1	1.0	-0.85	-0.28	-1.44
174.278	18.194	0.0215	1.5	1.7	1.1	-1.11	-0.58	-1.58
194.586	27.429	0.0252	1.5	3.5	0.9	-0.62	0.03	-1.30
172.417	24.762	0.0303	1.1	1.7	0.0	-0.21	0.22	-0.83
193.674	28.046	0.0256	1.8	5.3	0.9	-0.34	-	-0.94
189.353	23.864	0.0229	0.9	1.5	0.0	-0.09	-	-1.16
177.341	21.355	0.0224	3.5	13.7	1.7	-1.07	-0.55	-1.59
170.649	19.834	0.0327	1.7	3.3	1.0	-0.61	0.01	-1.14
176.294	31.197	0.0317	1.2	2.6	0.0	0.05	-	-0.82
184.715	31.740	0.0267	1.1	1.5	0.8	-0.65	-0.14	-1.41
196.880	25.505	0.0256	1.7	4.4	1.0	-0.66	0.05	-1.35
178.135	22.757	0.0238	1.0	1.1	0.0	-0.84	-0.21	-1.71
176.941	32.318	0.0326	2.2	5.1	1.3	-0.48	0.11	-0.97
194.845	26.026	0.0202	1.7	4.2	1.0	-0.56	0.14	-1.15
192.777	29.197	0.0221	1.9	3.6	1.1	-0.25	-	-0.67
198.669	29.997	0.0228	1.6	3.6	1.0	-0.77	-0.10	-1.43
181.447	28.120	0.0300	1.4	2.5	0.0	0.00	-	-0.64
173.782	21.632	0.0295	1.6	2.9	0.9	-0.17	-	-0.73
180.183	24.856	0.0155	1.3	2.5	0.8	-0.32	-	-1.05
198.301	30.362	0.0217	2.3	6.9	1.1	-0.32	-	-0.85
179.985	22.191	0.0227	0.9	2.7	0.0	0.03	-	-1.23
177.952	20.458	0.0221	1.1	2.0	0.0	-0.01	-	-0.67
182.238	21.889	0.0244	1.3	3.4	0.0	-0.44	-	-1.40
176.258	19.764	0.0274	1.8	3.4	1.3	-0.81	-0.35	-1.26
177.952	19.358	0.0232	2.1	5.6	1.2	-0.53	0.12	-1.06
173.553	32.243	0.0279	1.5	5.3	0.0	-0.22	-	-1.14
189.773	26.914	0.0239	1.0	1.7	0.0	0.01	-	-0.63
170.272	25.574	0.0260	2.4	5.9	1.5	-0.98	-0.48	-1.43
170.962	24.218	0.0254	2.2	6.1	1.1	-0.31	-	-0.83
172.255	28.821	0.0230	1.8	3.4	1.1	-0.42	0.18	-0.84
175.194	17.268	0.0221	1.6	3.1	1.1	-0.90	-0.25	-1.48
176.609	19.720	0.0243	1.7	3.9	1.0	-0.57	0.10	-1.17
196.149	28.628	0.0224	0.9	1.1	0.0	-0.73	-0.23	-1.43
189.980	27.827	0.0217	1.2	3.5	0.0	-0.36	-	-1.40
182.951	19.842	0.0258	2.0	4.8	1.3	-1.03	-0.37	-1.62
189.424	32.087	0.0233	2.4	9.5	1.2	-0.27	-	-0.83
178.057	29.076	0.0281	0.9	1.7	0.0	0.09	-	-0.70
184.502	18.496	0.0233	2.1	7.7	1.1	-0.75	0.01	-1.44
193.741	30.708	0.0263	2.0	4.4	1.1	-0.24	-	-0.70
177.224	21.294	0.0244	1.5	3.2	0.8	-0.43	-	-1.15
173.479	22.539	0.0275	2.6	13.3	1.4	-0.60	0.02	-1.18
196.652	25.430	0.0240	1.8	3.8	1.2	-0.77	-0.22	-1.30
171.870	19.853	0.0218	2.3	3.3	1.6	-1.37	-1.06	-1.66
173.417	17.591	0.0320	2.0	5.5	1.1	-0.76	-0.10	-1.37
182.729	32.929	0.0238	1.1	2.0	0.0	-0.09	-	-0.77
197.280	29.831	0.0231	1.6	3.2	0.8	-0.18	-	-0.81
173.202	22.765	0.0313	3.0	7.2	1.7	-1.09	-0.63	-1.53
177.900	23.342	0.0238	1.3	2.0	0.9	-0.63	-0.06	-1.32
195.890	28.239	0.0274	1.7	4.2	1.0	-0.74	-0.00	-1.47
198.397	29.127	0.0200	1.3	2.8	0.8	-0.55	0.08	-1.31
186.455	26.740	0.0236	2.2	5.4	1.3	-1.00	-0.38	-1.56
198.766	22.590	0.0230	2.5	3.7	1.6	-1.28	-0.86	-1.66
194.228	30.676	0.0241	1.4	2.1	0.9	-0.14	-	-0.61
198.051	22.868	0.0231	1.4	2.5	0.9	-0.35	-	-1.01
186.330	21.051	0.0313	1.1	1.5	0.9	-0.70	-0.25	-1.40

continued on next page..

Table A.1 – continued from previous page

RA (J2000)	Dec (J2000)	z	Age (Gyr)	Age upper (Gyr)	Age lower (Gyr)	Z (dex)	Z upper (dex)	Z lower (dex)
192.714	31.040	0.0295	0.8	1.1	0.0	-0.47	-0.03	-1.33
182.041	25.613	0.0218	2.0	5.2	1.2	-0.81	-0.20	-1.35
182.298	32.232	0.0296	2.4	10.4	1.2	-0.51	0.22	-1.14
183.061	17.283	0.0256	2.6	6.0	1.7	-0.83	-0.46	-1.21
184.916	20.147	0.0305	1.9	9.9	0.0	-0.10	-	-0.89
178.158	24.308	0.0165	2.8	12.5	1.6	-0.84	-0.29	-1.35
176.909	20.566	0.0224	1.2	2.3	0.0	-0.16	-	-0.88
194.434	29.020	0.0264	1.3	2.2	0.9	-0.58	0.02	-1.34
195.077	28.097	0.0261	2.2	7.2	1.1	-0.30	-	-0.89
177.008	32.970	0.0312	0.9	1.4	0.0	-0.11	-	-0.73
193.687	27.411	0.0258	1.4	2.9	0.0	0.17	-	-0.57
196.852	32.863	0.0176	1.4	3.4	0.0	-0.32	-	-1.07
179.060	25.354	0.0323	1.7	4.0	1.0	-0.56	0.13	-1.20
176.534	22.539	0.0215	2.2	11.4	1.1	-0.64	0.15	-1.35
179.241	24.129	0.0221	2.5	10.5	1.3	-0.56	0.10	-1.14
175.805	20.005	0.0234	1.7	3.4	1.2	-0.98	-0.38	-1.49
171.611	29.397	0.0226	2.1	5.4	1.3	-0.75	-0.16	-1.30
177.182	21.015	0.0259	1.8	4.5	1.0	-0.85	-0.11	-1.54
191.538	28.959	0.0236	1.4	1.9	1.1	-0.82	-0.34	-1.30
188.169	19.600	0.0309	1.5	4.6	0.0	-0.26	-	-1.15
198.677	28.472	0.0202	1.4	3.6	0.0	-0.59	-	-1.68
184.992	20.454	0.0309	2.1	5.5	1.2	-0.78	-0.13	-1.37
177.012	30.440	0.0211	1.4	2.1	0.9	-0.71	-0.13	-1.44
178.483	20.552	0.0232	1.1	1.3	0.8	-0.82	-0.30	-1.50
198.725	19.886	0.0303	1.2	2.4	0.0	0.00	-	-0.79
199.418	21.501	0.0223	2.2	11.0	1.0	-0.42	-	-1.10
181.751	22.388	0.0223	1.3	1.7	1.0	-0.86	-0.28	-1.51
184.824	21.087	0.0323	2.2	12.2	1.0	-0.65	0.18	-1.41
182.673	17.863	0.0222	1.6	5.9	0.0	-0.14	-	-1.00
185.797	27.766	0.0262	2.2	4.2	1.5	-0.51	-0.05	-0.90
199.184	28.200	0.0238	1.2	1.3	1.0	-1.10	-0.56	-1.59
194.788	27.898	0.0262	1.9	4.9	1.0	-0.26	-	-0.79
191.946	27.575	0.0324	1.6	4.0	1.0	-0.67	0.04	-1.37
173.766	22.515	0.0224	2.4	5.4	1.5	-0.97	-0.48	-1.41
179.362	23.918	0.0314	1.5	2.4	1.0	-0.62	-0.06	-1.21
189.009	26.785	0.0252	1.8	6.0	0.0	-0.03	-	-0.69
171.552	27.200	0.0238	1.9	3.6	1.1	-0.42	0.21	-0.85
174.712	19.601	0.0227	1.7	4.6	0.9	-0.51	0.22	-1.20
177.702	22.002	0.0265	1.5	4.0	0.0	0.12	-	-0.65
198.914	29.611	0.0217	1.8	9.0	0.0	-0.34	-	-1.11
188.334	27.451	0.0231	1.3	3.1	0.0	0.13	-	-0.74
198.478	28.296	0.0202	1.1	2.7	0.0	0.19	-	-0.67
182.285	22.697	0.0229	1.4	1.9	0.9	-0.78	-0.18	-1.50
170.251	21.337	0.0211	1.5	2.7	1.0	-0.60	-0.02	-1.16
176.677	18.849	0.0191	1.3	2.1	0.8	-0.49	0.07	-1.21
182.358	22.083	0.0243	0.9	1.5	0.0	-0.12	-	-0.82
176.699	21.032	0.0256	1.3	2.1	0.9	-0.31	0.17	-0.89
197.825	30.488	0.0282	2.0	6.5	1.0	-0.68	0.10	-1.40
181.993	21.919	0.0236	1.0	1.6	0.0	-0.15	-	-0.95
181.893	32.835	0.0252	2.1	4.7	1.3	-1.03	-0.41	-1.60
197.238	28.281	0.0195	1.3	2.7	0.0	-0.02	-	-0.84
195.334	26.887	0.0269	1.4	2.9	0.8	-0.60	0.13	-1.54
196.638	29.184	0.0313	1.9	4.1	1.1	-0.60	0.01	-1.12
176.465	22.225	0.0214	1.5	3.0	0.0	-0.15	-	-0.80
180.968	20.208	0.0227	1.7	3.4	1.1	-0.83	-0.18	-1.44

continued on next page..

Table A.1 – continued from previous page

RA (J2000)	Dec (J2000)	z	Age (Gyr)	Age upper (Gyr)	Age lower (Gyr)	Z (dex)	Z upper (dex)	Z lower (dex)
176.398	21.305	0.0233	1.1	2.2	0.0	0.08	-	-0.69
172.361	28.082	0.0227	1.8	3.6	1.1	-0.52	0.08	-1.00
188.802	26.533	0.0211	2.0	6.5	0.9	0.07	-	-0.53
184.840	25.769	0.0238	1.5	4.2	0.8	-0.57	0.18	-1.39
176.146	26.354	0.0309	1.7	3.9	1.0	-0.67	0.01	-1.32
178.747	31.134	0.0212	1.7	3.1	1.0	-0.18	-	-0.68
184.912	22.153	0.0228	1.1	1.5	0.8	-0.66	-0.14	-1.45
176.356	20.611	0.0264	2.1	5.8	1.2	-0.71	-0.09	-1.29
182.970	21.537	0.0224	1.6	3.9	0.9	-0.57	0.12	-1.24
187.242	32.674	0.0306	1.5	2.4	1.0	-0.76	-0.18	-1.40
198.749	30.905	0.0229	1.2	2.5	0.0	-0.38	-	-1.26
172.642	24.219	0.0227	1.7	3.3	1.1	-0.69	-0.12	-1.25
196.594	17.828	0.0323	2.0	5.3	1.1	-0.62	0.07	-1.22
194.529	29.035	0.0242	1.4	4.0	0.0	0.15	-	-0.72
186.617	31.458	0.0301	1.5	4.9	0.0	-0.10	-	-0.97
181.889	18.235	0.0326	2.3	14.0	1.1	-0.62	0.20	-1.34
185.319	17.191	0.0308	2.4	10.4	1.1	-0.31	-	-0.91
170.679	23.766	0.0232	1.1	2.5	0.0	0.02	-	-0.97
197.391	19.219	0.0230	2.1	5.4	1.1	-0.54	0.13	-1.09
196.527	28.702	0.0185	1.9	5.4	1.0	-0.49	-	-1.11
179.839	21.091	0.0246	1.5	2.4	1.0	-0.66	-0.11	-1.23
180.569	24.375	0.0220	1.6	4.6	0.8	-0.25	-	-0.92
174.452	30.927	0.0323	0.9	1.6	0.0	-0.05	-	-0.90
172.326	21.927	0.0326	1.5	3.6	0.0	0.01	-	-0.70
189.820	18.358	0.0224	1.9	7.8	0.9	-0.47	-	-1.19
192.919	28.053	0.0207	1.7	4.6	1.0	-0.61	0.11	-1.25
193.467	31.107	0.0299	1.8	3.9	1.1	-0.76	-0.16	-1.32
176.363	26.329	0.0301	1.2	2.4	0.0	-0.18	-	-0.97
180.022	21.647	0.0214	1.1	1.7	0.0	-0.29	-	-1.14
189.493	18.869	0.0309	1.8	4.1	1.0	-0.49	0.20	-1.04
171.713	26.197	0.0202	1.4	2.8	0.9	-0.42	0.19	-1.12
186.356	29.738	0.0270	1.9	4.0	1.2	-0.47	0.13	-0.92
175.607	30.264	0.0327	1.2	2.3	0.0	-0.42	-	-1.34
177.744	20.887	0.0269	1.5	3.6	0.0	-0.27	-	-1.01
181.943	25.520	0.0232	1.4	3.1	0.0	-0.27	-	-1.01
185.195	24.916	0.0221	2.5	10.5	1.4	-0.71	-0.10	-1.28
187.728	21.248	0.0276	1.9	4.3	1.3	-0.97	-0.36	-1.53
180.602	29.377	0.0276	2.0	7.5	1.0	-0.69	0.13	-1.48
173.857	22.424	0.0304	2.8	9.3	1.6	-0.95	-0.44	-1.42
178.184	18.614	0.0263	2.4	13.8	1.1	-0.50	-	-1.19
194.605	27.200	0.0268	1.8	5.1	0.9	-0.36	-	-0.95
197.137	30.748	0.0235	1.1	1.7	0.8	-0.56	-0.01	-1.39
177.243	20.376	0.0226	1.3	2.6	0.8	-0.45	0.17	-1.22
192.010	24.505	0.0317	1.7	2.9	1.1	-0.58	-0.02	-1.08
189.690	31.880	0.0224	1.1	1.6	0.0	-0.44	0.07	-1.26
174.466	20.458	0.0298	2.6	12.7	1.4	-0.62	-0.01	-1.19
192.349	29.321	0.0250	1.1	5.9	0.0	-0.07	-	-1.51
192.137	26.116	0.0214	1.3	1.8	0.9	-0.49	0.03	-1.14
187.151	31.482	0.0229	1.7	10.2	0.0	-0.32	-	-1.14
181.198	32.497	0.0257	3.0	11.3	1.6	-1.07	-0.50	-1.62
194.268	27.730	0.0296	1.7	4.5	0.9	-0.37	-	-0.95
186.786	28.957	0.0254	1.5	5.2	0.0	0.05	-	-0.79
193.475	28.187	0.0256	1.6	3.0	1.0	-0.82	-0.20	-1.42
185.665	27.747	0.0240	1.1	1.5	0.9	-0.70	-0.21	-1.44
192.584	26.750	0.0237	1.7	2.9	1.3	-1.19	-0.64	-1.66

continued on next page..

Table A.1 – continued from previous page

RA (J2000)	Dec (J2000)	z	Age (Gyr)	Age upper (Gyr)	Age lower (Gyr)	Z (dex)	Z upper (dex)	Z lower (dex)
173.138	20.401	0.0229	1.4	2.4	0.9	-0.70	-0.10	-1.44
198.990	17.165	0.0235	3.1	14.0	1.6	-1.05	-0.47	-1.63
175.916	18.741	0.0217	1.1	1.7	0.8	-0.53	0.01	-1.33
189.614	28.480	0.0237	1.0	2.4	0.0	-0.20	-	-1.47
182.434	31.023	0.0229	1.4	2.2	0.9	-0.63	-0.05	-1.30
175.249	21.010	0.0218	2.6	9.5	1.5	-0.70	-0.19	-1.22
182.610	26.367	0.0264	0.9	1.4	0.0	-0.43	0.11	-1.39
179.114	24.537	0.0299	1.3	2.7	0.8	-0.51	0.13	-1.33
185.060	17.347	0.0306	1.4	2.7	0.9	-0.67	-0.07	-1.33
183.280	27.468	0.0272	1.6	3.7	1.0	-0.58	0.10	-1.22
199.980	30.839	0.0312	1.8	4.8	1.0	-0.65	0.06	-1.27
177.035	24.216	0.0313	1.0	2.4	0.0	0.09	-	-0.93
175.565	19.070	0.0241	1.2	3.3	0.0	-0.35	-	-1.50
173.361	24.054	0.0235	1.2	1.4	0.9	-0.98	-0.31	-1.70
178.294	28.033	0.0285	1.6	3.4	1.0	-0.63	0.02	-1.25
172.103	27.447	0.0325	1.9	4.9	1.1	-0.79	-0.11	-1.42
179.670	25.316	0.0150	1.6	2.8	1.1	-0.75	-0.22	-1.29
192.435	27.670	0.0254	1.7	4.8	0.0	-0.18	-	-0.85
194.365	28.440	0.0259	2.0	5.5	1.1	-0.67	0.03	-1.29
180.239	28.954	0.0285	1.8	4.8	1.0	-0.73	-0.02	-1.39
172.371	22.565	0.0311	1.5	2.0	1.0	-0.92	-0.33	-1.47
180.238	26.955	0.0286	1.4	2.0	0.9	-0.69	-0.12	-1.39
198.454	31.746	0.0263	2.3	8.4	1.1	-0.86	-0.07	-1.59
194.606	28.129	0.0274	1.4	2.2	1.0	-0.55	0.01	-1.11
197.467	28.382	0.0237	1.6	7.0	0.0	-0.39	-	-1.29
180.322	31.278	0.0231	1.6	9.5	0.0	-0.03	-	-1.02
181.244	32.922	0.0313	1.2	6.5	0.0	-0.18	-	-1.58
188.243	19.922	0.0311	1.8	5.1	1.0	-0.39	-	-0.98
178.476	21.250	0.0230	1.0	1.6	0.0	-0.42	0.14	-1.37
175.880	23.011	0.0231	2.0	4.9	1.1	-0.59	0.05	-1.14
195.687	31.478	0.0241	1.6	8.2	0.0	-0.40	-	-1.38
193.265	32.327	0.0218	1.0	1.3	0.0	-0.64	-0.14	-1.43
176.837	32.923	0.0311	1.1	2.5	0.0	0.09	-	-0.82
174.379	24.680	0.0228	1.7	3.2	1.2	-0.75	-0.30	-1.23
192.025	29.443	0.0231	1.3	5.2	0.0	-0.36	-	-1.45
186.401	26.163	0.0318	1.7	6.6	0.9	-0.57	-	-1.37
176.764	32.895	0.0313	1.6	5.7	0.0	-0.34	-	-1.14
194.523	29.017	0.0257	2.4	11.4	1.2	-0.54	0.17	-1.17
179.125	26.736	0.0286	1.4	2.9	0.0	0.06	-	-0.71
190.706	22.773	0.0234	1.5	5.5	0.0	-0.33	-	-1.21
174.175	22.046	0.0308	2.3	10.5	1.1	-0.56	0.19	-1.21
177.548	21.237	0.0274	1.4	8.4	0.0	-0.01	-	-1.15
181.690	24.607	0.0258	1.0	1.6	0.0	-0.36	-	-1.39
197.281	28.668	0.0187	0.9	1.5	0.0	-0.13	-	-1.18
196.829	18.595	0.0225	1.6	8.5	0.0	-0.25	-	-1.19
190.047	18.062	0.0264	0.9	1.3	0.0	-0.46	-	-1.67
184.965	20.402	0.0304	1.0	1.4	0.0	-0.58	-0.04	-1.45
197.829	27.967	0.0244	1.6	7.1	0.0	-0.35	-	-1.25
174.611	20.365	0.0258	1.4	4.1	0.0	0.05	-	-0.81
171.980	27.347	0.0327	1.1	1.7	0.0	-0.29	0.21	-1.04
199.620	25.220	0.0301	2.5	7.5	1.4	-1.02	-0.36	-1.65
181.201	20.754	0.0239	2.0	8.3	0.9	-0.14	-	-0.81
183.845	21.878	0.0239	1.1	3.0	0.0	-0.27	-	-1.30
175.514	21.340	0.0255	0.9	1.8	0.0	-0.02	-	-1.05
186.556	31.395	0.0289	1.1	3.5	0.0	-0.32	-	-1.65

continued on next page..

Table A.1 – continued from previous page

RA (J2000)	Dec (J2000)	z	Age (Gyr)	Age upper (Gyr)	Age lower (Gyr)	Z (dex)	Z upper (dex)	Z lower (dex)
181.448	20.326	0.0233	1.6	3.1	0.9	-0.94	-0.13	-1.71
173.478	26.364	0.0322	1.9	4.1	1.3	-0.92	-0.34	-1.45
174.986	20.837	0.0233	1.5	6.9	0.0	-0.26	-	-1.23
176.306	32.312	0.0325	1.1	3.5	0.0	-0.26	-	-1.26
189.099	27.032	0.0244	0.9	4.8	0.0	0.11	-	-1.38
178.095	25.083	0.0224	1.7	4.7	0.9	-0.52	-	-1.22
188.477	20.167	0.0313	2.6	11.4	1.4	-0.92	-0.27	-1.50
185.557	28.245	0.0262	1.7	8.2	0.0	-0.23	-	-1.09
177.237	26.248	0.0303	1.4	4.9	0.0	-0.13	-	-1.12
190.246	27.970	0.0311	1.0	1.3	0.8	-0.77	-0.24	-1.52
184.488	25.077	0.0229	1.7	3.8	1.1	-0.95	-0.23	-1.60
175.268	26.272	0.0232	1.3	4.3	0.0	-0.29	-	-1.27
176.168	20.477	0.0203	0.9	1.5	0.0	0.01	-	-0.80
186.334	28.381	0.0151	2.3	11.2	1.1	-0.81	0.01	-1.57
194.329	26.938	0.0256	1.5	12.6	0.0	-0.06	-	-1.18
175.895	23.944	0.0225	1.4	7.7	0.0	-0.26	-	-1.38
191.381	26.393	0.0259	1.2	5.3	0.0	0.02	-	-1.16
192.248	27.376	0.0209	0.9	1.5	0.0	-0.33	-	-1.46
179.399	29.237	0.0224	2.2	13.8	1.0	-0.83	0.08	-1.70
181.924	25.254	0.0224	2.0	8.1	0.9	-0.33	-	-1.00
189.462	28.000	0.0243	1.1	1.9	0.0	-0.37	0.20	-1.23
179.501	31.800	0.0291	1.3	6.2	0.0	-0.11	-	-1.22
199.829	31.052	0.0251	1.1	3.0	0.0	-0.17	-	-1.26
196.323	28.583	0.0262	1.1	8.9	0.0	0.19	-	-1.19
185.683	18.549	0.0217	1.0	4.9	0.0	0.02	-	-1.54
182.571	22.489	0.0225	2.3	6.5	1.4	-0.40	0.16	-0.86
181.221	32.276	0.0276	13.1	-	5.7	-0.24	0.02	-0.49
179.978	22.718	0.0223	8.5	-	3.6	-0.44	-0.17	-0.76
194.449	27.769	0.0193	13.8	-	6.4	-0.27	-0.00	-0.51
196.817	28.284	0.0248	13.6	-	6.3	-0.18	0.09	-0.38
193.808	27.709	0.0223	8.3	-	3.0	-0.14	4.00	-0.44
176.086	32.846	0.0319	13.0	-	4.3	-0.02	4.00	-0.29
181.558	28.081	0.0266	7.6	-	3.0	-0.17	0.19	-0.45
194.445	28.141	0.0214	6.0	-	2.3	0.12	4.00	-0.21
195.276	27.398	0.0271	6.9	-	2.7	-0.05	4.00	-0.34
178.722	28.062	0.0286	5.4	-	2.3	0.14	4.00	-0.19
188.933	26.577	0.0226	14.0	-	5.8	-0.46	-0.20	-0.76
192.764	26.446	0.0200	11.1	-	4.3	-0.26	0.04	-0.54
193.581	28.091	0.0225	5.3	-	2.5	-0.18	0.20	-0.49
194.191	28.052	0.0231	13.0	-	5.0	-0.38	-0.11	-0.69
193.731	29.012	0.0214	10.1	-	3.5	-0.19	0.15	-0.48
176.432	19.649	0.0262	4.6	-	2.2	-0.18	4.00	-0.54
195.633	27.936	0.0221	7.8	-	2.9	-0.09	4.00	-0.37
195.036	28.160	0.0249	14.0	-	4.3	-0.13	4.00	-0.40
178.369	20.485	0.0223	12.1	-	4.2	-0.05	4.00	-0.30
181.537	28.043	0.0268	9.0	-	3.3	-0.22	0.10	-0.51
175.481	25.625	0.0304	8.5	-	3.1	-0.21	0.13	-0.49
195.369	27.927	0.0251	4.5	-	2.2	-0.25	0.19	-0.64
175.497	20.255	0.0224	5.8	-	2.6	-0.36	-0.01	-0.78
183.703	22.195	0.0243	6.1	-	2.5	0.00	4.00	-0.31
180.539	20.578	0.0237	9.0	-	2.9	-0.35	0.04	-0.73
196.285	27.513	0.0239	8.7	-	3.0	-0.25	0.12	-0.58
194.040	28.311	0.0264	11.4	-	4.6	-0.42	-0.16	-0.72
196.332	29.197	0.0270	4.0	-	1.6	0.05	4.00	-0.38
194.091	28.487	0.0220	5.6	-	2.6	-0.21	0.16	-0.54

continued on next page..

Table A.1 – continued from previous page

RA (J2000)	Dec (J2000)	z	Age (Gyr)	Age upper (Gyr)	Age lower (Gyr)	Z (dex)	Z upper (dex)	Z lower (dex)
181.359	20.541	0.0241	5.0	-	2.4	-0.36	0.00	-0.75
195.243	27.652	0.0174	6.5	-	2.4	0.03	4.00	-0.31
194.779	27.772	0.0208	13.3	-	4.8	-0.34	-0.03	-0.66
195.523	27.297	0.0243	6.2	-	2.6	-0.07	4.00	-0.38
184.910	28.408	0.0256	13.8	-	4.7	-0.26	0.07	-0.57
174.353	30.711	0.0276	13.2	-	4.6	-0.41	-0.10	-0.76
196.302	28.152	0.0217	11.2	-	4.6	-0.74	-0.44	-1.05
176.422	19.267	0.0219	12.7	-	4.8	-0.29	0.01	-0.58
180.938	20.106	0.0247	5.6	-	2.3	-0.14	4.00	-0.51
194.528	27.577	0.0250	4.7	-	1.8	-0.06	4.00	-0.46
194.377	27.543	0.0255	8.0	-	2.8	-0.24	0.16	-0.59
194.340	27.475	0.0232	6.9	-	1.7	0.17	4.00	-0.25
178.477	20.750	0.0213	4.7	-	2.5	-0.53	-0.24	-0.90
192.011	27.278	0.0261	9.2	-	2.9	-0.33	0.07	-0.71
182.195	31.555	0.0225	7.9	-	2.9	-0.21	0.20	-0.54
195.833	28.617	0.0199	10.3	-	3.6	-0.17	0.16	-0.44
193.440	27.250	0.0230	5.0	-	2.5	-0.37	-0.03	-0.75
176.110	19.997	0.0189	5.9	-	1.8	-0.09	4.00	-0.53
194.261	27.657	0.0227	14.0	-	3.3	-0.20	4.00	-0.60
194.728	27.796	0.0216	11.5	-	4.1	-0.19	0.13	-0.45
182.093	25.316	0.0227	10.0	-	3.1	-0.35	-0.01	-0.70
197.905	22.993	0.0230	5.6	-	2.3	-0.38	0.05	-0.88
183.819	24.037	0.0232	11.1	-	3.4	-0.24	0.14	-0.58
173.913	26.097	0.0306	6.4	-	2.8	-0.35	-0.02	-0.70
197.273	28.491	0.0258	4.8	-	2.6	-0.50	-0.20	-0.87
184.814	25.930	0.0224	5.4	-	2.1	-0.33	0.15	-0.82
196.688	29.372	0.0264	4.4	-	2.2	-0.33	0.05	-0.72
188.918	26.929	0.0257	9.4	-	2.9	-0.22	0.21	-0.59
195.329	28.128	0.0227	5.2	-	2.5	-0.43	-0.08	-0.87
195.616	29.488	0.0236	4.3	-	2.4	-0.43	-0.11	-0.83
195.431	29.178	0.0234	5.0	-	2.5	-0.45	-0.09	-0.87
184.824	28.264	0.0269	10.7	-	2.8	-0.38	0.09	-0.85
196.847	27.866	0.0205	12.5	-	3.0	-0.21	4.00	-0.61
180.866	28.160	0.0265	5.4	-	2.1	-0.20	4.00	-0.62
190.242	27.981	0.0243	3.3	-	2.0	-0.40	-0.04	-0.88
178.286	20.648	0.0240	7.6	-	2.8	-0.41	-0.04	-0.83
194.798	28.009	0.0230	12.4	-	3.0	-0.28	0.19	-0.69
191.968	27.267	0.0265	6.5	-	1.7	0.08	4.00	-0.34
194.964	28.073	0.0250	5.5	-	2.2	-0.28	0.19	-0.73
194.017	27.150	0.0245	5.4	-	2.5	-0.36	-0.00	-0.76
175.579	20.096	0.0226	4.7	-	1.9	-0.12	4.00	-0.52
194.963	27.833	0.0263	7.4	-	2.8	-0.31	0.08	-0.67
198.606	21.587	0.0226	4.1	-	2.0	-0.41	0.04	-0.94
184.064	17.801	0.0296	10.9	-	3.1	-0.41	-0.04	-0.83
194.268	27.526	0.0277	12.7	-	3.3	-0.49	-0.09	-0.93
195.084	27.843	0.0262	5.7	-	2.4	-0.35	0.08	-0.83
190.318	27.853	0.0258	8.2	-	3.4	-1.35	-1.01	-4.00
195.183	28.416	0.0209	5.6	-	2.6	-0.40	-0.07	-0.83
188.809	26.472	0.0229	5.3	-	1.8	-0.03	4.00	-0.42
194.670	27.827	0.0206	13.9	-	3.4	-0.44	-0.02	-0.89
195.648	26.662	0.0247	7.3	-	2.0	-0.03	4.00	-0.46
180.148	18.020	0.0235	3.9	-	1.8	-0.21	4.00	-0.65
194.313	26.466	0.0216	7.6	-	2.9	-0.38	-0.04	-0.75
195.316	28.872	0.0238	8.8	-	3.0	-0.62	-0.25	-1.03
194.525	27.419	0.0192	9.4	-	2.8	-0.22	4.00	-0.59

continued on next page..

Table A.1 – continued from previous page

RA (J2000)	Dec (J2000)	z	Age (Gyr)	Age upper (Gyr)	Age lower (Gyr)	Z (dex)	Z upper (dex)	Z lower (dex)
195.803	28.172	0.0243	4.3	-	2.2	-0.46	-0.07	-0.95
193.673	27.041	0.0236	5.1	-	2.3	-0.36	0.03	-0.79
183.988	23.868	0.0227	11.4	-	3.0	-0.31	0.12	-0.71
173.433	17.396	0.0192	5.3	-	2.3	-0.53	-0.11	-1.05
182.970	25.443	0.0227	5.5	-	2.5	-0.38	0.00	-0.84
176.051	19.943	0.0207	8.3	-	2.8	-0.49	-0.09	-0.94
195.454	28.172	0.0254	12.6	-	3.1	-0.55	-0.13	-0.97
175.476	20.343	0.0198	5.9	-	2.7	-0.41	-0.09	-0.82
194.097	27.544	0.0245	9.6	-	1.3	0.04	4.00	-0.52
194.721	28.234	0.0202	2.7	-	0.0	0.09	4.00	-0.63
194.748	27.935	0.0192	7.9	-	1.6	-0.12	4.00	-0.65
190.697	27.272	0.0197	6.2	-	2.4	-0.23	0.20	-0.62
181.954	20.645	0.0238	2.8	-	1.5	-0.34	4.00	-0.93
176.181	20.320	0.0244	6.8	-	2.3	-0.17	4.00	-0.59
188.883	26.451	0.0207	7.2	-	2.4	-0.15	4.00	-0.56
182.321	22.250	0.0242	7.4	-	3.0	-0.77	-0.44	-1.11
191.449	28.419	0.0261	3.7	-	1.5	-0.41	4.00	-1.08
182.222	25.550	0.0224	7.1	-	2.7	-0.55	-0.20	-0.95
190.308	22.595	0.0287	5.3	-	2.6	-0.91	-0.58	-1.25
195.057	27.867	0.0247	5.9	-	1.4	0.14	4.00	-0.32
181.822	25.264	0.0225	12.0	-	3.0	-0.43	-0.02	-0.88
194.770	28.050	0.0269	13.1	-	3.8	-0.51	-0.13	-0.91
179.553	27.915	0.0276	12.6	-	3.0	-0.45	0.02	-0.94
173.771	22.540	0.0305	6.5	-	1.5	-0.19	4.00	-0.82
181.590	28.127	0.0269	13.6	-	3.1	-0.80	-0.32	-1.20
195.115	27.625	0.0196	9.5	-	3.1	-0.56	-0.21	-0.95
175.695	26.536	0.0306	3.4	-	1.6	-0.13	4.00	-0.59
195.406	28.016	0.0238	6.9	-	1.5	0.04	4.00	-0.46
194.486	27.382	0.0174	3.5	-	1.3	-0.02	4.00	-0.56
188.781	26.909	0.0227	5.4	-	2.3	-0.42	0.00	-0.93
185.115	30.454	0.0285	5.0	-	2.2	-0.43	0.01	-0.93
175.959	21.500	0.0238	3.3	-	1.8	-0.38	0.05	-0.90
170.737	24.286	0.0257	12.7	-	4.3	-0.80	-0.46	-1.12
181.323	21.273	0.0229	5.4	-	2.2	-0.34	0.13	-0.84
193.837	27.150	0.0209	4.4	-	1.5	0.00	4.00	-0.47
177.516	21.783	0.0269	10.2	-	1.8	-0.06	4.00	-0.53
175.881	22.725	0.0230	11.9	-	3.8	-0.60	-0.26	-0.97
175.755	24.370	0.0304	3.1	-	1.8	-0.47	-0.04	-0.99
174.365	22.063	0.0302	6.6	-	2.1	-0.99	-0.41	-1.58
192.833	21.230	0.0232	4.2	-	2.3	-0.59	-0.28	-1.01
175.969	26.203	0.0311	4.4	-	2.2	-0.63	-0.25	-1.11
182.021	28.667	0.0280	3.8	-	1.1	-0.24	4.00	-1.05
177.507	21.316	0.0262	13.9	-	4.4	-0.56	-0.21	-0.95
176.256	32.646	0.0214	14.0	-	3.0	-0.38	0.12	-0.88
178.224	20.591	0.0224	13.1	-	1.5	-0.07	4.00	-0.66
183.318	21.622	0.0245	4.8	-	2.1	-0.55	-0.05	-1.11
175.664	24.823	0.0210	5.3	-	2.2	-0.31	0.16	-0.78
194.340	27.023	0.0267	3.2	-	1.8	-0.67	-0.24	-1.20
175.986	20.031	0.0227	5.1	-	2.5	-0.54	-0.20	-0.97
196.540	28.065	0.0257	13.8	-	3.1	-0.39	0.07	-0.87
195.413	28.246	0.0253	13.9	-	3.1	-0.61	-0.14	-1.07
199.917	27.706	0.0231	4.7	-	2.3	-1.20	-0.82	-1.58
176.451	19.426	0.0208	4.3	-	1.6	-0.15	4.00	-0.69
195.943	27.987	0.0206	6.1	-	2.5	-0.70	-0.31	-1.19
197.229	29.041	0.0314	3.5	-	1.9	-0.56	-0.14	-1.08

continued on next page..

Table A.1 – continued from previous page

RA (J2000)	Dec (J2000)	z	Age (Gyr)	Age upper (Gyr)	Age lower (Gyr)	Z (dex)	Z upper (dex)	Z lower (dex)
194.827	27.514	0.0202	2.8	-	1.1	-0.06	4.00	-0.70
195.105	27.552	0.0242	10.3	-	3.4	-0.69	-0.33	-1.07
183.515	20.735	0.0243	7.6	-	2.7	-0.39	0.01	-0.83
194.150	26.905	0.0263	3.5	-	1.5	-0.20	4.00	-0.73
174.879	22.493	0.0228	4.1	-	2.1	-0.55	-0.16	-1.03
183.015	29.417	0.0226	3.2	-	1.2	-0.20	4.00	-0.90
181.547	20.566	0.0247	5.8	-	2.0	-0.24	4.00	-0.73
192.594	27.175	0.0234	2.8	-	1.6	-0.49	0.08	-1.06
181.598	31.034	0.0236	7.6	-	2.5	-0.66	-0.17	-1.19
194.471	27.707	0.0215	6.6	-	1.6	-0.18	4.00	-0.79
178.707	22.103	0.0235	1.7	2.1	1.3	-1.33	-0.86	-
179.030	24.395	0.0283	3.3	-	1.6	-0.61	-0.01	-1.24
170.664	24.155	0.0264	3.2	-	0.0	0.19	4.00	-0.55
195.008	28.435	0.0270	6.5	-	2.5	-0.43	0.02	-0.93
175.665	26.531	0.0322	12.3	-	3.9	-0.83	-0.45	-1.15
195.633	28.439	0.0199	11.7	-	3.0	-0.19	4.00	-0.57
181.688	25.495	0.0227	2.6	-	1.0	-0.06	4.00	-0.70
172.205	28.317	0.0228	1.3	1.7	0.8	-1.06	-0.20	-
176.212	24.931	0.0312	3.0	-	1.7	-0.53	-0.08	-1.05
182.506	31.385	0.0300	3.2	-	1.8	-0.60	-0.16	-1.12
173.447	24.317	0.0235	6.2	-	2.4	-0.69	-0.24	-1.23
181.471	28.616	0.0295	5.5	-	1.7	-0.24	4.00	-0.78
175.663	18.345	0.0243	5.5	-	2.3	-0.78	-0.34	-1.26
171.554	28.366	0.0299	4.2	-	2.3	-0.51	-0.16	-0.95
183.079	24.100	0.0219	3.6	-	1.6	-0.78	-0.19	-1.39
194.875	28.700	0.0237	5.7	-	1.7	-0.09	4.00	-0.54
183.260	21.551	0.0238	9.8	-	2.7	-0.72	-0.24	-1.20
181.689	27.908	0.0263	6.7	-	2.2	-0.17	4.00	-0.62
182.197	32.538	0.0244	0.8	1.0	0.0	-1.06	-0.30	-
194.354	28.496	0.0239	2.3	-	0.0	0.12	4.00	-0.72
184.771	28.656	0.0244	5.9	-	2.4	-0.53	-0.13	-1.02
174.340	21.873	0.0230	2.8	-	1.6	-0.65	-0.12	-1.18
170.265	24.772	0.0250	1.3	1.5	0.9	-1.25	-0.44	-
195.324	28.097	0.0268	3.1	-	1.1	0.01	4.00	-0.63
195.361	28.436	0.0192	9.7	-	2.7	-0.38	0.11	-0.87
184.849	30.501	0.0284	13.7	-	2.5	-0.66	0.00	-1.25
198.857	27.303	0.0216	2.6	-	1.1	-0.57	4.00	-1.35
177.474	23.386	0.0318	2.3	9.6	1.1	-1.14	-0.26	-
175.726	19.648	0.0224	2.7	-	1.3	-0.25	4.00	-0.87
196.671	27.884	0.0235	9.9	-	2.5	-0.62	-0.07	-1.18
177.836	22.054	0.0272	2.7	-	1.0	0.14	4.00	-0.52
194.099	27.234	0.0202	3.6	-	1.6	-0.62	0.02	-1.27
174.727	32.499	0.0328	5.1	-	2.2	-0.45	0.00	-0.97
182.025	25.267	0.0193	10.8	-	2.9	-0.48	-0.08	-0.91
181.723	25.541	0.0225	3.9	-	1.7	-0.16	4.00	-0.60
177.183	21.190	0.0227	4.1	-	2.0	-0.70	-0.28	-1.23
171.018	24.097	0.0244	4.4	-	2.0	-0.96	-0.48	-1.45
194.772	27.644	0.0181	1.5	1.7	1.3	-1.41	-1.04	-
193.434	27.781	0.0222	12.7	-	3.4	-0.34	0.07	-0.75
178.030	27.652	0.0289	11.0	-	2.8	-0.81	-0.32	-1.25
182.040	24.677	0.0229	3.9	-	1.6	-0.58	0.05	-1.21
195.525	27.765	0.0241	3.5	-	1.6	-0.26	4.00	-0.83
194.990	28.065	0.0195	7.2	-	2.5	-0.85	-0.37	-1.30
181.605	20.116	0.0246	4.4	-	2.3	-0.66	-0.30	-1.12
196.535	30.209	0.0161	2.9	-	1.1	-0.43	4.00	-1.21

continued on next page..

Table A.1 – continued from previous page

RA (J2000)	Dec (J2000)	z	Age (Gyr)	Age upper (Gyr)	Age lower (Gyr)	Z (dex)	Z upper (dex)	Z lower (dex)
189.532	22.699	0.0232	3.3	-	1.7	-0.77	-0.26	-1.31
195.430	28.298	0.0257	10.3	-	2.6	-0.52	-0.01	-1.05
193.155	27.325	0.0264	7.5	-	2.3	-0.69	-0.14	-1.26
176.412	21.318	0.0226	3.1	-	1.6	-0.47	0.11	-1.09
178.348	17.373	0.0228	6.1	-	1.6	-0.91	-0.12	-1.66
188.933	27.281	0.0241	2.7	-	1.4	-0.49	0.14	-1.11
194.160	28.106	0.0216	3.1	-	1.5	-0.37	4.00	-1.06
197.317	29.368	0.0209	1.2	1.3	1.0	-1.41	-0.81	-
187.548	26.433	0.0209	3.9	-	1.0	-0.18	4.00	-1.03
195.046	28.065	0.0245	14.0	-	2.7	-1.03	-0.45	-1.53
180.984	22.980	0.0226	5.2	-	1.9	-0.37	0.21	-0.95
177.350	21.111	0.0263	7.5	-	2.3	-0.92	-0.37	-1.46
197.245	27.614	0.0247	3.0	-	1.5	-0.71	-0.08	-1.34
170.502	24.079	0.0280	2.9	-	1.1	-0.46	4.00	-1.30
176.396	19.592	0.0232	11.8	-	2.1	-0.38	4.00	-1.01
183.188	21.563	0.0237	3.1	-	1.3	-0.26	4.00	-0.97
176.322	27.276	0.0309	4.3	-	2.0	-0.48	-0.04	-1.00
182.838	18.600	0.0253	2.8	-	1.3	-1.01	-0.17	-4.00
197.950	30.973	0.0248	3.1	-	1.8	-0.63	-0.23	-1.14
194.864	27.785	0.0220	7.0	-	2.2	-0.52	0.01	-1.08
196.205	28.661	0.0262	4.8	-	2.0	-0.34	0.16	-0.85
173.363	17.419	0.0215	2.2	-	0.9	-0.84	0.14	-4.00
179.007	24.321	0.0283	9.2	-	2.2	-0.69	-0.02	-1.33
181.979	25.017	0.0221	2.8	-	1.1	-0.64	4.00	-1.49
194.198	27.292	0.0262	2.7	-	1.0	0.10	4.00	-0.52
181.550	25.487	0.0211	3.5	-	1.5	-0.38	4.00	-1.06
181.718	27.863	0.0273	10.4	-	1.4	-0.11	4.00	-0.76
197.465	28.900	0.0258	3.1	-	1.6	-0.47	0.08	-1.09
194.565	27.087	0.0257	7.5	-	1.7	-0.89	-0.12	-1.62
180.967	28.122	0.0305	4.7	-	1.8	-0.64	-0.09	-1.24
181.527	20.785	0.0245	4.6	-	2.0	-1.04	-0.52	-1.57
192.632	27.314	0.0267	1.5	1.9	1.0	-1.10	-0.33	-
193.993	28.407	0.0200	4.1	-	1.7	-0.71	-0.09	-1.37
176.134	20.107	0.0240	3.2	6.6	1.7	-1.44	-0.99	-
175.990	20.190	0.0197	10.9	-	2.2	-0.57	0.11	-1.19
195.659	28.502	0.0192	7.4	-	2.3	-0.63	-0.09	-1.20
181.576	20.612	0.0240	4.5	-	1.8	-0.50	0.05	-1.11
193.837	27.669	0.0237	10.3	-	1.7	-0.04	4.00	-0.56
179.324	26.517	0.0228	2.7	9.4	1.4	-1.10	-0.40	-
183.337	32.674	0.0306	13.4	-	3.0	-0.81	-0.32	-1.23
198.336	30.560	0.0199	2.6	-	1.3	-0.63	0.11	-1.30
171.700	22.558	0.0225	4.1	-	1.8	-0.88	-0.38	-1.45
179.892	28.717	0.0270	10.7	-	2.6	-0.70	-0.18	-1.21
192.985	27.088	0.0265	11.9	-	2.6	-1.08	-0.53	-1.59
193.211	27.746	0.0200	7.2	-	1.6	-0.11	4.00	-0.67
178.257	27.157	0.0284	3.0	-	1.6	-0.89	-0.30	-1.46
175.877	21.412	0.0230	6.7	-	1.8	-0.30	4.00	-0.90
178.020	28.116	0.0287	11.5	-	2.4	-1.25	-0.63	-4.00
185.089	28.413	0.0272	3.8	-	0.0	0.04	4.00	-0.82
197.899	29.063	0.0243	3.3	-	1.9	-0.64	-0.23	-1.15
192.960	27.361	0.0215	10.3	-	2.9	-0.84	-0.42	-1.21
195.539	27.589	0.0215	4.1	-	2.0	-0.54	-0.12	-1.06
188.978	26.819	0.0239	4.2	-	1.0	-0.14	4.00	-0.96
175.007	18.566	0.0269	2.9	-	1.6	-0.40	0.17	-1.01
182.168	17.957	0.0255	6.3	-	2.2	-1.26	-0.68	-4.00

continued on next page..

Table A.1 – continued from previous page

RA (J2000)	Dec (J2000)	z	Age (Gyr)	Age upper (Gyr)	Age lower (Gyr)	Z (dex)	Z upper (dex)	Z lower (dex)
178.126	19.761	0.0212	9.4	-	0.0	0.19	4.00	-0.81
187.631	25.309	0.0223	4.7	-	1.3	-0.26	4.00	-0.97
176.400	19.280	0.0214	3.1	-	1.4	-0.35	4.00	-1.08
178.733	29.343	0.0213	1.4	1.6	1.0	-1.15	-0.53	-
196.317	25.958	0.0217	3.1	-	1.7	-0.38	0.11	-0.94
186.402	32.183	0.0291	4.1	-	1.4	-1.24	-0.40	-4.00
191.289	23.039	0.0227	5.6	-	1.7	-0.31	4.00	-0.94
180.987	20.088	0.0203	5.4	-	2.3	-0.56	-0.13	-1.07
178.305	25.566	0.0289	1.5	2.7	0.9	-1.22	-0.31	-
180.197	22.435	0.0222	1.2	2.1	0.0	-0.71	0.07	-
182.123	25.266	0.0243	5.8	-	2.3	-0.58	-0.12	-1.11
178.380	20.340	0.0201	6.8	-	2.3	-1.12	-0.57	-1.65
195.092	28.247	0.0251	3.7	-	1.8	-0.54	-0.08	-1.09
197.719	24.865	0.0248	5.0	-	1.2	-0.46	4.00	-1.29
181.857	27.949	0.0272	2.8	-	1.0	0.12	4.00	-0.51
184.837	20.152	0.0289	3.3	-	1.6	-0.52	0.08	-1.15
184.746	21.306	0.0292	1.3	1.7	0.9	-0.99	-0.23	-
194.233	27.462	0.0254	3.0	-	1.6	-0.58	-0.01	-1.17
194.150	27.719	0.0224	9.1	-	2.1	-0.54	0.09	-1.14
196.695	29.131	0.0264	6.1	-	2.2	-0.77	-0.27	-1.32
174.378	19.043	0.0295	2.2	4.0	1.4	-1.23	-0.61	-
175.954	20.248	0.0204	3.4	9.9	1.6	-1.25	-0.75	-
187.147	26.163	0.0317	1.7	2.4	1.4	-1.41	-0.99	-
183.198	27.714	0.0277	2.5	-	0.9	-0.61	4.00	-1.57
195.447	27.622	0.0260	7.9	-	1.8	-0.76	-0.03	-1.49
173.060	29.939	0.0273	2.6	-	1.0	-0.84	0.14	-4.00
177.862	18.965	0.0206	2.8	-	1.4	-0.36	4.00	-1.03
193.302	27.323	0.0221	12.1	-	2.7	-0.41	0.15	-0.96
183.207	20.562	0.0279	5.2	-	1.0	-0.21	4.00	-1.09
185.037	25.586	0.0224	4.9	-	1.8	-0.59	-0.03	-1.19
186.012	21.760	0.0324	1.3	1.7	0.9	-1.05	-0.23	-
173.034	28.056	0.0241	2.9	-	1.6	-0.41	0.12	-0.99
198.657	27.846	0.0327	3.8	-	1.6	-1.24	-0.56	-4.00
170.816	24.035	0.0250	3.9	7.7	2.0	-1.40	-1.01	-
185.464	26.364	0.0238	1.5	2.5	1.0	-1.23	-0.41	-
196.666	28.518	0.0262	8.8	-	1.6	-0.29	4.00	-0.96
195.807	31.321	0.0260	2.6	7.5	1.5	-1.11	-0.47	-
194.008	26.921	0.0190	4.8	-	1.1	-0.57	4.00	-1.49
185.088	32.848	0.0304	1.7	-	0.0	-0.51	-	-
177.860	25.809	0.0221	3.6	-	1.5	-0.95	-0.24	-1.65
191.878	27.957	0.0318	5.7	-	1.2	-0.13	4.00	-0.83
177.665	20.907	0.0213	5.8	-	2.3	-1.12	-0.63	-1.61
180.631	23.839	0.0223	2.2	-	0.9	-0.42	4.00	-1.21
195.143	27.935	0.0292	3.6	-	1.0	-0.25	4.00	-1.09
178.185	23.572	0.0221	4.5	-	1.7	-1.06	-0.45	-1.68
195.497	28.709	0.0202	3.0	-	1.3	-0.92	-0.02	-1.71
191.110	27.193	0.0218	1.5	2.9	1.0	-1.07	-0.24	-
178.204	29.340	0.0284	3.7	-	1.5	-0.37	4.00	-1.06
194.578	27.311	0.0247	5.2	-	2.1	-1.64	-1.06	-4.00
171.104	23.649	0.0278	3.1	-	1.7	-0.68	-0.21	-1.23
183.981	28.378	0.0279	11.9	-	1.9	-0.86	-0.03	-1.62
192.564	27.060	0.0222	5.0	-	1.7	-0.25	4.00	-0.78
179.337	25.196	0.0143	2.7	-	1.2	-0.47	4.00	-1.17
181.462	31.048	0.0251	2.8	-	1.6	-0.64	-0.08	-1.20
189.202	27.549	0.0245	10.8	-	2.2	-0.49	0.18	-1.11

continued on next page..

Table A.1 – continued from previous page

RA (J2000)	Dec (J2000)	z	Age (Gyr)	Age upper (Gyr)	Age lower (Gyr)	Z (dex)	Z upper (dex)	Z lower (dex)
179.487	22.190	0.0309	4.4	-	1.6	-0.33	4.00	-0.95
183.049	18.094	0.0251	1.7	4.2	0.9	-1.09	-0.14	-
182.643	28.396	0.0280	2.5	-	1.0	-0.58	4.00	-1.45
195.601	29.452	0.0260	12.9	-	2.6	-1.12	-0.52	-1.66
183.673	23.853	0.0221	5.4	-	2.2	-1.00	-0.51	-1.52
174.871	22.373	0.0301	6.1	-	1.9	-0.73	-0.11	-1.41
193.648	26.751	0.0268	1.9	-	0.0	-0.26	4.00	-1.47
197.985	22.247	0.0316	2.8	-	1.6	-0.55	-0.02	-1.11
177.077	18.938	0.0198	9.8	-	1.1	-0.20	4.00	-0.99
181.712	28.278	0.0273	5.1	-	1.6	-0.31	4.00	-0.95
187.819	31.341	0.0287	2.2	-	0.0	-0.29	4.00	-1.23
190.162	26.968	0.0222	1.3	2.1	0.9	-1.49	-0.48	-
194.270	27.677	0.0261	9.3	-	2.1	-0.52	0.14	-1.14
170.569	32.659	0.0276	2.6	6.4	1.5	-1.17	-0.56	-
196.095	28.811	0.0265	1.4	1.5	1.0	-1.13	-0.50	-
195.819	32.721	0.0319	2.8	-	1.0	-0.02	4.00	-0.70
198.695	24.513	0.0320	1.4	2.2	1.0	-1.42	-0.60	-
179.243	22.347	0.0308	3.8	-	1.7	-1.34	-0.73	-4.00
181.111	31.911	0.0306	2.0	3.9	1.3	-1.38	-0.67	-
184.454	17.475	0.0299	2.7	-	1.2	-1.05	-0.12	-4.00
176.753	19.458	0.0180	2.5	-	1.1	-0.43	4.00	-1.12
195.148	27.943	0.0233	13.3	-	2.6	-0.29	4.00	-0.83
195.126	28.160	0.0236	10.2	-	1.5	-0.26	4.00	-0.99
174.516	19.862	0.0207	3.8	-	1.5	-0.81	-0.09	-1.53
173.282	24.653	0.0234	5.1	-	1.9	-0.84	-0.30	-1.44
178.744	26.203	0.0172	5.1	-	1.9	-0.97	-0.41	-1.58
193.861	27.604	0.0226	5.6	-	2.1	-0.63	-0.11	-1.21
199.174	31.368	0.0192	1.3	1.6	0.9	-1.19	-0.32	-
175.588	26.531	0.0288	4.7	-	1.5	-0.46	4.00	-1.18
193.867	27.950	0.0208	8.1	-	2.4	-1.16	-0.60	-1.70
194.346	26.988	0.0278	3.6	-	0.0	0.10	4.00	-0.82
195.333	27.961	0.0263	5.5	-	1.5	-0.42	4.00	-1.18
179.562	21.900	0.0206	3.3	-	1.3	-0.78	0.06	-1.57
173.393	24.534	0.0232	1.1	1.3	0.9	-1.47	-0.67	-
193.830	27.925	0.0215	5.4	-	1.4	-0.76	0.20	-1.64
192.193	30.889	0.0292	3.1	-	1.4	-1.02	-0.24	-4.00
181.759	20.659	0.0250	3.4	-	1.7	-0.62	-0.12	-1.19
174.718	23.447	0.0213	3.7	-	1.5	-1.23	-0.47	-4.00
187.748	25.562	0.0222	2.9	-	1.5	-0.34	4.00	-0.95
173.921	20.533	0.0210	2.9	-	1.4	-0.73	0.00	-1.43
181.961	19.767	0.0247	5.4	-	2.2	-0.68	-0.20	-1.24
184.846	29.024	0.0254	12.8	-	2.6	-0.98	-0.38	-1.52
190.380	27.243	0.0246	2.4	-	0.0	-0.05	4.00	-0.93
194.917	28.631	0.0178	1.6	2.1	1.1	-1.32	-0.64	-
178.543	20.747	0.0214	1.1	1.4	0.0	-1.45	-0.33	-
176.274	21.412	0.0261	1.0	1.1	0.8	-1.11	-0.38	-
194.786	28.728	0.0237	2.4	-	1.0	-0.30	4.00	-1.03
184.955	28.604	0.0282	4.4	-	1.3	-1.01	-0.03	-4.00
174.905	26.560	0.0302	5.4	-	1.3	-0.35	4.00	-1.14
194.461	27.644	0.0227	13.4	-	2.5	-1.16	-0.55	-1.70
195.300	29.664	0.0239	2.4	-	1.0	-0.89	0.14	-4.00
178.379	25.170	0.0296	2.5	-	1.1	-0.58	4.00	-1.26
175.758	26.258	0.0316	3.0	-	1.6	-0.85	-0.28	-1.42
179.680	25.043	0.0155	2.8	-	1.4	-0.63	0.03	-1.25
177.490	21.646	0.0259	2.2	-	0.9	-0.51	4.00	-1.44

continued on next page..

Table A.1 – continued from previous page

RA (J2000)	Dec (J2000)	z	Age (Gyr)	Age upper (Gyr)	Age lower (Gyr)	Z (dex)	Z upper (dex)	Z lower (dex)
170.594	24.184	0.0292	4.9	-	1.7	-0.51	0.19	-1.19
180.962	20.427	0.0255	2.6	-	1.0	-0.18	4.00	-0.97
194.769	26.958	0.0270	3.1	-	1.6	-0.82	-0.20	-1.46
182.180	21.742	0.0241	2.4	-	1.1	-1.15	-0.17	-4.00
199.222	31.599	0.0299	1.4	2.9	0.9	-1.49	-0.41	-
184.162	24.370	0.0212	7.7	-	2.3	-1.30	-0.71	-4.00
181.347	28.021	0.0282	8.0	-	2.2	-0.72	-0.10	-1.34
175.712	20.442	0.0190	4.1	-	1.1	-0.29	4.00	-1.13
197.694	28.642	0.0261	2.6	-	1.0	-0.29	4.00	-1.05
180.210	31.878	0.0268	3.7	-	1.2	-0.97	0.06	-4.00
177.461	19.145	0.0201	5.8	-	1.8	-0.68	-0.00	-1.40
189.125	26.249	0.0219	6.0	-	1.2	-0.38	4.00	-1.23
173.490	30.373	0.0275	8.0	-	1.9	-1.14	-0.43	-4.00
188.125	20.466	0.0309	3.1	-	1.5	-1.08	-0.45	-1.70
181.918	17.303	0.0225	1.5	2.3	1.3	-1.57	-1.04	-
178.759	32.075	0.0310	3.5	-	1.6	-1.45	-0.76	-4.00
183.838	28.180	0.0220	1.4	2.4	0.9	-0.97	-0.12	-
178.558	20.028	0.0207	2.7	-	1.4	-0.86	-0.19	-1.48
194.212	27.628	0.0270	3.4	-	1.8	-0.77	-0.32	-1.29
173.692	20.205	0.0319	2.5	-	1.1	-0.51	4.00	-1.21
172.727	27.309	0.0320	2.3	-	1.1	-0.67	0.16	-1.45
177.977	30.502	0.0302	2.9	-	1.1	-0.54	4.00	-1.38
179.844	24.497	0.0224	1.4	1.7	1.0	-1.21	-0.47	-
195.757	32.211	0.0237	4.0	-	1.8	-1.11	-0.59	-1.61
193.681	27.455	0.0262	2.0	-	0.8	-1.12	0.13	-4.00
178.931	31.342	0.0301	1.5	2.9	1.0	-1.45	-0.36	-
177.775	32.781	0.0267	1.3	1.7	0.8	-0.84	-0.13	-
190.409	28.569	0.0252	4.5	-	1.4	-0.87	0.02	-1.68
179.448	22.020	0.0209	2.3	-	1.0	-1.26	-0.19	-4.00
199.674	21.891	0.0316	1.1	1.4	0.8	-1.42	-0.37	-
173.866	20.001	0.0319	2.1	-	0.0	-0.67	-	-
189.529	22.314	0.0230	2.0	-	0.8	-0.55	4.00	-1.48
170.444	25.972	0.0202	1.9	5.9	1.1	-1.51	-0.53	-
184.797	19.813	0.0307	1.7	4.6	0.9	-0.86	0.03	-
171.756	22.592	0.0313	2.5	-	1.2	-0.60	0.17	-1.27
188.718	26.175	0.0214	10.5	-	2.1	-1.10	-0.40	-4.00
176.343	27.852	0.0297	2.8	9.4	1.5	-1.46	-0.70	-
179.977	26.069	0.0320	2.7	-	1.0	-0.65	4.00	-1.64
177.740	23.309	0.0232	5.8	-	0.0	-0.16	4.00	-1.03
172.035	27.386	0.0325	2.3	-	1.0	-0.69	0.16	-1.50
191.329	21.536	0.0225	3.3	-	1.6	-1.16	-0.57	-4.00
181.657	20.645	0.0236	1.6	-	0.0	0.09	4.00	-1.33
174.960	26.615	0.0300	2.8	-	1.4	-1.05	-0.31	-4.00
194.395	27.310	0.0248	4.5	-	1.7	-0.61	0.00	-1.24
178.680	23.160	0.0227	1.8	6.7	0.9	-0.93	0.02	-
170.346	24.123	0.0250	3.1	-	1.5	-0.93	-0.21	-1.63
179.659	27.969	0.0273	7.5	-	1.6	-1.67	-0.55	-4.00
182.036	25.718	0.0207	3.8	-	1.1	-1.37	-0.27	-4.00
190.152	26.508	0.0226	5.6	-	1.7	-1.22	-0.48	-4.00
173.885	25.024	0.0324	3.3	-	1.6	-1.49	-0.84	-4.00
195.006	27.731	0.0269	13.8	-	2.7	-0.61	-0.02	-1.14
180.388	21.085	0.0223	5.5	-	1.0	-1.42	0.06	-4.00
193.939	27.796	0.0229	2.9	-	1.0	-0.68	4.00	-1.65
189.362	27.202	0.0256	0.9	1.3	0.0	-0.76	0.13	-
184.977	30.216	0.0306	2.1	4.4	1.4	-1.55	-0.81	-

continued on next page..

Table A.1 – continued from previous page

RA (J2000)	Dec (J2000)	z	Age (Gyr)	Age upper (Gyr)	Age lower (Gyr)	Z (dex)	Z upper (dex)	Z lower (dex)
174.968	17.318	0.0221	1.5	2.9	1.0	-1.43	-0.44	-
180.725	21.645	0.0245	2.6	-	1.1	-1.17	-0.15	-4.00
182.749	31.987	0.0222	6.8	-	1.9	-1.55	-0.76	-4.00
180.275	21.375	0.0258	2.8	-	1.4	-0.93	-0.21	-1.60
181.255	31.328	0.0251	8.5	-	1.5	-1.00	0.02	-4.00
178.166	20.768	0.0214	3.7	-	1.1	-0.99	0.07	-4.00
191.089	20.024	0.0223	5.8	-	1.9	-1.30	-0.64	-4.00
190.709	31.890	0.0147	3.5	-	1.5	-0.92	-0.21	-1.61
192.965	27.256	0.0228	2.4	-	1.0	-0.52	4.00	-1.36
173.332	26.557	0.0326	3.0	-	0.0	-0.56	-	-
183.120	17.972	0.0226	2.3	-	1.1	-0.76	0.10	-1.57
174.911	32.338	0.0321	1.3	1.6	0.9	-1.28	-0.49	-
183.341	19.499	0.0229	4.7	-	1.5	-1.22	-0.37	-4.00
188.400	20.060	0.0313	1.9	4.0	1.4	-1.48	-0.73	-
176.659	21.089	0.0226	2.0	-	0.0	0.20	4.00	-0.76
185.159	17.045	0.0255	1.3	2.6	0.0	-0.71	0.05	-
176.598	21.753	0.0222	6.0	-	1.7	-1.13	-0.37	-4.00
195.019	27.032	0.0232	10.5	-	2.3	-1.21	-0.55	-4.00
193.904	26.912	0.0198	2.5	-	1.2	-1.10	-0.23	-4.00
196.413	26.107	0.0211	1.4	2.9	1.0	-1.62	-0.63	-
190.926	27.373	0.0245	1.5	2.8	0.9	-1.08	-0.17	-
173.891	24.963	0.0231	7.4	-	1.9	-1.46	-0.66	-4.00
174.617	19.981	0.0233	13.5	-	1.2	-0.20	4.00	-0.95
189.476	32.005	0.0308	2.0	-	0.9	-1.23	-0.09	-4.00
178.450	23.151	0.0266	2.3	-	0.0	-0.40	4.00	-1.57
180.620	20.224	0.0230	1.7	4.7	1.0	-1.37	-0.36	-
195.449	28.660	0.0287	14.0	-	1.6	-0.42	4.00	-1.18
183.963	24.007	0.0224	5.1	-	1.9	-0.77	-0.23	-1.38
176.171	19.053	0.0194	4.9	-	1.5	-1.21	-0.34	-4.00
197.742	28.519	0.0245	0.8	2.7	0.0	0.00	-	-
188.378	28.936	0.0306	4.9	-	0.9	-0.41	4.00	-1.46
179.987	31.874	0.0262	1.5	3.6	0.9	-1.14	-0.09	-
196.438	27.315	0.0211	4.4	-	1.2	-1.16	-0.05	-4.00
182.688	25.844	0.0209	4.2	-	2.2	-1.63	-1.15	-4.00
181.815	25.116	0.0257	8.6	-	1.8	-0.81	-0.06	-1.54
178.214	23.595	0.0227	1.6	-	0.0	-0.36	4.00	-1.62
174.278	21.545	0.0303	1.4	2.9	0.8	-1.10	-0.09	-
171.002	26.559	0.0210	7.1	-	1.4	-1.21	-0.14	-4.00
174.574	22.479	0.0303	2.8	-	0.9	-1.34	-0.04	-4.00
176.227	20.017	0.0243	2.8	-	1.0	-1.31	-0.14	-4.00
180.827	20.936	0.0245	2.3	-	0.0	-1.02	-	-
180.650	20.383	0.0243	5.2	-	1.8	-1.29	-0.62	-4.00
176.551	21.227	0.0221	1.7	7.3	0.8	-0.83	0.18	-
176.691	19.018	0.0205	4.1	-	1.9	-0.68	-0.19	-1.25
194.845	29.888	0.0247	3.9	-	1.7	-1.10	-0.56	-1.65
184.947	30.354	0.0279	13.6	-	1.3	-0.41	4.00	-1.25
183.306	21.710	0.0250	7.3	-	1.8	-0.91	-0.20	-1.62
184.932	28.273	0.0265	7.4	-	1.7	-1.14	-0.34	-4.00
182.075	25.594	0.0222	9.0	-	1.5	-1.13	-0.17	-4.00
189.685	27.718	0.0222	3.0	-	0.0	-1.28	0.22	-4.00
175.814	17.369	0.0225	3.3	-	1.5	-1.06	-0.38	-4.00
181.781	31.060	0.0226	2.9	7.5	1.4	-1.35	-0.63	-
174.410	21.972	0.0288	2.3	-	0.8	-0.58	4.00	-1.61
182.013	31.284	0.0230	1.9	5.9	1.1	-1.47	-0.46	-
180.647	20.411	0.0249	3.1	-	1.2	-1.23	-0.29	-4.00

continued on next page..

Table A.1 – continued from previous page

RA (J2000)	Dec (J2000)	z	Age (Gyr)	Age upper (Gyr)	Age lower (Gyr)	Z (dex)	Z upper (dex)	Z lower (dex)
181.399	20.203	0.0235	5.8	-	1.7	-1.00	-0.29	-1.71
195.295	27.246	0.0206	2.8	-	1.2	-0.81	0.13	-1.64
177.092	31.456	0.0308	3.0	-	1.0	-0.54	4.00	-1.56
194.549	27.542	0.0237	1.3	-	0.0	-0.77	-	-
196.133	32.823	0.0324	7.3	-	2.8	-1.33	-0.95	-4.00
184.550	29.252	0.0255	1.2	2.4	0.0	-0.76	0.07	-
195.546	28.457	0.0205	12.9	-	1.6	-1.31	-0.31	-4.00
192.637	27.320	0.0267	1.5	-	0.0	-0.01	4.00	-1.35
177.589	18.551	0.0215	3.1	-	1.0	-1.13	0.08	-4.00
170.584	24.058	0.0260	2.8	-	1.4	-0.67	0.03	-1.30
195.354	28.677	0.0292	2.2	4.4	1.5	-1.60	-0.97	-
182.542	26.424	0.0211	9.0	-	2.2	-1.34	-0.65	-4.00
188.208	28.959	0.0278	1.4	2.1	1.2	-1.65	-1.00	-
182.096	17.330	0.0224	4.1	-	1.5	-0.95	-0.18	-1.69
191.693	29.389	0.0318	1.4	2.1	0.9	-1.37	-0.30	-
191.596	27.112	0.0231	3.7	-	1.4	-1.20	-0.36	-4.00
182.012	19.790	0.0245	1.0	2.9	0.0	-0.92	-	-
174.676	19.910	0.0226	11.7	-	2.3	-1.40	-0.71	-4.00
175.557	26.445	0.0311	2.3	-	1.1	-0.82	0.07	-1.65
175.793	25.813	0.0305	0.9	3.6	0.0	-1.40	-	-
176.146	17.059	0.0239	10.5	-	2.1	-1.24	-0.51	-4.00
176.333	21.339	0.0258	1.6	2.9	1.0	-1.46	-0.54	-
170.769	29.458	0.0283	2.4	-	0.8	-1.38	0.07	-4.00
181.374	31.012	0.0236	3.6	-	1.0	-0.84	-	-
188.920	27.205	0.0243	1.0	1.8	0.0	-0.65	-	-
196.641	24.963	0.0210	2.6	-	0.9	-0.83	-	-
175.688	26.343	0.0306	0.9	1.1	0.0	-0.69	0.08	-
177.330	20.692	0.0234	5.4	-	1.6	-0.69	0.09	-1.49
177.388	21.448	0.0280	1.5	2.4	1.1	-1.38	-0.61	-
196.638	29.366	0.0243	1.6	14.0	0.9	-1.58	-0.27	-
197.988	24.701	0.0236	1.3	1.9	0.9	-0.96	-0.15	-
184.685	29.380	0.0267	8.7	-	2.0	-0.79	-0.08	-1.49
187.062	25.433	0.0232	2.4	-	0.9	-0.26	4.00	-1.07
196.522	28.787	0.0231	1.6	-	0.0	-0.16	4.00	-1.48
185.952	27.746	0.0260	1.7	3.6	1.2	-1.53	-0.66	-
192.578	32.547	0.0230	2.3	6.3	1.3	-1.37	-0.59	-
196.362	25.191	0.0237	2.0	-	0.9	-0.99	0.09	-4.00
191.796	29.188	0.0231	1.0	1.4	0.0	-1.06	-0.06	-
177.589	21.326	0.0226	2.9	-	1.1	-1.27	-0.27	-4.00
174.915	26.344	0.0304	9.1	-	1.1	-0.89	-	-
197.487	28.558	0.0230	1.0	4.7	0.0	-0.35	-	-
175.789	26.064	0.0310	4.9	-	0.0	-0.35	4.00	-1.61
196.264	27.537	0.0217	4.5	-	1.5	-1.43	-0.56	-4.00
181.743	28.327	0.0278	7.4	-	1.3	-1.19	-0.01	-4.00
179.693	28.809	0.0283	2.1	-	0.0	0.03	4.00	-1.07
184.600	28.099	0.0278	2.9	-	1.1	-0.66	4.00	-1.58
174.523	20.699	0.0222	6.1	-	1.6	-1.57	-0.58	-4.00
193.820	25.957	0.0316	1.3	14.0	0.0	-0.75	-	-
181.381	28.127	0.0272	2.8	-	1.5	-0.64	0.04	-1.27
179.335	22.162	0.0228	1.4	2.2	1.1	-1.44	-0.64	-
193.530	27.216	0.0272	2.3	-	0.0	-0.55	4.00	-1.61
184.721	27.492	0.0324	1.7	3.6	1.0	-1.40	-0.37	-
176.468	23.867	0.0327	2.0	10.9	1.0	-1.01	-0.01	-
176.269	20.608	0.0200	3.0	-	1.3	-0.95	-0.09	-1.70
194.701	28.019	0.0236	1.7	-	0.0	-0.40	4.00	-1.41

continued on next page..

Table A.1 – continued from previous page

RA (J2000)	Dec (J2000)	z	Age (Gyr)	Age upper (Gyr)	Age lower (Gyr)	Z (dex)	Z upper (dex)	Z lower (dex)
186.873	26.103	0.0243	2.3	7.5	1.2	-1.05	-0.23	-
188.140	18.473	0.0232	2.3	-	0.9	-1.08	0.07	-4.00
171.966	21.409	0.0218	7.0	-	1.1	-1.63	-0.11	-4.00
174.317	19.620	0.0205	2.7	-	1.1	-0.94	0.01	-4.00
179.118	24.665	0.0170	4.7	-	1.5	-1.45	-0.57	-4.00
199.914	26.788	0.0325	5.7	-	1.8	-1.70	-0.86	-4.00
190.732	31.473	0.0293	5.1	-	1.5	-0.99	-0.13	-4.00
174.604	23.517	0.0307	5.3	-	1.0	-0.68	-	-
171.414	23.695	0.0245	1.0	1.8	0.0	-0.37	-	-
174.870	17.049	0.0211	2.8	-	1.1	-0.67	4.00	-1.56
170.541	24.312	0.0284	3.2	-	1.4	-0.92	-0.11	-1.67
193.069	23.530	0.0324	11.4	-	2.3	-1.30	-0.62	-4.00
190.053	28.361	0.0248	1.4	-	0.0	-1.69	-	-
171.913	23.758	0.0197	1.3	1.5	0.9	-1.02	-0.32	-
194.490	28.062	0.0271	1.3	1.6	1.0	-1.42	-0.67	-
198.609	30.250	0.0253	1.2	3.2	0.0	-0.59	-	-
185.157	28.634	0.0275	11.3	-	1.3	-0.95	-	-
172.623	22.396	0.0221	0.9	1.3	0.9	-1.66	-0.76	-
177.548	21.795	0.0264	2.4	-	0.0	-0.38	4.00	-1.30
181.513	28.312	0.0276	2.6	-	0.0	-0.56	-	-
171.186	17.763	0.0205	1.5	-	0.0	-1.41	0.12	-4.00
181.131	31.876	0.0219	1.7	6.1	0.9	-1.06	-0.04	-
193.444	27.386	0.0277	3.0	-	1.1	-0.72	4.00	-1.61
172.424	24.864	0.0204	2.1	-	0.9	-0.69	4.00	-1.65
176.439	19.692	0.0205	1.8	-	0.0	-0.51	4.00	-1.68
195.739	28.376	0.0295	2.1	-	0.0	-1.27	-	-
192.495	32.389	0.0230	1.3	2.9	0.9	-1.62	-0.40	-
176.101	21.290	0.0257	1.6	3.6	1.0	-1.41	-0.46	-
196.387	29.012	0.0175	4.3	-	1.7	-0.88	-0.30	-1.51
188.784	26.740	0.0258	1.0	3.7	0.0	-0.33	-	-
186.510	25.795	0.0231	1.7	14.0	1.1	-1.66	-0.50	-
199.205	18.861	0.0229	1.3	3.6	0.0	-0.79	-	-
197.590	31.378	0.0271	8.7	-	1.2	-1.21	0.08	-4.00
188.358	32.975	0.0305	4.5	-	1.0	-1.37	0.06	-4.00
178.651	23.863	0.0216	2.8	-	1.0	-1.51	-0.21	-4.00
186.898	26.540	0.0213	1.4	4.1	0.0	-0.72	-	-
175.574	25.690	0.0300	1.7	5.7	0.9	-1.13	-0.03	-
181.418	27.904	0.0275	6.0	-	2.1	-1.19	-0.55	-4.00
171.573	28.367	0.0301	1.1	-	0.0	-1.66	-0.14	-4.00
181.517	20.537	0.0237	4.5	-	1.6	-0.22	4.00	-0.81
181.886	32.813	0.0261	5.7	7.9	3.9	-0.04	0.09	-0.14
182.325	24.968	0.0219	6.0	8.2	4.0	-0.04	0.08	-0.16
192.100	26.858	0.0247	9.4	13.0	6.8	-0.19	-0.07	-0.29
182.055	24.943	0.0226	6.2	8.8	3.9	-0.01	0.12	-0.13
181.544	25.557	0.0211	6.1	8.5	4.2	-0.10	0.01	-0.22
191.925	26.982	0.0239	9.4	13.4	6.6	-0.32	-0.22	-0.42
182.476	25.311	0.0231	5.6	8.1	3.9	-0.12	0.00	-0.24
192.725	27.842	0.0253	6.8	9.9	4.7	-0.11	0.01	-0.23
182.193	24.946	0.0214	6.0	8.5	4.1	-0.13	-0.00	-0.24
181.476	20.573	0.0238	9.4	13.3	6.5	-0.34	-0.23	-0.45
190.220	26.728	0.0157	8.7	12.3	6.0	-0.17	-0.05	-0.28
190.971	26.863	0.0251	4.3	7.1	3.0	0.09	-	-0.05
181.047	20.410	0.0239	9.2	13.1	6.4	-0.31	-0.20	-0.41
182.038	25.079	0.0241	8.4	12.2	5.8	-0.24	-0.13	-0.35
192.859	27.421	0.0244	4.9	7.5	3.2	0.05	0.21	-0.09

continued on next page..

Table A.1 – continued from previous page

RA (J2000)	Dec (J2000)	z	Age (Gyr)	Age upper (Gyr)	Age lower (Gyr)	Z (dex)	Z upper (dex)	Z lower (dex)
180.798	19.729	0.0239	6.2	9.3	4.3	-0.22	-0.10	-0.34
192.932	27.963	0.0231	5.5	8.7	3.4	0.02	0.20	-0.12
181.993	25.321	0.0219	5.8	8.7	3.6	-0.02	0.14	-0.15
181.515	20.608	0.0244	8.8	13.1	5.9	-0.39	-0.28	-0.52
198.739	17.225	0.0231	6.1	9.2	4.1	-0.16	-0.03	-0.29
192.617	27.435	0.0214	3.7	5.2	2.8	-0.15	-0.01	-0.27
182.842	19.088	0.0253	6.4	9.4	4.4	-0.18	-0.06	-0.30
175.818	19.749	0.0250	7.1	11.0	4.5	-0.08	0.06	-0.23
174.908	20.455	0.0232	8.4	12.6	5.6	-0.23	-0.10	-0.35
194.401	27.485	0.0241	7.6	12.0	4.4	-0.09	0.07	-0.24
179.754	25.223	0.0145	2.5	3.0	1.9	0.21	-	0.04
196.961	18.415	0.0217	7.3	11.5	5.1	-0.40	-0.29	-0.53
199.116	31.031	0.0196	7.2	11.1	4.4	-0.06	0.09	-0.21
182.023	25.237	0.0225	9.9	14.0	6.2	-0.53	-0.39	-0.65
182.561	25.309	0.0199	7.0	10.9	5.0	-0.35	-0.25	-0.48
172.925	28.154	0.0230	5.1	7.5	3.5	-0.19	-0.05	-0.30
180.481	20.748	0.0241	8.1	12.3	5.5	-0.28	-0.15	-0.39
182.231	25.192	0.0221	7.6	11.6	5.1	-0.25	-0.13	-0.37
194.041	27.844	0.0253	8.5	13.0	5.2	-0.05	0.11	-0.19
181.406	20.556	0.0241	5.9	9.6	4.5	-0.38	-0.29	-0.53
182.643	25.427	0.0219	9.1	13.6	6.0	-0.36	-0.24	-0.48
194.183	30.719	0.0263	6.5	10.1	4.2	-0.18	-0.04	-0.31
176.079	19.845	0.0213	4.3	6.7	2.9	-0.04	0.14	-0.19
194.878	27.884	0.0157	5.4	8.0	3.7	-0.29	-0.16	-0.41
194.142	27.539	0.0237	5.2	7.9	3.4	-0.11	0.05	-0.24
194.387	27.610	0.0201	9.0	13.6	6.0	-0.35	-0.23	-0.47
177.014	30.359	0.0210	2.9	4.2	2.4	0.06	-	-0.11
181.211	19.248	0.0233	6.9	10.4	4.6	-0.25	-0.13	-0.37
193.408	27.784	0.0171	8.2	12.8	5.4	-0.27	-0.14	-0.40
178.424	20.882	0.0232	5.6	8.9	3.7	-0.17	-0.02	-0.31
181.006	20.232	0.0245	5.0	7.3	3.6	-0.40	-0.28	-0.54
176.113	32.677	0.0314	8.8	13.7	5.5	-0.18	-0.03	-0.32
193.037	27.477	0.0195	6.1	9.6	3.6	0.02	0.19	-0.13
194.758	28.225	0.0268	7.4	11.6	4.8	-0.26	-0.12	-0.38
173.316	24.447	0.0231	5.5	8.8	3.4	-0.08	0.09	-0.23
181.135	20.205	0.0207	3.6	5.3	2.8	-0.15	0.01	-0.28
195.038	28.170	0.0225	7.8	12.3	4.5	-0.04	0.12	-0.20
194.121	26.957	0.0235	5.9	9.5	4.0	-0.23	-0.10	-0.36
175.153	20.314	0.0216	8.0	12.8	5.0	-0.19	-0.04	-0.33
176.209	19.533	0.0209	6.9	11.0	4.6	-0.26	-0.13	-0.38
184.451	26.031	0.0254	4.9	7.5	3.1	-0.14	0.01	-0.28
195.128	28.346	0.0199	5.9	9.2	3.6	-0.07	0.09	-0.22
194.651	27.104	0.0265	6.1	9.5	3.8	-0.08	0.08	-0.22
195.958	28.186	0.0232	7.8	12.2	5.1	-0.27	-0.14	-0.39
181.820	32.076	0.0296	5.7	9.1	3.8	-0.19	-0.04	-0.33
180.437	20.328	0.0236	5.8	9.5	3.7	-0.15	0.00	-0.29
195.754	28.032	0.0179	7.0	11.1	4.6	-0.31	-0.18	-0.45
194.591	27.968	0.0201	6.7	10.5	4.5	-0.27	-0.14	-0.39
196.907	27.499	0.0221	6.0	10.2	3.5	-0.09	0.09	-0.25
183.596	32.415	0.0220	5.1	7.5	3.3	-0.29	-0.14	-0.41
194.712	28.084	0.0203	6.4	10.4	3.9	-0.13	0.03	-0.28
176.198	19.876	0.0261	7.7	12.0	4.8	-0.08	0.07	-0.22
195.446	28.095	0.0194	6.7	10.3	4.2	-0.13	0.02	-0.27
182.810	32.385	0.0239	9.0	13.8	5.8	-0.23	-0.08	-0.36
176.266	19.974	0.0169	5.9	9.2	4.1	-0.24	-0.12	-0.37

continued on next page..

Table A.1 – continued from previous page

RA (J2000)	Dec (J2000)	z	Age (Gyr)	Age upper (Gyr)	Age lower (Gyr)	Z (dex)	Z upper (dex)	Z lower (dex)
176.127	20.077	0.0224	2.9	4.0	2.4	-0.06	0.10	-0.21
195.033	28.079	0.0241	5.4	8.1	3.5	-0.12	0.04	-0.25
176.237	19.732	0.0258	6.0	9.7	3.9	-0.19	-0.05	-0.33
195.054	28.075	0.0250	6.3	10.0	3.8	-0.08	0.08	-0.23
194.626	28.015	0.0238	7.6	12.1	5.0	-0.32	-0.20	-0.46
176.003	20.029	0.0227	4.6	6.9	3.1	-0.19	-0.04	-0.31
194.703	27.810	0.0197	8.5	13.2	5.5	-0.35	-0.23	-0.49
179.351	27.878	0.0218	7.8	12.7	5.3	-0.34	-0.21	-0.48
176.337	32.722	0.0215	8.5	13.6	5.5	-0.36	-0.23	-0.50
194.116	26.987	0.0215	2.9	4.2	2.4	-0.01	0.16	-0.18
198.247	22.426	0.0224	2.7	3.7	2.1	0.12	-	-0.07
175.450	20.104	0.0191	6.0	9.7	4.1	-0.26	-0.12	-0.39
175.985	19.895	0.0210	5.6	9.3	4.1	-0.36	-0.25	-0.52
177.014	20.006	0.0241	5.9	9.3	3.7	-0.10	0.05	-0.25
191.545	27.938	0.0231	5.4	8.3	3.6	-0.17	-0.02	-0.30
194.124	27.940	0.0221	6.8	11.2	4.6	-0.32	-0.20	-0.46
194.881	28.047	0.0231	6.7	11.0	3.8	0.00	0.17	-0.18
181.528	28.256	0.0295	6.1	9.7	3.7	-0.09	0.08	-0.24
195.323	27.809	0.0244	5.4	8.7	3.4	-0.14	0.02	-0.29
171.207	23.945	0.0236	3.1	4.8	2.5	-0.06	0.12	-0.23
178.902	29.996	0.0227	5.8	9.2	3.8	-0.19	-0.04	-0.33
175.174	20.343	0.0218	7.5	12.4	5.1	-0.40	-0.28	-0.55
192.104	30.710	0.0270	4.5	7.2	3.0	-0.09	0.09	-0.24
172.779	22.768	0.0215	8.6	13.5	5.5	-0.26	-0.12	-0.39
198.895	29.676	0.0220	6.4	10.4	3.8	-0.09	0.07	-0.25
181.372	20.247	0.0236	4.6	7.5	3.0	-0.14	0.04	-0.29
181.058	20.210	0.0218	3.7	5.5	2.8	-0.13	0.04	-0.27
181.021	20.247	0.0223	7.7	12.2	5.0	-0.28	-0.15	-0.40
174.184	22.992	0.0234	7.7	12.5	4.7	-0.18	-0.02	-0.32
174.493	20.779	0.0231	8.1	12.9	5.2	-0.26	-0.12	-0.38
194.455	31.275	0.0262	2.9	4.6	2.4	0.01	0.20	-0.18
173.009	27.006	0.0327	7.2	11.8	4.7	-0.33	-0.20	-0.48
194.450	27.883	0.0195	8.4	13.2	5.3	-0.24	-0.10	-0.37
195.590	28.231	0.0186	5.7	9.6	3.6	-0.17	-0.01	-0.32
195.203	28.091	0.0232	5.9	9.6	3.9	-0.25	-0.10	-0.38
194.775	27.997	0.0256	5.4	8.9	3.3	-0.09	0.09	-0.24
172.554	24.170	0.0233	6.1	9.9	3.8	-0.13	0.03	-0.28
181.417	20.556	0.0256	7.2	11.7	4.4	-0.22	-0.07	-0.36
197.903	31.508	0.0231	5.3	8.4	3.2	-0.11	0.07	-0.25
183.040	17.757	0.0233	7.8	12.5	5.2	-0.31	-0.19	-0.45
183.899	28.178	0.0219	6.2	10.1	4.1	-0.24	-0.10	-0.38
181.366	20.309	0.0244	3.1	4.8	2.6	-0.07	0.09	-0.22
183.847	26.885	0.0249	8.4	13.2	5.4	-0.32	-0.19	-0.45
174.817	20.428	0.0258	4.3	6.8	2.9	-0.10	0.08	-0.25
193.523	27.069	0.0252	6.2	10.1	3.8	-0.13	0.03	-0.28
194.651	28.114	0.0227	7.0	11.3	4.3	-0.15	0.01	-0.30
175.746	20.087	0.0201	6.8	11.1	4.6	-0.30	-0.17	-0.43
186.748	22.640	0.0228	4.8	7.4	3.1	-0.08	0.09	-0.22
181.004	20.337	0.0228	6.6	10.6	4.3	-0.23	-0.09	-0.37
194.833	28.084	0.0153	3.4	5.1	2.7	-0.22	-0.07	-0.36
176.069	20.217	0.0225	5.6	9.5	4.0	-0.38	-0.26	-0.54
181.594	27.965	0.0287	7.8	12.6	4.8	-0.21	-0.05	-0.35
183.882	24.729	0.0228	2.8	4.1	2.4	0.00	0.17	-0.17
194.320	27.618	0.0242	7.5	12.3	4.9	-0.33	-0.19	-0.47
182.689	23.710	0.0223	7.7	13.1	5.1	-0.38	-0.26	-0.55

continued on next page..

Table A.1 – continued from previous page

RA (J2000)	Dec (J2000)	z	Age (Gyr)	Age upper (Gyr)	Age lower (Gyr)	Z (dex)	Z upper (dex)	Z lower (dex)
194.758	26.816	0.0239	3.3	5.1	2.6	-0.12	0.06	-0.27
194.935	27.912	0.0224	7.0	11.7	4.7	-0.35	-0.23	-0.50
182.064	25.036	0.0239	5.4	9.5	3.1	-0.05	0.16	-0.22
194.402	27.031	0.0245	4.9	8.6	3.0	0.00	0.22	-0.17
172.143	21.011	0.0208	5.1	8.0	3.1	-0.06	0.12	-0.21
177.714	20.497	0.0231	4.3	7.0	2.8	-0.06	0.15	-0.22
193.781	30.513	0.0214	6.0	10.4	3.4	-0.12	0.07	-0.29
176.773	19.837	0.0194	4.6	6.8	3.1	-0.26	-0.10	-0.38
194.506	27.490	0.0254	5.9	10.4	3.2	0.12	-	-0.07
195.092	28.047	0.0273	4.4	7.5	2.9	0.00	0.22	-0.17
178.193	23.476	0.0220	6.4	11.1	3.7	-0.18	-0.01	-0.35
194.515	27.815	0.0238	8.7	13.8	5.5	-0.34	-0.21	-0.48
194.875	27.956	0.0227	7.0	11.5	4.3	-0.17	-0.01	-0.32
185.089	25.599	0.0228	8.0	13.1	4.9	-0.17	-0.01	-0.31
193.593	27.084	0.0282	8.4	13.4	5.1	-0.21	-0.05	-0.34
194.647	27.596	0.0256	1.6	1.9	1.4	-0.11	0.09	-0.29
195.069	27.968	0.0155	3.1	5.1	2.5	0.01	0.21	-0.16
183.816	23.958	0.0223	4.8	7.1	3.2	-0.33	-0.19	-0.46
195.178	27.971	0.0213	7.5	12.4	4.8	-0.31	-0.17	-0.45
194.814	27.971	0.0161	5.8	9.4	3.8	-0.25	-0.10	-0.38
185.291	28.165	0.0283	8.8	14.0	5.5	-0.34	-0.20	-0.48
193.567	27.304	0.0215	3.8	6.2	2.7	-0.01	0.21	-0.17
176.373	19.400	0.0249	4.9	8.3	3.0	0.00	0.21	-0.17
194.892	27.947	0.0240	4.1	6.0	2.8	-0.16	0.01	-0.30
195.383	27.848	0.0182	7.3	12.2	4.6	-0.31	-0.17	-0.46
182.387	17.014	0.0224	7.2	11.8	4.5	-0.30	-0.16	-0.44
183.479	21.756	0.0243	6.9	11.7	4.1	-0.16	0.01	-0.32
176.023	19.996	0.0188	3.9	6.4	2.7	-0.03	0.18	-0.19
192.426	26.892	0.0229	3.3	5.0	2.7	-0.26	-0.12	-0.40
193.795	29.578	0.0249	4.5	7.6	2.9	-0.02	0.19	-0.19
175.998	19.779	0.0187	5.3	8.5	3.3	-0.24	-0.08	-0.38
188.542	20.211	0.0310	6.7	11.4	4.0	-0.16	0.01	-0.32
194.429	26.852	0.0213	6.7	11.1	4.0	-0.12	0.05	-0.28
195.019	27.988	0.0213	8.0	13.1	5.0	-0.28	-0.14	-0.42
176.783	29.578	0.0222	6.9	11.1	4.3	-0.22	-0.07	-0.36
195.178	27.963	0.0281	6.0	10.0	3.6	-0.14	0.02	-0.30
176.428	17.748	0.0210	7.3	11.9	4.6	-0.26	-0.12	-0.40
193.184	26.470	0.0213	3.7	5.4	2.8	-0.25	-0.11	-0.38
194.453	28.180	0.0241	6.1	10.8	4.0	-0.32	-0.18	-0.49
195.015	26.898	0.0198	5.9	9.9	4.0	-0.25	-0.11	-0.39
195.234	27.791	0.0266	4.8	7.6	3.1	-0.17	0.01	-0.31
188.922	26.523	0.0222	8.6	13.9	5.3	-0.53	-0.37	-0.68
180.523	17.823	0.0229	8.8	14.0	5.2	-0.17	-0.01	-0.32
176.271	19.606	0.0216	8.8	13.8	5.5	-0.48	-0.33	-0.63
194.111	27.831	0.0209	4.9	7.7	3.1	-0.16	0.01	-0.31
185.504	28.431	0.0272	6.4	10.9	4.0	-0.23	-0.07	-0.38
179.463	22.258	0.0302	6.2	10.4	4.0	-0.26	-0.12	-0.41
196.355	29.296	0.0235	7.4	12.5	4.2	-0.15	0.03	-0.31
193.262	32.107	0.0227	2.9	4.6	2.4	-0.10	0.08	-0.27
183.714	23.907	0.0222	2.8	4.3	2.1	0.11	-	-0.10
194.942	27.857	0.0270	7.3	12.4	4.2	-0.11	0.07	-0.27
177.268	27.334	0.0223	7.1	12.2	4.3	-0.20	-0.04	-0.36
190.381	26.043	0.0159	4.6	6.7	3.1	-0.40	-0.28	-0.54
180.055	31.830	0.0258	7.9	13.2	4.9	-0.28	-0.13	-0.42
176.495	19.529	0.0183	6.5	10.9	4.3	-0.32	-0.19	-0.48

continued on next page..

Table A.1 – continued from previous page

RA (J2000)	Dec (J2000)	z	Age (Gyr)	Age upper (Gyr)	Age lower (Gyr)	Z (dex)	Z upper (dex)	Z lower (dex)
193.317	27.094	0.0205	4.1	5.9	2.8	-0.25	-0.08	-0.38
185.783	31.051	0.0282	8.5	13.5	5.1	-0.14	0.02	-0.29
176.442	19.774	0.0180	7.9	12.9	5.2	-0.49	-0.35	-0.64
178.365	30.697	0.0281	7.6	13.2	4.5	-0.24	-0.07	-0.39
175.776	19.939	0.0212	3.6	6.6	2.5	0.06	-	-0.13
181.525	28.238	0.0273	5.6	9.7	3.6	-0.24	-0.09	-0.39
182.579	31.550	0.0219	8.1	13.3	5.1	-0.30	-0.16	-0.44
189.338	28.208	0.0256	8.0	13.7	4.6	-0.20	-0.02	-0.36
195.023	27.808	0.0219	4.7	8.1	2.9	-0.10	0.12	-0.27
195.184	28.337	0.0264	7.8	12.8	4.9	-0.26	-0.11	-0.39
176.009	19.972	0.0211	4.8	7.8	3.0	-0.16	0.03	-0.31
193.171	26.366	0.0205	6.5	11.1	3.9	-0.21	-0.05	-0.37
196.729	28.548	0.0209	3.0	4.9	2.5	-0.05	0.15	-0.23
194.236	28.623	0.0219	4.7	8.9	2.8	0.03	-	-0.17
180.823	20.637	0.0208	3.6	5.6	2.7	-0.17	0.01	-0.32
194.781	27.768	0.0212	5.7	9.8	3.6	-0.25	-0.10	-0.40
195.937	28.084	0.0188	3.7	6.1	2.7	-0.07	0.14	-0.23
195.198	27.922	0.0286	4.3	8.0	2.8	0.06	-	-0.13
177.927	21.003	0.0235	6.2	10.6	3.7	-0.17	0.00	-0.33
175.675	20.300	0.0210	5.4	9.7	3.1	-0.03	0.21	-0.20
195.026	27.776	0.0206	8.0	13.7	4.0	0.01	0.22	-0.18
173.090	28.048	0.0232	5.4	9.7	3.6	-0.38	-0.24	-0.56
180.983	20.430	0.0218	5.7	10.2	3.7	-0.31	-0.17	-0.48
194.147	28.275	0.0243	7.6	13.2	4.3	-0.15	0.03	-0.31
176.024	20.248	0.0220	6.5	11.2	4.0	-0.22	-0.06	-0.37
195.117	27.956	0.0234	8.5	14.1	5.0	-0.18	-0.01	-0.34
184.973	28.386	0.0265	7.8	13.3	4.3	-0.09	0.09	-0.26
181.889	25.316	0.0255	5.3	9.0	3.2	-0.21	-0.05	-0.36
195.058	28.828	0.0245	4.4	7.6	2.8	-0.11	0.11	-0.28
194.510	26.860	0.0245	7.1	11.7	4.5	-0.26	-0.11	-0.40
194.856	27.973	0.0203	7.4	12.3	4.4	-0.16	0.01	-0.31
197.756	29.637	0.0235	5.7	9.3	3.8	-0.26	-0.12	-0.40
189.821	26.678	0.0220	7.3	12.3	4.6	-0.31	-0.16	-0.46
178.178	20.631	0.0222	6.8	11.5	4.5	-0.53	-0.38	-0.69
186.960	26.994	0.0238	2.8	3.8	2.3	-0.10	0.08	-0.26
188.969	26.992	0.0260	7.9	13.7	4.4	-0.19	-0.00	-0.35
195.075	27.957	0.0212	5.5	9.4	3.3	-0.24	-0.07	-0.39
183.173	25.996	0.0228	7.3	13.5	4.4	-0.36	-0.20	-0.55
175.043	25.326	0.0224	4.3	6.9	2.8	-0.19	0.01	-0.34
183.967	24.346	0.0227	3.7	5.9	2.7	-0.12	0.08	-0.28
192.787	28.788	0.0158	4.4	7.3	2.8	-0.16	0.03	-0.32
189.166	26.830	0.0244	4.5	7.1	2.9	-0.24	-0.06	-0.39
174.118	19.811	0.0222	2.6	3.1	2.2	-0.18	-0.01	-0.32
194.358	27.546	0.0186	5.6	9.9	4.0	-0.40	-0.28	-0.58
175.343	19.963	0.0218	2.9	4.4	2.4	-0.08	0.09	-0.24
170.610	24.299	0.0251	7.7	13.5	4.9	-0.42	-0.28	-0.60
180.695	20.163	0.0239	5.7	9.8	3.8	-0.27	-0.13	-0.42
170.625	24.279	0.0296	6.0	10.6	3.9	-0.29	-0.14	-0.46
186.727	26.690	0.0223	3.4	6.8	2.3	0.20	-	-0.03
178.723	28.262	0.0283	4.4	6.8	2.9	-0.22	-0.04	-0.36
194.634	27.456	0.0234	6.4	11.2	3.5	-0.06	0.13	-0.25
196.042	28.248	0.0198	3.1	5.1	2.4	-0.07	0.13	-0.26
175.554	18.404	0.0233	8.3	13.9	5.2	-0.36	-0.23	-0.53
194.556	28.948	0.0256	3.1	5.1	2.5	-0.07	0.13	-0.24
194.383	28.477	0.0226	7.6	12.9	4.9	-0.35	-0.21	-0.50

continued on next page..

Table A.1 – continued from previous page

RA (J2000)	Dec (J2000)	z	Age (Gyr)	Age upper (Gyr)	Age lower (Gyr)	Z (dex)	Z upper (dex)	Z lower (dex)
181.641	28.144	0.0254	7.8	13.3	4.8	-0.27	-0.12	-0.42
177.850	30.413	0.0296	5.2	8.6	3.2	-0.26	-0.09	-0.40
174.531	21.845	0.0316	7.8	13.3	4.5	-0.20	-0.02	-0.35
198.033	27.331	0.0204	5.4	9.6	3.5	-0.50	-0.33	-0.68
193.730	27.413	0.0262	4.3	6.9	2.8	-0.27	-0.09	-0.42
171.732	22.601	0.0312	8.6	14.0	5.1	-0.27	-0.11	-0.41
181.398	22.309	0.0300	3.1	5.2	2.5	-0.13	0.07	-0.31
181.714	20.819	0.0243	2.5	2.8	2.0	-0.20	-0.03	-0.33
196.572	29.063	0.0234	3.6	5.5	2.7	-0.24	-0.07	-0.39
194.447	27.833	0.0202	8.3	14.0	5.1	-0.30	-0.15	-0.45
195.061	28.041	0.0191	4.8	7.5	3.0	-0.21	-0.04	-0.35
194.346	27.493	0.0275	4.7	8.4	2.9	-0.12	0.11	-0.30
181.021	28.165	0.0303	4.6	7.2	3.0	-0.33	-0.17	-0.48
180.175	21.108	0.0324	5.7	10.6	3.7	-0.33	-0.18	-0.51
179.496	23.125	0.0218	4.8	8.0	3.0	-0.11	0.09	-0.27
190.401	23.425	0.0288	5.3	8.8	3.2	-0.18	-0.01	-0.32
199.985	30.119	0.0234	5.7	10.3	3.6	-0.28	-0.12	-0.46
196.546	27.700	0.0224	5.5	9.7	3.2	-0.15	0.04	-0.32
177.517	21.280	0.0256	6.4	11.8	3.5	-0.19	0.01	-0.37
175.823	19.384	0.0212	5.9	10.3	3.3	-0.08	0.13	-0.26
184.911	28.495	0.0277	6.4	11.9	4.2	-0.38	-0.23	-0.56
176.294	19.533	0.0215	6.1	10.6	3.6	-0.18	-0.01	-0.34
178.083	21.102	0.0225	3.1	5.4	2.4	-0.04	0.19	-0.23
195.186	28.101	0.0220	3.0	5.2	2.3	0.03	-	-0.18
191.437	19.177	0.0224	5.2	8.9	3.1	-0.27	-0.09	-0.43
184.720	27.744	0.0267	5.7	10.1	3.2	-0.08	0.12	-0.25
194.221	27.929	0.0204	5.6	10.5	3.8	-0.37	-0.24	-0.57
183.238	21.427	0.0237	3.4	6.4	2.4	0.06	-	-0.15
194.899	28.551	0.0253	5.8	10.8	3.4	-0.22	-0.04	-0.39
191.686	29.735	0.0156	5.1	8.7	3.1	-0.27	-0.10	-0.42
188.900	26.567	0.0227	6.1	11.2	3.4	-0.15	0.04	-0.34
176.367	20.294	0.0190	4.8	8.3	2.9	-0.18	0.04	-0.34
181.229	19.982	0.0195	3.1	5.1	2.5	-0.21	-0.03	-0.39
183.308	21.790	0.0253	6.0	10.5	3.6	-0.16	0.02	-0.33
187.129	32.548	0.0302	4.0	8.8	2.5	0.16	-	-0.08
196.498	29.279	0.0264	3.3	5.9	2.4	0.07	-	-0.13
174.812	17.144	0.0212	8.1	13.9	5.1	-0.34	-0.19	-0.50
196.930	27.510	0.0253	7.4	12.8	4.1	-0.15	0.04	-0.32
195.027	29.463	0.0218	3.5	6.0	2.6	-0.08	0.14	-0.26
195.026	27.685	0.0252	5.4	9.5	3.4	-0.29	-0.13	-0.45
172.083	27.622	0.0321	1.9	2.3	1.6	-0.32	-0.09	-0.47
194.854	27.739	0.0201	6.5	11.4	3.7	-0.21	-0.03	-0.38
180.017	31.797	0.0261	3.3	5.7	2.5	-0.01	0.22	-0.20
195.080	27.554	0.0196	4.7	8.2	2.9	-0.07	0.16	-0.25
195.727	23.657	0.0248	6.0	10.6	3.7	-0.22	-0.05	-0.38
195.685	28.045	0.0208	7.6	13.2	4.9	-0.38	-0.24	-0.55
194.375	28.188	0.0231	5.7	10.5	3.3	-0.19	-0.01	-0.36
176.312	19.846	0.0258	5.1	8.5	3.1	-0.17	0.01	-0.33
176.032	19.738	0.0259	6.6	11.7	3.7	-0.14	0.05	-0.32
196.648	27.169	0.0258	3.1	5.4	2.5	-0.06	0.17	-0.24
175.733	27.277	0.0300	2.9	4.7	2.3	-0.06	0.15	-0.25
194.784	27.784	0.0234	6.8	11.9	4.4	-0.36	-0.22	-0.53
174.887	26.302	0.0301	6.4	11.6	4.0	-0.31	-0.16	-0.49
194.007	26.757	0.0192	7.3	13.0	4.4	-0.31	-0.14	-0.48
172.305	19.773	0.0196	7.5	12.9	4.9	-0.49	-0.34	-0.66

continued on next page..

Table A.1 – continued from previous page

RA (J2000)	Dec (J2000)	z	Age (Gyr)	Age upper (Gyr)	Age lower (Gyr)	Z (dex)	Z upper (dex)	Z lower (dex)
171.187	23.615	0.0225	4.1	6.5	2.8	-0.17	0.03	-0.33
185.418	22.352	0.0232	5.5	10.5	3.0	-0.13	0.11	-0.32
193.002	26.159	0.0206	4.0	7.6	2.6	-0.05	0.21	-0.27
176.356	19.818	0.0282	2.7	3.6	2.2	-0.14	0.05	-0.30
198.362	27.802	0.0213	4.8	8.3	2.9	-0.19	0.02	-0.35
195.345	28.196	0.0254	7.1	13.3	4.4	-0.39	-0.23	-0.59
175.854	20.558	0.0189	2.6	3.7	1.8	0.13	-	-0.10
199.376	20.620	0.0235	3.1	5.6	2.3	-0.05	0.20	-0.26
190.354	31.482	0.0311	4.1	6.1	2.8	-0.22	-0.04	-0.36
194.717	27.785	0.0189	5.6	9.8	3.6	-0.28	-0.13	-0.44
181.440	31.079	0.0233	5.9	10.6	3.6	-0.24	-0.07	-0.40
177.975	27.578	0.0290	4.2	7.9	2.6	-0.02	-	-0.23
185.961	28.199	0.0260	5.0	10.1	2.8	0.02	-	-0.20
178.336	21.022	0.0220	7.0	12.4	4.1	-0.23	-0.06	-0.39
176.375	19.445	0.0213	4.8	7.8	2.9	-0.18	0.02	-0.34
181.166	20.228	0.0239	3.7	6.0	2.6	-0.18	0.02	-0.34
199.438	27.570	0.0233	2.3	2.8	1.7	-0.10	0.15	-0.27
189.703	31.985	0.0232	5.6	10.0	3.9	-0.41	-0.29	-0.60
184.922	28.786	0.0258	5.8	11.1	3.4	-0.24	-0.06	-0.42
195.288	28.360	0.0230	3.8	6.7	2.6	-0.04	0.19	-0.22
182.152	17.212	0.0230	5.4	10.2	3.3	-0.40	-0.24	-0.61
177.056	19.448	0.0226	2.9	5.0	2.2	0.11	-	-0.13
193.510	29.604	0.0211	5.4	10.3	3.2	-0.37	-0.21	-0.57
194.806	27.775	0.0228	6.6	12.4	3.7	-0.22	-0.03	-0.39
193.193	27.907	0.0190	7.0	13.1	4.0	-0.30	-0.12	-0.47
194.077	29.808	0.0234	6.7	12.1	3.7	-0.19	0.01	-0.36
174.465	21.974	0.0303	4.3	7.3	2.8	-0.18	0.03	-0.36
175.230	20.325	0.0220	5.6	10.6	3.0	0.01	-	-0.18
194.926	27.925	0.0230	7.5	13.6	4.6	-0.49	-0.33	-0.68
194.558	28.183	0.0240	4.8	8.9	2.9	-0.14	0.10	-0.32
174.596	20.525	0.0258	6.7	12.6	3.2	-0.02	-	-0.24
194.295	27.405	0.0207	3.1	5.2	2.4	-0.04	0.18	-0.23
199.897	25.411	0.0300	6.3	11.3	3.7	-0.21	-0.04	-0.37
190.334	30.122	0.0271	7.4	12.8	4.2	-0.18	-0.00	-0.34
179.542	28.354	0.0278	7.5	13.2	3.9	-0.06	0.14	-0.25
175.235	25.781	0.0229	3.7	6.6	2.5	0.04	-	-0.15
175.989	20.301	0.0194	7.3	12.9	4.3	-0.26	-0.09	-0.42
198.612	21.297	0.0228	4.9	8.2	3.0	-0.17	0.03	-0.33
172.247	22.960	0.0321	4.1	7.2	2.7	-0.06	0.18	-0.25
194.348	27.766	0.0304	3.9	7.3	2.6	0.01	-	-0.19
176.085	19.981	0.0211	7.7	13.8	4.8	-0.46	-0.30	-0.64
174.951	23.532	0.0306	1.3	1.6	1.1	0.19	-	-0.05
188.919	26.643	0.0200	4.6	8.3	2.8	-0.10	0.13	-0.29
199.375	20.684	0.0233	1.8	2.3	1.5	-0.04	0.20	-0.25
176.217	19.610	0.0216	4.6	8.7	2.8	-0.09	0.17	-0.29
195.118	27.972	0.0257	6.3	12.2	3.4	-0.18	0.03	-0.37
191.957	27.009	0.0212	7.0	12.9	4.0	-0.29	-0.11	-0.46
194.297	29.045	0.0250	3.9	5.9	2.8	-0.27	-0.10	-0.42
177.713	21.390	0.0264	7.3	13.6	4.1	-0.24	-0.05	-0.42
193.854	27.798	0.0246	7.0	13.2	4.1	-0.34	-0.17	-0.53
194.750	27.967	0.0277	3.4	6.2	2.4	0.09	-	-0.12
183.353	21.669	0.0254	6.9	12.3	3.9	-0.21	-0.03	-0.38
194.918	27.968	0.0253	2.9	5.1	2.1	0.10	-	-0.14
194.870	28.041	0.0188	5.4	9.5	3.1	-0.20	-0.01	-0.36
178.335	20.752	0.0207	2.0	2.5	1.6	-0.29	-0.04	-0.46

continued on next page..

Table A.1 – continued from previous page

RA (J2000)	Dec (J2000)	z	Age (Gyr)	Age upper (Gyr)	Age lower (Gyr)	Z (dex)	Z upper (dex)	Z lower (dex)
194.915	27.954	0.0268	7.2	13.5	3.8	-0.22	-0.02	-0.40
182.050	25.757	0.0240	1.8	2.3	1.5	-0.07	0.18	-0.27
197.038	27.827	0.0231	4.6	8.9	2.8	-0.09	0.17	-0.29
180.716	32.402	0.0256	4.2	7.2	2.7	-0.21	0.01	-0.39
171.996	25.272	0.0233	4.8	7.8	3.0	-0.30	-0.13	-0.46
181.459	20.477	0.0225	2.5	3.1	1.9	-0.18	0.03	-0.34
171.111	29.867	0.0244	5.4	10.3	3.0	-0.10	0.15	-0.29
195.295	27.803	0.0223	6.0	11.2	3.1	-0.10	0.13	-0.29
171.179	24.001	0.0230	4.5	8.4	2.8	-0.03	-	-0.23
176.365	20.807	0.0231	5.1	8.7	3.1	-0.44	-0.27	-0.62
191.401	28.120	0.0227	2.0	2.5	1.6	-0.07	0.18	-0.25
186.586	26.144	0.0321	7.5	13.4	4.2	-0.20	-0.00	-0.36
195.670	28.371	0.0247	5.5	11.8	2.9	-0.16	0.10	-0.38
195.148	28.146	0.0182	2.9	4.9	2.1	0.06	-	-0.17
195.363	27.999	0.0255	6.8	12.2	4.2	-0.31	-0.15	-0.47
180.984	20.218	0.0213	5.5	9.9	3.1	-0.17	0.02	-0.34
176.421	19.770	0.0181	4.7	7.8	2.9	-0.24	-0.05	-0.40
198.635	30.706	0.0249	2.9	4.8	2.3	-0.09	0.13	-0.30
188.285	26.349	0.0242	5.1	9.9	2.9	-0.18	0.06	-0.37
191.868	27.458	0.0221	1.7	2.1	1.4	-0.26	-0.00	-0.44
190.371	26.089	0.0164	2.3	2.8	1.9	-0.36	-0.20	-0.52
184.473	17.442	0.0301	5.7	10.6	3.3	-0.22	-0.03	-0.39
173.668	20.242	0.0312	6.3	11.8	3.2	-0.07	0.17	-0.27
176.289	19.554	0.0251	3.6	7.8	2.2	0.18	-	-0.09
183.506	23.010	0.0245	3.3	5.6	2.5	-0.22	-0.02	-0.39
176.266	26.828	0.0301	2.6	3.3	2.1	-0.15	0.05	-0.31
176.194	19.758	0.0214	6.2	11.8	3.8	-0.29	-0.12	-0.47
194.834	27.886	0.0216	4.6	8.4	2.8	-0.13	0.11	-0.31
195.590	28.256	0.0227	5.2	10.1	2.8	0.04	-	-0.17
180.284	20.405	0.0227	2.9	4.9	2.3	-0.10	0.13	-0.31
182.128	21.927	0.0225	3.5	6.2	2.5	-0.08	0.16	-0.27
195.121	26.675	0.0240	6.5	11.4	3.9	-0.24	-0.07	-0.40
176.482	21.026	0.0225	6.7	13.1	3.5	-0.23	-0.03	-0.43
181.666	28.026	0.0280	6.1	11.4	3.5	-0.25	-0.07	-0.43
180.470	22.531	0.0223	5.9	11.9	3.3	-0.30	-0.12	-0.51
170.190	24.518	0.0265	5.7	10.3	3.2	-0.14	0.06	-0.31
194.878	27.791	0.0259	6.9	12.7	4.0	-0.31	-0.14	-0.50
193.894	32.206	0.0228	7.2	13.9	4.2	-0.40	-0.23	-0.60
182.734	31.658	0.0224	4.2	7.6	2.8	-0.37	-0.18	-0.57
197.132	24.701	0.0238	6.9	13.6	3.5	-0.21	0.00	-0.41
195.979	28.188	0.0229	5.0	9.4	2.9	-0.03	-	-0.22
183.892	24.003	0.0209	4.5	9.1	2.7	0.02	-	-0.19
193.376	27.675	0.0198	6.6	13.8	3.1	-0.10	0.18	-0.33
191.397	28.762	0.0232	2.3	2.7	1.9	-0.41	-0.26	-0.55
178.609	21.447	0.0260	3.0	5.1	2.3	0.00	-	-0.21
194.861	27.998	0.0222	2.9	5.0	2.1	0.10	-	-0.14
183.939	24.070	0.0216	6.3	12.1	3.4	-0.24	-0.04	-0.43
193.496	26.444	0.0236	5.0	8.6	3.0	-0.30	-0.12	-0.47
188.529	26.671	0.0261	7.8	13.9	4.5	-0.26	-0.08	-0.43
177.492	20.954	0.0273	3.7	6.9	2.5	-0.12	0.13	-0.33
189.159	24.429	0.0231	1.7	2.1	1.5	-0.41	-0.17	-0.57
197.469	24.560	0.0234	6.5	12.2	3.2	-0.10	0.13	-0.30
182.561	23.888	0.0220	2.7	4.8	1.8	0.03	-	-0.24
178.352	23.071	0.0268	6.1	12.6	3.6	-0.36	-0.19	-0.58
172.767	29.302	0.0306	5.8	11.3	3.1	-0.23	-0.03	-0.42

continued on next page..

Table A.1 – continued from previous page

RA (J2000)	Dec (J2000)	z	Age (Gyr)	Age upper (Gyr)	Age lower (Gyr)	Z (dex)	Z upper (dex)	Z lower (dex)
176.345	18.656	0.0273	7.2	12.8	4.0	-0.15	0.04	-0.32
190.688	27.118	0.0219	5.9	11.6	3.0	0.09	-	-0.13
175.996	20.077	0.0245	2.5	3.1	2.1	-0.45	-0.30	-0.61
181.188	31.192	0.0250	6.2	11.5	3.6	-0.24	-0.07	-0.42
181.011	28.183	0.0309	1.7	2.5	1.3	0.15	-	-0.13
194.986	27.930	0.0257	3.8	7.0	2.5	-0.03	-	-0.24
172.178	23.010	0.0321	5.9	12.0	3.0	-0.14	0.11	-0.34
171.944	26.000	0.0327	5.3	11.3	3.1	-0.36	-0.16	-0.59
177.376	21.043	0.0218	4.7	7.7	3.0	-0.35	-0.18	-0.52
178.090	20.652	0.0230	2.7	4.7	1.9	0.03	-	-0.22
177.801	21.974	0.0260	4.8	9.2	2.8	-0.13	0.13	-0.33
172.973	28.358	0.0236	2.9	4.6	2.4	-0.47	-0.31	-0.65
185.125	25.515	0.0233	2.0	2.5	1.6	-0.32	-0.05	-0.49
177.432	23.445	0.0215	1.8	2.3	1.5	-0.16	0.10	-0.34
173.500	22.310	0.0269	6.6	12.7	3.2	-0.06	0.19	-0.27
197.114	28.320	0.0217	7.0	12.9	3.9	-0.23	-0.04	-0.40
184.176	18.378	0.0300	3.7	7.3	2.5	0.05	-	-0.17
195.208	27.406	0.0220	4.7	8.9	2.8	-0.05	0.21	-0.25
174.807	17.051	0.0206	4.8	9.0	2.8	-0.17	0.08	-0.35
185.440	25.885	0.0230	3.1	6.3	2.2	0.08	-	-0.16
184.589	25.217	0.0231	3.5	6.2	2.6	-0.30	-0.11	-0.50
171.730	18.833	0.0188	5.4	10.7	3.1	-0.35	-0.17	-0.56
185.019	28.897	0.0253	7.3	13.6	4.3	-0.33	-0.16	-0.51
193.724	28.417	0.0246	2.1	2.7	1.6	-0.02	-	-0.21
190.025	28.618	0.0310	4.5	7.8	2.8	-0.27	-0.06	-0.45
173.614	25.876	0.0315	7.2	14.0	3.9	-0.33	-0.14	-0.54
195.240	19.687	0.0299	2.7	3.5	2.1	-0.09	0.11	-0.26
174.621	28.504	0.0233	2.1	2.6	1.6	-0.13	0.12	-0.31
194.213	26.899	0.0208	3.0	4.9	2.4	-0.24	-0.05	-0.42
195.845	27.936	0.0201	5.7	12.0	3.0	-0.14	0.13	-0.35
186.252	28.559	0.0302	5.9	11.4	3.6	-0.31	-0.13	-0.50
181.410	27.869	0.0281	6.3	12.5	3.2	-0.17	0.05	-0.37
176.349	19.158	0.0197	4.1	8.9	2.5	0.02	-	-0.22
194.856	27.968	0.0257	7.0	13.2	3.5	-0.08	0.15	-0.28
185.951	27.394	0.0245	7.7	13.5	4.6	-0.28	-0.12	-0.44
195.483	29.323	0.0237	6.6	12.8	3.4	-0.14	0.08	-0.34
199.954	22.867	0.0229	4.2	8.1	2.6	-0.15	0.10	-0.35
193.844	28.468	0.0234	3.5	5.7	2.6	-0.23	-0.03	-0.40
176.323	26.767	0.0303	6.6	13.2	3.6	-0.26	-0.06	-0.46
181.348	17.920	0.0142	2.9	4.9	2.4	-0.25	-0.06	-0.44
175.469	20.249	0.0228	3.9	8.1	2.4	0.08	-	-0.16
181.494	27.715	0.0270	5.1	10.2	2.9	-0.31	-0.09	-0.52
183.855	23.948	0.0229	7.3	13.2	4.3	-0.30	-0.12	-0.47
170.678	29.880	0.0230	6.5	12.3	3.4	-0.16	0.05	-0.35
176.270	19.682	0.0212	5.5	11.9	3.1	-0.37	-0.19	-0.61
173.931	25.827	0.0312	5.9	12.4	3.0	-0.21	0.03	-0.41
194.542	32.017	0.0266	4.6	8.2	2.8	-0.19	0.04	-0.36
180.657	20.103	0.0214	3.1	5.6	2.3	-0.01	-	-0.22
170.647	20.704	0.0146	5.3	10.5	3.0	-0.22	0.01	-0.41
183.289	32.596	0.0249	1.8	2.3	1.5	-0.21	0.05	-0.38
181.764	18.532	0.0240	5.8	11.2	3.1	-0.18	0.03	-0.36
195.431	29.045	0.0237	3.8	7.4	2.5	-0.17	0.08	-0.38
178.499	20.573	0.0226	4.6	8.8	2.8	-0.27	-0.05	-0.47
193.638	27.633	0.0244	2.4	3.2	1.7	-0.02	-	-0.24
195.504	27.653	0.0236	3.9	8.3	2.4	0.04	-	-0.21

continued on next page..

Table A.1 – continued from previous page

RA (J2000)	Dec (J2000)	z	Age (Gyr)	Age upper (Gyr)	Age lower (Gyr)	Z (dex)	Z upper (dex)	Z lower (dex)
193.476	26.966	0.0206	6.9	13.8	3.2	0.00	-	-0.24
194.733	27.833	0.0251	3.7	6.4	2.6	-0.19	0.03	-0.37
196.075	29.030	0.0228	5.6	11.4	2.9	-0.13	0.14	-0.34
176.233	19.494	0.0212	6.5	12.6	3.8	-0.32	-0.15	-0.52
192.039	26.939	0.0230	6.3	12.0	3.8	-0.32	-0.16	-0.50
175.064	26.648	0.0228	6.2	12.1	3.2	-0.20	0.02	-0.39
194.818	27.158	0.0223	7.1	14.0	3.6	-0.20	0.03	-0.39
174.474	21.936	0.0313	7.2	13.2	4.2	-0.26	-0.08	-0.43
194.612	29.612	0.0195	2.6	4.0	1.7	0.18	-	-0.09
178.930	25.492	0.0284	4.9	9.2	3.0	-0.39	-0.20	-0.59
194.576	29.129	0.0263	1.8	2.4	1.5	-0.03	-	-0.24
194.626	28.859	0.0266	5.2	11.5	2.7	-0.09	-	-0.32
183.110	23.728	0.0250	4.1	8.5	2.6	-0.19	0.08	-0.41
179.542	26.453	0.0231	3.8	7.3	2.5	-0.06	0.21	-0.28
174.942	20.554	0.0206	3.4	6.5	2.4	-0.03	-	-0.25
194.592	28.152	0.0223	5.2	11.2	2.8	-0.10	0.20	-0.32
194.015	28.435	0.0228	2.9	4.8	2.3	-0.05	0.18	-0.26
195.775	26.531	0.0191	2.2	2.6	1.6	-0.21	0.05	-0.39
181.131	28.152	0.0277	2.2	3.0	1.6	0.09	-	-0.16
193.282	27.038	0.0255	6.0	12.4	2.8	0.04	-	-0.20
177.703	27.864	0.0286	5.1	10.9	2.8	-0.12	0.18	-0.33
184.967	28.208	0.0268	5.3	10.8	2.9	-0.09	0.19	-0.30
176.200	19.688	0.0163	1.5	1.9	1.1	0.19	-	-0.11
189.019	26.596	0.0217	5.3	11.3	2.8	-0.09	0.21	-0.31
177.487	27.939	0.0291	2.7	3.8	2.2	-0.27	-0.08	-0.44
192.282	27.797	0.0209	7.2	13.7	4.1	-0.34	-0.17	-0.53
195.871	26.551	0.0221	2.7	4.0	2.0	-0.19	0.04	-0.39
193.653	26.935	0.0198	5.2	10.8	2.9	-0.14	0.13	-0.34
183.283	21.494	0.0233	2.0	2.5	1.6	-0.28	-0.01	-0.46
190.236	27.932	0.0310	2.8	4.8	2.0	-0.01	-	-0.25
173.785	21.230	0.0209	4.9	10.3	2.8	-0.19	0.08	-0.40
196.928	24.811	0.0211	2.8	4.3	2.3	-0.23	-0.04	-0.40
194.618	27.559	0.0253	1.1	1.4	0.9	0.05	-	-0.26
198.720	17.233	0.0240	3.1	6.4	2.0	0.14	-	-0.12
183.870	24.092	0.0231	4.1	7.4	2.7	-0.18	0.05	-0.37
189.223	27.862	0.0249	2.7	4.1	2.1	-0.30	-0.10	-0.50
187.448	27.243	0.0246	2.8	4.7	2.0	-0.02	-	-0.27
172.113	22.873	0.0313	1.7	2.2	1.4	-0.07	0.21	-0.30
177.159	32.641	0.0233	3.4	5.8	2.6	-0.32	-0.15	-0.51
189.931	28.197	0.0311	5.0	9.3	3.0	-0.40	-0.22	-0.61
181.313	20.311	0.0226	2.7	3.9	2.2	-0.44	-0.28	-0.61
184.953	30.366	0.0274	4.1	9.0	2.4	-0.03	-	-0.28
174.852	19.535	0.0226	2.8	4.8	2.0	0.03	-	-0.22
173.892	30.947	0.0326	7.3	13.6	4.4	-0.47	-0.30	-0.66
173.015	23.704	0.0322	1.5	2.0	1.2	0.10	-	-0.20
175.688	20.032	0.0211	1.7	2.3	1.4	-0.05	-	-0.28
174.374	32.252	0.0327	2.1	2.5	1.7	-0.63	-0.49	-0.82
184.614	20.110	0.0291	6.2	12.3	3.4	-0.26	-0.06	-0.46
194.181	27.035	0.0187	4.5	8.5	2.7	-0.22	0.02	-0.41
185.043	28.389	0.0255	7.2	13.8	4.2	-0.49	-0.30	-0.69
171.202	19.774	0.0262	3.1	5.2	2.4	-0.20	0.00	-0.39
176.275	20.438	0.0229	2.7	4.2	2.1	-0.22	-0.01	-0.41
178.127	20.625	0.0220	2.4	2.8	1.7	-0.23	0.01	-0.40
177.639	17.858	0.0213	2.2	2.7	1.7	-0.45	-0.25	-0.64
193.263	26.477	0.0257	3.1	5.6	2.5	-0.33	-0.15	-0.54

continued on next page..

Table A.1 – continued from previous page

RA (J2000)	Dec (J2000)	z	Age (Gyr)	Age upper (Gyr)	Age lower (Gyr)	Z (dex)	Z upper (dex)	Z lower (dex)
187.456	22.372	0.0225	2.5	3.2	2.1	-0.38	-0.22	-0.55
173.691	28.716	0.0229	3.3	6.1	2.4	-0.16	0.09	-0.36
176.625	19.774	0.0225	5.3	11.0	2.9	-0.19	0.06	-0.39
172.150	23.405	0.0245	2.4	3.2	1.6	-0.05	-	-0.29
175.759	19.650	0.0232	5.7	13.1	2.9	-0.19	0.09	-0.43
176.443	32.801	0.0297	2.8	5.4	1.8	0.05	-	-0.23
178.422	23.382	0.0215	2.1	2.8	1.5	-0.01	-	-0.24
178.549	25.035	0.0221	2.9	4.9	2.2	-0.08	0.16	-0.30
170.627	24.300	0.0251	4.3	7.9	2.7	-0.09	0.16	-0.29
172.751	25.221	0.0318	1.6	2.0	1.3	-0.46	-0.19	-0.64
194.874	31.336	0.0251	2.7	3.8	2.3	-0.29	-0.11	-0.45
180.327	17.534	0.0231	6.1	11.9	3.1	-0.15	0.07	-0.35
184.913	28.391	0.0273	5.7	12.3	2.9	-0.16	0.12	-0.38
190.464	23.511	0.0286	2.5	3.3	1.8	-0.27	-0.01	-0.46
197.345	28.321	0.0191	6.4	13.8	3.6	-0.39	-0.19	-0.63
170.795	24.137	0.0254	4.9	11.3	2.7	-0.27	-0.00	-0.52
174.400	20.164	0.0258	4.2	9.0	2.6	-0.24	0.02	-0.48
183.317	21.697	0.0251	4.4	9.3	2.6	-0.08	-	-0.31
170.202	32.290	0.0279	2.5	3.2	1.9	-0.23	0.00	-0.40
194.027	27.648	0.0254	2.2	3.1	1.5	0.00	-	-0.27
173.425	23.413	0.0238	3.0	6.0	2.0	0.10	-	-0.16
193.656	27.692	0.0282	5.4	12.3	2.9	-0.27	-0.02	-0.51
198.357	27.763	0.0205	2.4	2.9	1.8	-0.27	-0.04	-0.44
195.772	27.784	0.0256	5.7	11.8	3.1	-0.22	0.00	-0.42
195.452	27.604	0.0275	3.7	7.2	2.6	-0.26	-0.04	-0.48
172.925	26.876	0.0324	3.8	7.9	2.5	-0.22	0.05	-0.45
195.543	28.192	0.0191	4.5	10.8	2.5	0.03	-	-0.23
182.721	19.097	0.0255	3.8	9.0	2.3	-0.12	0.21	-0.38
179.516	21.248	0.0248	1.9	2.7	1.4	0.08	-	-0.18
192.063	17.774	0.0206	1.1	1.3	0.9	0.01	0.16	-0.27
195.501	27.783	0.0237	0.9	1.0	0.8	-0.12	0.05	-0.30
189.801	27.743	0.0263	2.4	3.0	1.9	-0.35	-0.15	-0.52
194.180	26.742	0.0232	5.1	11.9	2.8	-0.29	-0.02	-0.54
193.741	28.308	0.0211	2.9	5.6	2.0	0.08	-	-0.19
183.587	32.450	0.0217	2.4	3.1	1.6	0.07	-	-0.18
193.709	26.325	0.0226	2.7	4.6	2.0	-0.24	0.02	-0.47
176.493	29.333	0.0230	4.1	8.6	2.7	-0.61	-0.40	-0.86
181.180	31.177	0.0250	4.2	6.5	2.8	-0.54	-0.37	-0.71
194.341	27.880	0.0248	1.6	2.2	1.2	0.09	-	-0.20
170.797	29.941	0.0239	2.8	5.1	2.1	-0.23	0.03	-0.46
194.120	26.543	0.0258	4.2	10.1	2.4	-0.03	-	-0.29
186.485	30.844	0.0228	2.6	3.7	1.8	-0.08	0.21	-0.30
192.981	26.783	0.0203	2.7	4.4	2.2	-0.36	-0.15	-0.58
184.837	22.325	0.0220	2.8	5.5	1.8	0.07	-	-0.22
193.029	27.026	0.0214	2.0	2.6	1.5	-0.27	0.04	-0.47
198.459	17.076	0.0226	2.6	3.7	2.1	-0.45	-0.27	-0.63
180.856	20.242	0.0195	2.2	2.8	1.6	-0.08	0.20	-0.28
176.440	19.164	0.0203	2.7	4.3	2.0	-0.10	0.16	-0.33
197.378	28.986	0.0206	2.4	3.1	1.7	-0.20	0.09	-0.40
195.818	28.030	0.0203	2.9	4.9	2.3	-0.24	-0.04	-0.43
179.882	30.156	0.0292	5.6	13.4	3.1	-0.50	-0.29	-0.77
176.013	19.740	0.0229	3.1	7.3	1.8	0.04	-	-0.27
179.755	28.339	0.0281	4.4	11.8	2.2	0.17	-	-0.13
174.962	20.395	0.0226	2.4	3.1	1.7	-0.20	0.10	-0.41
189.154	26.235	0.0228	3.1	6.3	2.2	-0.07	-	-0.31

continued on next page..

Table A.1 – continued from previous page

RA (J2000)	Dec (J2000)	z	Age (Gyr)	Age upper (Gyr)	Age lower (Gyr)	Z (dex)	Z upper (dex)	Z lower (dex)
180.693	22.335	0.0251	4.7	10.9	2.6	-0.13	0.19	-0.37
182.415	23.289	0.0230	2.3	3.1	1.5	0.05	-	-0.22
170.911	24.158	0.0260	4.6	10.0	2.6	-0.13	0.15	-0.36
194.199	27.421	0.0259	3.1	5.7	2.3	-0.26	-0.03	-0.47
180.520	17.913	0.0227	2.4	3.1	1.9	-0.37	-0.17	-0.56
183.594	22.187	0.0238	3.3	6.7	2.3	-0.16	0.12	-0.39
179.645	24.117	0.0298	5.3	11.7	2.9	-0.29	-0.04	-0.52
183.893	21.833	0.0224	2.2	2.9	1.6	-0.27	0.06	-0.50
181.105	20.080	0.0253	4.2	7.7	2.7	-0.19	0.05	-0.38
172.835	28.201	0.0231	1.7	2.3	1.3	-0.07	-	-0.35
180.535	17.690	0.0219	6.2	13.3	3.1	-0.23	0.01	-0.45
178.820	17.488	0.0225	2.3	2.8	1.7	-0.21	0.07	-0.40
176.079	20.304	0.0255	1.7	2.6	1.1	0.21	-	-0.14
180.848	20.022	0.0214	2.5	3.1	2.0	-0.32	-0.13	-0.49
178.757	32.094	0.0310	2.8	5.1	2.1	-0.19	0.06	-0.43
195.926	28.906	0.0223	2.5	3.8	1.7	0.01	-	-0.25
195.660	28.115	0.0249	3.6	7.7	2.3	-0.01	-	-0.26
173.710	25.531	0.0235	2.9	4.9	2.4	-0.34	-0.16	-0.55
190.930	25.471	0.0174	2.5	3.9	1.7	-0.21	0.09	-0.44
194.569	31.159	0.0260	4.2	8.6	2.7	-0.57	-0.37	-0.80
182.675	17.888	0.0240	2.1	2.6	1.6	-0.31	-0.07	-0.49
170.493	24.787	0.0245	2.3	2.8	1.7	-0.20	0.07	-0.38
193.223	28.371	0.0236	2.6	3.5	2.0	-0.29	-0.08	-0.46
184.896	28.354	0.0284	4.0	9.8	2.2	0.06	-	-0.22
197.287	28.893	0.0248	2.3	3.5	1.5	0.10	-	-0.20
183.496	17.549	0.0200	5.4	12.3	2.9	-0.31	-0.08	-0.55
173.412	24.685	0.0227	4.0	8.1	2.5	-0.22	0.03	-0.45
198.545	17.261	0.0238	5.0	12.9	2.6	-0.20	0.14	-0.47
195.025	27.978	0.0255	5.4	13.4	3.0	-0.56	-0.34	-0.84
188.789	29.744	0.0268	3.1	5.7	2.5	-0.30	-0.10	-0.51
188.179	29.712	0.0270	4.4	10.2	2.5	-0.08	-	-0.33
189.014	26.987	0.0314	4.8	11.5	2.6	-0.19	0.12	-0.44
198.031	27.323	0.0209	4.3	12.2	2.3	-0.09	-	-0.39
173.907	25.089	0.0320	2.9	5.1	2.3	-0.31	-0.12	-0.53
190.280	27.462	0.0239	1.9	2.7	1.4	0.02	-	-0.26
176.016	20.099	0.0186	5.5	12.6	2.6	0.00	-	-0.26
196.348	29.510	0.0201	5.5	14.0	2.8	-0.32	-0.04	-0.61
190.870	29.467	0.0312	2.7	4.6	2.0	-0.17	0.08	-0.39
195.026	27.301	0.0263	2.6	4.7	1.6	0.04	-	-0.26
194.740	27.785	0.0231	4.4	10.8	2.4	-0.07	-	-0.34
183.146	22.785	0.0223	2.4	3.1	1.9	-0.42	-0.23	-0.61
175.566	20.216	0.0241	2.8	5.5	2.1	-0.25	0.02	-0.51
194.486	27.038	0.0247	2.5	3.7	1.7	-0.04	-	-0.29
179.488	22.249	0.0299	2.7	4.8	1.9	-0.16	0.14	-0.40
194.531	26.327	0.0190	3.0	6.6	1.9	-0.01	-	-0.29
199.320	20.691	0.0228	1.7	2.2	1.3	-0.44	-0.12	-0.65
194.523	28.243	0.0240	3.4	7.5	2.5	-0.39	-0.20	-0.66
173.211	24.974	0.0325	3.0	5.9	2.2	-0.08	0.22	-0.31
181.201	28.198	0.0271	2.8	4.9	2.0	-0.12	0.16	-0.36
189.798	28.005	0.0242	1.5	1.8	1.1	-0.22	0.09	-0.50
185.166	28.122	0.0269	3.1	7.8	1.8	0.03	-	-0.27
195.013	28.240	0.0257	4.2	8.8	2.7	-0.41	-0.20	-0.67
192.404	30.846	0.0269	1.7	2.4	1.3	-0.32	0.08	-0.57
178.944	29.941	0.0227	2.5	3.8	1.7	-0.09	-	-0.33
180.435	17.899	0.0230	4.1	8.3	2.6	-0.25	0.00	-0.48

continued on next page..

Table A.1 – continued from previous page

RA (J2000)	Dec (J2000)	z	Age (Gyr)	Age upper (Gyr)	Age lower (Gyr)	Z (dex)	Z upper (dex)	Z lower (dex)
185.233	24.669	0.0245	2.3	3.2	1.8	-0.56	-0.34	-0.79
195.022	28.024	0.0197	2.4	3.3	1.6	0.06	-	-0.20
199.332	20.638	0.0229	1.9	2.4	1.5	-0.27	0.05	-0.47
194.324	27.811	0.0238	1.4	1.8	1.1	-0.30	0.04	-0.59
190.310	20.666	0.0221	2.0	2.6	1.5	-0.33	-0.02	-0.53
194.922	27.660	0.0225	2.7	5.3	1.6	0.15	-	-0.17
194.211	28.930	0.0270	2.0	2.5	1.5	-0.32	-0.02	-0.52
176.695	21.271	0.0222	2.0	2.6	1.6	-0.53	-0.26	-0.75
175.976	25.998	0.0315	2.4	3.8	1.6	-0.08	-	-0.34
194.262	31.626	0.0233	2.0	2.6	1.5	-0.41	-0.09	-0.63
170.559	24.300	0.0274	4.6	10.2	2.6	-0.24	0.03	-0.48
173.297	19.792	0.0326	2.1	2.9	1.5	-0.08	-	-0.35
188.755	25.780	0.0295	2.0	2.5	1.6	-0.54	-0.32	-0.72
175.223	30.573	0.0320	2.2	2.9	1.6	-0.12	-	-0.35
171.324	17.808	0.0164	2.5	3.7	1.9	-0.35	-0.14	-0.56
184.632	25.999	0.0248	2.3	3.1	1.7	-0.26	0.04	-0.47
195.560	28.353	0.0288	3.9	10.5	2.0	0.04	-	-0.28
173.008	25.623	0.0324	3.5	7.5	2.5	-0.35	-0.13	-0.62
195.043	27.595	0.0187	2.6	4.1	1.8	-0.12	0.20	-0.35
183.476	25.169	0.0227	2.4	3.6	1.6	-0.17	0.19	-0.41
199.993	28.247	0.0227	1.7	2.2	1.3	-0.18	0.16	-0.44
196.910	31.487	0.0262	2.0	2.6	1.5	-0.39	-0.07	-0.62
185.868	30.984	0.0285	4.1	9.1	2.6	-0.36	-0.13	-0.63
173.350	32.603	0.0209	4.3	10.8	2.4	-0.10	-	-0.36
185.086	28.384	0.0275	5.0	10.8	2.9	-0.36	-0.12	-0.59
181.290	22.008	0.0220	1.6	2.0	1.3	-0.46	-0.15	-0.66
172.830	28.383	0.0296	2.7	6.5	1.5	0.16	-	-0.21
181.222	19.886	0.0241	2.4	3.1	1.7	-0.20	0.12	-0.41
189.211	27.278	0.0220	5.1	13.1	2.6	-0.19	0.14	-0.46
188.567	27.862	0.0231	2.5	3.2	1.7	-0.20	0.09	-0.39
192.757	28.928	0.0214	1.9	2.4	1.5	-0.57	-0.31	-0.78
194.858	28.187	0.0258	3.1	7.0	2.1	-0.18	0.14	-0.46
184.997	30.360	0.0278	3.7	9.4	2.1	0.01	-	-0.28
187.212	26.700	0.0221	5.4	13.1	3.0	-0.48	-0.26	-0.76
193.899	27.767	0.0223	3.7	9.2	2.2	-0.13	-	-0.40
171.389	22.819	0.0215	2.2	3.0	1.5	0.02	-	-0.25
194.623	28.301	0.0197	2.4	3.6	1.6	-0.01	-	-0.27
190.289	29.539	0.0235	1.4	2.1	1.0	0.21	-	-0.21
195.433	29.927	0.0307	1.0	1.2	0.8	0.01	0.16	-0.26
173.138	22.116	0.0220	2.4	3.9	1.5	0.01	-	-0.29
195.536	28.387	0.0253	3.1	7.2	2.1	-0.11	-	-0.39
183.906	28.170	0.0223	1.9	2.5	1.5	-0.45	-0.15	-0.64
192.366	27.268	0.0266	2.5	3.4	1.7	-0.21	0.08	-0.40
184.563	20.011	0.0291	2.5	4.3	1.7	-0.31	-0.01	-0.57
181.785	32.996	0.0265	1.8	2.2	1.5	-0.59	-0.35	-0.79
176.879	19.872	0.0192	1.9	2.5	1.5	-0.24	0.10	-0.46
184.826	30.342	0.0260	3.7	7.7	2.5	-0.26	-0.01	-0.50
177.571	27.131	0.0299	3.5	8.9	2.1	-0.06	-	-0.35
182.034	25.033	0.0227	2.4	4.0	1.6	0.06	-	-0.23
189.225	27.749	0.0258	1.4	1.7	1.0	-0.19	0.12	-0.52
175.760	26.274	0.0309	1.3	1.6	1.0	-0.34	-0.03	-0.63
174.822	28.663	0.0233	2.7	5.1	2.0	-0.28	-0.01	-0.54
187.146	18.590	0.0235	4.9	11.1	2.7	-0.25	0.02	-0.50
189.783	30.407	0.0234	2.0	2.5	1.5	-0.22	0.10	-0.43
185.319	19.499	0.0304	3.8	9.7	2.3	-0.22	0.11	-0.52

continued on next page..

Table A.1 – continued from previous page

RA (J2000)	Dec (J2000)	z	Age (Gyr)	Age upper (Gyr)	Age lower (Gyr)	Z (dex)	Z upper (dex)	Z lower (dex)
177.704	22.127	0.0239	5.6	13.6	3.0	-0.32	-0.08	-0.59
174.937	22.685	0.0231	2.8	5.6	2.0	-0.26	0.02	-0.53
195.937	28.546	0.0258	4.7	11.8	2.5	-0.09	-	-0.36
172.423	28.260	0.0327	1.7	2.0	1.4	-0.64	-0.43	-0.86
183.146	29.828	0.0284	1.1	1.4	0.9	0.00	0.18	-0.32
188.229	32.911	0.0305	1.4	1.8	1.0	-0.11	0.20	-0.47
184.782	30.013	0.0283	3.8	8.6	2.3	-0.07	-	-0.33
170.709	24.225	0.0252	4.1	11.4	2.1	-0.06	-	-0.37
180.487	20.625	0.0227	1.7	2.1	1.3	-0.57	-0.28	-0.79
190.234	29.466	0.0311	2.3	3.2	1.5	0.05	-	-0.23
186.593	25.886	0.0211	2.1	2.7	1.5	-0.17	0.17	-0.39
179.569	24.316	0.0221	1.6	2.5	1.1	0.13	-	-0.23
182.032	25.373	0.0209	3.6	10.8	1.9	-0.05	-	-0.37
194.580	27.762	0.0182	5.2	13.8	2.7	-0.24	0.07	-0.52
170.010	30.581	0.0258	1.6	2.1	1.2	-0.03	-	-0.34
173.858	21.485	0.0294	4.3	10.0	2.5	-0.21	0.09	-0.47
174.479	21.986	0.0300	5.1	11.8	2.8	-0.35	-0.11	-0.61
192.496	27.153	0.0262	5.3	12.7	2.7	-0.22	0.07	-0.47
170.233	19.632	0.0143	2.5	3.8	1.7	-0.35	-0.07	-0.58
177.836	27.726	0.0288	2.3	3.7	1.4	0.09	-	-0.24
194.218	26.488	0.0254	4.2	9.5	2.6	-0.34	-0.11	-0.61
170.108	24.496	0.0251	5.5	12.8	2.9	-0.23	0.04	-0.48
179.775	27.978	0.0270	2.8	5.6	1.9	-0.23	0.09	-0.50
186.367	29.164	0.0304	2.6	4.0	1.8	-0.27	-0.00	-0.48
179.408	25.241	0.0161	1.6	2.2	1.2	-0.15	0.22	-0.45
172.940	26.476	0.0323	1.3	1.8	1.0	0.12	-	-0.30
183.630	18.251	0.0291	4.0	8.1	2.6	-0.56	-0.35	-0.82
196.077	28.468	0.0258	4.6	12.5	2.3	0.00	-	-0.30
193.246	26.720	0.0271	2.9	5.5	2.1	-0.23	0.03	-0.47
176.277	20.156	0.0205	2.4	3.5	1.6	-0.11	-	-0.35
194.859	28.288	0.0267	2.7	4.6	2.1	-0.45	-0.23	-0.68
195.433	29.000	0.0214	5.2	13.0	2.7	-0.31	-0.02	-0.59
192.908	27.311	0.0235	2.5	3.6	1.8	-0.51	-0.28	-0.75
175.974	26.183	0.0314	3.1	6.5	2.2	-0.16	0.13	-0.42
190.309	26.736	0.0158	1.4	1.7	1.1	-0.21	0.11	-0.53
174.874	26.309	0.0229	2.6	3.9	1.8	-0.15	0.13	-0.37
170.217	31.460	0.0240	1.7	2.3	1.2	0.02	-	-0.29
174.290	19.898	0.0209	1.4	1.8	1.0	-0.03	-	-0.42
170.428	24.291	0.0255	3.7	9.8	2.3	-0.31	-0.02	-0.62
195.748	28.275	0.0239	3.1	7.7	2.1	-0.19	0.14	-0.48
194.906	28.166	0.0191	5.7	14.0	2.8	-0.23	0.06	-0.49
185.280	20.129	0.0315	2.4	3.6	1.6	-0.21	0.15	-0.46
173.124	28.112	0.0325	4.3	10.9	2.5	-0.31	-0.02	-0.60
181.516	20.606	0.0257	2.3	3.0	1.7	-0.57	-0.36	-0.82
196.020	27.851	0.0213	2.3	4.2	1.4	0.13	-	-0.23
194.683	28.283	0.0254	4.9	11.4	2.7	-0.32	-0.06	-0.58
182.122	28.242	0.0270	2.9	5.5	2.2	-0.37	-0.14	-0.63
182.090	25.191	0.0200	2.9	6.4	1.9	-0.17	0.17	-0.45
175.373	26.360	0.0298	2.6	5.4	1.6	0.01	-	-0.32
193.340	26.361	0.0193	4.0	10.9	2.2	-0.12	-	-0.41
188.736	26.627	0.0229	4.8	12.9	2.5	-0.25	0.09	-0.55
199.995	29.427	0.0316	3.4	7.6	2.4	-0.39	-0.17	-0.68
173.991	23.012	0.0237	2.4	3.6	1.8	-0.66	-0.46	-0.92
177.755	20.399	0.0215	2.0	2.8	1.3	-0.18	-	-0.46
180.964	20.053	0.0222	2.5	3.7	1.9	-0.50	-0.28	-0.71

continued on next page..

Table A.1 – continued from previous page

RA (J2000)	Dec (J2000)	z	Age (Gyr)	Age upper (Gyr)	Age lower (Gyr)	Z (dex)	Z upper (dex)	Z lower (dex)
187.413	32.913	0.0224	1.6	2.2	1.2	-0.33	0.05	-0.59
191.840	28.006	0.0321	2.8	5.8	2.0	-0.34	-0.06	-0.62
193.949	28.256	0.0270	1.6	2.3	1.0	0.04	-	-0.36
183.855	19.292	0.0207	2.1	2.7	1.6	-0.47	-0.16	-0.71
199.086	30.678	0.0189	1.7	2.4	1.3	-0.29	0.09	-0.54
175.758	23.944	0.0230	2.3	3.0	1.7	-0.42	-0.16	-0.65
176.591	19.484	0.0176	2.8	6.5	1.6	-0.02	-	-0.36
188.571	27.452	0.0229	2.6	5.1	1.6	-0.05	-	-0.37
194.213	29.378	0.0238	4.1	11.4	2.4	-0.32	-0.00	-0.64
182.108	22.417	0.0224	1.3	1.8	1.0	0.19	-	-0.17
174.342	25.850	0.0316	1.9	2.5	1.5	-0.56	-0.26	-0.81
183.264	21.024	0.0239	2.7	5.2	2.0	-0.50	-0.26	-0.77
186.442	26.082	0.0237	1.7	2.5	1.1	-0.03	-	-0.35
182.902	22.995	0.0297	1.7	2.3	1.3	-0.36	0.01	-0.59
177.999	21.108	0.0221	1.3	1.7	1.0	-0.03	-	-0.41
174.562	31.640	0.0328	2.1	2.7	1.6	-0.59	-0.34	-0.86
187.082	22.417	0.0322	5.6	13.8	3.0	-0.38	-0.15	-0.67
189.757	18.201	0.0265	2.8	7.7	1.6	-0.02	-	-0.37
181.234	21.240	0.0225	1.6	2.6	1.0	0.16	-	-0.26
177.496	21.304	0.0264	3.1	7.6	2.1	-0.21	0.11	-0.50
180.622	21.537	0.0306	4.7	11.9	2.6	-0.35	-0.07	-0.65
197.010	28.251	0.0251	2.6	5.3	1.6	0.00	-	-0.31
190.814	27.086	0.0227	1.9	2.6	1.4	-0.41	-0.04	-0.65
184.361	23.904	0.0243	2.7	5.3	1.8	-0.22	0.13	-0.51
184.845	20.392	0.0307	2.9	7.0	2.0	-0.22	0.12	-0.52
182.644	25.928	0.0214	2.3	3.4	1.6	-0.54	-0.26	-0.81
183.904	21.909	0.0222	2.4	3.2	1.7	-0.51	-0.27	-0.75
179.474	28.655	0.0228	1.7	2.4	1.3	-0.23	0.16	-0.48
180.934	23.706	0.0257	2.0	2.7	1.6	-0.67	-0.43	-0.96
184.059	28.763	0.0262	2.7	6.2	1.6	0.05	-	-0.30
196.033	27.965	0.0198	2.7	5.4	1.7	-0.04	-	-0.33
184.933	28.863	0.0255	2.3	3.8	1.5	0.06	-	-0.25
175.992	20.806	0.0213	2.4	3.5	1.6	-0.18	0.16	-0.42
175.561	20.098	0.0198	3.1	6.4	2.2	-0.18	0.11	-0.42
178.577	23.086	0.0271	1.6	2.4	1.1	-0.09	-	-0.44
177.740	21.189	0.0212	2.3	3.0	1.6	-0.27	0.06	-0.50
195.078	27.937	0.0176	3.5	9.5	2.1	-0.13	-	-0.42
180.954	20.202	0.0225	1.6	2.2	1.1	-0.05	-	-0.37
181.856	29.147	0.0294	2.9	6.2	1.9	-0.10	-	-0.38
194.477	27.491	0.0166	1.6	2.3	1.1	0.13	-	-0.24
196.495	25.466	0.0218	1.7	2.3	1.3	-0.46	-0.08	-0.71
181.665	20.457	0.0243	2.1	2.8	1.5	-0.28	0.10	-0.53
192.631	30.847	0.0308	2.5	3.9	1.9	-0.47	-0.24	-0.71
182.381	19.210	0.0261	2.5	4.0	1.7	-0.25	0.05	-0.49
194.380	26.512	0.0241	1.0	1.3	0.8	-0.01	0.20	-0.39
181.466	20.435	0.0245	1.7	2.6	1.1	0.00	-	-0.35
175.602	20.119	0.0200	1.9	2.6	1.5	-0.64	-0.35	-0.94
184.164	28.048	0.0279	1.3	1.7	1.0	-0.34	0.02	-0.67
173.539	28.595	0.0231	3.2	8.6	2.1	-0.22	0.12	-0.52
198.876	21.403	0.0310	2.8	5.5	2.0	-0.46	-0.20	-0.73
195.139	27.824	0.0273	2.0	2.8	1.3	-0.19	-	-0.49
184.868	21.574	0.0320	2.9	6.1	2.0	-0.31	-0.02	-0.61
173.686	19.033	0.0326	2.9	5.6	2.2	-0.45	-0.22	-0.70
193.073	27.158	0.0213	2.1	3.8	1.2	0.19	-	-0.20
175.722	20.179	0.0211	2.0	3.8	1.1	0.19	-	-0.24

continued on next page..

Table A.1 – continued from previous page

RA (J2000)	Dec (J2000)	z	Age (Gyr)	Age upper (Gyr)	Age lower (Gyr)	Z (dex)	Z upper (dex)	Z lower (dex)
185.966	32.355	0.0304	2.3	3.1	1.6	-0.39	-0.07	-0.64
178.417	23.639	0.0243	2.8	5.8	2.0	-0.34	-0.06	-0.63
191.214	28.504	0.0245	1.3	1.8	1.0	0.01	-	-0.43
194.662	27.954	0.0200	2.0	2.9	1.3	0.02	-	-0.30
181.500	28.327	0.0300	2.4	4.0	1.6	-0.27	0.09	-0.55
192.567	27.380	0.0223	3.1	8.3	2.0	-0.24	0.10	-0.57
176.126	22.231	0.0279	1.6	2.2	1.1	-0.18	0.22	-0.51
175.323	20.831	0.0239	2.2	3.1	1.6	-0.44	-0.08	-0.71
177.115	21.157	0.0227	2.6	5.0	1.7	-0.21	0.14	-0.49
193.753	27.483	0.0232	2.5	4.9	1.6	-0.26	0.13	-0.58
179.264	28.216	0.0271	1.6	2.3	1.1	0.15	-	-0.23
194.046	28.163	0.0290	1.8	2.4	1.3	-0.47	-0.08	-0.70
185.662	29.439	0.0265	1.7	2.6	1.2	-0.12	-	-0.45
191.058	20.031	0.0291	1.5	2.3	1.0	0.13	-	-0.29
184.858	25.038	0.0224	2.5	4.6	1.8	-0.64	-0.40	-0.95
184.550	18.093	0.0253	1.3	1.8	1.0	-0.34	0.04	-0.68
191.178	27.014	0.0230	2.5	4.2	1.8	-0.37	-0.09	-0.63
175.989	19.936	0.0234	4.9	12.8	2.7	-0.39	-0.12	-0.70
182.029	22.101	0.0237	1.6	2.2	1.2	-0.48	-0.10	-0.75
170.270	31.252	0.0237	2.2	3.2	1.7	-0.70	-0.47	-1.00
198.108	28.538	0.0212	1.7	2.4	1.3	-0.48	-0.09	-0.71
176.067	20.268	0.0240	3.5	10.9	1.8	-0.08	-	-0.42
189.700	32.092	0.0145	1.1	1.6	0.9	-0.12	0.15	-0.52
180.103	31.112	0.0232	1.6	2.2	1.1	-0.24	0.18	-0.57
184.973	30.269	0.0279	2.5	4.5	1.6	-0.07	-	-0.36
181.358	27.943	0.0267	2.7	5.8	1.7	-0.12	-	-0.43
174.640	25.398	0.0254	3.1	8.9	2.2	-0.42	-0.15	-0.78
178.675	25.614	0.0200	1.2	1.6	1.0	-0.49	-0.16	-0.86
196.154	28.251	0.0187	4.8	13.1	2.5	-0.32	0.00	-0.63
187.845	29.136	0.0152	1.9	2.5	1.5	-0.59	-0.32	-0.86
196.908	28.326	0.0226	1.4	2.0	1.0	0.12	-	-0.32
181.565	31.968	0.0216	2.2	2.9	1.6	-0.40	-0.06	-0.65
194.826	27.716	0.0223	3.0	7.7	2.1	-0.39	-0.10	-0.73
197.854	30.599	0.0282	2.2	3.8	1.4	0.09	-	-0.25
175.437	19.432	0.0222	2.2	3.2	1.5	-0.27	0.16	-0.55
195.164	21.692	0.0223	2.4	4.1	1.8	-0.73	-0.50	-1.04
181.685	17.715	0.0143	2.5	4.6	1.7	-0.25	0.12	-0.54
198.657	29.318	0.0218	1.7	2.4	1.1	-0.25	0.21	-0.58
194.922	28.507	0.0275	2.9	7.1	1.7	-0.03	-	-0.36
193.049	26.875	0.0206	2.4	4.1	1.7	-0.47	-0.16	-0.76
184.954	20.841	0.0312	2.4	3.5	1.9	-0.68	-0.50	-0.93
193.398	27.759	0.0250	2.8	5.5	1.8	-0.17	0.16	-0.45
181.541	31.126	0.0230	2.5	4.9	1.5	-0.07	-	-0.40
191.564	30.635	0.0219	1.5	2.1	1.0	-0.12	-	-0.53
197.448	28.907	0.0186	3.4	7.4	2.4	-0.77	-0.53	-1.06
181.409	27.388	0.0259	1.4	2.0	1.0	-0.10	-	-0.50
188.693	19.423	0.0309	2.4	3.6	1.6	-0.15	-	-0.42
181.745	23.705	0.0235	2.4	4.5	1.6	-0.31	0.08	-0.62
198.092	17.551	0.0305	1.8	2.6	1.2	-0.12	-	-0.42
195.923	29.818	0.0234	2.3	4.0	1.4	0.00	-	-0.34
181.550	21.226	0.0226	2.1	2.8	1.5	-0.44	-0.06	-0.72
182.616	22.270	0.0234	1.8	2.5	1.3	-0.45	-0.04	-0.69
190.203	27.271	0.0216	2.2	3.3	1.6	-0.67	-0.39	-0.99
190.047	31.177	0.0236	1.6	2.3	1.1	-0.26	0.17	-0.58
178.233	22.625	0.0265	1.8	2.7	1.1	0.15	-	-0.20

continued on next page..

Table A.1 – continued from previous page

RA (J2000)	Dec (J2000)	z	Age (Gyr)	Age upper (Gyr)	Age lower (Gyr)	Z (dex)	Z upper (dex)	Z lower (dex)
195.636	27.296	0.0254	2.5	5.1	1.5	-0.10	-	-0.44
181.494	28.126	0.0297	2.6	5.5	1.6	-0.23	0.19	-0.57
189.040	17.053	0.0270	1.9	2.8	1.5	-0.82	-0.52	-1.16
178.896	25.889	0.0168	1.1	1.3	0.9	-0.35	-0.09	-0.69
184.535	24.688	0.0227	2.0	2.8	1.5	-0.48	-0.12	-0.76
194.819	27.106	0.0280	2.9	6.9	2.1	-0.36	-0.09	-0.67
177.647	20.213	0.0205	2.2	5.1	1.1	0.18	-	-0.27
196.043	29.015	0.0221	2.6	6.4	1.4	0.17	-	-0.24
174.226	19.997	0.0222	2.8	6.7	1.8	-0.33	0.01	-0.66
192.875	18.065	0.0216	2.1	3.1	1.6	-0.57	-0.25	-0.88
175.441	21.508	0.0226	1.6	2.4	1.1	-0.20	-	-0.57
185.722	22.447	0.0223	1.2	1.5	1.0	-0.47	-0.16	-0.83
171.566	27.867	0.0240	1.6	2.1	1.4	-0.95	-0.62	-1.24
188.749	26.884	0.0253	2.7	5.6	1.6	-0.16	-	-0.48
181.631	20.851	0.0258	2.9	8.2	2.0	-0.42	-0.12	-0.79
194.219	31.295	0.0264	2.1	3.0	1.4	-0.28	0.14	-0.57
196.047	27.490	0.0178	2.9	6.7	2.2	-0.63	-0.39	-0.92
181.618	20.020	0.0247	2.2	3.6	1.7	-0.88	-0.60	-1.15
190.997	22.567	0.0311	3.1	8.5	2.1	-0.65	-0.38	-0.99
175.666	20.173	0.0215	2.4	5.1	1.4	-0.08	-	-0.46
193.771	26.724	0.0222	1.9	2.7	1.3	-0.38	0.09	-0.68
185.219	25.430	0.0241	3.5	10.8	2.3	-0.57	-0.30	-0.92
176.349	20.325	0.0233	11.4	-	7.7	-0.18	-0.05	-0.29
192.287	27.369	0.0220	12.4	-	8.4	-0.32	-0.21	-0.42
177.730	30.851	0.0226	11.1	-	7.2	-0.19	-0.05	-0.31
194.289	27.466	0.0249	9.8	-	6.7	-0.22	-0.08	-0.34
183.980	23.596	0.0215	10.5	-	6.7	-0.13	0.03	-0.26
182.576	26.431	0.0218	9.8	-	6.5	-0.22	-0.08	-0.34
192.583	27.324	0.0255	11.5	-	7.4	-0.28	-0.15	-0.39
181.816	25.285	0.0215	10.8	-	6.9	-0.34	-0.22	-0.48
192.833	31.060	0.0228	12.4	-	8.3	-0.29	-0.17	-0.39
192.611	26.709	0.0187	12.8	-	8.7	-0.41	-0.30	-0.55
193.954	27.906	0.0231	9.8	-	6.2	-0.10	0.05	-0.25
194.179	28.020	0.0209	9.7	-	6.2	-0.29	-0.15	-0.41
182.265	32.669	0.0239	9.6	-	6.2	-0.20	-0.05	-0.33
192.260	26.893	0.0246	10.5	-	6.7	-0.30	-0.17	-0.42
193.871	27.521	0.0233	10.6	-	6.9	-0.29	-0.16	-0.41
183.521	24.067	0.0223	11.9	-	7.6	-0.37	-0.25	-0.51
183.558	32.421	0.0211	9.8	-	6.6	-0.26	-0.13	-0.38
193.866	27.656	0.0234	12.0	-	7.6	-0.30	-0.16	-0.42
194.783	27.855	0.0219	11.0	-	7.1	-0.27	-0.13	-0.38
194.991	28.247	0.0224	10.1	-	6.6	-0.37	-0.25	-0.51
193.637	28.377	0.0234	10.2	-	6.3	-0.11	0.06	-0.26
193.922	27.251	0.0237	13.6	-	9.0	-0.48	-0.35	-0.62
195.474	27.624	0.0262	13.0	-	8.8	-0.36	-0.24	-0.50
193.542	28.093	0.0210	12.4	-	8.3	-0.25	-0.12	-0.37
194.946	27.710	0.0280	11.4	-	7.3	-0.25	-0.10	-0.38
195.720	27.867	0.0274	9.6	-	6.2	-0.24	-0.09	-0.36
190.096	25.551	0.0213	11.2	-	6.9	-0.22	-0.07	-0.35
192.556	26.776	0.0236	11.4	-	7.2	-0.29	-0.16	-0.41
183.907	23.982	0.0224	11.2	-	7.2	-0.47	-0.34	-0.61
194.391	28.482	0.0209	13.4	-	8.8	-0.22	-0.08	-0.34
182.231	21.777	0.0242	9.4	-	6.0	-0.18	-0.03	-0.31
198.539	17.367	0.0235	13.8	-	8.7	-0.21	-0.05	-0.34
182.279	25.237	0.0216	13.7	-	8.0	-0.29	-0.13	-0.44

continued on next page..

Table A.1 – continued from previous page

RA (J2000)	Dec (J2000)	z	Age (Gyr)	Age upper (Gyr)	Age lower (Gyr)	Z (dex)	Z upper (dex)	Z lower (dex)
194.241	30.716	0.0242	11.3	-	7.3	-0.37	-0.25	-0.51
194.134	27.056	0.0204	13.2	-	8.5	-0.29	-0.16	-0.41
194.553	26.397	0.0197	12.4	-	7.9	-0.40	-0.28	-0.55
172.249	20.739	0.0211	10.5	-	6.6	-0.20	-0.05	-0.34
193.892	27.842	0.0233	9.4	-	5.3	-0.12	0.06	-0.28
181.464	20.522	0.0238	11.1	-	7.0	-0.45	-0.32	-0.60
181.025	20.324	0.0255	12.2	-	7.6	-0.35	-0.21	-0.50
195.203	28.158	0.0194	10.3	-	6.1	-0.10	0.07	-0.25
181.033	20.846	0.0245	10.2	-	5.8	-0.07	0.11	-0.23
196.302	27.570	0.0230	9.8	-	6.0	-0.29	-0.14	-0.42
199.965	23.000	0.0230	11.6	-	7.3	-0.40	-0.27	-0.56
170.800	24.566	0.0261	10.9	-	6.7	-0.23	-0.07	-0.37
182.094	28.334	0.0273	9.7	-	5.9	-0.15	0.01	-0.30
194.513	26.916	0.0274	11.7	-	7.2	-0.23	-0.07	-0.36
182.561	19.194	0.0256	10.8	-	7.0	-0.39	-0.27	-0.54
176.526	19.790	0.0189	11.3	-	7.2	-0.31	-0.17	-0.44
182.258	24.955	0.0224	8.7	-	4.9	-0.11	0.07	-0.26
176.431	31.452	0.0278	13.7	-	8.9	-0.37	-0.24	-0.52
199.064	20.048	0.0304	9.6	-	6.0	-0.37	-0.23	-0.51
194.399	27.493	0.0244	10.1	-	6.2	-0.30	-0.15	-0.44
183.202	27.501	0.0275	11.5	-	7.1	-0.24	-0.08	-0.37
194.590	28.149	0.0263	10.8	-	6.8	-0.15	0.01	-0.30
191.547	30.723	0.0218	14.0	-	8.7	-0.46	-0.32	-0.62
194.257	29.063	0.0250	8.9	-	5.3	-0.14	0.03	-0.29
194.697	27.675	0.0280	10.8	-	6.7	-0.28	-0.12	-0.41
187.131	23.305	0.0218	9.9	-	6.1	-0.41	-0.28	-0.57
195.217	28.366	0.0255	12.1	-	7.6	-0.28	-0.13	-0.41
178.197	29.329	0.0287	14.0	-	9.0	-0.39	-0.26	-0.56
194.887	27.984	0.0194	9.2	-	5.7	-0.37	-0.23	-0.52
189.865	27.102	0.0235	10.5	-	6.3	-0.33	-0.17	-0.48
184.892	25.586	0.0230	10.7	-	6.6	-0.27	-0.12	-0.39
172.907	26.111	0.0324	12.0	-	7.3	-0.38	-0.24	-0.54
195.359	27.886	0.0183	8.9	-	5.4	-0.32	-0.18	-0.47
175.904	19.605	0.0219	12.6	-	7.6	-0.46	-0.32	-0.62
175.907	19.090	0.0226	9.4	-	5.8	-0.44	-0.30	-0.60
185.020	27.975	0.0277	9.2	-	5.1	-0.23	-0.05	-0.39
195.517	29.253	0.0243	9.2	-	5.6	-0.35	-0.21	-0.51
184.993	25.772	0.0225	13.4	-	8.0	-0.44	-0.30	-0.61
194.730	27.965	0.0189	13.0	-	7.7	-0.48	-0.33	-0.64
194.422	31.275	0.0263	9.7	-	5.8	-0.31	-0.16	-0.46
179.542	25.122	0.0149	10.1	-	6.2	-0.34	-0.19	-0.49
194.983	28.035	0.0272	10.8	-	6.6	-0.26	-0.10	-0.40
181.993	22.796	0.0217	11.0	-	6.4	-0.19	0.00	-0.34
175.933	20.273	0.0229	9.6	-	5.9	-0.28	-0.13	-0.41
179.601	30.650	0.0294	10.0	-	5.7	-0.23	-0.06	-0.38
194.908	27.907	0.0267	10.7	-	6.6	-0.28	-0.13	-0.42
194.899	27.959	0.0239	9.8	-	5.7	-0.43	-0.28	-0.60
184.949	30.339	0.0282	12.0	-	7.2	-0.45	-0.30	-0.62
182.077	25.161	0.0194	10.5	-	6.2	-0.49	-0.34	-0.64
194.110	27.727	0.0228	9.1	-	4.8	-0.15	0.05	-0.33
178.528	25.567	0.0208	9.0	-	5.3	-0.54	-0.37	-0.71
174.435	22.021	0.0316	12.1	-	6.9	-0.14	0.05	-0.30
179.350	29.927	0.0287	10.6	-	6.4	-0.32	-0.16	-0.47
199.654	30.865	0.0325	10.5	-	6.1	-0.41	-0.27	-0.59
194.873	27.850	0.0226	9.9	-	6.0	-0.42	-0.28	-0.59

continued on next page..

Table A.1 – continued from previous page

RA (J2000)	Dec (J2000)	z	Age (Gyr)	Age upper (Gyr)	Age lower (Gyr)	Z (dex)	Z upper (dex)	Z lower (dex)
195.071	28.064	0.0205	13.7	-	7.8	-0.37	-0.21	-0.55
194.945	27.974	0.0314	10.8	-	6.5	-0.17	0.01	-0.33
194.769	27.911	0.0214	9.6	-	5.6	-0.27	-0.11	-0.42
190.808	31.085	0.0234	10.7	-	6.2	-0.16	0.03	-0.32
181.137	22.275	0.0278	11.0	-	6.4	-0.31	-0.14	-0.47
178.236	20.479	0.0217	8.9	-	5.0	-0.14	0.04	-0.30
176.643	19.110	0.0204	10.2	-	5.8	-0.47	-0.30	-0.64
176.009	19.950	0.0208	9.7	-	5.7	-0.48	-0.32	-0.65
180.656	21.159	0.0249	11.0	-	6.5	-0.37	-0.22	-0.54
182.085	25.335	0.0219	11.9	-	6.8	-0.29	-0.13	-0.44
195.490	28.006	0.0257	13.4	-	7.8	-0.45	-0.30	-0.62
176.697	20.675	0.0234	9.7	-	5.7	-0.33	-0.17	-0.49
184.860	21.170	0.0318	8.9	-	5.1	-0.25	-0.08	-0.41
181.696	27.910	0.0260	9.6	-	5.7	-0.34	-0.19	-0.51
199.619	31.777	0.0324	11.7	-	6.9	-0.39	-0.25	-0.57
179.760	21.808	0.0215	12.8	-	7.5	-0.22	-0.04	-0.37
195.791	28.584	0.0228	10.8	-	6.4	-0.30	-0.13	-0.45
192.654	27.483	0.0221	9.6	-	5.4	-0.23	-0.06	-0.38
185.105	30.521	0.0280	10.0	-	5.6	-0.25	-0.07	-0.40
177.745	30.570	0.0213	11.4	-	6.5	-0.37	-0.21	-0.54
175.637	26.489	0.0303	13.0	-	7.5	-0.55	-0.38	-0.71
173.831	20.034	0.0317	8.6	-	5.2	-0.35	-0.21	-0.52
177.711	20.049	0.0217	12.2	-	7.0	-0.21	-0.02	-0.36
185.100	25.561	0.0229	9.0	-	5.4	-0.46	-0.30	-0.63
177.884	27.647	0.0288	9.7	-	5.7	-0.28	-0.12	-0.42
181.662	28.174	0.0282	12.2	-	7.0	-0.48	-0.32	-0.65
183.904	27.012	0.0254	10.4	-	5.8	-0.45	-0.29	-0.63
176.551	20.392	0.0231	10.1	-	5.8	-0.39	-0.24	-0.57
171.470	18.599	0.0205	10.7	-	6.4	-0.29	-0.13	-0.44
186.535	20.336	0.0309	10.7	-	6.2	-0.30	-0.14	-0.46
192.275	17.026	0.0221	9.6	-	5.5	-0.32	-0.16	-0.49
194.932	27.995	0.0223	14.0	-	8.6	-0.43	-0.29	-0.60
180.717	26.253	0.0321	14.0	-	8.3	-0.50	-0.34	-0.67
184.923	28.725	0.0254	9.2	-	5.3	-0.34	-0.19	-0.52
176.105	19.828	0.0148	11.5	-	6.8	-0.34	-0.19	-0.50
181.624	27.950	0.0273	10.9	-	6.0	-0.39	-0.23	-0.58
181.867	24.951	0.0220	9.5	-	5.4	-0.36	-0.21	-0.54
199.175	21.980	0.0233	9.0	-	5.2	-0.24	-0.08	-0.39
195.656	27.176	0.0183	7.7	-	4.8	-0.41	-0.26	-0.61
195.518	28.895	0.0271	13.4	-	7.6	-0.25	-0.06	-0.41
181.932	28.320	0.0293	12.4	-	7.0	-0.28	-0.10	-0.44
181.095	20.258	0.0211	8.9	-	5.1	-0.28	-0.11	-0.43
181.612	32.843	0.0242	11.9	-	6.8	-0.30	-0.13	-0.46
174.271	19.924	0.0208	12.0	-	6.9	-0.41	-0.26	-0.60
195.576	32.891	0.0253	11.2	-	6.0	-0.24	-0.04	-0.41
183.326	21.634	0.0244	12.3	-	7.1	-0.53	-0.36	-0.69
181.396	25.097	0.0235	9.5	-	5.3	-0.37	-0.20	-0.56
170.251	24.303	0.0282	10.5	-	6.0	-0.28	-0.11	-0.43
195.170	27.997	0.0236	12.4	-	7.3	-0.29	-0.13	-0.43
178.760	27.298	0.0219	11.6	-	6.7	-0.22	-0.03	-0.38
194.844	27.897	0.0172	10.4	-	5.9	-0.37	-0.21	-0.56
194.913	28.896	0.0204	10.3	-	5.5	-0.47	-0.29	-0.66
184.965	28.423	0.0265	12.2	-	6.7	-0.46	-0.28	-0.65
174.794	26.435	0.0233	11.3	-	6.2	-0.15	0.05	-0.33
190.703	26.640	0.0222	7.4	-	4.1	-0.34	-0.14	-0.56

continued on next page..

Table A.1 – continued from previous page

RA (J2000)	Dec (J2000)	z	Age (Gyr)	Age upper (Gyr)	Age lower (Gyr)	Z (dex)	Z upper (dex)	Z lower (dex)
196.991	28.711	0.0252	13.9	-	7.7	-0.43	-0.26	-0.63
175.043	25.310	0.0225	10.2	-	6.1	-0.39	-0.24	-0.56
179.686	28.290	0.0274	8.7	-	5.2	-0.38	-0.23	-0.56
175.799	26.559	0.0301	13.2	-	7.6	-0.39	-0.24	-0.58
186.449	29.663	0.0304	13.7	-	7.4	-0.18	0.04	-0.35
184.788	20.432	0.0309	7.8	-	4.6	-0.33	-0.16	-0.51
189.054	26.941	0.0246	10.4	-	5.8	-0.21	-0.03	-0.38
181.878	31.348	0.0227	11.2	-	6.2	-0.54	-0.36	-0.70
199.985	29.448	0.0319	9.6	-	5.2	-0.24	-0.05	-0.41
196.243	29.122	0.0197	8.7	-	5.2	-0.55	-0.38	-0.72
172.393	21.726	0.0326	11.1	-	6.2	-0.39	-0.23	-0.59
178.435	23.126	0.0272	11.1	-	6.4	-0.27	-0.09	-0.42
194.660	27.544	0.0199	9.4	-	5.4	-0.31	-0.15	-0.47
180.547	27.742	0.0280	8.2	-	4.9	-0.34	-0.19	-0.52
182.199	25.471	0.0229	12.0	-	6.8	-0.47	-0.31	-0.64
176.868	18.053	0.0195	8.4	-	4.7	-0.30	-0.11	-0.49
191.036	25.416	0.0174	12.5	-	7.2	-0.48	-0.32	-0.65
174.083	20.522	0.0214	11.8	-	6.4	-0.56	-0.38	-0.75
184.619	17.266	0.0255	7.9	-	4.4	-0.23	-0.03	-0.39
180.991	20.312	0.0247	9.9	-	5.5	-0.44	-0.27	-0.63
176.108	20.103	0.0247	7.6	-	4.1	-0.27	-0.08	-0.46
180.650	20.545	0.0243	12.9	-	7.1	-0.54	-0.36	-0.72
186.966	24.942	0.0228	8.1	-	4.8	-0.35	-0.19	-0.54
195.225	27.784	0.0277	12.7	-	6.6	-0.59	-0.39	-0.78
179.731	28.399	0.0282	12.3	-	6.8	-0.53	-0.35	-0.70
179.682	22.217	0.0294	11.8	-	6.4	-0.34	-0.16	-0.54
195.161	28.015	0.0254	8.5	-	4.7	-0.29	-0.10	-0.47
194.633	28.050	0.0190	8.5	-	5.0	-0.39	-0.24	-0.59
186.924	28.698	0.0234	8.2	-	4.5	-0.26	-0.07	-0.43
196.576	27.255	0.0253	10.5	-	5.7	-0.31	-0.13	-0.49
171.021	24.615	0.0255	8.5	-	4.4	-0.25	-0.05	-0.44
186.022	28.309	0.0306	12.5	-	6.7	-0.42	-0.25	-0.63
189.020	26.900	0.0261	8.9	-	4.9	-0.23	-0.05	-0.39
172.013	27.386	0.0320	11.4	-	6.2	-0.39	-0.21	-0.59
196.454	28.107	0.0244	10.9	-	5.8	-0.44	-0.27	-0.64
197.348	28.281	0.0209	10.0	-	5.0	-0.28	-0.07	-0.47
175.305	27.665	0.0233	11.1	-	5.8	-0.40	-0.23	-0.62
195.390	29.131	0.0245	7.9	-	4.9	-0.49	-0.33	-0.67
184.922	28.826	0.0250	11.8	-	5.6	-0.20	0.03	-0.39
176.086	19.826	0.0185	10.1	-	5.7	-0.27	-0.10	-0.44
194.000	28.187	0.0187	10.6	-	5.5	-0.51	-0.32	-0.70
185.015	20.402	0.0309	11.5	-	6.0	-0.52	-0.32	-0.70
174.416	21.562	0.0287	9.8	-	4.9	-0.28	-0.07	-0.48
195.686	32.085	0.0244	10.6	-	5.6	-0.40	-0.22	-0.61
176.526	19.634	0.0208	13.5	-	7.0	-0.34	-0.14	-0.56
193.878	27.544	0.0234	8.5	-	4.4	-0.31	-0.11	-0.53
194.834	28.198	0.0316	10.9	-	4.9	-0.21	0.04	-0.42
194.257	27.372	0.0234	12.9	-	6.4	-0.18	0.05	-0.37
194.980	28.128	0.0252	11.5	-	6.0	-0.34	-0.15	-0.54
195.307	27.914	0.0195	7.3	-	3.9	-0.34	-0.15	-0.56
181.051	20.174	0.0216	7.6	-	3.9	-0.16	0.06	-0.34
194.793	27.620	0.0191	13.8	-	7.7	-0.44	-0.27	-0.64
194.070	27.446	0.0214	8.4	-	4.4	-0.23	-0.02	-0.40
195.846	28.864	0.0219	13.1	-	6.4	-0.27	-0.03	-0.48
181.139	28.382	0.0271	12.6	-	6.5	-0.38	-0.19	-0.60

continued on next page..

Table A.1 – continued from previous page

RA (J2000)	Dec (J2000)	z	Age (Gyr)	Age upper (Gyr)	Age lower (Gyr)	Z (dex)	Z upper (dex)	Z lower (dex)
176.093	19.775	0.0222	8.0	-	4.6	-0.39	-0.21	-0.60
181.894	25.281	0.0215	9.3	-	4.3	-0.25	-0.01	-0.47
188.072	27.291	0.0207	11.8	-	5.3	-0.12	0.14	-0.33
172.787	23.057	0.0310	10.3	-	5.4	-0.28	-0.09	-0.46
194.721	27.813	0.0184	11.2	-	5.9	-0.21	-0.00	-0.38
184.548	28.544	0.0285	9.2	-	4.7	-0.20	0.01	-0.38
192.397	27.198	0.0208	9.6	-	4.9	-0.19	0.02	-0.37
194.934	27.958	0.0230	9.8	-	4.6	-0.19	0.04	-0.38
194.368	28.176	0.0272	9.0	-	4.6	-0.23	-0.02	-0.41
181.679	28.191	0.0286	9.7	-	4.9	-0.28	-0.07	-0.47
194.446	29.150	0.0239	12.6	-	6.9	-0.31	-0.12	-0.49
179.808	30.891	0.0294	10.9	-	5.5	-0.27	-0.07	-0.46
193.151	26.750	0.0263	7.3	-	3.4	-0.19	0.06	-0.40
185.251	28.535	0.0265	9.1	-	4.5	-0.22	0.01	-0.40
186.173	29.866	0.0303	8.0	-	4.0	-0.16	0.07	-0.36
178.193	32.310	0.0317	13.6	-	7.4	-0.58	-0.39	-0.77
184.088	17.769	0.0304	7.5	-	4.0	-0.34	-0.14	-0.57
194.916	28.927	0.0201	10.7	-	5.7	-0.46	-0.28	-0.65
184.743	24.186	0.0245	11.0	-	5.4	-0.39	-0.20	-0.63
194.461	27.879	0.0232	7.7	-	4.0	-0.25	-0.03	-0.44
177.675	32.697	0.0321	12.8	-	6.9	-0.49	-0.30	-0.69
173.955	21.739	0.0297	7.7	-	4.4	-0.44	-0.26	-0.65
195.434	28.214	0.0261	9.6	-	4.1	-0.23	0.03	-0.47
195.301	27.604	0.0252	6.8	-	3.0	-0.09	0.22	-0.34
199.698	30.884	0.0318	10.0	-	4.5	-0.23	0.02	-0.43
195.288	27.818	0.0197	9.8	-	4.9	-0.53	-0.32	-0.76
198.186	31.809	0.0211	7.8	-	4.1	-0.38	-0.18	-0.62
176.513	19.437	0.0173	11.4	-	5.5	-0.22	0.01	-0.41
175.692	19.949	0.0207	8.5	-	4.2	-0.20	0.02	-0.39
189.016	27.078	0.0241	8.8	-	3.8	-0.14	0.13	-0.37
182.521	17.625	0.0253	11.5	-	5.7	-0.34	-0.14	-0.56
177.500	17.006	0.0203	8.6	-	4.1	-0.26	-0.02	-0.47
195.807	27.369	0.0213	11.1	-	4.5	-0.14	0.14	-0.36
184.961	28.405	0.0283	10.5	-	4.3	-0.13	0.14	-0.34
194.442	27.757	0.0204	11.5	-	5.1	-0.24	0.01	-0.46
194.767	27.959	0.0235	7.5	-	3.7	-0.15	0.08	-0.35
179.531	26.523	0.0226	9.1	-	4.9	-0.66	-0.45	-0.90
174.586	20.433	0.0241	9.5	-	4.7	-0.30	-0.09	-0.51
193.989	27.905	0.0219	8.8	-	3.6	-0.20	0.09	-0.45
175.796	20.030	0.0235	7.5	-	3.9	-0.42	-0.21	-0.67
172.114	27.397	0.0325	10.5	-	5.1	-0.53	-0.31	-0.76
188.922	26.482	0.0225	9.0	-	4.7	-0.46	-0.26	-0.70
195.840	28.309	0.0184	9.4	-	4.0	-0.19	0.08	-0.40
194.146	30.769	0.0261	8.9	-	4.5	-0.51	-0.30	-0.76
185.684	27.737	0.0235	8.6	-	4.6	-0.41	-0.22	-0.65
194.548	27.940	0.0284	8.6	-	4.4	-0.35	-0.14	-0.59
176.914	19.939	0.0205	8.9	-	4.4	-0.48	-0.26	-0.72
182.088	25.364	0.0224	13.0	-	5.5	-0.40	-0.18	-0.67
175.431	21.166	0.0216	8.2	-	3.5	-0.05	4.00	-0.28
176.504	19.384	0.0242	10.7	-	4.9	-0.39	-0.16	-0.65
194.507	27.854	0.0190	7.5	-	3.3	-0.16	0.13	-0.38
171.253	27.525	0.0244	8.6	-	4.0	-0.30	-0.07	-0.55
176.229	19.776	0.0274	7.2	-	3.8	-0.38	-0.19	-0.62
175.987	19.956	0.0210	10.6	-	5.4	-0.44	-0.25	-0.67
185.294	25.325	0.0231	7.9	-	3.5	-0.32	-0.06	-0.59

continued on next page..

Table A.1 – continued from previous page

RA (J2000)	Dec (J2000)	z	Age (Gyr)	Age upper (Gyr)	Age lower (Gyr)	Z (dex)	Z upper (dex)	Z lower (dex)
183.929	24.004	0.0224	6.0	-	2.7	-0.14	0.20	-0.40
196.261	28.739	0.0279	6.8	-	3.2	-0.30	-0.06	-0.56
176.126	20.329	0.0196	7.9	-	3.7	-0.13	0.12	-0.34
170.464	24.608	0.0241	9.9	-	4.3	-0.19	0.07	-0.40
176.550	19.853	0.0183	10.4	-	4.4	-0.37	-0.12	-0.65
193.525	27.019	0.0284	8.3	-	3.6	-0.15	0.13	-0.38
196.213	25.839	0.0242	11.7	-	5.4	-0.39	-0.17	-0.65
184.960	28.729	0.0270	6.9	-	2.8	-0.08	4.00	-0.35
194.061	27.506	0.0248	6.4	-	2.8	-0.12	0.20	-0.37
194.834	28.074	0.0239	10.6	-	4.8	-0.40	-0.17	-0.67
194.979	27.796	0.0275	7.1	-	3.3	-0.15	0.11	-0.37
174.595	21.839	0.0313	12.7	-	6.0	-0.54	-0.31	-0.77
194.084	29.300	0.0221	9.9	-	4.2	-0.41	-0.15	-0.71
189.125	32.080	0.0235	6.5	-	3.2	-0.43	-0.20	-0.71
178.366	20.694	0.0226	8.2	-	3.6	-0.16	0.11	-0.38
189.826	31.990	0.0236	11.1	-	5.0	-0.45	-0.22	-0.71
178.800	24.790	0.0284	11.3	-	5.2	-0.41	-0.19	-0.66
193.570	28.077	0.0228	8.1	-	3.5	-0.42	-0.16	-0.72
194.207	27.094	0.0231	5.7	-	2.9	-0.40	-0.15	-0.72
194.910	27.987	0.0227	13.1	-	6.1	-0.27	-0.02	-0.49
199.750	30.817	0.0315	7.5	-	3.3	-0.29	-0.04	-0.55
176.268	19.571	0.0215	10.7	-	4.4	-0.35	-0.09	-0.63
179.910	27.774	0.0272	7.4	-	3.2	-0.40	-0.14	-0.70
194.904	27.826	0.0209	7.2	-	3.4	-0.54	-0.29	-0.83
196.589	29.170	0.0243	9.2	-	3.8	-0.17	0.12	-0.39
194.947	21.813	0.0238	5.6	-	3.0	-0.67	-0.45	-0.96
185.010	28.327	0.0284	8.0	-	3.5	-0.24	0.03	-0.49
174.296	20.274	0.0254	6.1	-	3.1	-0.35	-0.13	-0.62
188.927	26.909	0.0264	6.2	-	3.0	-0.37	-0.10	-0.68
174.412	22.041	0.0289	5.9	-	2.8	-0.20	0.13	-0.49
196.463	29.810	0.0236	7.6	-	3.5	-0.56	-0.30	-0.87
186.580	26.129	0.0311	6.5	-	3.1	-0.38	-0.13	-0.68
179.913	28.165	0.0272	5.4	-	2.6	-0.31	0.01	-0.64
198.951	19.636	0.0228	13.4	-	5.4	-0.64	-0.36	-0.94
194.959	27.925	0.0328	9.3	-	3.8	-0.30	-0.03	-0.57
195.053	27.782	0.0234	8.9	-	4.4	-0.69	-0.44	-0.97
176.356	19.298	0.0215	10.2	-	4.7	-0.64	-0.39	-0.91
193.833	27.867	0.0233	5.6	-	2.8	-0.38	-0.09	-0.72
197.340	28.312	0.0201	11.3	-	4.8	-0.63	-0.37	-0.93
195.165	29.019	0.0242	5.5	-	2.7	-0.28	0.02	-0.59
186.018	26.419	0.0315	5.8	-	2.8	-0.24	0.07	-0.53
176.471	19.612	0.0225	7.9	-	3.3	-0.37	-0.10	-0.68
183.720	27.693	0.0289	5.4	-	2.8	-0.40	-0.13	-0.73
194.839	27.974	0.0202	6.7	-	2.9	-0.43	-0.13	-0.78
179.743	28.367	0.0274	10.9	-	4.5	-0.65	-0.36	-0.96
182.430	18.930	0.0246	5.5	-	2.7	-0.29	0.03	-0.61
171.439	24.140	0.0237	13.7	-	5.3	-0.60	-0.32	-0.90
194.939	32.045	0.0227	7.6	-	3.3	-0.81	-0.52	-1.11
175.802	20.336	0.0203	5.5	-	2.6	-0.31	0.02	-0.65
196.218	26.919	0.0231	5.2	-	2.6	-0.24	0.12	-0.55